Ion tempeture measurements in the scrape-off layer of the Tore Supra Tokamak

Martin Kocan

Nancy-Université
Université Henri Poincaré

U.F.R. Sciences & Techniques de la Matière et des Procédés
Ecole Doctorale EMMA
Département de Formation Doctorale POEM

Thèse

présentée pour l'obtention du titre de

Docteur de l'Université Henri Poincaré, Nancy-I

en Physique des plasmas

par **Martin KOČAN**

Ion temperature measurements in the scrape-off layer of the Tore Supra tokamak

Soutenance publique prévue l'Octobre 6, 2009

Membres du jury :

Président :	M. Michel VERGNAT	Professeur, U.H.P., Nancy I
Rapporteurs :	M. Jan STÖCKEL	Chercheur (HDR) IPP, Prague
	M. Volker ROHDE	Chercheur (HDR) IPP, Garching
Examinateurs :	M. Gerard BONHOMME (Directeur de thèse)	Professeur, U.H.P., Nancy I
	M. James Paul GUNN (Directeur de thèse CEA)	Chercheur CEA, Cadarache
	M. André GROSMAN	Chercheur CEA, Cadarache
	M. Guido Van OOST	Professeur, Gent University

Laboratoire de Physique des Milieux Ionisés et Applications
Faculté des Sciences & Techniques - 54500 Vandoeuvre-lès-Nancy

Abstract

The thesis describes measurements of the scrape-off layer (SOL) ion temperature T_i with a retarding field analyzer (RFA) in the limiter tokamak Tore Supra. In the first chapter, some well known facts about nuclear fusion, limiter SOL, Langmuir probes, etc. are briefly recalled. Various diagnostics for SOL T_i measurements developed in the past are addressed as well. The second chapter is dedicated to the RFA. The principle of the RFA, technical details and operation of the Tore Supra RFA, and the influence of instrumental effects on RFA measurements are addressed. In the third chapter, the experimental results are presented in the form of papers published (or submitted for publication) during the thesis. Three ongoing projects to validate RFA T_i measurements in Tore Supra are summarized in the last chapter.

Considerable emphasis is placed on study of the instrumental effects of RFAs and their influence on T_i measurements. In general, the influence of instrumental effects on T_i measurements is found to be relatively small. Selective ion transmission through the RFA slit is found to be responsible for an overestimation of T_i by less than 14% even for relatively thick slit plates. The effect of positive space charge inside the analyzer, the influence of the electron repelling grid, the misalignment of the probe head with respect to the magnetic field, and the attenuation of the incident ion current by some of the probe components on T_i measurements is negligible.

The instrumental study is followed by systematic measurements of T_i (as well as other parameters) in the Tore Supra SOL. This includes the scaling of SOL temperatures and electron density with the main plasma parameters (such as the plasma density, toroidal magnetic field, working gas, and the radiated power fraction). Except at very high densities or in detached plasmas, SOL T_i is found to be higher than T_e by up to a factor of 7. While SOL T_i is found to vary by almost two orders of magnitude, following the variation of the core temperatures, SOL T_e changes only little and seems to be decoupled from the core plasma. The first continuous T_i / T_e profile from the edge of the confined plasma into the SOL is constructed using data from different tokamaks. It is shown that $T_i / T_e > 1$ in the SOL but also in the confined plasma, and increases with radius. Measurements of edge T_i / T_e in JET L-mode are analyzed.

The first evidence of poloidal asymmetry of the radial ion and electron energy transport in the SOL is reported. Implications for ITER start-up phase are discussed. Correlation of the asymmetries of SOL T_i and T_e measured from both directions along the magnetic field lines with changes of the parallel Mach number is studied.

SOL T_i was measured for the first time in Tore Supra by charge exchange recombination spectroscopy (CXRS) and compared to RFA data. A factor of 4 higher T_i measured by CXRS is a subject of further analysis.

The segmented tunnel probe (STP) for fast measurements of SOL T_i and T_e has been designed, built, calibrated by particle simulations, and used for the first time in a large tokamak. Preliminary results from the STP measurements in Tore Supra are presented. The disagreement between the currents to the probe electrodes predicted by simulations and the measurements is addressed. Large floating potentials measured by the side of the probe connected to the ICRH antenna are reported.

Acknowledgement

I owe my thanks to many people who made this thesis possible. Foremost I thank my thesis supervisor Jamie Gunn. His foresight and physical intuition has been a constant guide throughout this entire work. Although my name appears alone on this thesis, he certainly deserves to be a co-author.

I also thank my wife Hana for being so tolerant the past few months and my daughter Judita for relatively calm nights.

Thanks are also due to Professor Gerard Bonhomme for his support as a thesis director.

I am greatly indebted to Jean Yves Pascal for his excellent technical expertise.

I thank the members of the jury for reading this thesis and for constructive comments.

I also record my appreciation for enlightening discussions with Vincent Basiuk, Sophie Carpentier, Frederic Clairet, Yann Corre, Nicolas Fedorczak, Christel Fenzi, Xavier Garbet, Thomas Gerbaud, Remy Guirlet, Philippe Ghendrih, Tuong Hoang, Frederic Imbeaux, Philippe Lotte, Yannick Marandet, Philippe Moreau, Pascale Monier-Garbet, Bernard Pegourie, Jean-Luc Segui, Jean-Claude Vallet and other members of the IRFM.

I would like to thank Michael Komm for running SPICE simulations, Patrick Tamain for helping me with a simple edge power balance model and Richard Pitts for useful comments.

I thank IRFM for supporting this work as well as my participations at the conferences, workshops, summer schools and stays on MAST and JET. The leaders of the Tore Supra task-force AP3 (Patrick Maget, Remy Guirlet and Pascale Hannequin) are gratefully acknowledged for the experimental time offered for the measurements reported in this thesis. I also thank CEA for financing my thesis.

I thank Yasmin Andrew for her help and many useful discussions during my stay on JET.

Finally, I would like to thank the members of the IPP Prague mechanical workshop for the high quality work with which they manufactured the segmented tunnel probe for Tore Supra.

Contents

Chapter 1

Introduction

1.1. Basic principle of magnetic confinement fusion

1.1.1. Why fusion?

In 2005, the total worldwide energy consumption was about 5 x 10^{20} J, which corresponds to an energy consumption rate of 15 TW (figure 1.1, left). This is equivalent to three cubic miles of oil (CMO), an energy unit (1.6×10^{20} J) introduced by American engineer H. Crane in order to provide an illustrative concept of the world's energy consumption and resources. About 85% of the consumption was provided by combustion of fossil fuels such as oil, coal and gas (figure 1.1, right).

Global proven oil reserves are estimated at approximately 43 CMO[1] and, at the current rate of use, they would last for about 40 years. However, the annual consumption of oil is needed to increase by 50% in the next 25 years, mostly due to the economical development of India and China[2]. However, discoveries of new oil fields have been declining since the 1960's, and in fact the difference between annual discoveries and annual consumption became negative in 1980. The current rate of oil consumption cannot be maintained and some expert analysis shows that it might already be declining[3]. With

[1] "World Proved Reserves of Oil and Natural Gas, Most Recent Estimates", Energy Information Administration, 2008, http://www.eia.doe.gov/emeu/international/reserves.html.
[2] "World Energy Outlook 2005", International Energy Agency, 2005, http://www.iea.org/textbase/nppdf/free/2005/weo2005.pdf.
[3] http://www.peakoil.net/

only 30 years of proven reserves, nuclear fission also faces a problem of supplying a fissionable material (basically uranium) as some countries, like for example China, are accelerating the development of their fission industry. For the coal and the natural gas the proven reserves are 121 and 42 CMO respectively, which corresponds to 150 and 69 years at the current rate of consumption).

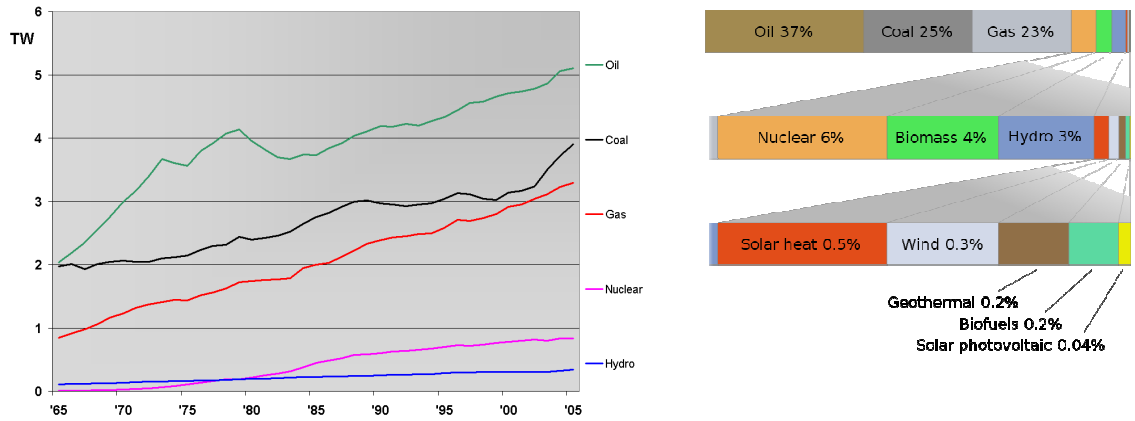

Figure 1.1. Left: rate of world energy usage in terawatts in 1965-2005 (source: Energy Information Administration, U.S. Department of Energy, July 31, 2006). Right: Energy sources in 2005 (source: "BP Statistical review of world energy June 2006", British Petroleum, June 2006).

Therefore, the fossil fuels may not be able to meet an increasing demand for energy. It is also unlikely that alternative sources like for example wind, solar or biomass will make substantial contribution in the near future.

The CMO is a powerful means of understanding the difficulty of replacing oil by other sources. Table 1.1 illustrates the problem of replacing one cubic mile of oil with energy from five different alternative sources [4] (for comparison, 10^{12} USD is the approximate gross domestic product of the United Kingdom, 270000 km^2 is the area of New Zealand, and the cost of one CMO of oil was about $3x10^{12}$ USD) in 2008.

Source	Number	Cost (10^{12} USD)	Area [km^2]
Hydroelectric dams	200	6	1200000
Nuclear plants	2600	13	10000
Coal plants	5200	3.4	10000
Wind turbines	1600000	3.3	270000
Photovoltaic	4500000000	68	63000

Table 1.1. Replacement of one CMO by alternative sources. One dam is rated as a world largest Three Gorges Dam (18 GW in its full power). An average nuclear power plant is equivalent of a 1 GW, a coal plant is rated at 0.5 GW. A wind turbine is one with a 100-meter blade span, and rated at 1.65 MW. A solar panel is assumed to be a 2.1-kW home-roof system (source: http://www.spectrum.ieee.org/jan07/4820).

[4] http://www.spectrum.ieee.org/jan07/4820

The environmental, social, and financial costs of such replacement are, however, immense and require flooding large areas and displacing millions of people (hydro energy), produces radioactive waste (nuclear plants), contribute to acid rain, global warming, and air pollution, and may obtain its fuel via controversial methods such as mountaintop removal (coal plants). An alternative source like wind turbines, photovoltaic, or biomass requires a location with an abundance of steady wind or sun, may be visually obtrusive, requires large areas or are relatively expensive. An inexhaustible, safe, and clean energy source is currently not available.

Large quantities of energy can be generated by fusing the nuclei of light isotopes (section 1.1.2). Nuclear fusion promises to be a safe, inexhaustible and relatively little polluting method of energy production and to become the best compromise between nature and the energy needs of mankind. However tantalizing the potential of fusion energy, it should be also noted that controlled fusion is a very difficult process to master and after fifty years of active research an economically viable fusion power plant is still many years away.

1.1.2. The principle of nuclear fusion

The energy released in the nuclear fusion reactions of light nuclei (nucleon number $A < 60$) comes from the difference in the nuclear binding energy ΔE, figure 1.2. Masses of such nuclei are smaller by Δm compared to the individual masses of the protons and the neutrons which constitute the nuclei. According to Einstein's energy-mass relation $\Delta E = \Delta m c^2$ ($\approx$ MeV, i.e. 6 orders of magnitude larger than the energy released in chemical reactions of burning fossil fuels).

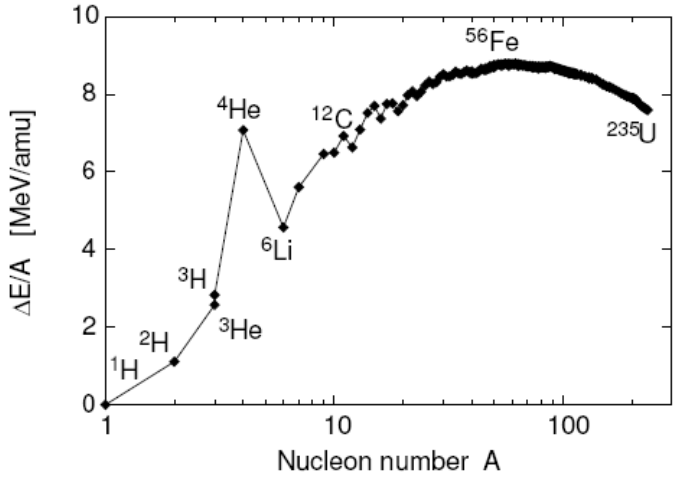

Figure 1.2. Nuclear binding energy ΔE per nucleon as a function of the nucleon number A.

Nuclear fusion reactions are governed by the strong nuclear force acting over a distance of the order of the nucleon radius. Above this distance the repulsive Coulomb force between the positively charged nuclei dominates. To overcome the Coulomb repulsion and to approach a pair of nuclei close enough so that the fusion reaction can

occur requires the kinetic energies of the fusing nuclei to be of the order of several hundreds of keV,

$$E_{crit} \propto P_{tunneling} \propto \exp\left(-\frac{Z_1 Z_2 e^2}{hv}\right) \tag{1.1}$$

where $P_{tunneling}$ is the tunneling probability, eZ_1 and eZ_2 are charges of the colliding nuclei and v is their relative velocity. The fusion reactions of the lightest nuclei (hydrogen isotopes) are thus most probable.

From the possible nuclear fusion reactions, the deuterium-tritium (D-T) reaction

$$D + T \rightarrow {}^4He + n \tag{1.2}$$

(with $\Delta E \cong 17.6\,\text{MeV}$) has the largest cross-section with the maximum at relatively low kinetic energies (figure 1.3) and is therefore the most promising candidate for future fusion reactors. The distribution of ΔE between the ^{4}He (α particle) and the neutron is inversely proportional to their masses $m_n / m_\alpha = E_\alpha / E_n = 3.54\,\text{MeV} / 14.05\,\text{MeV}$.

The kinetic energies needed for fusion reactions are in contrast to the fission reactions of the nuclei with $A > 60$ which are triggered by the capture of a neutron and can thus occur at room temperatures.

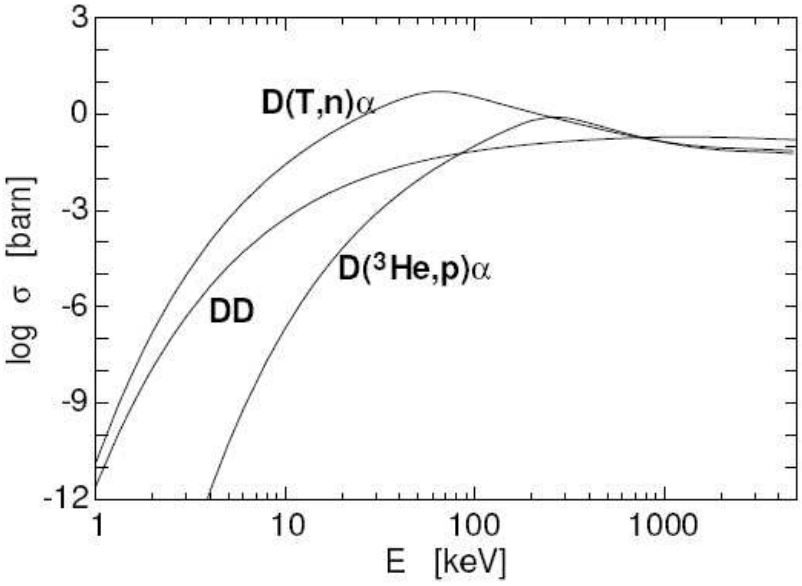

Figure 1.3. Cross-sections for the reactions D-T, D-D and D-^{3}He. The two D-D reactions ($D + D \rightarrow {}^3He + n$ and $D + D \rightarrow T + p$) have similar cross-sections and the graph shows their sum.
1 barn = 10^{-28} m^2.

1.1.3. Ignition

A thermonuclear fusion reactor is supposed to be a system in which the energy produced in D-T reactions is substantially larger than that used for its operation. The term "ignition" is used for the state of the system at which all energy losses are compensated by collisions of the α particles from the D-T reactions with the background particles so that external heating in order to sustain the reactions is not required. The neutrons are

supposed to leave the plasma without interaction so that in the reactor their kinetic energy can be transferred into utilizable heat.

The ignition criterion [Lawson 1957] can be derived from a simple energy balance in the fusion reactor:

$$n\tau_E T > \frac{12kT^2}{\langle\sigma v\rangle E_\alpha (1+5/Q)} \tag{1.3}$$

where n is the density of the colliding particles, τ_E is the energy confinement time that equals to the total energy inside the reactor volume ($\propto nT$) divided by the total power losses from the reactor volume, T is the temperature of the colliding particles in the reactor which are assumed to be Maxwellian, $\langle\sigma v\rangle$ [$m^3\,s^{-1}$] is the mean of the product of the reaction cross-section and the relative velocity of the colliding particles and Q is the ratio of the power released by the fusion reactions to the external heating power. Ignition is thus reached when $Q=\infty$, i.e. when $n\tau_E T \cong 3\cdot 10^{21}\,m^{-3}\,s\,keV$ at $T \cong 10\,keV$. However, the fusion reactor can operate economically at finite $Q>1$. The approach of the $n\tau_E T$ values obtained in different experimental fusion reactors to the region of of $Q=\infty$ is illustrated in figure 1.4.

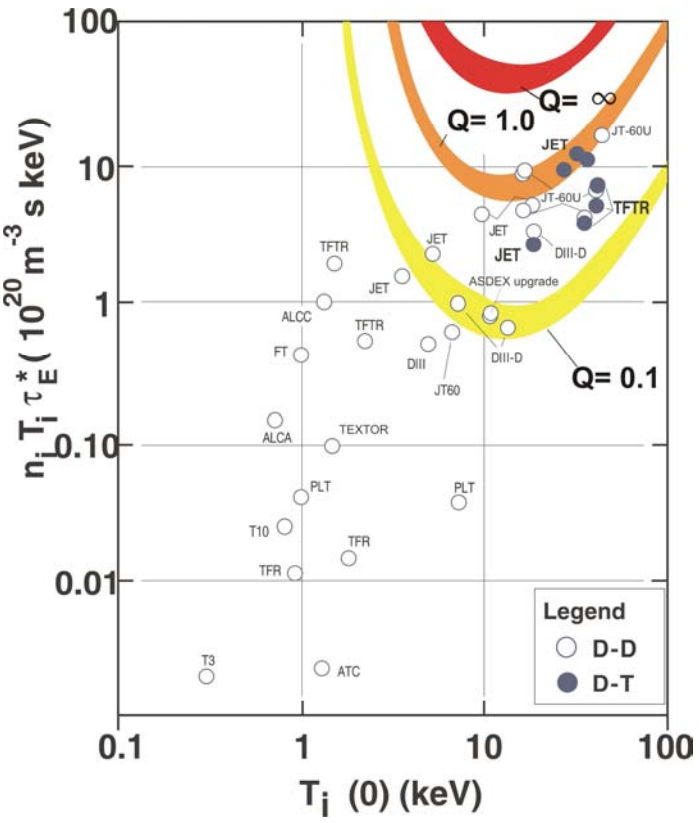

Figure 1.4. Diagram of $n\tau_E T$ values obtained in different tokamaks in the fifty years of research progress. Ignition is reached at $Q=\infty$.

1.1.4. Magnetic Confinement Fusion

In the core of the sun the nuclei are confined by the gravitation force which provides sufficient pressure for igniting proton-proton nuclear fusion reactions (or ^{12}C-based catalytic reactions in heavier stars).

The simplest approach to achieving controlled fusion on earth would be to accelerate beams of light nuclei to sufficient kinetic energies and bring them into collision. However, for single collision events, Coulomb scattering would dominate over fusion reactions due to its much larger cross-section, leading to negative energy balance. This problem can be overcome by confining a population of thermalized particles at temperatures of several tens of keV for a sufficiently long time that a large fraction of the particles would have kinetic energies high enough to fuse. At such energies light particles are completely ionized and form a plasma consisting of ions and electrons.

A charged particle in a magnetic field experiences the Lorentz force and its orbit describes a helical motion along the magnetic field lines. The radius of the gyro-motion is referred to as Larmor radius

$$r_L = mv_\perp /(q|\mathbf{B}|) \tag{1.4}$$

where m, q and $v_\perp$ are the mass, charge and velocity component of a charged particle perpendicular to the magnetic field vector **B**. For **B** of several Tesla the Larmor radius of hydrogen isotopes with the temperature of 10 – 100 eV is typically a few hundreds of μm.

Charged particles can be, therefore, confined by a magnetic field generated by a system of coils. Reactor concepts based on this approach are referred to as "magnetic confinement fusion" (MCF) reactors. (Another concept, the "inertial confinement fusion" (ICF), uses lasers or particle beams to heat frozen D-T pellets, either directly or indirectly via conversion into X-rays, in order to reach the temperatures necessary for fusion reaction. ICF is not a subject of this thesis.)

In order to avoid the end losses of the early linear configurations (i.e. devices with zero curvature of the magnetic field on the axis and thus open field lines), the confining field line structure is given a toroidal shape. In a simple toroidal magnetic field system the magnetic field curvature and gradient, together with the different sign of the ion and electron charge, would result in a vertical electric field **E**, leading to particle losses due to the outward $\mathbf{E}\times\mathbf{B}$ drift. Such losses can be suppressed by twisting the magnetic field lines by means of an additional poloidal magnetic field component created by the toroidal electric current in the plasma (the plasma current I_p) or by twisting the external magnetic coils (either toroidally continuous or modular) around the confined region. The first principle is used in tokamaks (section 1.1.5), the latter is the used in stellarators. Because of the absence of the plasma current, stellarators provide more stable (eventually steady-state) operation. These advantages are, however, outnumbered by the complexity of the magnetic coils structure, smaller plasma volume (thus reactor efficiency) and worse plasma accessibility due to smaller diagnostic ports. Stellarators are not discussed further in this thesis.

A single-particle description of the tokamak plasma is not possible due to a large number of charges in the confined volume ($10^{19} \rightarrow 10^{23}$). Magnetically confined plasma

can be, however, described by a magnetic fluid model known as magnetohydrodynamics (MHD). The MHD equations of the steady state the equilibrium configuration are

$$\begin{aligned} \mathbf{J} \times \mathbf{B} &= \nabla p \\ \nabla \times \mathbf{B} &= \mu_0 \mathbf{J} \\ \nabla \cdot \mathbf{B} &= 0 \end{aligned} \tag{1.5}$$

where **J** represents the current density in the plasma and p is the plasma pressure. Eqs.(1.5) imply $\mathbf{B} \cdot \nabla p = 0$ and $\mathbf{J} \cdot \nabla p = 0$, meaning that the magnetic field and the plasma current density lie in surfaces of constant plasma pressure and, as shown in figure 1.5, the tokamak plasma forms a series of nested surfaces.

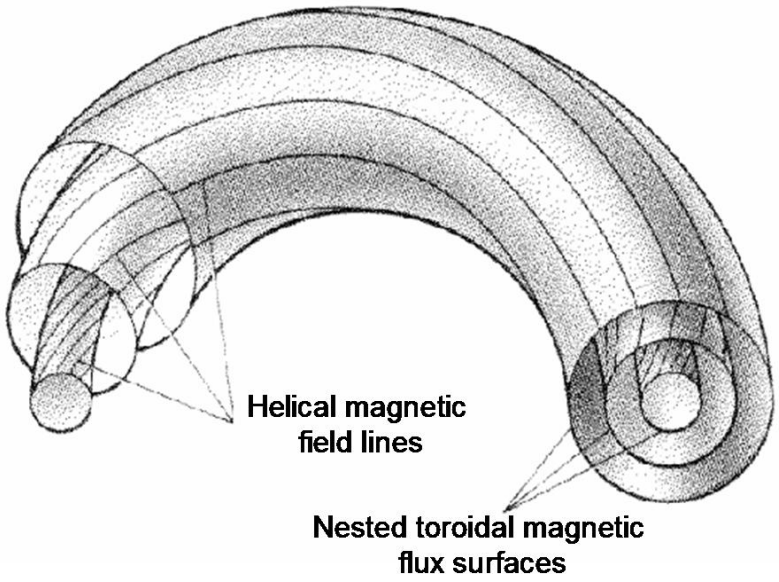

Figure 1.5. Helical magnetic flux surfaces forming a set of nested toroids.

1.1.5. Tokamak

A tokamak is a toroidal magnetic confinement system proposed by two Russian physicists, Tamm and Sakharov, in 1952 and realized for a first time by another Russian physicist Artsimovitch.

In tokamaks, the principal magnetic field, the toroidal field B_ϕ, is generated by a current flowing in the coils linking the plasma and the poloidal magnetic field B_θ is produced by the plasma current flowing in the toroidal direction. B_θ is typically an order of magnitude smaller than B_ϕ (typically several Tesla in large tokamaks). The combination of B_ϕ and B_θ gives rise to helical trajectories of the magnetic field lines. Additional suitably placed magnetic coils are used to control the plasma shape and position as well as to compensate the radial outward force due to plasma pressure gradient. The schematic of the tokamak principle is shown in figure 1.6.

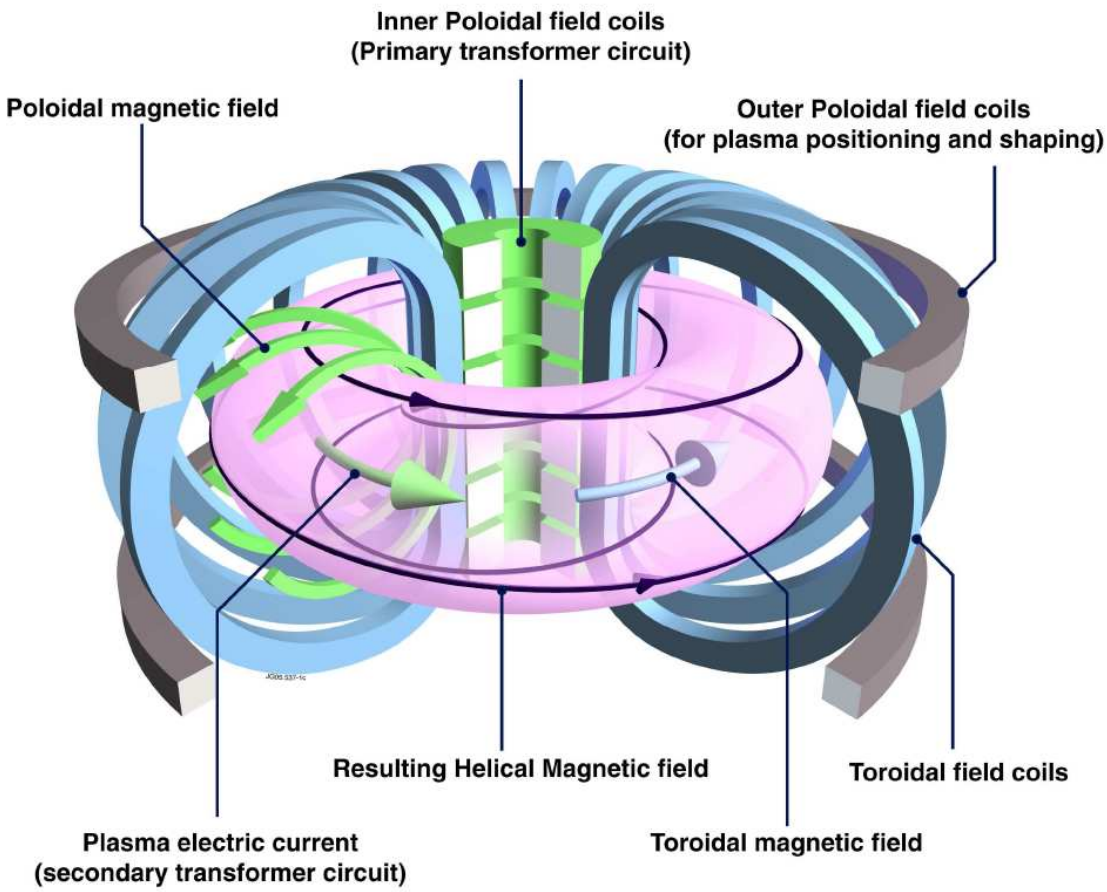

Figure 1.6. Schematic description of the tokamak principle. Twisted magnetic field lines in tokamaks are produced by the combination of toroidal and poloidal magnetic fields. The principal toroidal magnetic field is produced by current in external toroidal field coils. The poloidal magnetic field is produced by the plasma current which is driven by the change of the flux through the torus produced by primary winding of the transformer.

The helical magnetic field line goes around the torus on its magnetic flux surface and returns to the same poloidal location after a change of toroidal angle $\Delta\phi$, corresponding to $q = \Delta\phi / 2\pi$ toroidal circumferences. q is called the safety factor (because of the role it plays in determining the stability of tokamak plasma). When the plasma small radius a (the minor radius) is substantially smaller compared to the plasma major radius R (this is referred to as large aspect ratio), $q \cong rB_\phi / RB_\theta$ where r is the horizontal distance from the plasma centre.

The current in the plasma serves also for plasma build-up and ohmic heating and is usually driven by a toroidal electric field induced by transformer action. In present large tokamaks, plasma current of several MA is produced. As long as the plasma current is generated by induction (alternative current drive methods have been developed), the tokamak is a pulsed system. Another disadvantage of the plasma current is a potential danger of a sudden termination of the discharge, known as disruption, which can give rise to large mechanical forces on the machine.

Since the plasma resistivity decreases with the plasma temperature ($\propto T^{-3/2}$), I_p can heat the tokamak plasma only to temperatures of a few keV. The temperatures >10 keV, needed to reach a reasonable probability for fusion reactions to occur, can be achieved by additional heating by neutral particle beams or by electromagnetic waves. The first is based on charge-exchange reactions between thermal fuel ions and fast injected neutrals with energies of ≈ 100 keV and total current up to 100 A. The latter is based on the absorption of the RF wave at a cyclotron resonance with plasma ions or electrons.

Tokamak plasma is contained in a vacuum vessel. Since the impurities in the plasma can give rise to radiation losses and dilute the fuel, the restriction of their entry into the plasma is critical for successful reactor operation. Therefore, the plasma must be separated as much as possible from the walls of the vacuum vessel either by defining the outer boundary of the confined plasma with a material limiter or by modifying the magnetic field by means of additional coils to produce a magnetic divertor, section 1.2.

1.1.6. Progress in tokamak research

Steady progress in tokamak research has been made from the late 1950s. The first tokamaks were characterized by ion temperatures of a few hundred electron volts and energy confinement times of several milliseconds. From that time, more than 208 tokamaks were built worldwide[5]. 35 are still in operation.

Tokamak	R [m]	I_p [MA]	B_t [T]	Start year (Upgrade)
Alcator-C MOD	0.67	1.1	9	1993
ASDEX Upgrade	1.62	2.0	3.9	1991
DITE	1.17	0.26	2.7	1975 (closed)
JET	2.96	5-7	3.8	1983 (1992)
JT 60U	3.4	5	4.2	1991 (closed)
MAST	0.7	>1	0.6	1999
TEXTOR-94	1.7	0.8	2.8	1981 (1994)
TFTR	3.1	3.0	6.0	1982 (closed)
Tore Supra	2.38	2.0	4.5	1988 (2000)

Table 1.3. Selected tokamak devices and their basic parameters. I_p and B_t are the maximum values.

Larger tokamaks built by 1980 (see table 1.2) achieved confinement times of about 100 ms. Scaling laws obtained from these devices indicated that $\tau_E \propto a^2$ and a minor radius of about 2 m would be needed for fusion reactor. Plasma temperatures of several keV were produced by additional heating. However, the confinement time was found to be a decreasing function of the applied heating power. Fortunately, with the introduction of the divertor and at a sufficiently high level of plasma heating, the spontaneous formation of an edge transport barrier associated with improved confinement

[5] http://www.toodlepip.com/tokamak

(so-called H-mode) was found in ASDEX tokamak [Wagner 1982]. On the other hand, the occurrence of various types of instabilities was found to seriously restrict the operating regimes of the tokamaks. For example, a new kind of instability, termed the ELM (Edge Localized Modes), appeared in the H-mode [ASDEX Team 1989], and is associated with a periodic expulsion of the outermost layers of hot, dense, confined plasma onto the wall.

In largest tokamak JET several important milestones were passed. Confinement times greater than 1 s, ion temperatures more than 30 keV and pulse lengths of up to one minute were achieved, although not simultaneously. Another large tokamak TFTR produced a fusion power of almost 11 MW using a 50-50 D-T mixture. After the closure of TFTR, JET became the only tokamak able to operate with a D-T mixture. In JET, a maximum transient fusion power output of 16.1 MW was obtained in an ELM-free H-mode with $Q = 0.62$. A quasi steady-state ELMy H-mode discharge produced 4 MW of fusion power for about 4 seconds [Jaquinot 1999].

1.1.7. ITER

ITER is a joint international research and development project that aims to demonstrate the scientific and technical feasibility of fusion power. ITER is a device based on divertor tokamak concept. It is believed that ITER is the final step before a prototype of a commercial fusion reactor is built.

ITER is aimed to be the first fusion device with significant Q and extended plasma burn. ITER is designed as an experimental device with extensive diagnostics and flexibility in fusion power, plasma density, beta, shaping, heating and current drive, fuelling methods, and replaceable in-vessel components. This flexibility has been deemed essential for accommodating uncertainty in projections from current (much smaller) tokamaks, and for investigating and optimising the burning plasmas well as to facilitate the exploration of new operation regimes attractive for a reactor.

Parameter	Attributes
Fusion power	500 MW (700 MW*)
Fusion power gain (Q)	≥10 (for 400 s inductively driven burn) ≥5 (steady-state burn)
Plasma major radius (R)	6.2 m
Plasma minor radius (a)	2 m
Plasma current (I_p)	15 MA (17 MA*)
Toroidal field at 6.2 m radius	5.3 T
Installed auxiliary heating / current drive power (initial)	73 MW
Plasma volume	830 m^3

Table 1.4. The nominal parameters of ITER [Shimada 2007].
**Increase possible with limitation on burn duration.*

The ITER physics basis was addressed in the special issue of Nuclear Fusion[6]. The performance specifications require ITER[7]: (i) to achieve extended burn in inductively driven D-T plasma operation with $Q \geq 10$, not precluding ignition, with a burn duration of between 300 and 500 s, (ii) to aim at demonstrating steady-state operation using non-inductive current drive with $Q \geq 5$. The reference plasma operating scenario for ITER inductive operation is the ELMy H-mode. The nominal parameters of ITER using inductive current drive are stated in table 1.4 [Shimada 2007].

The prediction of plasma performance in ITER is based on scaling laws derived from the experimental results achived in today's devices. Two essential scaling laws enter the prediction of the ITER ELMy H-mode plasmas performance: L-H transition power threshold P_{LH} and (ii) the thermal energy confinement time τ_E [Shimada 2007]. For illustration, a comparison of the measured H-mode thermal energy confinement times (vertical axis) with the scaling (horizontal axis) for a subset of ELMy data in the ITER H-mode database is shown in figure 1.7. Since ITER will be considerably larger than the largest current devices, large uncertainties in extrapolating from current experience to unprecedented domains may be expected.

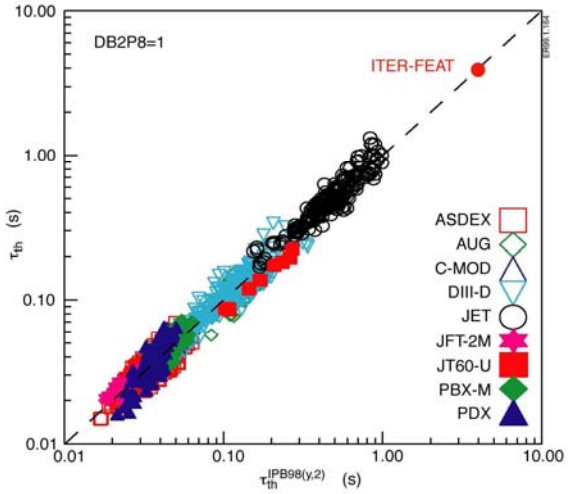

Figure 1.7. Experimental values of the energy confinement time from current tokamaks plotted against the scaling law. Prediction to ITER is also shown.

It is still not certain whether ITER will be able to reach the H-mode with its plasma heating capability. For ITER a threshold power for L-H transition, based on empirical scaling from current devices, is in the range of ~50MW [Doyle 2007], which is within the capability of the ITER heating system, table 1.4. However, there is uncertainty in the projection and experiments suggest that heating powers ~50% above the threshold power are required to reach good H-mode [Shimada 2007]. In addition, transient heat loads in the form of ELMs, disruptions, tritium retention, and high neutron fluxes are the most serious challenges to the integrity and lifetime of the ITER plasma-facing components [Loarte 2007].

[6] 2007 *Nucl. Fusion* **47** S1-S414
[7] 1998 ITER Council Proc. (ITER Documentation Series No 15) (Vienna: IAEA) p 148

1.1.8. Fusion power plant

The tokamak reactor can be used for production of energy in two ways: as a "pure" fusion power plant or as a part of a hybrid fission-fusion power plant. While the first is currently the mainstream of the fusion research because of its attractiveness with regards to environmental and safety issues, the latter might be easier to put into practice in the not too distant future.

Compared to the current experimental devices, a "pure" fusion power plant with tokamak reactor will require additional elements in order to convert the fusion power into electricity. The vacuum vessel will be surrounded by a blanket that will (i) absorb the energy of the neutrons from the fusion reactions and transform it to heat carried away by a coolant, (ii) protect the outer components of the reactor from the neutron flux and (iii) allow for breeding of tritium to fuel the reactions. This may be accomplished by composing the blanket of Li_2O. Additional elements like e.g. the blanket coolant, heat exchanger, turbine and the generator will be needed. Since the tokamak transformer action can drive the electric field only for limited period, the reactor will work in pulsed operation. Alternatively, continuous current drive could be provided by combining the bootstrap current produced by plasma itself with that produced by injection of the neutral particle beams or electromagnetic waves.

The idea of the hybrid fission-fusion reactor is to surround the fusion reactor with a blanket of abundant "fertile" materials such as uranium-238 or thorium-232. Fast neutrons produced in D-T reactions in the tokamak plasma will convert these materials into fissile isotopes (uranium-233 or plutonium-239). The fissile material will then be used as a fuel for ordinary fission reactors. The fission-fusion power plant should consist of a relatively small ($Q = 2 - 5$) pulsed tokamak (i.e. current drive might not be necessary) that could breed enough fuel for several satellite fission reactors. The feasibility of the hybrid fission-fusion systems has been addressed e.g. in [Bethe 1979, Nifnecker 1999, Gohar 2001, Hoffman 2002, Stacey 2002]. The fusion-fission hybrid system has potential attractiveness because of the large amount of produced energy and the abundance of fuel available compared to the fission reactor. Hybrid reactors are expected to be able to provide energy for more than 10000 years, giving a comfortable fuel assurance. The conditions for making such reactors economical may be considerably less stringent than those for fusion reactors producing electric power alone. Hybrids seem to be a practical path to the early application of fusion for energy production and would provide enough time to continue the progress towards pure fusion reactor, which is now many years away. However, apart of the political and public objections that the hybrid concept will probably provoke (because of the risk of proliferation as well as the fact that hybrid reactors involve nuclear fission), a number of technical issues needs to be solved. This includes e.g. the increase of the neutron fluence, the problems related to the first wall materials, and the design of the fissile fuel breeding blanket.

1.2. Plasma boundary in tokamaks

In tokamaks all four states of matter (solid walls of the vessel, liquid melting layer, gas consisting of neutral atoms, as well as plasma consisting of ionized atoms, molecules, and electrons) interact in a very small space. The transition between the plasma and the outer world is the biggest challenge of controlled fusion. The interaction of plasma with first-wall surfaces will have a considerable impact on the performance of fusion plasmas, the lifetime of plasma facing components and the retention of tritium in the next step experiment ITER.

In addition to the motion along **B**, magnetically confined charged particles diffuse across magnetic field lines from the confining region towards the inner wall of the vacuum vessel. The interaction of the charged particles with the material wall leads to the production of impurities and subsequent dilution of the plasma. In addition, large concentrated heat fluxes from the plasma can damage (i.e. by melting, sputtering, or brittle destruction) the plasma facing components. If the first wall were parallel with **B** at every point, the total radial heat flux from the plasma would be dissipated over large area, leading to very low heat flux densities. However, such a configuration could not be built in reality because of the finite edges of the wall tiles, diagnostic ports, screws, etc. that must inevitably appear. Another reason why the uniform distribution of the incident heat flux density could not be achieved is that the particle and energy fluxes from the plasma are poloidally non-uniform (e.g. [Asakura 2007, Kočan 2009] because of the curvature of the magnetic field lines. In addition, fast particles can be detrapped from the magnetic ripple wells due to the finite number of the toroidal magnetic field coils [Basiuk 2001], leading to a localized damage of the inner vessel components. Therefore, instead of bringing the whole plasma surface in contact with the material surface, tokamak plasmas are separated as much as possible from the vessel wall.

The simplest and oldest method to separate the tokamak plasma from the vessel wall is to insert an annulus of solid material called a “limiter”. Limiters can be either discrete or continuous in the toroidal or poloidal direction. Curved inner walls of the vessel covered by protective tiles are used as a wall-limiter. Additional limiters are used to protect the RF heating antennas . In fact, any object that is inserted into the plasma and is large enough (see section 1.2.4.2) acts as a limiter. Obviously, the price paid for the separation of the first wall from the plasma by means of a limiter is in the high flux densities to the limiter surface.

The poloidal cross-section of a limiter tokamak is shown in figure 1.8. The magnetic field lines which lie on flux surfaces that are not in contact with the limiter are termed “closed”. Those which intersect a solid surface are termed “open”. The outermost flux surface with closed magnetic field lines is termed “last closed flux surface” (LCFS). LCFS separates the “confined” region (being the region inside the LCFS) from the scrape-off layer (SOL) which is localized outside the LCFS (more accurate definition of the SOL is given in section 1.2.2.1).

Once inside the SOL, the particles move along the field lines towards the limiter strike zones. Because the parallel movement of particles (which in this thesis coincides with the movement along B) is much faster compared to the perpendicular movement, the particles only have time to diffuse a short distance beyond the LCFS – typically a few centimetres in large tokamaks, section 1.2.2.1. The limiter thus effectively separates the

vessel wall from the plasma. On the other hand, since the limiter strike zones are much smaller compared to the total vessel wall, the heat flux from the plasma is concentrated on a smaller area. This may result in large heat flux densities to the limiter because of localized power deposition. Although separated from the main vessel wall, the confined plasma is in fact in direct contact with the limiter. Therefore, there is high probability that the impurities produced by the impact of charged particles from the plasma onto the limiter surface will enter directly the confined region.

More appropriate in the control of the plasma dilution by impurities is the magnetic divertor. The divertor is produced by an additional toroidal coil, which, together with the plasma current, produces a figure-of-eight shape of the magnetic field in the poloidal plane, figure 1.8. Plasma sink is achieved by intersecting the flux surface around the additional coil by solid plates (divertor targets). The magnetic flux surface passing through the X-point is called the "separatrix". The SOL is localized outside the separatrix, except the region between the X-point legs which is called the "private flux region". In divertor configuration the plasma wetted area is separated from the confined region which makes it easier to maintain lower impurity level in the plasma. This is because the impurities sputtered from the divertor plates are ionized more likely in the SOL (so that they can return to the wall along the open field lines) and are less likely to enter the confined plasma compared to the limiter configuration. The divertor also provides optimized plasma shape and allows for exploring possible advantages of the small aspect ratio. On the other hand, the divertor configuration is less efficient in the use of magnetic volume.

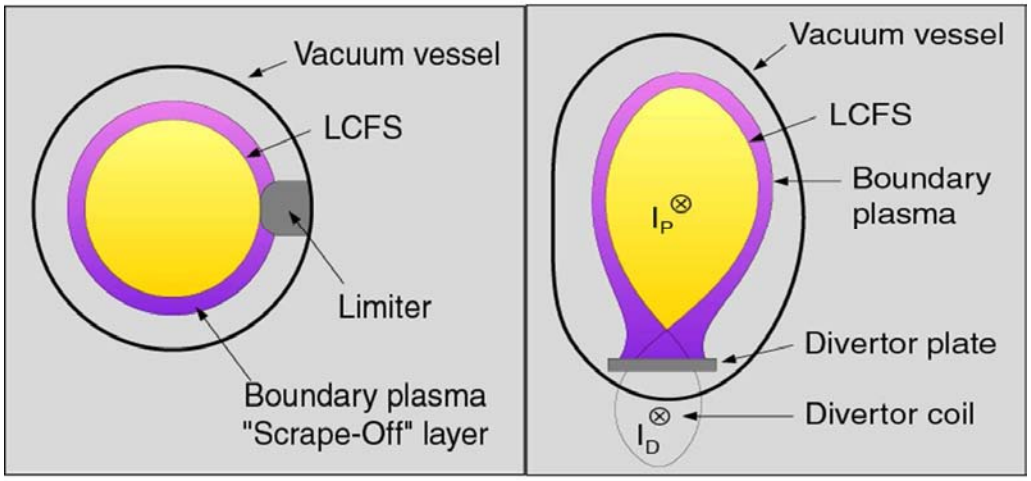

Figure 1.8. Schematic of the poloidal cross section of the limiter (left) and divertor (right) tokamaks.

1.2.1. Impurities

The main source of impurities in the tokamak is the release of neutrals from solid surfaces (such as limiters, divertor targets, or the first wall) by sputtering and evaporation. The neutrals enter the plasma, get ionized, and subsequently either return to the solid

surface or are transported further into the plasma. The most important consequence of impurities in tokamaks is the cooling of the plasma by radiation. Impurities can have both harmful as well as beneficial effects on tokamak performance. First negative effect of the impurities is the radiation power loss that could account of a large fraction of the heating power at relatively low impurity concentrations. Much more preferable in this sense are low Z materials: while high-Z elements retain some orbital electrons also at the core plasma temperatures and act as "effective" radiators, low-Z atoms become completely stripped of the orbital electrons at low temperatures and therefore radiate only in the plasma edge. This has in fact a beneficial effect since up to 100% of the input power can be radiated over the whole reactor surface rather than deposited by particle impact on much smaller limiter or divertor targets, leading to a localized power deposition. Strong peripheral radiation by impurities, referred to as "detachment" or "cold plasma mantle", has been observed in many tokamaks (e.g. [Strachan 1985, O'Rourke 1985, Allen 1986, McCracken 1987, Bush 1990, Samm 1993]). In addition to the radiative losses, impurities can dilute the fuel and thus cause the degradation of the reactor performance. Since the total number of the ion and electron charges in the quasi-neutral plasma is approximately equal, already a small number of high-Z impurities can replace a large fraction of fuel ions and significantly reduce the fusion power output.

Two quantities have important role in the quantification of the impurity content in the tokamak plasma: the effective ion charge Z_{eff} and the radiated power P_{rad}. An empirical relation between Z_{eff} and P_{rad} was found by Behringer [Behringer 1986] on JET data and confirmed later on by Matthews [Matthews 1997] on the multi-machine database. Although this relation is not fully understood, its robustness allows for relatively reliable extrapolation to ITER.

Large progress in impurity control has been achieved since the first magnetic fusion devices. This includes e.g. the ultra-high vacuum technology, refractory (tungsten, molybdenum) or low-Z materials (carbon) for the limiters, oxygen gettering with boron, beryllium or lithium [Winter 1990]. In parallel, Monte Carlo neutral codes like EIRENE [Reiter 1991, Reiter 1991b], DEGAS [Heifetz 1982] or NIMBUS [Radford 1996], coupled with the fluid codes, improved the understanding of the transport of impurity atoms and molecules in the edge plasma.

Ideal material for a fusion reactor does not exist and the price for e.g. low radiative losses (C, Be compared to W) is paid in the higher retention of the hydrogen isotopes (C) or lower limits for the peak heat loads (Be).

1.2.2. Limiter SOL

Since the experiments described in this thesis were performed in the limiter tokamak Tore Supra, in this section we focus on the limiter SOL and address some of its well known basic properties. We also define some basic quantities such as the e-folding length, sheath potential drop and the heat transmission coefficient. We do not attempt to make a comprehensive survey of the limiter SOL which is provided in the references stated below.

1.2.2.1 Radial drop of density and temperatures in the SOL

In the simplest case with no particle sources and sinks (such as ionization or recombination) in the SOL, the particle flow perpendicular to the magnetic field lines into the SOL is balanced by the parallel particle losses at the limiter targets, i.e.

$$L_c \frac{d}{dr}\Gamma_\perp \approx \Gamma_{//} \tag{1.6}$$

with $\Gamma_\perp = -D_\perp dn/dr$ and $\Gamma_{//} \propto nv_{//}$, figure 1.9. Here $D_\perp$ is the cross-field particle diffusion coefficient and L_c is the magnetic connection length defined in figure 1.9. A large fraction of the perpendicular transport is believed to originate by the intermittent expulsion of plasma filaments, or "blobs", from the last closed flux surface (LCFS) (e.g. [Hidalgo 1995, Naulin 2007]). Turbulent transport makes $D_\perp$ "anomalously" high compared to what is expected from the neoclassical (collisional) theory.

Assuming for simplicity that L_c, $v_{//}$ and $D_\perp$ are independent of radius in the SOL and $D_\perp$ is poloidally uniform, Eq.(1.6) gives

$$n(r) \approx n_{LCFS} \exp\left[-(r-a)/\lambda_n\right] \tag{1.7a}$$

with n_{LCFS} and $\lambda_n \approx \sqrt{D_\perp L_c / v_{//}}$ being the plasma density at the LCFS and the density e-folding length, respectively. Analogous consideration for the electron and ion energy balance (neglecting all heat sources and sinks in the SOL) gives

$$T_i(r) \approx T_{i\,LCFS} \exp\left[-(r-a)/\lambda_{Ti}\right] \tag{1.7b}$$

$$T_e(r) \approx T_{e\,LCFS} \exp\left[-(r-a)/\lambda_{Te}\right] \tag{1.7c}$$

with λ_{Ti} and λ_{Te} being respectively the ion and electron temperature e-folding lengths. Within the accuracy inherent to the model used here the measurements of the SOL e-folding lengths give gives approximate values of the particle and heat transport coefficients (e.g. $D_\perp = \lambda_n^2 v_{//} / L_c$). The e-folding lengths also define the approximate width of the SOL. As demonstrated experimentally in most divertor and limiter tokamak [Asakura 2007], the poloidal asymmetry in the particle transport through the LCFS makes the e-folding lengths strongly dependent on the position of the plasma contact point. Similar asymmetry was recently measured also for the ion and electron energy transport [Kočan 2009]. It is also worth noticing that the SOL temperatures and density profiles are often not characterized by a single e-folding length as L_c, $v_{//}$ and particle and heat diffusivities may vary radially and the particle and heat sources and sinks in the SOL, neglected in Eqs.(1.7a-c), may play a role. For example, insertion of various limiters at

different radial positions in the SOL varies L_c radially and leads to a radial variation of the e-folding lengths (figure 5 in [Kočan 2008].

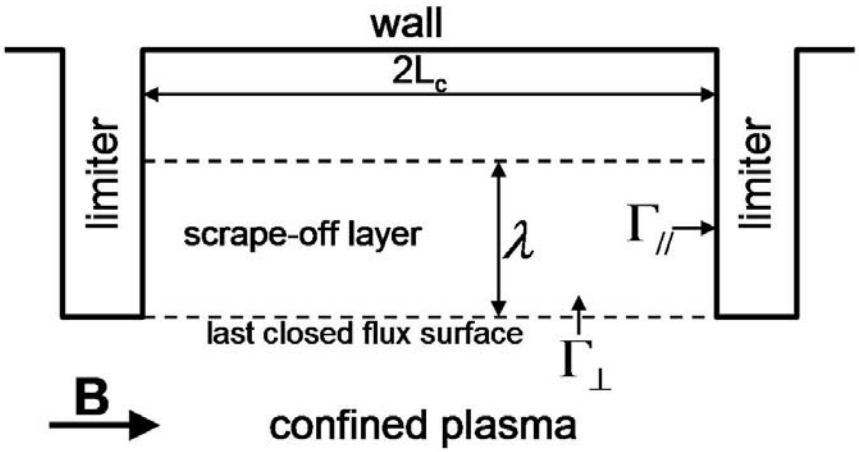

Figure 1.9. Schematic one-dimensional representation of the limiter SOL. Plasma flows from the confined region through the last closed flux surface into the SOL and then along the magnetic field lines to the limiters.

1.2.2.2. The Debye sheath

Because of the large difference in the ion and electron mass, a potential drop – the Debye sheath – spontaneously arises between the plasma and the solid surface (such as the limiter target or probe). It can be shown (e.g. [Stangeby 2000]) that the characteristic scale length of the Debye sheath is the Debye length $\lambda_D = \sqrt{\varepsilon_0 T_e / en}$ (with T_e in eV). Typically $\lambda_D \approx 10\,\mu$m in the tokamak SOL.

To have a non-oscillatory solution of Poisson's equation for the electric potential in the Debye sheath requires ions to enter it with parallel velocity

$$v_{//} \geq c_s \tag{1.8}$$

where $c_s = \sqrt{e(T_i + T_e)/m_i}$ is the ion sound speed. Eq.(1.8) is referred to as generalized Bohm criterion [Allen 1976].

The potential drop in the Debye sheath can be obtained from the equation for the net (ion and electron) current to the surface which needs to be zero $j_i + j_e = 0$. The sheath is assumed to be sourceless so that the ion current is conserved through the sheath. The ion current to the surface is $j_i = n_{se} e c_s$ (with n_{se} being the electron density at the sheath entrance or "sheath edge"). Neglecting secondary electron emission from the surface and assuming Boltzmann electrons, the electron current to the surface $j_e = \frac{1}{4} n_{se} e \bar{c}_e \exp(eV_0 / T_e)$ where $\bar{c}_e = \sqrt{8T_e / \pi m_e}$ is the average electron speed and V_0 is

the potential of the surface (with $V_{se} = 0$). Hence the potential drop between the sheath edge and the electrically floating surface

$$V_{sf} = 0.5 \frac{T_e}{e} \ln\left[2\pi \frac{m_e}{m_i} \left(1 + \frac{T_i}{T_e} \right) \right]. \tag{1.9}$$

Again, Eq.(1.9) is derived assuming zero secondary electron emission from the surface. Allowing for secondary electron emission, additional factor of $(1-\delta)^{-2}$ (with δ being the secondary electron emission coefficient) will appear inside the logarithm. V_{sf} decreases with the increase of T_i / T_e and δ, and with the decrease of ion mass. $V_{sf} \cong 3T_e$ for $T_i = T_e$, $\delta = 0$ and $m_i = m_D$ (where m_D is the deuteron mass). The existence of the sheath has an important consequence for plasma-wall interactions: in the sheath the kinetic energy of ions is increased by $eZ_i V_{sf}$ and can thus exceed the threshold for the physical sputtering, increasing the impurity production rate.

1.2.2.3. The heat flux density and the heat transmission coefficient

The parallel heat flux density $q_{//}$ in the SOL plays a key role in the determination of the power loads on the plasma-facing components in tokamaks.

$$q_{//} = \gamma T_e \Gamma_{//}, \tag{1.10}$$

where γ is the total (ion and electron) heath transmission coefficient. $\gamma\, T_e$ is thus the amount of heat [W] removed from plasma per each ion-electron pair. $\Gamma_{//}$ is equivalent to j_{sat} / e, the parallel ion current density which, together with T_e, is directly accessible by Langmuir probes, section 1.2.4. The details of the derivation of the heat transmission coefficient can be found e.g. in [Stangeby 2000b]. We state here only the final relation which is derived for electrically floating surface and assuming that the floating potential is negligible compared to V_{sf}:

$$\gamma \cong \frac{2.5 T_i}{T_e} - 0.5 \ln\left[2\pi \frac{m_e}{m_i} \left(1 + \frac{T_i}{T_e} \right) (1-\delta)^{-2} \right] + \frac{2}{1-\delta}. \tag{1.11}$$

δ is again the secondary electron emission coefficient which includes true secondary as well as reflected electrons. First term on the RHS of Eq.(1.11) accounts for the kinetic energy of ions increased by the sheath acceleration. T_e in the denominator of the first term is due to the fact that $q_{//}$ in Eq.(1.11) is scaled in T_e. The remaining two terms account for the kinetic energy of electrons. $1-\delta$ in the denominator of the third term appears because of the secondary electrons re-injected into the plasma (either true secondary electrons or reflected ones). The heat flux density of the Maxwellian electrons to the wall $q_e = (2T_e - V_{sf}) j_e + V_{sf} j_{\mathrm{sec}}$ with j_e being the electron current density to the

wall and j_{sec} being the current density of the secondary electrons re-injected into the plasma. V_{sf} (with $V_{sf} < 0$, Eq. (1.9)) accounts for the deceleration (acceleration) of the incident (secondary) electrons in the Debye sheath. Since the net ion and electron current densities to the walls are equal (section 1.2.2.2), $j_{sat} = j_{net}$ with $j_{net} = j_e(1-\delta)$ so that the electron component of the heat flux density to the wall can be written as $q_e = \gamma_e T_e j_{net}$ with $\gamma_e = 2/(1-\delta) - V_s / T_e$. At fixed j_{sat}, higher δ coincides with higher j_e (i.e. higher electron heat flux density to the wall). This is why $1-\delta$ appears in the denominator of Eq.(1.11) and why γ (Eq.(1.11)) increases with δ. In figure 1.10, γ is plotted against T_i / T_e. For example, within the typical range of SOL $\Gamma_{//}$ and T_e in most tokamaks (10^{22}-10^{24} m^{-2}, 10-100 eV) $q_{//} \cong 0.07 \rightarrow 70\,\text{MW m}^{-2}$ for $T_i = T_e$ and $q_{//} \cong 0.14 \rightarrow 140\,\text{MW m}^{-2}$ for $T_i = 4T_e$.

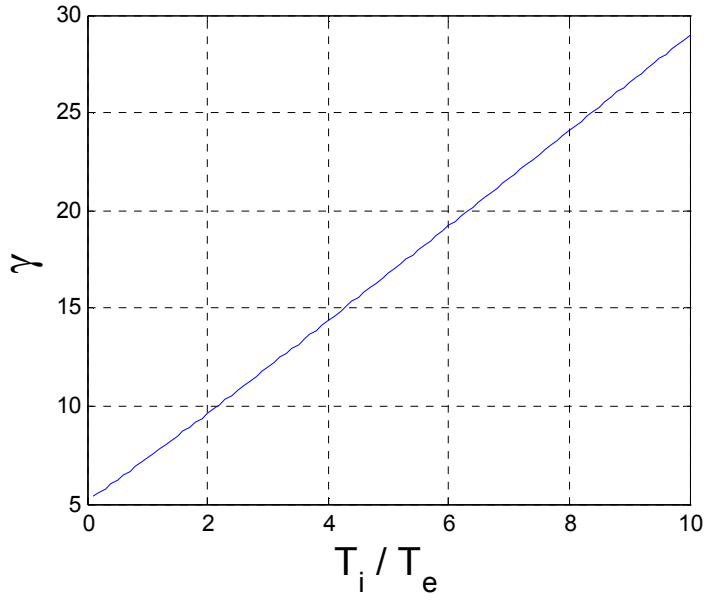

Figure 1.10. Total, ion and electron, heat transmission coefficient γ from Eq.(1.11) plotted against the ion-to-electron temperature ratio. γ is calculated for zero secondary electron emission.

1.2.2.4. Parallel density and potential gradients in the pre-sheath

Assuming steady-state, isothermal 1D flow along the magnetic field lines in the SOL, the conservation of particles and momentum gives

$$\frac{d}{dx}\left(p + nmv_{//}^2\right) = 0, \tag{1.12}$$

(with $p = n(T_i + T_e)$) so that

$$n(M_{//}) = n_0 \frac{1}{1 + M_{//}^2}, \tag{1.13}$$

where n_0 is the density at the stagnation point ($v_{//} = 0$) and $M_{//} = v_{//} / c_s$ is the parallel Mach number. Eq.(1.13) predicts a factor of ~2 drop of density along the magnetic field lines between the stagnation point and the sheath edge ($M_{//} = 1$) [Stangeby 1984]. Allowing ions to diffuse not only into but also out of the collecting region defined by the radial extension of the collecting object (such as the probe or limiter) gives a numerical factor $n(M_{//} = 1) = 0.35 n_0$ [Hutchinson 1987] instead of 0.5 given by Stangeby. Assuming that the electron density is given by Boltzmann relation, Eq.(1.13) gives

$$\varphi(M_{//}) = -\frac{T_e}{e} \ln(1 + M_{//}^2) \tag{1.14}$$

for the potential drop along the field lines. The potential drop between the stagnation point and the sheath edge (referred to as pre-sheath) is thus $\varphi_{ps} \cong -0.7 T_e / e$. Compared to the Debye sheath with the thickness of the order of $\lambda_D = 0.01$ m, the quasineutral pre-sheath extends over the total connection length (10 – 100 m).

1.2.4. Langmuir probes

Langmuir probes (LP) are one of the most important and widely used diagnostics in the tokamak plasma boundary. They are relatively easy to build, can be operated in the SOL plasma, and provide information about the SOL parameters with relatively good spatial and temporal resolution. It is also worth notice that the interpretation of the LP measurements is often a subject of discussions.

The simplest LP consists of an electrode inserted into the plasma. A swept voltage is applied to the electrode with respect to the vacuum vessel ground (often termed torus ground) and the current to the probe is measured. The analysis of the LP current-voltage (*I-V*) characteristics can yield measurements of the electron temperature and density. From the Eqs.(2.61)-(2.71) in [Stangeby 2000c] for the current to an electrically biased surface inserted into the plasma it follows that

$$I = I_{sat} \left(1 - e^{(V - V_f)/T_e}\right), \tag{1.15}$$

where I is the current measured by the LP collector and V is the voltage external bias voltage applied to the collector. An idealized LP current-voltage (*I-V*) characteristic is illustrated in figure 1.11. A least-squares fit (Eq. 1.15) to the *I-V* characteristic gives the floating potential V_f, the ion saturation current I_{sat} and the electron temperature T_e.

The floating potential V_f equals the external bias potential at which the current to the probe is zero.

The ion "saturation" current I_{sat} is measured by applying sufficiently negative bias voltage so that all thermal electrons are repelled from the collector and $I = I_{sat}$. I_{sat} divided by the probe collection area A_{col} gives the (parallel) ion saturation current density j_{sat}. j_{sat}/e gives the parallel ion (or particle) flux density $\Gamma_{//}$. However, the measurements of j_{sat} are often a subject of uncertainty because of uncertainty in A_{col}. If the Debye length λ_D as well as the ion Larmor radius r_L were much smaller compared to the probe cross-field dimension, $A_{col} \cong A_{geo}$ (with A_{geo} being the geometrical projection of the LP electrode along **B**). Small cylindrical tips (diameter of 0.5 – 3 mm) are often used as a Langmuir probes in tokamak plasma [Garcia-Cortes 2000, Kirnev 2004, Mizuuchi 2005] so that A_{geo} is only slightly larger than r_L (which is typically 0.1 – 1 mm). The probe therefore collects the fluxes that are larger than the flux of the ion guiding centres on A_{geo}. This could lead to an overestimation of j_{sat}. In addition, the gradient of the electric field in the magnetic pre-sheath deflects the ions towards the probe surface, leading to additional enhancement of the current collected by the probe [Dejarnac 2007]. This phenomena is referred to as "sheath expansion". It scales with the local parameters (like n_e, T_i, T_e and **B**) which makes its analytical description not possible and its effect on LP measurements needs to be modelled by kinetic simulations [Dejarnac 2007]. A new concave electrostatic probe, the so called tunnel probe, that is immune to the sheath expansion effect and has clearly defined collection area has been recently developed and used in Tore Supra as well in a small-size CASTOR tokamak [Gunn 2002, Kočan 2007, Dejarnac 2007].

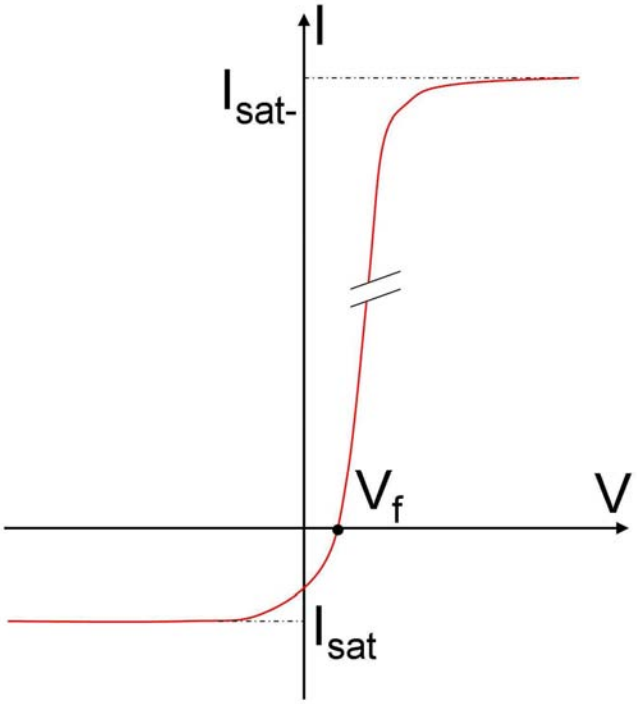

Figure 1.11. Idealized Langmuir probe I-V characteristic. Current measured by the probe is plotted against the bias voltage.

T_e can be measured by the LP from the slope of the *I-V* characteristic, Eq. (1.15). Sheath theory predicts the electron current to rise exponentially for bias voltages above V_f (often called the electron branch of the *I-V* characteristic) until the probe potential equals to the plasma potential. At this point the electron current to the probe $I_{sat-} = \frac{1}{4} e n_{se} \bar{c}_e A_{col} = I_{sat} \sqrt{m_i T_e / (m_e T_i)} >> I_{sat}$. Ideally, the fit to the decaying part of the characteristics between I_{sat} and I_{sat-} would give T_e. However, much lower I_{sat-} / I_{sat} ratios are observed experimentally in tokamaks [Gunther 1990]. In addition, as shown in [Tagle 1987], T_e inferred from the electron side of the *I-V* characteristics raises a factor of 2 as more points from the electron side of the characteristic are included in the fit (Eq. (1.15)) to the measured *I-V* characteristic. In [Stangeby 1982] the non-ideal behaviour of the net electron collection was explained by electron momentum loss to the ions that can be neglected for probe voltages below V_f. Therefore, the experimental data on the *I-V* characteristic measured above V_f are often ignored in the calculation of T_e. As a consequence, the fit comprises only a small fraction of the electron distribution, restricted to the high-energy tail.

Since $j_{sat} = j_i = e n_{se} c_s$ and $n_{se} \cong n_0$, section 1.2.2.4, the measurements of j_{sat} and T_e give an estimate of the SOL electron density $n_e = n_0 \cong j_{sat} / (0.35 e c_s)$, with $c_s = \sqrt{e(T_i + T_e)/m_i}$. Since the LP does not measure the ion temperature, $T_i > T_e$ leads to an overestimation of the electron density by a factor $\sqrt{(1 + T_i / T_e)/2}$ (i.e. 1.2 for $T_i = 2T_e$ and 2 for $T_i = 7T_e$).

1.2.4.1. Mach probe

The simplest Mach probe consists of two electrically insulated Langmuir probes mounted back-to-back and aligned with the magnetic field lines, measuring the ion saturation current density separately from both directions along **B**. The difference in j_{sat} measured by each side of the Mach probe is interpreted as a flow of the unperturbed plasma. The Mach probe theory, either fluid [Hutchinson 1987] or kinetic [Chung 1988], provides the calibration between the ion saturation current ratio and the parallel flow velocity $u_{//} = c_s M_{//}$ where

$$M_{//} \cong 0.4 \ln\left(\frac{j_{sat}^A}{j_{sat}^B} \right) \tag{1.16}$$

A or B indicates the side of the probe. One of the basic assumption of the fluid Mach probe theory is that the parallel electron velocity distribution is Maxwellian, in which case the same electron temperature would be measured by each side of the Mach probe. However, strong asymmetries of T_e on each side of the Mach probes are often observed in experiment [LaBombard 2004, Kočan 2009]. A theory that could explain the asymmetries on T_e is not available.

1.2.4.2. Disturbance of the plasma by probe insertion

The insertion of the probe into the plasma can significantly modify the parameters which the probe is supposed to measure. Stangeby quantified the degree of disturbance of an electrically floating object (like a probe) inserted into a magnetized plasma using a simple model based on the ambipolar collection length L_{col}. L_{col} in his model equals to the length of the density depression (or wake) created by the probe. Particles enter the wake by cross-field transport, follow the magnetic field lines and are neutralized on the probe surface. The plasma inside wake is assumed to be source-free so that the total flux of ions into the wake due to the cross-field diffusion $4\Gamma_{\perp}L_{col}d$ is balanced by the parallel losses on the probe surface $d^2\Gamma_{//}$, i.e.

$$\frac{1}{2}nc_s d^2 \cong D_{\perp}\frac{dn}{dr}4dL_{col} \cong 4D_{\perp}nL_{col}\,, \tag{1.17}$$

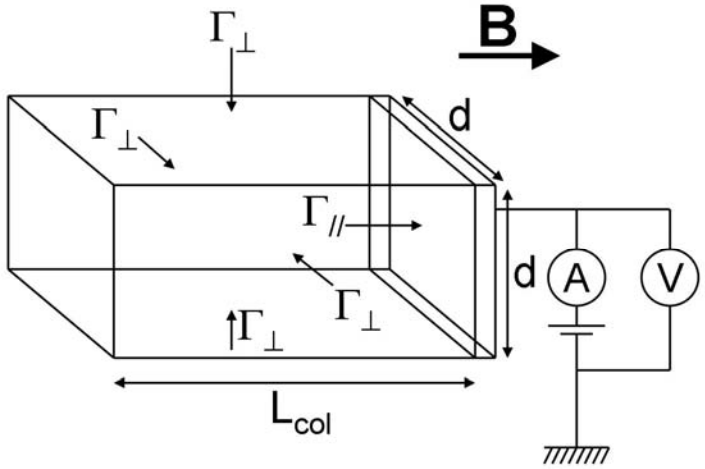

Figure 1.12. Schematic of a rectangular probing object inserted into the magnetized plasma. Inflow of charged particles due to the cross-field diffusion into the wake created by the probe is balanced by the particle losses on the probe surface. Particle sources inside the wake are neglected.

(where $D_{\perp}$ is the cross-field particle diffusivity) so that the length of the wake or collection length

$$L_{col} \cong \frac{d^2 c_s}{8D_{\perp}}. \tag{1.18}$$

When $L_{col} > L_{con}$ (with L_{con} being the magnetic connection length of the field line between the probe and another solid object like limiter or divertor target) the probe is considered to be perturbing. This is because the probe will establish a new shorter collection length and thus modify the SOL *e*-folding lengths in the wake. However,

although the probe can be considered as non-perturbing for $L_{col} < L_{con}$ it can only measure the quantities spatially averaged along the wake it creates.

Figure 1.13 shows the ratio of the collection length to the connection length $L_{col} / L_{con} = d^2 c_s /(8 D_\perp q \pi R)$ (with $L_{con} = \pi q R$, q being the edge safety factor) calculated for $d = 0.04\,\mathrm{m}$, $m_i = m_D$ and $D_\perp = 1\,\mathrm{m^2\,s^{-1}}$, two different major radii R = 2 and 3 m and three different values of q (this corresponds to a typical range of parameters in Tore Supra tokamak). L_{col} / L_{con} is plotted against $T_i + T_e$. As seen from figure 1.13, the effects of the finite collection length become important only when $T_i + T_e > 100\,\mathrm{eV}$ and both q and R are small.

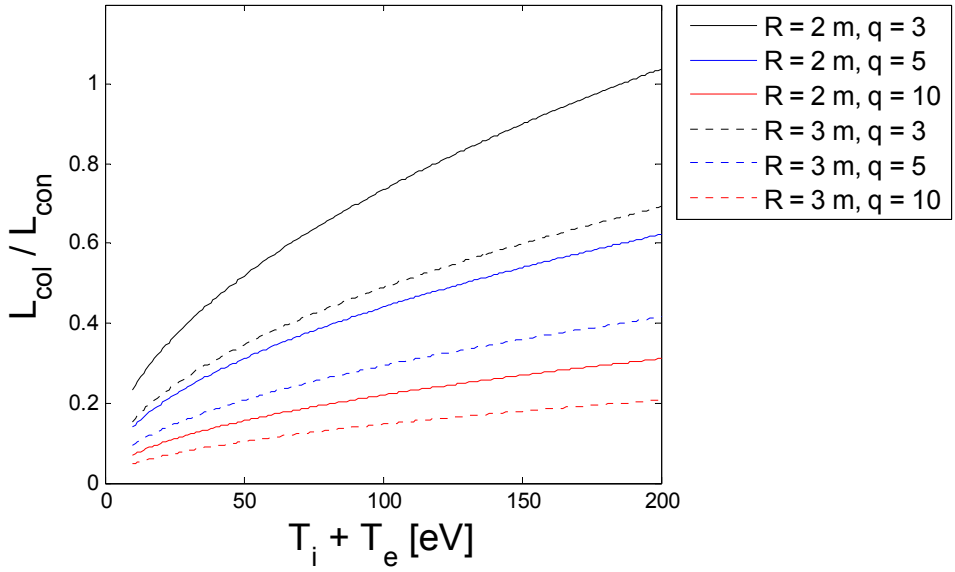

Figure 1.13. Ratio of the collection length to the connection length plotted against the sum of the ion and electron temperatures. L_{col} / L_{con} is calculated for $d = 0.04\,m$, $m_i = m_D$, two different major radii R = 2 and 3 m and for three different values of the edge safety factor q = 3, 5 and 10.

1.3. Tore Supra

Tore Supra (TS) is a tokamak operated by the "commissariat a l'énergie atomique" (CEA) in Cadarache, France. The construction of Tore Supra started in 1982 and the first plasma was achieved in April 1988. Tore Supra is a limiter tokamak with a circular cross plasma section ($R = 2.39\,\mathrm{m},\ a = 0.72\,\mathrm{m}$) whose LCFS is typically defined by the intersection of the plasma with the bottom toroidal pump limiter. The maximum plasma current and the toroidal magnetic field are $I_p < 2\,\mathrm{MA},\ B_t < 4\,\mathrm{T}$, respectively, both oriented in the negative toroidal direction, i.e. clockwise viewed from above.

The primary mission of Tore Supra is the investigation of physics and technology issues of steady state tokamak operation [Giruzzi 2009].

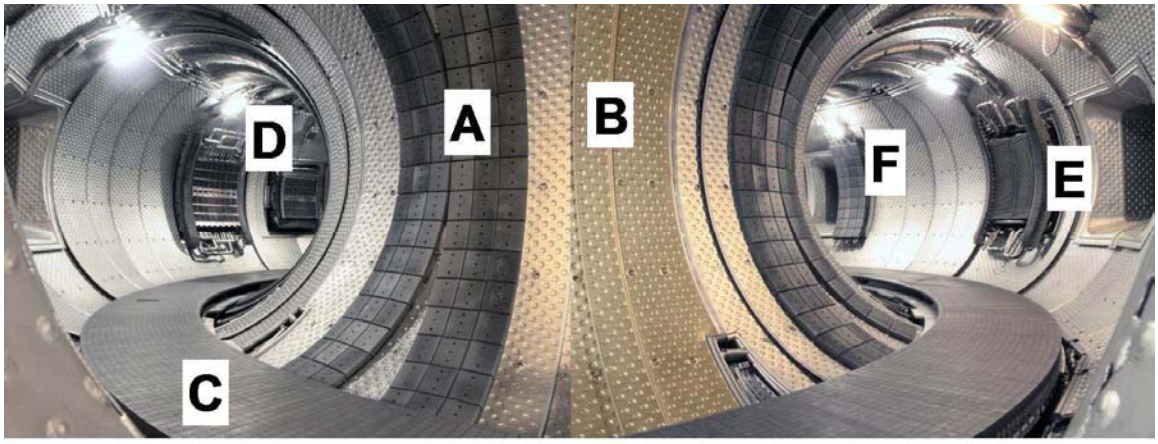

Figure 1.14. View inside the Tore Supra vacuum vessel. A – HFS bumper limiter, B – stainless steel plates, C – toroidal pumped limiter, D – lower hybrid launcher, E – ICRH antenna, F – LFS antenna protection limiter. Limiter tiles are made of carbon fibre composite (CFC).

The combination of the superconducting magnetic coils, actively cooled plasma facing components (figure 1.14) and a non-inductive current drive allows for long pulse operation. Within the twenty years of the operation several major upgrades were performed in Tore Supra, including e.g. the installation of a new continuous toroidal limiter. In 1996 a record was reached with plasma duration of two minutes with an induced current of ~1 MA generated non-inductively by 2.3 MW of power delivered to the plasma by lower hybrid waves. A new CIEL ("Components Internal and Limiter") limiter configuration has been implemented in 2002. Tore Supra milestones are summarized in table 1.5.

The poloidal cross section of the Tore Supra plasma in standard configuration ($R = 2.39\,\mathrm{m},\ a = 0.72\,\mathrm{m}$, contact point on the continuous bottom toroidal pump limiter, TPL) is shown in figure 1.15. Alternatively, a set of six discrete bumper limiters (BL) located on the HFS or a set of six discrete antenna protection limiter (APL) located on the LFS can be used to define the plasma LCFS.

1977	Conceptual design of Tore Supra
1980	Toroidal field model coil testing
1981	Decision to launch the Tore Supra project
1982-1986	Manufacture of main components
1986-1988	Machine assembly
1988	First plasma
1990-1995	Optimization of components for long pulse operation
2002	First operation in CIEL limiter configuration, non-inductive current drive operation
2007	Installation and test of a new ITER-like ICRH antenna
2009	Installation of a new LH antenna with PAM technology

Table 1.5. Tore Supra milestones.

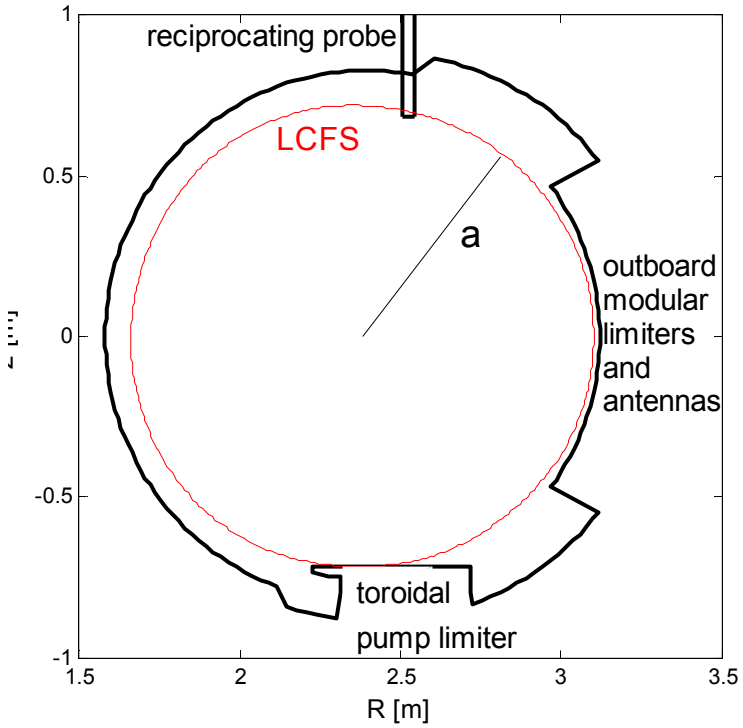

Figure 1.15. Poloidal cross section of a standard plasma configuration in Tore Supra (a = 0.72 m, R = 2.39 m). Also indicated is the position of the reciprocating probe.

In addition to the ohmic heating, the plasma in Tore Supra can be heated by ion cyclotron resonance heating and lower hybrid heating. The maximum achieved heating power was 12 MW. Neutral beam injection system is also available in Tore Supra (<0.4 MW) but serves only as a core diagnostic in combination with charge exchange recombination spectroscopy (CXRS).

Plasma boundary research in Tore Supra involves e.g. the study of the antenna-wall interaction [Gunn 2009], issues related to deuterium retention [Pégourié 2009], study of the plasma flows and intermittent transport in the SOL [Gunn 2007, Fedorczak 2009], study of the heat flux deposition on the limiter [Carpentier 2009], etc.

The main components of the Langmuir probe system in Tore Supra are two vertical reciprocating drives located at $R = 2.526\,\mathrm{m}$ (figure 1.16). Some general details about the reciprocating probe system are stated in section 2.3.1. In this thesis, only the data measured by the reciprocating probes are analyzed. A toroidal array of four fixed Langmuir probes is located at the entrance of pumping throats under the TPL [Dionne 2005].

Typical values of the SOL ion and electron temperatures, plasma density, Debye length, and ion Larmor radius are $T_i = 5 \rightarrow 200\,\mathrm{eV}$, $T_e = 5 \rightarrow 100\,\mathrm{eV}$, $\lambda_D = 20 \rightarrow 30\,\mu\mathrm{m}$, and $r_L = 150 \rightarrow 800\,\mu\mathrm{m}$, respectively.

More details about Tore Supra performance as well as the main results achieved in the past can be found e.g. in [Jacquinot 2004, Giruzzi 2009]

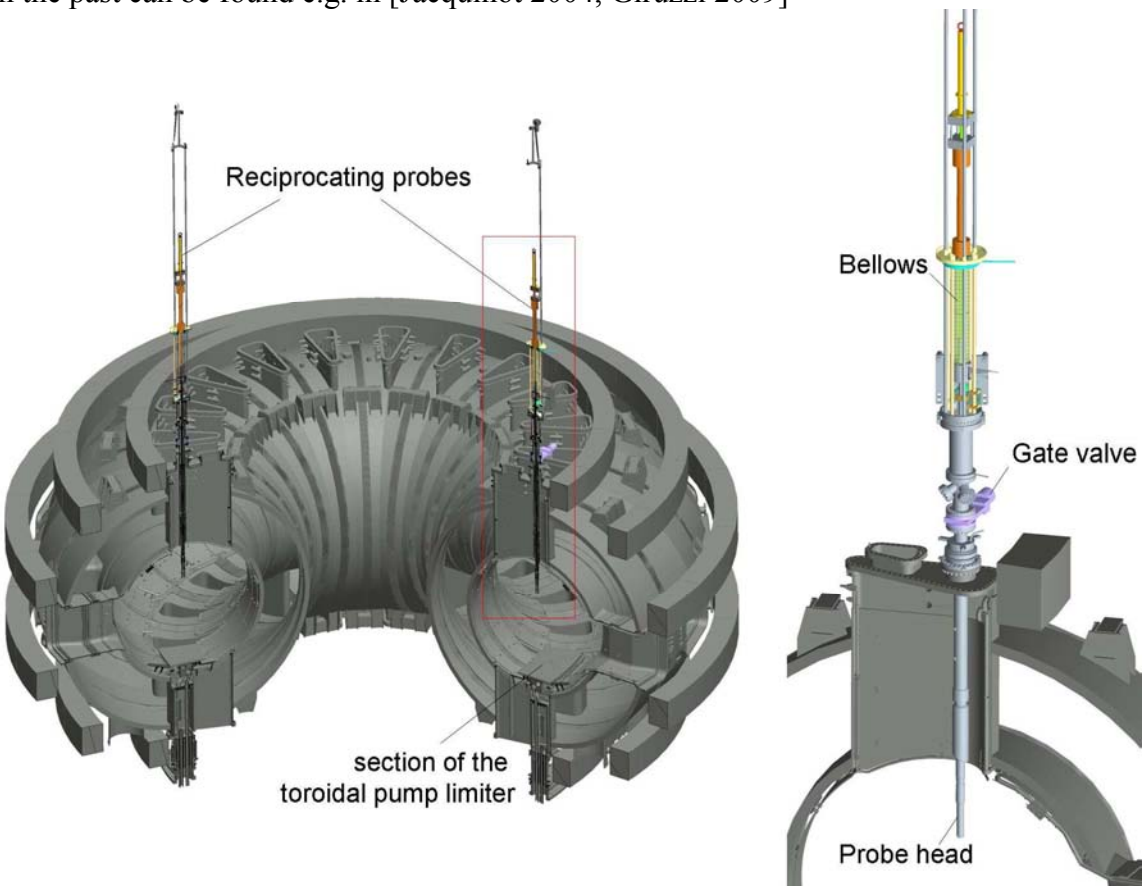

Figure 1.16. Left: Schematic view on the Tore Supra vacuum vessel with two reciprocating probes drives. Right: a detail view on the reciprocating probe system.

1.4. Ion temperature measurements in the tokamak plasma boundary

1.4.1. The importance of SOL T_i measurements

The ion temperature T_i in the tokamak SOL is of key importance for modelling plasma surface interaction processes such as physical sputtering, reflection and impurity release, estimation of the amount of the heat flux deposited on the divertor tiles and main chamber walls, calculation of the importance of the classical drift flows compared to turbulence driven flows, etc. These are critical parameters for designing tokamak plasma facing components. In addition, the ion temperature at the LCFS is, in addition to T_e, an important boundary condition for core modelling.

It is often argued that SOL T_i is very difficult to measure compared to the SOL T_e (which is accessible by a simple Langmuir probes) and the measurements of SOL T_i are therefore not available. In the models, the lack of T_i measurements is often followed by the assumption $T_i = T_e$ (e.g. [Federici 2007]). In some cases, experimentally measured edge temperature profiles are arbitrarily shifted radially to make the two temperatures agree [Saarelma 2005] and to make the model consistent with this assumption.

Most models are relatively sensitive to the exact value of the ion-to-electron temperature ratio and a significant error can be therefore anticipated if, in reality, T_i and T_e are not equal. One example is the calculation of the parallel heat flux density in the SOL $q_{//}$, Eq.(1.10). As shown in section 1.2.2.3., $q_{//}$ is proportional to the heat transmission coefficient which increases with T_i / T_e, Eq.(1.11). For example, $T_i = 4T_e$ would imply two times higher $q_{//}$ compared to $T_i = T_e$. Another example is the calculation of the electron density which is inversely proportional to the ion sound speed c_s so that $n_e \propto (T_i + T_e)^{-1/2}$. T_i plays a role in the estimation of the pressure driven (Pfirsch-Schlüter) flows (e.g. [Asakura 2000, Pitts 2007]) which are proportional to the ion pressure, in the estimation of the physical sputtering rates, etc.

It is true that SOL T_i cannot be measured like T_e by a simple electrode swept with respect to the plasma potential. However, several techniques have been developed for SOL T_i measurements and successfully applied in many tokamaks (see references below and in section 1.4.2). Also true is that the database of SOL T_i measurements is very limited, but sporadic measurements of SOL T_i were already reported from most tokamaks like e.g.

- Alcator C [Wan 1986],
- ASDEX (Upgrade) [Staib 1980, Staib 1982, Reich 2004, Reich 2004b],
- CASTOR [Kočan 2005, Kočan 2006, Kočan 2007, Adamek 2008],
- DITE [Erents 1982, Stangeby 1983, Pitts 1989, Matthews 1991, Pitts 1991, Pitts 1996],
- JET [Guo 1996, Pitts 2003],
- JFT-2M [Uehara 1998],

• JT-60U [Asakura 1997],
• Petula [El Shaer 1981],
• PLT and PDX [Wampler 1983],
• TEXTOR [Höthker 1990, Bogen 1995, Huber 2000, Kreter 2001],
• TFR 600 [Staudenmaier 1980],
• Tore Supra [Kočan 2008, Kočan 2009, Kočan 2009b, Kočan 2009c].

These measurements have clearly demonstrated that in the SOL but also in the edge of the confined region and for most plasma conditions the SOL temperatures are far from equipartition with $T_i > T_e$, figure 1.17 [Kočan 2008]. This is in contrast to what is often assumed in models.

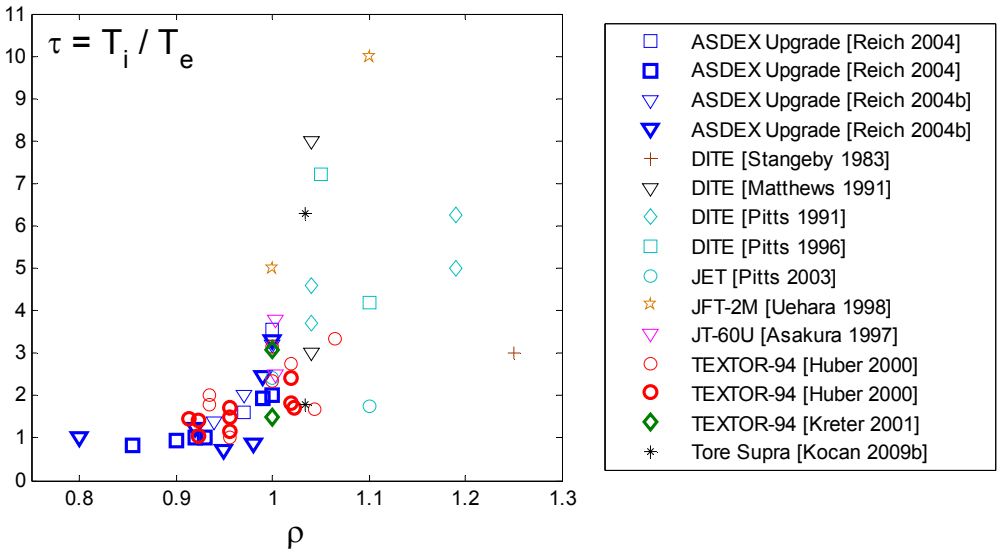

Figure 1.17. Ion-to-electron temperature ratio plotted as a function of the distance from the plasma centre normalized to minor radius (from [Kočan 2008]).

On the other hand, most papers mentioned in the previous paragraphs only demonstrate the capability of a newly developed [Wampler 1983, Stangeby 1983, Matthews 1984, Höthker 1990, Ratynskaia 2002, Kočan 2007] or newly built (e.g. [Wan 1986, Guo 1996, Pitts 2003, Nedzelskiy 2006, Adamek 2008]) diagnostic for T_i measurements. In addition, only a very few data are often presented. T_i is usually studied by varying a single parameter (most often the plasma density), to demonstrate that T_i (or T_i/T_e respectively) varies in agreement with simple physical models (like for example the decrease T_i/T_e with n_e because of the increase of the ion-electron collisionality). Systematic studies of SOL T_i are rare [Matthews 1991, Pitts 1991, Uehara 1998, Kočan 2008, Kočan 2009c].

From the point of view of theory, the tendency for $T_i > T_e$ in the edge plasma and in the SOL is only partially understood. $T_i > T_e$ in the SOL is often related to the existence of the Debye sheath. Ions and electrons enter the SOL by cross-field particle transport and follow the magnetic field lines towards the limiter or divertor targets. Only those electrons with kinetic energies higher than that needed to overcome the repulsive

force of the Debye sheath (Eq.(1.9)) can reach the targets, meaning that most of the thermal electrons are reflected back into the plasma. The removal of the fastest electrons from the distribution has a cooling effect on the electron population and decreases the effective electron temperature of the distribution. In the radial sense, the cooling effect of the sheath on electrons can be considered as a volumetric loss term so that T_e in the SOL becomes lower than T_i and T_i/T_e increases with radius [Stangeby 2000d]. The ions simply follow the magnetic field lines towards the targets and are absorbed. The Debye sheath only shifts the ion distribution towards higher energies but the characteristic temperature of the distribution is unaffected. Both SOL temperatures become equal only when the ion-electron collisionality is strong enough to restore equipartition, i.e. when the ion-electron equipartition time $\tau_{th}^{ie} \propto T_e^{3/2}/n_e$ becomes substantially smaller than the ion parallel transit time through the SOL $\tau_{//}^{i} \propto L_{con}/\sqrt{T_i + T_e}$ (i.e. at high plasma density, low electron temperature or long connection length). The variation of SOL T_i/T_e with the plasma density measured experimentally agrees with this model.

As seen from figure 1.17 $T_i/T_e > 1$ is also measured at the LCFS as well as in the edge of the confined plasma [Uehara 1998, Kreter 2001, Reich 2004, Reich 2004b, Kočan 2008] i.e. in the region where the field lines are not terminated by the Debye sheath. It is not yet clear whether the faster drop of T_e just inside the LCFS is due to the cooling of the edge electrons by the propagation of the cold electrons from the SOL or by the difference in the ion and electron transport (i.e. different heat diffusivities or volumetric loss terms like e.g. charge-exchange reactions, interaction of electrons with impurity ions and neutrals, etc.) in the edge plasma. In addition, sheath cooling effect on electrons is governed by parallel transport, so it certainly cannot explain e.g. the strong variation of T_i/T_e with B_t reported recently in [Kočan 2009b].

Moreover, as mentioned above, the simple model for the radial dependence of SOL temperatures predicts infinite ion temperature *e*-folding lengths λ_{Ti} [Stangeby 2000d]. λ_{Ti} measured experimentally is, however, comparable to or, in some cases, even smaller than λ_{Te} [Uehara 1998, Kočan 2009, Kočan 2009c]. This suggests that other processes (like for example the power conducted by ions, volumetric power losses in the SOL), neglected in a simple model, need to be taken into account.

The poloidal asymmetry in the radial ion energy transport is also studied very poorly. Recent result from Tore Supra [Kočan 2009] demonstrated for a first time that the ion energy transport is poloidally enhanced on the low-field-side, similar to the particle transport [Asakura 2007, Gunn 2007]. However, the database of T_i measurements shown in [Kočan 2009] is very small, yet such measurements could help to evaluate an appropriate plasma start-up scenario for ITER [Gribov 2004].

Only a very few results are available on the measurements of the energies of ELM ions in the far SOL. In [Pitts 2006] it was demonstrated experimentally that during ELMs the ions arrive to the non-divertor components with the impact energies that would provide non-negligible physical sputtering in ITER where higher pedestal temperatures and hence more energetic ELMs are expected. More systematic measurements could help to validate the model of radial ELM filament energy evolution in the SOL [Fundamenski 2006, Fundamenski 2007] and enhance its predictive capability to ITER.

1.4.2. Techniques for SOL T_i measurements

Technique	Principle	Advantage	Disadvantage
Ratynskaia probe	Difference in ion and electron Larmor radii		Technically challenging for typical tokamak **B**, T_i influenced by impurities
Katsumata probe	Difference in ion and electron Larmor radii	Easy to build, direct $f(E_{i\perp})$ measurement	Interpretation based on a simple analytical model – requires particle simulations, T_i influenced by impurities
Rotating double probe	Modulation of the shadowing effect of two collectors as a function of rotation angle and T_i		Poor time resolution, requires simulations, mounting on fast scanning probe drive difficult, T_i influenced by impurities
E×**B** probe	Effect of the **E**×**B** field on ion trajectories	High time resolution, direct $f(E_{i//})$ measurement	T_i influenced by impurities and ion beam defocusing, relatively low resolution of $f(E_{i//})$
Plasma ion mass spectrometer	$f(E_{i//})$ from stretching of ion cycloids along **B**	Rough estimation of $f(E_{i//})$, measurements of the impurity charge state distribution in the SOL	Requires Monte Carlo simulations because of the limited number of collectors
Langmuir probe with a thermocouple	Relation between measured T_e, I_{sat} and power to the probe $P(T_i, T_e, I_{sat})$ provides the estimate of T_i	Easy to build, simultaneous measurements of T_i, T_e and n_e	Measurements interpreted by a simple analytical model for singly charged ions, T_i influenced by impurities and secondary electron emission from probe surface
Thermal desorption probe	Utilizes the relation between the amount of trapped deuterium atoms and T_i	Easy to build, simultaneous measurements of T_i, T_e and n_e	No temporal resolution, requires separate vacuum chamber to analyse samples
Retarding field analyzer (RFA)	Retardation of ions in the potential applied to a semi permeable grid	Direct measurements of $f(E_{i//})$, simultaneous measurements of T_i, T_e, n_e and the sheath voltage V_s	Influenced by impurities
Segmented tunnel probe (STP)	Deflection of ions in the electric field of the magnetic pre-sheath	High time resolution, simultaneous measurements of T_i, T_e, n_e and the floating potential V_f	Interpretation of the measured signals requires particle simulations, T_i influenced by impurities
Carbon resistance probe	Change in the resistance of a thin carbon film is a function of the energy of bombarding particles	Easy to build	Requires simulation to calibrate the probe
Surface collection probe	Distribution of the ion current transmitted through an orifice as a function of T_i	Easy to build	No temporal resolution, only a rough estimate of T_i
Charge exchange recombination spectroscopy (CXRS)	T_i from the Doppler broadening of the line radiation of impurity ions	Does not perturb plasma	Spectra might be influenced by various effects (atomic fine structure, Zeeman effect, other impurity ions), operation limited to NBI-heated discharges

Table 1.6. Survey of available techniques for SOL ion temperature measurements

Simple Langmuir probe can tell us nothing about the SOL ion temperature. This is because the measurements of the ion energy distribution $f(E_i)$ would require to sweep the probe from zero to high positive voltage with respect to the torus ground and to measure the *I-V* characteristics of only the ion current. However, in experiment the probe measures the total (ion and electron) current which, at high positive bias, will be dominated by electron current because of their much lower mass compared to ions.

A dozen techniques for T_i measurements in the SOL have been developed in the past and most of them have been successfully tested in tokamaks. Table 1.6 provides the survey of available techniques for SOL T_i measurements. The table briefly defines their principle as well as the most significant advantages and disadvantages of individual diagnostics. More details are given in sections 1.4.2.1-1.4.2.10. The retarding field analyzer (RFA) and the segmented tunnel probe (STP) are described in dedicated Chapters 2 and 4, respectively.

1.4.2.1. Ratynskaia probe

A probe for the measurement of the ion energy distribution in the magnetized plasma, based on the method suggested in [Demidov 1999], was built by Ratynskaia [Ratynskaia 2002]. The probe described therein consists of a molybdenum wire, 0.25 mm in diameter and 0.35 mm length, closed at both ends by electrically insulating ceramic plugs with a diameter of 0.4 mm. The wire was oriented parallel to the magnetic field, preventing the electrons to reach the wire.

The probe utilizes the Druyvesteyn formula for cylindrical probe in magnetized plasma and for singly charged ions [Druyvesteyn 1930]:

$$f(E_i) = \frac{m_i^2}{2\pi e^3}\left|\frac{d^2 j}{dV^2}\right| \tag{1.19}$$

to obtain the ion energy distribution $f(E_i)$ from the measured probe current density *j* and bias voltages *V*. Eq.(1.19) is valid only for

$$r_{Li,e} >> L \tag{1.20}$$

where $r_{Li,e} = mv_\perp / eB$ are the ion and electron Larmor radii, respectively and *L* is the wire length. The probe was tested in toroidal plasma device Blaamann [Demidov 1999b] which has a magnetic field of only 4 – 40 mT.

However, the application of the probe in tokamak plasma is practically impossible since the central wire will need to be much shorter than 0.1 – 1 mm (which is the typical values of the ion Larmor radius in the SOL). Moreover, since the currents measured in the SOL are subject to noise, second derivative of the measured current could hardly give any information about T_i.

1.4.2.2. Katsumata probe

Katsumata probe [Katsumata 1967] is also based on differentiating between ion and electron Larmor radii. The probe is basically a Langmuir probe slightly inserted into an electrically insulated tube with the tube axis perpendicular to **B**. The electrons are assumed to be not able to reach the probe because of much smaller Larmor radii compared to ions. It is therefore assumed that the probe collects only the ion current. It is argued that the ion current to the collector scales as $\exp(-eV / kT_i)$. This expression is obtained from the model which assumes Maxwellian ion beam and neglects the cross-field diffusion as well as the effects on the ion energy distribution arising from the presence of electrons (that are neglected in the model).

In Petula tokamak T_i measured by the Katsumata probe was found to be a factor of 2 lower compared to T_i from the RFA [El Shaer 1981]. More recently, a Katsumata probe has been used in small-size CASTOR tokamak [Adamek 2008]. Good agreement has been found between the SOL T_i measured by Katsumata probe and by the segmented tunnel probe.

1.4.2.3. Rotating double probe

A rotating double probe for SOL T_i measurements was proposed by Höthker and used in TEXTOR tokamak [Höthker 1990]. The probe consists of two symmetric cylindrical pins, 5 mm in diameter and length, separated by 10 mm. During the discharge the system rotates around its axis which is perpendicular to **B** with a frequency of 2 Hz.

The ion saturation current collected by probe pins showed a dependence on the angle of rotation, reaching a minimum value when the pins magnetically shadow each other. In [Höthker 1990] the observed ion current modulation with the rotation angle was associated with finite ion Larmor radius effects and studied by Monte Carlo simulations. T_i was determined by fitting a calculated profile of the collected particle flux to the measured ion saturation current profiles.

The accuracy of T_i measurements could be, however, affected by simplifications used in the Monte Carlo simulations. For example, the model assumes a simple Maxwellian distribution (i.e. it neglects the pre-sheath effects on the parallel ion velocity distribution) and neglects the space charge effects [Höthker 1990]. Some other effects that can influence T_i measurements are discussed in [Höthker 1990] and the authors claim the error on T_i is around 30%. Obviously, measurement of the radial profile of SOL T_i by the rotating probe mounted on a fast reciprocating drive will be technically challenging since much higher rotation frequencies will be required.

A similar double probe with asymmetric electrodes [Amemiya 1989, Maeda 1997, Amemiya 1994] as well as the rotating double probe with symmetric and asymmetric electrodes [Uehara 1998] were used to measure T_i in the JFT-2 tokamak.

1.4.2.4. E×B probe

The probe consists of a series of collectors (each being thinner than the ion Larmor radius) located at the end of a gap created by two electrodes parallel to **B**. The electrodes are used to create an electric field **E** perpendicular to **B**. The second end of the gap is terminated by a plate with a thin aperture (width of λ_D). The ions enter the probe cavity through the aperture while the electrons are repelled by the aperture plate. The collector currents provide measurements of the parallel ion velocity distribution. The energy resolution of the probe is limited by number of collectors. The advantage of the E×B probe is that it can be operated in DC mode with high time resolution.

E×B probe was used for a first time by Staib in ASDEX [Staib 1980, Staib 1982] and later on by Matthews in DITE [Matthews 1984].

Since the ion current distribution on collectors corresponds to the distribution of parallel ion velocities $v_{//} = \sqrt{2eE_{i//}/m_i}$ and not energies $E_{i//}$, it can be influenced by impurities. Defocusing of ions inside the probe cavity may also contribute to the blurring of the image measured on probe collectors. These two effects were observed in [Staib 1982] and [Matthews 1984] and studied in [Matthews 1994].

1.4.2.5. Plasma ion mass spectrometers (PIMS)

Three types of mass spectrometers, used in the tokamak plasma boundary to measure the charge state distribution of impurities, are usually referred to as "180°" [Kojima 1984], "omegatron" [Nachtrieb 2000, Nachtrieb 2000b], and "cycloidal focusing" [Matthews 1989, Matthews 1990] spectrometers.

Only two of them, omegatron used in Alcator-C MOD and cycloidal focusing PIMS used in DITE, can also measure the ion temperature. Omegtron PIMS utilizes the RFA principle (Chapter 2) to measure T_i and is therefore irrelevant to this section.

DITE PIMS is based on the principle of cycloidal focusing [Matthews 1989, Matthews 1990] which is produced by perpendicular magnetic and electric fields inside the probe cavity. The electric field is produced by two parallel plates. The ions enter the probe through a thin aperture (width of λ_D) and are focused onto an array of three electrically insulated collectors that are parallel to **B**. The principal application of the DITE PIMS is the measurement of the charge state distribution of SOL ions, which is inferred from the mass spectra obtained by ramping the electric field in time to sweep the various foci across the collector array.

The measurements of T_i by PIMS are similar to that of the E×B probe. Since the ions have different parallel energies, their cycloids are stretched along the collectors. The collector currents can be used to measure $f(E_{i//})$. The ion temperature is obtained from the least squares fit of the distributions calculated by Monte Carlo simulations to the experimental collector current ratios. In Monte Carlo simulations it is assumed that the different charge state distributions are isothermal, isotropic and Maxwellian with a velocity shift associated with the Debye sheath acceleration [Matthews 1991]. Since the ion energy distribution at the sheath edge in front of the probe is known to be perturbed

by the presence of the probe combined with the plasma flow [Chung 1988] such assumptions could provide only very approximate values of T_i.

1.4.2.6. Langmuir probe with a thermocouple

The probe consists of a thermocouple that works simultaneously as a Langmuir probe. The analysis of the measured data is carried as follows:

(i) The Langmuir probe provides the measurements of T_e and I_{sat}.

(ii) The thermocouple measures the incident power P.

(iii) Assuming that $P = AI_{sat}E(T_i, T_e)$ (with A being the thermocouple area and $E(T_i, T_e)$ the energy transferred to the thermocouple per one ion-electron pair) T_i, the only unknown, can be obtained by an iterative process.

The probe was successfully used in the SOL of DITE [Stangeby 1983] and PLT [Manos 1982].

The advantage of this probe is in its relative simplicity and robustness. In addition, the measurements of T_i, T_e and I_{sat} provide also the information about the SOL electron density, $n_e \propto I_{sat} / c_s(T_i, T_e)$.

On the other hand, $E(T_i, T_e)$ is calculated using a simple sheath theory for Maxwellian electrons and singly charged ions [Stangeby 1983] and is a function of other parameters that are not measured (e.g. the coefficient of the secondary electron emission from the thermocouple surface). Moreover, the statistical error on T_i includes the errors on T_e, I_{sat} and P and can be, therefore, relatively large.

1.4.2.7. Thermal desorption probe

In the thermal desorption probe the population of trapped ions in a sample is associated to the ion impact energies. The carbon thermal desorption probe was operated in DITE [Erents 1982]. The probe bias voltage was changed on shot-to-shot basis. After each discharge the probe was withdrawn into a separate vacuum chamber, thermally desorbed, and the amount of trapped deuterium was measured. T_i, averaged over the set of discharges, was obtained from the slope of the fluence versus the probe bias voltage [Cohen 1979, Wampler 1981]. The advantage of the thermal desorption probe is that it can measure the electron density and temperature using the sample as a Langmuir probe [Erents 1982]. On the other hand, since the probe requires exposure to cumulative discharges, it has virtually no spatial and temporal resolution.

1.4.2.8. Carbon resistance probe

Carbon resistance probe was used in the edge plasma in the PLT and PDX tokamaks to measure the incident ion energies [Wampler 1983]. The technique is based on measurements of the change in resistance of a thin carbon film due to bombardment of energetic particles (the change in the resistance is due to the damage of the lattice [Wampler 1982]). The probe was calibrated by measuring the resistance change caused

by the implantation of ions at different incident energies. Compared to other collecting probes, a carbon resistance probe does not require the analysis of an exposed sample in a separate facility so that the results are known during the exposure sequence. The probe described in [Wampler 1983] was calibrated by Monte Carlo simulations performed for a broad range of energies of the bombarding ions and two different ion energy distributions (Maxwellian and monoenergetic). Samples were exposed to plasma at different positions outside the LCFS in a series of successive discharges in PLT and PDX tokamaks. The mean ion energy was estimated by fitting the measured change in the sample resistance to the calculated curves. The ion energies obtained using the calibration curves calculated for Maxwellian and monoenergetic ions were different by a factor of ~2. Another disadvantage is that the scatter of the experimentally measured change in the sample resistance does not allow resolving the variation of the ion energies less than several tens of eV.

1.4.2.9. Surface collection probe

This method utilizes the fact that in the presence of a magnetic field the transmission of ions through a thick aperture aligned with **B** is a function of the perpendicular ion energy. The probe consists of two plates. The first plate, the shield, is exposed to the plasma and has an aperture with a radius comparable to the ion Larmor radius. The shield is made sufficiently thick so that most ions make at least one revolution inside the aperture, meaning that the ion transmission is only a function of the perpendicular ion energy. The second plate, the collector, is placed behind the aperture. The ion current distribution on the collector is a function of T_i.

Such probe was used e.g. in TFR 600 tokamak [Staudenmaier 1980]. After exposure, the ion current distribution on the collector was determined by four different surface analysis techniques. Experimental results were juxtaposed by a set of the ion current distribution profiles after transmission, calculated theoretically for different ion temperatures and ion species, assuming isotropic Maxwellian ion energy distribution and neglecting the electric field (i.e. only the geometrical effects are taken into account which makes the model similar to the Larmor radius skimming model described in [Gunn 2001]). The ion temperature was given by T_i of the theoretical profile that was closest to the experimental ion deposition profile. The experimental error on T_i which includes the statistical errors on measured fluences as well as the uncertainty of the effective aperture diameter was estimated to be about 25%.

Several effects neglected in the model (e.g. the electric field at the aperture edges, the defocusing of the transmitted ion beam, the misalignment of the aperture axis from **B**, the effects of the finite aperture thickness, etc.) can modify the ion deposition profile on collector and increase further the error on T_i [Staudenmaier 1980].

More sophisticated diagnostic, combining the surface collection technique with a simple RFA arrangement was used in DITE to determine the charge state distribution of impurity ions [Pitts 1989].

1.4.2.10. Charge exchange recombination spectroscopy (CXRS)

This method, based on the measurements of the Doppler broadening of the spectral lines of impurity ions (mainly C^{5+} ions), has been applied for the SOL measurements of T_i in several tokamaks (e.g. [Kimura 1979, Bogen 1995, Reich 2004, Reich 2004b]). Ion temperature, toroidal rotation velocity and the concentration of impurities can be obtained from the Doppler width, Doppler shift and the intensity of the radiation, respectively. C^{5+} ions are formed in excited state mainly by charge-exchange recombination of C^{6+} ions with fuel atoms. The atoms are provided by means of the neutral beam injector.

In the SOL, the spectroscopic measurements of T_i are subject of several difficulties [Bogen 1995]. Because of relatively low densities the energy equipartition time between the impurity ions might be longer than the life time (ionization time) of impurity ions so that $T_i(impurities) \neq T_i(fuel\,ions)$ [Spitzer 1962, Hey 1994]. For example, at $T_e = 30\,\mathrm{eV}$, $T_i = 60\,\mathrm{eV}$ and $n_e = 5 \cdot 10^{18}\,\mathrm{m^{-3}}$, the lifetime (ionization time) of a C^+ ion is only 15 μs, whereas the energy equipartition time between C^+ and D^+ ions is about 500 μs, i.e. thermal equilibrium cannot normally be established between these ions. For C^{6+} ions the lifetime is mainly determined by recombination on the wall or limiter and is rather long, whereas energy equipartition times of C^{6+} ions are a factor $Z_i^{-2} = 1/36$ shorter than those of C^+ ions. Moreover, possible overlapping of the C VI line with hydrogen-like lines of other ions (e.g. O^{5+}, figure 1 in [Bogen 1995]) may occur. Finally, atomic fine structure and Zeeman effect may appear in the Doppler-broadened profile and confuse the spectral analysis. Also important factor is that the measurements usually require a neutral beam and cannot be therefore performed in all discharges.

In [Kimura 1979], SOL T_i measured from the Doppler broadening of impurity lines was found to be consistent with T_i from Katsumata probe. Similar measurements were performed recently in Tore Supra and revealed a large discrepancy between T_i measured by RFA and CXRS, Chapter 4.

Chapter 2

Retarding field analyzer

2.1. RFA in the tokamak plasma boundary

The retarding field analyzer (RFA) was one of the earliest devices used for the measurement of the energy distribution of charged particles [Simpson 1961]. In theory, an energy analyzer for charged particles could hardly be simpler than the planar RFA – an equipotential plane (established by a biased semi permeable grid placed between the sample and a detector) that discriminates particles entering the analyzer. The RFA is one of the only widely accepted diagnostics for SOL T_i measurements in tokamaks.

Kimura [Kimura 1978, Kimura 1979] was the first who used the RFA for measurements of the ion energy distribution in the tokamak scrape-off layer. Later on, Molvik used a RFA to measure the energy distribution of ions escaping along the magnetic field lines in the 2XIIB magnetic mirror (and later on in the Tandem Mirror Experiment, TMX) [Molvik 1981]. Kimura and Molvik also addressed some instrumental effects such as the appropriate aperture width, secondary electron suppression, the space charge limits inside the analyzer, appropriate bias voltage sweep rates, etc. Molvik also provided an excellent review on the principles of the design of a RFA for tokamak plasma.

A RFA combined with an **E**×**B** probe, mounted on a reciprocating probe drive, was used by Matthews [Matthews 1984] to measure the ion energy distribution in the SOL of DITE tokamak. Several important results were achieved using the RFA in plasma boundary of DITE, including e.g. the simultaneous measurements of SOL T_i and T_e for wide range of the plasma parameters [Pitts 1991, Matthews 1991], in-situ measurements of the secondary electron emission [Pitts 1991], the influence of impurities with a

different charge-to-mass ratio on the measured energy distribution [Pitts 1991, Pitts 1996], the comparison of the experimentally measured ion energy distribution with theory [Pitts 1991, Pitts 1991b, Pitts 1996], etc.

A multiple-function bi-directional probe whose components included RFA, Langmuir probe and calorimeter was used by Wan in the boundary plasma of the Alcator C [Wan 1986] tokamak. The RFA was used to measure both the ion and electron energy distribution. Wan also addressed several RFA design considerations such as the appropriate aperture width and the space charge effect inside the analyzer.

A bi-directional RFA mounted on a reciprocating drive was used in the JET tokamak to measure simultaneously the SOL ion and electron temperatures in NBI-heated L-mode discharges [Guo 1996]. The design of the JET RFA was similar to the DITE RFA. Later on, a new RFA [Pitts 2003, Pitts 2003b] characterized by a more compact design was used in JET to measure the SOL T_i as well as the ion energies in the far SOL during ELMs [Pitts 2006].

The ion energy distribution in rf-sustained argon discharges was measured by a RFA in H-1 heliac [Shats 1997]. The design of this RFA was similar to that used in Alcator C and DITE.

A RFA was used in Indian tokamak SINP [Raychaudhuri 1999]. However, the relatively good performance of the RFA used in SINP is quite surprising as the analyzer worked without the protective slit plate, with the ion repelling grid being directly exposed to plasma.

A small unidirectional RFA with a circular aperture has been also used for the measurements of ion temperature in plasma boundary of ISTTOK tokamak [Nedzelskiy 2006].

An omegatron $\mathbf{E}\times\mathbf{B}$ ion mass spectrometer combined with a retarding field analyzer equipped with three grids has been used in the plasma boundary of Alcator C-Mod [Nachtrieb 2000, Nachtrieb 2000b].

It is appropriate to mention that the RFA is used more widely (and was used much earlier) in, for example, high-energy colliders, plasma etching and the plasma-assisted deposition devices, where the energy distribution of the charge particles is a subject of technological and research interest. Several different types of RFA's have been used for such applications, including planar, cylindrical and spherical RFAs [Simpson 1961] with a number of grids varying from one [Zou 2000, Stenzel 1982] up to eight [Enloe 1992], grid-less analyzers [Johnson 2003], simple compact analyzers [Simpson 1961], [Charles 2000, Bohm 1993], sophisticated commercial ones [Olthoff 1994, Cebulla 1998], the analyzers combined with the mass spectrometer [Jiang 2005], etc. A large number of studies focus on the instrumental effects of such devices like e.g. the divergence of the charged particle beam inside the analyzer [Zou 2002], the improvement of the energy resolution [Goto 1972, Staib 1972], the ionization of the neutral gas inside the analyzer [Bohm 1993], problems associated with a non-ideal retarding field due to the finite number of the grid wires [Enloe 1992], etc. A vast number of further references related to the RFA in low temperature plasmas or high-energy particle beams can be found in the studies referred to above. However, in most cases, the design of these analyzers is adjusted for the measurements of energies above 1 keV without the confining magnetic field and under relatively low heat fluxes, which makes them different compared to the RFAs used in tokamak plasma boundary.

2.2 RFA principle

The schematic of the analyzer and the biasing scheme for ion temperature measurements are shown in figure 2.1. The operational principle of T_i measurements by the RFA can be briefly summarized as follows.

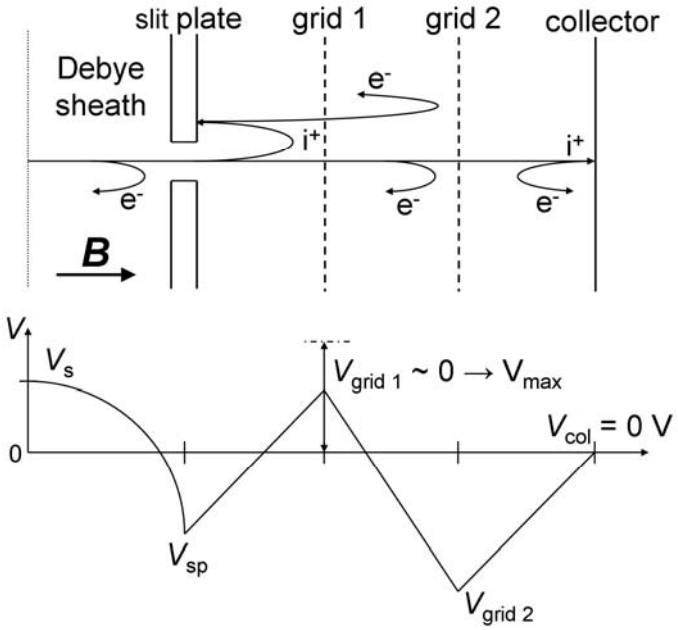

Figure 2.1. Main components of the RFA and the biasing scheme applied for ion temperature measurements.

A fraction of the incident ion flux is transmitted through the slit. The slit plate is biased negatively to repel most of the thermal electrons. The transmitted ions are retarded in the electric field created by a swept positive voltage applied to grid 1, V_{grid1}. A constant negative bias is applied on grid 2, $V_{\text{grid 2}}$, to repel the remaining fast electrons from the tail of the distribution and to suppress the secondary electrons emitted from the collector or from the rear of the slit plate due to ion impact. $V_{\text{grid 2}}$ is the lowest voltage in the system. The collector measures the ion current, I_{col}. Figure 2.2 shows a typical *I-V* characteristic. For a certain range of $V_{\text{grid1}} = 0 \rightarrow |V_s|$ the collector current remains at I_0; all ions gain a parallel energy of $eZ_i|V_s|$ (with eZ_i being the ion charge and V_s the sheath potential) in the collisionless Debye sheath. For $V_{\text{grid1}} > |V_s|$ the current to the collector starts to decrease. Assuming that fuel ions of charge eZ_i dominate the incident flux, I_0 can be expressed as (see e.g. [Guo96]):

$$I_{\text{col}} = A_{\text{slit}} eZ_i \int_u^{\infty} dv_{//} v_{//} \xi f(v_{//}) \ , \tag{2.1}$$

where A_{slit} is the slit area, ξ is the total transmission factor that includes the transmission of the slit and the grids, $u = \sqrt{2eZ_{\text{i}}V_{\text{grid1}} / m_{\text{i}}}$ (with m_{i} being the ion mass), and $f(v_{//})$ is the parallel ion velocity distribution.

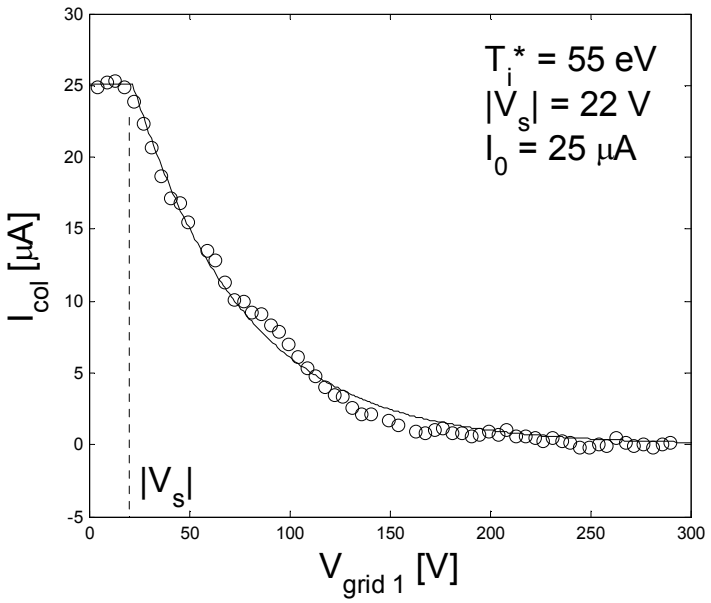

Figure 2.2. Typical RFA I–V characteristic (measured by Tore Supra RFA). Current to the collector, I_{col}, is plotted against the bias voltage of grid 1, V_{grid1}. For $V_{\text{grid1}} < |V_{\text{s}}|$, I_{col} remains constant, since all ions are shifted towards higher energies due to the Debye sheath potential drop in front of the slit plate, V_{s}. A fit to the decaying part of the characteristic gives the effective ion temperature T_{i}^{*}.

Far from the probe, the ions are assumed to be characterized by a Maxwellian distribution, with a well defined temperature T_{i}. However, in the vicinity of the probe the plasma is perturbed by the shadowing effect induced by the probe itself, which depends significantly on the bulk ion flow past the probe. $f(v_{//})$ is distorted from Maxwellian, and an exponential fit to the high-energy tail of the *I-V* characteristic yields an effective ion temperature T_{i}^{*}. Except when the parallel flow velocity $\mathbf{U} = 0$, $T_{\text{i}}^{*} \neq T_{\text{i}}$. In addition, as shown by Valsaque *et al* [Valsaque 2002], the effective ion temperatures measured on the two sides of the probe are different. Figure 2.3 shows a schematic of the RFA inserted into the plasma. The probe consists of two analyzers mounted back-to-back, aligned with $\mathbf{U}$. The Maxwellian distribution gets distorted in the pre-sheath, both on the upstream ("u") side (where $\mathbf{U}$ is directed towards the probe) and on the downstream ("d") side (where $\mathbf{U}$ is directed away from the probe), with $T_{\text{i}}^{*\text{u}} > T_{\text{i}}^{*\text{d}}$. As shown theoretically, an accurate estimation of T_{i} is given by $T_{\text{i}} \cong (T_{\text{i}}^{*\text{u}} + T_{\text{i}}^{*\text{d}})/2$ [Valsaque 2002]. T_{i}^{*} can be obtained by the RFA from a fit to the decaying part of the I-V characteristics (see also section 2.3.6.2), figure 2.2:

$$I_{\mathrm{col}} = I_0 \exp\left[-\frac{Z_{\mathrm{i}}}{T_{\mathrm{i}}^*}\left(V_{\mathrm{grid1}} - V_{\mathrm{s}}\right)\right]. \tag{2.2}$$

Upstream-dowstream asymmetry of T_{i}, in addition to the asymmetries of the other parameters such as j_{sat} and T_e, is a reason why it is better to use a bi-directional RFA rather than a uni-directional one. The averaging procedure which provides unperturbed, i.e. "real", T_{i} with an accuracy of a few percent (provided that the measurements is not influenced by instrumental effects) for the typical SOL ion temperatures [Valsaque 2002] is much more accurate than a single measurement on either side of the analyzer (this applies for other probes that measure the parallel ion temperature as well).

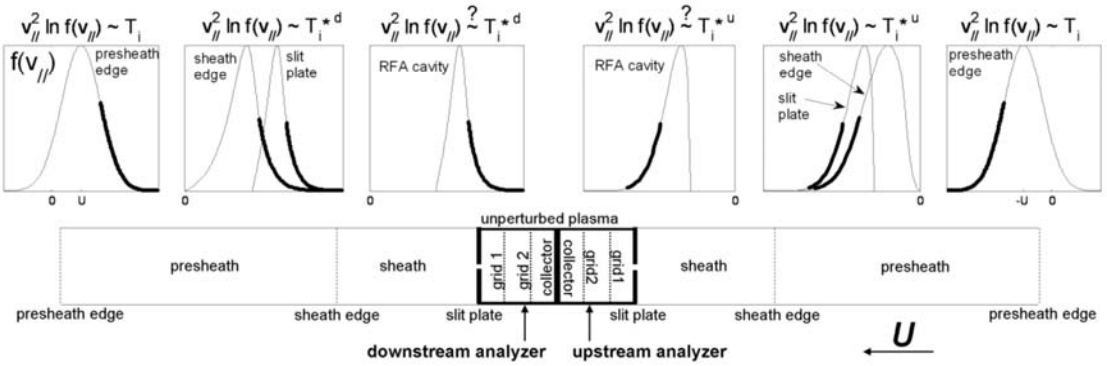

Figure 2.3. Schematic of the RFA inserted into the plasma. The probe consists of two identical analyzers mounted back-to-back. In the unperturbed plasma the parallel ion velocity distribution is Maxwellian with well defined temperature T_{i}. T_{i} is given by the decaying part of the distribution, shown schematically by thick line. In the presheath the Maxwellian distribution gets distorted both on the upstream ("u") side (where flow velocity U is directed towards the probe) and on the downstream ("d") side (where U is directed away from the probe). The effective ion temperature $T_{\mathrm{i}}^{*\mathrm{u}} > T_{\mathrm{i}}^{*\mathrm{d}}$, with $T_{\mathrm{i}} \cong (T_{\mathrm{i}}^{*\mathrm{u}} + T_{\mathrm{i}}^{*\mathrm{d}})/2$ [Valsaque 2002]. Inside the analyzer the distribution can be further influenced by instrumental effects (selective ion transmission through the slit, etc.) so that the measured temperature can differ from T_{i}^* (see section 2.3.3.3)

Alternative grid configurations have been also used in RFA. For example, a more refined design included a third grid, using grid 1 to repel thermal electrons, grid 2 to repel ions and grid 3 biased to a constant negative voltage to suppress the secondary electrons due to ion impact inside the analyzer [Molvik 1981, Nedzelskiy 2008, Wan 1986]. However, such refinements make the design of the probe more complicated since they require additional space as well more cables.

An alternative bias scheme in which grid 1 is held at a large positive potential to repel ions and grid 2 is swept can be used to measure the electron energy distribution. The value of the electron temperature measured in such a way can be compared with T_{e} measured e.g. by the slit plate working as a Langmuir probe, providing a proof of the

principle of a RFA. Such comparison has been reported by Wan [Wan 1986], showing good agreement between T_e measured by the RFA and by the Langmuir probe. In addition, in [Pitts 1991] it was demonstrated that a RFA with an alternative bias scheme can be used to measure the ion and electron induced secondary electron emission coefficient.

In principle, a RFA could measure directly the parallel ion velocity distribution function $f(v_{//})$ from the differentiation of the collector current (i.e. $f(v_{//}) \propto -dI_{col} / dV_{grid1}$ with $v_{//}^2 \propto V_{grid1}$). The velocity distributions measured experimentally could help validating the kinetic models for $f(v_{//})$ at the sheath edge (e.g. [Emmert 1980, Bissel 1987, Chung 1988]). For example, the models predict different pre-sheath (non-Maxwellian) parts of $f(v_{//})$. Unfortunately, the experimental noise does not permit the straightforward differentiation of the collector current. This is illustrated in figure 2.4 which shows typical RFA *I-V* characteristic, plotted in a semi-logarithmic scale, as well as the pseudo-distribution $f(v^*)$ calculated, for simplicity, as $-dI_{col} / dV_{grid1}$ with $v^* = \sqrt{V_{grid1}}$. As seen from figure 2.4, I_{col} clearly decreases exponentially above $V_{grid1} \approx 20$ V so that it seems reasonable to apply the fit Eq.(2.2) to that part of the *I-V* characteristic. However, because of the noise on I_{col}, increased by the differentiation, the corresponding velocity distribution is very scattered, making the comparison with the models impossible.

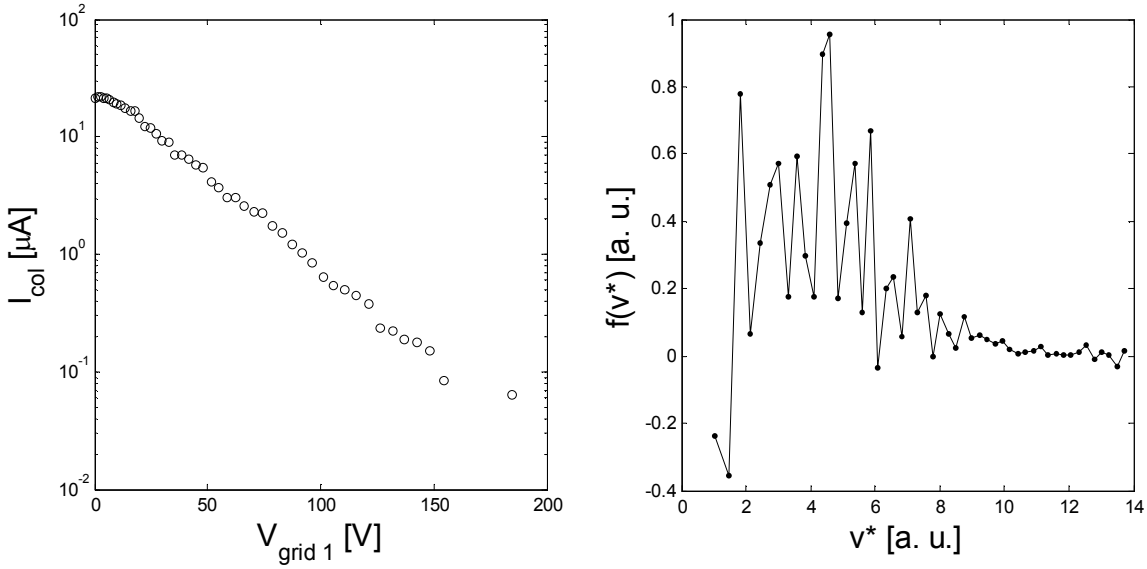

Figure 2.4. Left: RFA I-V characteristic measured ~1 cm outside the LCFS in the TS discharge #42671. Collector current is plotted against the bias voltage applied to grid 1. Right: Ion velocity distribution obtained from the differentiation of the collector current $-dI_{col} / dV_{grid1}$. $v^* = \sqrt{V_{grid1}}$.

2.3. Tore Supra RFA

A RFA based on an earlier JET design [Guo 1996] was mounted in Tore Supra for the first time in 1999. Between 2003 and 2008 the RFA was mounted six times on a fast reciprocating drive and performed 3220 reciprocations in total, with only a single accident (in which the probe protective housing was lost) due to the failure on the real time position control system. Up to 15 reciprocations per shot, a maximum target position of more than 4 cm inside the LCFS, and measurements near the LCFS in a plasma heated by up to 8.5 MW are included in the database. Figure 2.5 (left) shows the total heating power at the moment of the RFA reciprocation plotted against the vertical distance of the deepest point of measurement with respect to the LCFS for all reciprocations. Most of the RFA reciprocations were performed very close to the LCFS. The depth of the reciprocation is almost independent of the heating power, attesting to the confidence the Tore Supra operations team have in the probe system. Also plotted in figure 2.5 is the total number of reciprocations per year, culminating shortly after the start of this thesis in 2006 (however, a large number of reciprocations in 2007 was performed during experiments aimed at the measurement of fast electrons [Gunn 2009] which are not directly related to the subject of this thesis). During a single experimental campaign in Tore Supra in autumn 2008, four experimental sessions were dedicated to RFA measurements. At the time of writing the RFA is mounted on the reciprocating drive in the Mega-amp spherical tokamak (MAST) [Lloyd 2007] to measure the ELM ion energy in the SOL.

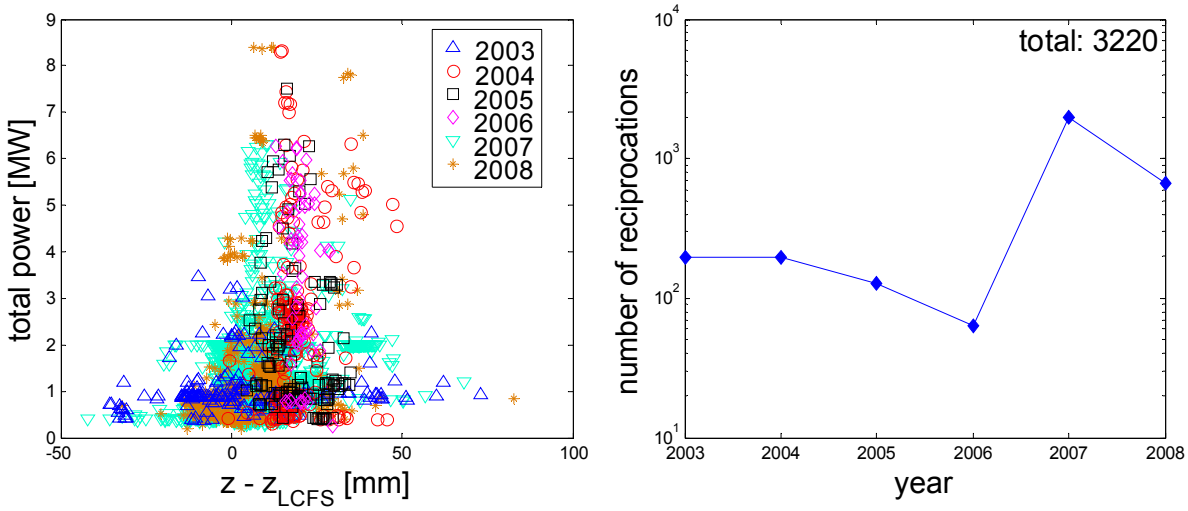

Figure 2.5. Left: Total heating power at the RFA reciprocation plotted against the vertical distance of the deepest point of measurements from the LCFS. All RFA reciprocations in 2003 – 2008 are plotted. Right: Number of the RFA reciprocations per year.

The secret of the successful RFA operation in Tore Supra is mainly in the relatively simple and robust probe design, good technical support, the adjustments of some of the probe components and operation scenarios as well as the implementation of

various safety feedbacks. Also important factor is the reciprocating probe operation in Tore Supra is much more flexible and administratively easier that e.g. in JET (we shall note that Tore Supra SOL is also less hostile than JET SOL).

2.3.1. Probe design, electronics, operation and data analysis

2.3.1.1. Probe design

The probe head consists of a two identical analyzers, figure 2.6, mounted back-to-back, sampling plasma from both directions along the magnetic field lines. Each analyzer consists of the slit plate, two principal grids and the collector (see section 2.2 and figure 2.1), separated by spacers (alumina 99.6%) with the thickness of 2 mm, a distance given by tight spatial restrictions.

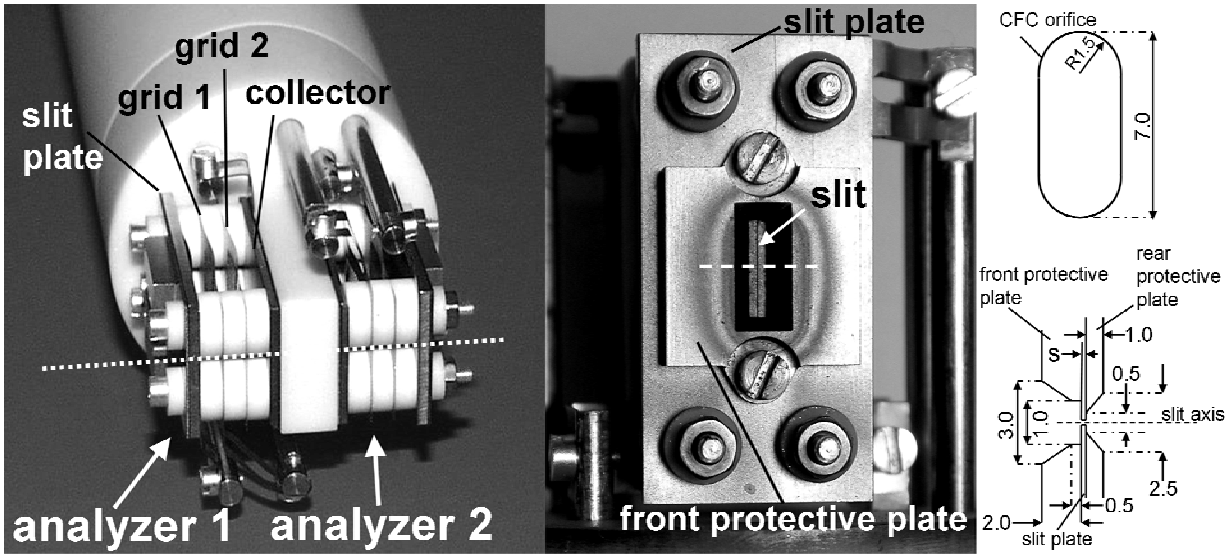

Figure 2.6. Tore Supra RFA. Left: the probe head with two identical analyzers mounted back-to-back. The probe head axis, aligned with the magnetic field, is indicated by dotted line. Right: Plasma facing components of each analyzer consist of the front protective plate and the slit plate. The 'shadow' of the CFC orifice, caused by the deposition of carbon, which is visible on the protective plate, defines the plasma wetted area, A_{orifice}. Orifice dimensions are stated upper right. Horizontal dashed line through the slit indicates a cut of the slit plate which is given lower right (not in scale). Note that this figure shows the configuration with the 'vertical' slit plate aperture. 'Horizontal' slit plate aperture (with the cut in the slit plate as well as the opening in the protective plates rotated by 90°) is used more recently for Tore Supra RFA (see figure 2.9).

The slit plate (figure 2.6, right) is made of a thin foil (99.9% nickel) and pressed between two protective plates (Inconel 750) with a chamfered opening. The protective plates serve as a heat sink. A rectangular slit with a width $w = 30\,\mu\mathrm{m}$ is laser cut into the foil. The typical value of the Debye length λ_D in Tore Supra SOL is 20 → 30 μm so that the slit width is small enough to assure the continuity of the sheath potential surface

across the slit. Slits with different lengths ($h = 5$ mm and $h = 3$ mm) and foils with different thicknesses ($s = 250,\ 150$ and 100 μm) have been used for the TS RFA. The ion transmission factor of the 250 μm thick slit plate was found to be too low (the collector current was only a few μA at the lowest plasma densities, see also section 2.3.3.4) so that the slit plate thickness was steadily decreased in the consecutive experimental campaigns. On the other hand, for the 100 μm thick slit plate the collector current exceeds 100 μA in high density discharges, approaching the space charge limit inside the analyzer cavity (section 2.3.4). Therefore, the slit length was reduced from 5 to 3 mm, reducing the transmitted ion current by almost a factor of ~1.7. The initial 250 μm slit plate was used during plasma start-up phase after an opening and work inside the machine and was blocked by dust particles after only a few reciprocations, figure 2.7. The RFA measurements performed later on were, therefore, routinely preceded by series of reciprocations with no plasma in order to remove the dust accumulated on the vessel walls by mechanical vibrations created by the movement of the reciprocating probe drive.

Both the vertical and the horizontal orientations of the slit plate were used in Tore Supra RFA. Vertical (horizontal) orientation means that the cut is parallel (perpendicular) to the probe movement (for example, the cut shown in figure 2.6 is vertical). Obviously, a horizontal cut provides better radial resolution (section. 2.3.1.3).

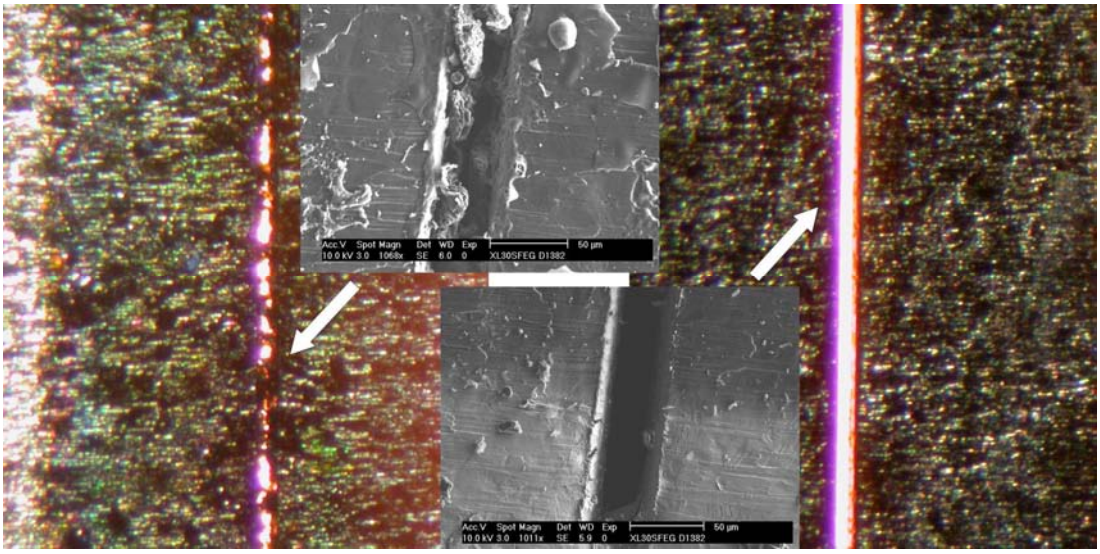

Figure 2.7. Left: Photograph of the aperture blocked by dust particles. Right: Clean aperture shown for comparison.

Using the code CASTEM 2000 developed at the CEA[8], the temperature rise of the slit plate itself was estimated to be 150 → 700 °C for a 40 ms pulse at 10 MW/m² for the plate thickness of 150 μm. The melting point of nickel is 1453 °C. Since the slit plate is pressed between two thick protective plates (figure 2.6) that were neglected in the simulations, the real peak temperatures of the slit plate are probably lower. The probe has been exposed to heat flux densities up to 30 MW/m² for ~10 ms, without any damage on the slit plate.

[8] http: www-cast3m.cea.fr

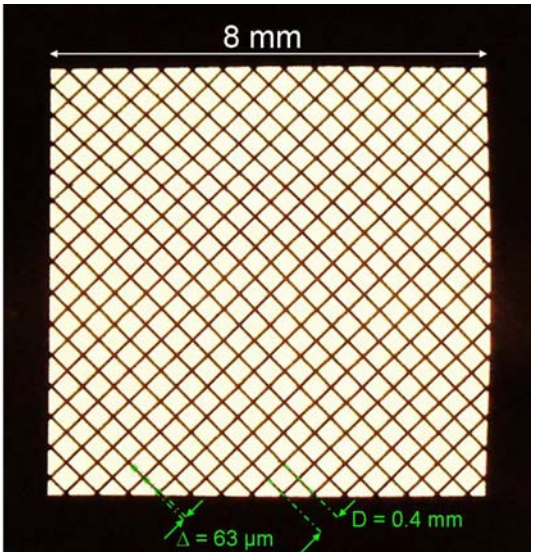

Figure 2.8. Photograph of the grid area.

The grids are laser-cut in a 99.9% nickel plates. The plate thickness is 30 μm. Grid wires with width of $\Delta = 63$ μm are separated by $D = 0.4$ mm, giving an optical transmission factor of the grid $\xi_{\text{opt}} = (D - \Delta)^2 / D^2 \cong 0.71$. The grid area is 8 × 8 mm, figure 2.8, meaning that the length of the grid area exceeds the 5 mm long slit plate aperture by 1.5 mm on each end of the aperture. This distance is larger than ion Larmor radius ($r_L \cong 150 - 800$ μm in the Tore Supra SOL), meaning that the grid transmission factor is not affected by the collection of ions outside the grid area even for relatively large probe head misalignment with respect to B. The grid wires are diagonal to the slit plate aperture to ensure that no single wire will block the trajectories of the particles transmitted through the aperture. In addition to the principal grids 1 and 2, another grid, referred to as "grid 0" (not shown in the schematic figure 2.1), is attached to the rear Inconel protective plate of the slit plate in order to render the electric field behind the chamfered opening of the protective plate as planar as possible.

The collector is made of oxygen-free high conductivity (OFHC) copper.

Taking the absorption of ions on the grid wires into account, the relative transmission factor of the slit plate calculated from the experimentally measured quantities approximately equals to:

$$\xi_{\text{r}}^{\text{exp}} \cong \frac{I_0}{j_{+\text{sat}} h w \xi_{\text{opt}}^3}. \tag{2.3}$$

For all three grids, the transmission factor is assumed to be equal to ξ_{opt}. The total grid transmission factor ξ_{opt}^3 is only approximate as the attenuation by subsequent grids could be a function of the alignment of grids relative to one other. Additional uncertainty in $\xi_{\text{r}}^{\text{exp}}$ can be due to e.g. ion induced secondary electron emission from the slit plate, which, if non-zero, would cause $j_{+\text{sat}}$ to be overestimated (and thus underestimate $\xi_{\text{r}}^{\text{exp}}$). The

deflection of ions towards the protective plate walls may also attenuate the incident ion current and thus further decrease the $\xi_{\mathrm{r}}^{\mathrm{exp}}$. These effects are studied in section 2.3.

The probe body consists of four cylinders (the lowest one providing also the support for the RFA electrodes) with the total length of ~18 cm, machined from 99.6% alumina. The photograph of the entire RFA probe is shown in figure 2.9. Inside the cylinders, the cables from the probe electrodes are redistributed in order to achieve the final arrangement compatible with the standard Tore Supra reciprocating drive socket. The fact that the cables inside the probe body are separated into several parts connected by joints might be the reason for the intermittent loss of connection observed in many RFA reciprocations.

Figure 2.9. Photograph of the entire RFA probe. The electrodes are followed by ~18 cm long alumina body which consists of four individual cylinders. The total weight of the probe shown here is ~650 g, in addition to ~190 g of the CFC protective housing (not shown).

The alignment of the probe head with the magnetic field is achieved by rotating the probe head axis (see figure 2.6) in the horizontal plane by 7° with respect to the toroidal magnetic field, an angle optimized for the edge safety factor $q_a = aB_\Phi /(RB_\theta) \approx 3$ operation. Here a, R, B_Φ and B_θ are, respectively, tokamak major and minor radii and local toroidal and poloidal magnetic fields. Since q_a varies between the discharges as well as over the probe reciprocation, alignment within about 3° is guaranteed.

The probe head is protected by a housing with outer diameter of 40 mm made of carbon fiber composite (CFC). The thickness of the housing is 3.5 mm. Plasma is transmitted to the slit plate through an orifice ($A_{\mathrm{orifice}} = 19.6 \times 10^{-6}\ \mathrm{m}^2$) drilled into the CFC housing. The dimensions and the shape of the orifice are indicated in figure 2.6. The orientation of the orifice follows the orientation of the slit plate aperture (i.e. two different protective housings were fabricated).

2.3.1.2 Electronics

A very schematic description of the probe cabling is illustrated in figure 2.10. The signal from the RFA electrodes are guided through the probe body using the coaxial shielding (figure 2.10). The coaxial shielding is used along the whole probe body except ~2 cm just near the electrodes. The cable screens are on torus ground which is carried away from the probe head via dedicated earthing cable, forming the ninth signals output in addition to two slit plates, four principal grids and two collectors. The probe protective housing is held on torus ground, providing electrical shielding of the RFA electrodes.

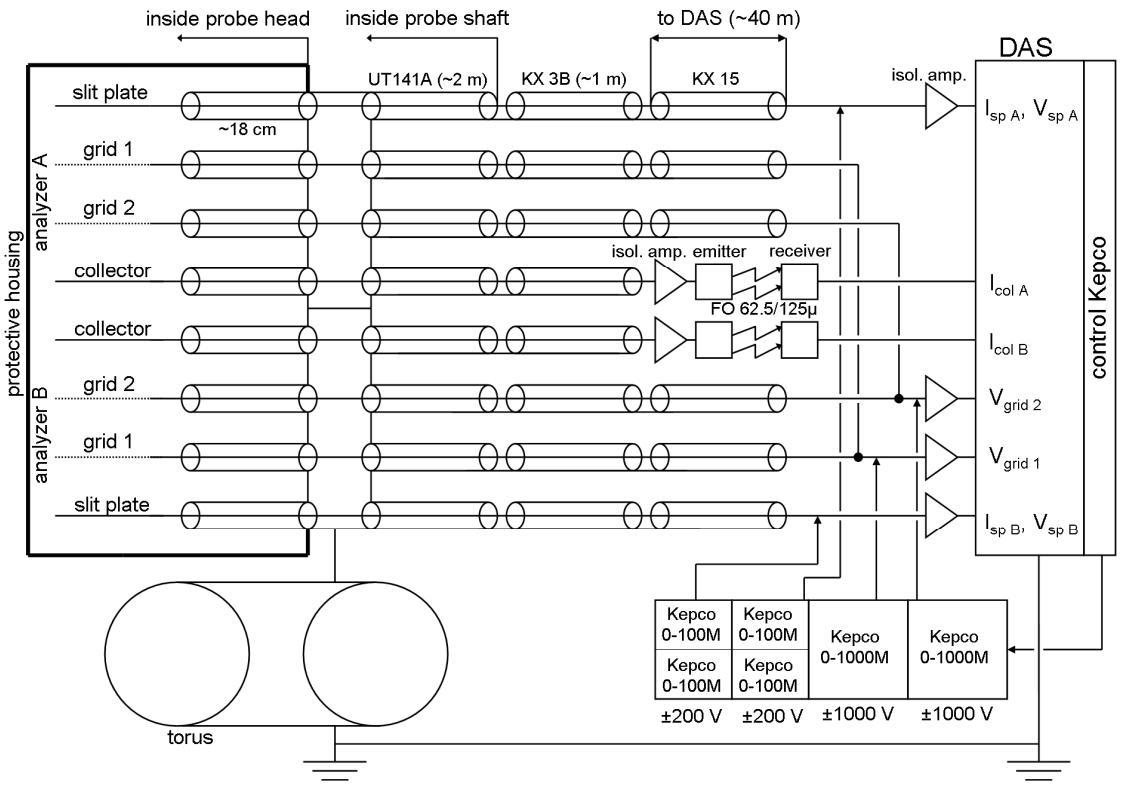

Figure 2.10. Schematic description of the Tore Supra RFA wiring and electronics with the approximate distances of all cables. Coaxial shielding with the cable screen on torus ground is used along the whole path between the electrodes and the data acquisition system (DAS) except ~2 cm just near the RFA electrodes. Outside the probe shaft the collector signal is guided to DAS through the optical cables.

Inside the reciprocating probe shaft the signal is guided through UT141A coaxial cables with the length of ~2 m, followed by more flexible KX 3B coaxial cables outside the probe shaft with the length of ~1 m, which slightly bend during the reciprocation. In order to reduce the effect of the noise on relatively low signals from collectors (current of 1 – 100 µA are typically measured, figure 2.12) along its path to the data acquisition system (DAS) separated from the probe head by ~40 m, the signal from both collectors is amplified by a sensitive isolation amplifier located near the probe head, and converted to an optical signal. The optical signal is then guided through optical fibres (FO 62.5/125µ) to the DAS and transformed back to an electrical signal. The receiver is characterized by a constant gain of about $3.3 \cdot 10^3$ V/A for the signal frequencies up to 20 kHz (typical I-V characteristic sweeping frequency is only about 1 kHz). KX 15 coax cables are used to guide the signals from the slit plates and the grids to the DAS. Two bipolar 0-100M Kepco power supplies provide -200→200 V bias range for each slit plate. The bias range of -1000→1000 V for the grids is provided by two 0-1000M bipolar Kepco power supplies (one for each pair of grids). Although the grid currents were not measured at the time of writing, new modules which allow the grid current measurements were recently fabricated on Tore Supra and will be tested in the forthcoming campaigns. Such measurements could be of large assistance in interpreting ambiguous collector signal as well as in better understanding of the instrument itself.

2.3.1.3 Operation and data analysis

The pneumatic reciprocating drives in Tore Supra allow for reciprocations with a frequency of 1 Hz. If several reciprocations are performed during a single discharge, different target positions of the probe can be defined for each of them. Real-time feedback based on fast magnetic reconstruction controls the probe position during reciprocation. This guarantees safe probe operation as the user does not need to know anything about the plasma configuration prior the discharge.

Figure 2.11 illustrates the time trace of the vertical distance of the RFA from the LCFS. Seven reciprocations are performed during the discharge. Last reciprocation is magnified in a widow on right. As seen from this figure, the inward-outward movement of the probe is not symmetric. There is transient slow-down of the probe at a certain position during retraction, which is characteristic for the Tore Supra reciprocating probe drive. The advantage of this is more detailed measurement at a certain radial position. Also added in figure 2.11 are the time traces of the plasma current, volume-averaged density and the total heating power.

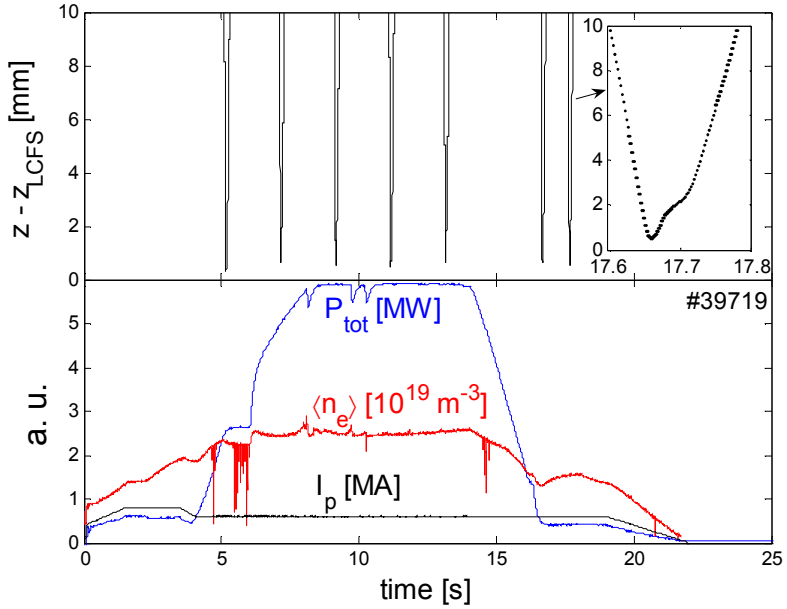

Figure 2.11. RFA operation in TS discharge #39719 with seven reciprocations in total. Top: Time trace of the RFA vertical distance from the LCFS. Last reciprocation is magnified in a small window. Bottom: Time traces of the plasma current I_p, volume-averaged density $\langle n_e \rangle$ and the total injected power P_{tot}.

The RFA electrodes are usually biased as follows. The slit plate is operating as a Langmuir probe, providing the measurements of T_e, j_{sat}, and V_f. The bi-directional capability of the RFA provides also measurements of the parallel Mach number [Hutchinson 1991] from which the parallel ion fluid flow velocity can be evaluated (see definitions below). Once the slit plate voltage is negative enough to repel most of the thermal electrons (typically -70 → -150 V depending on plasma conditions), the voltage

on grid 1, $V_{grid\,1}$, is swept from $0 \rightarrow V_{\max}$ (with $V_{\max} > 0$ and 0 referring to torus ground) to obtain the ion current characteristic on the collector. A constant negative bias is applied on grid 2, $V_{grid\,2}$. $V_{grid\,2}$ is typically -200 V. The collector is held at torus ground.

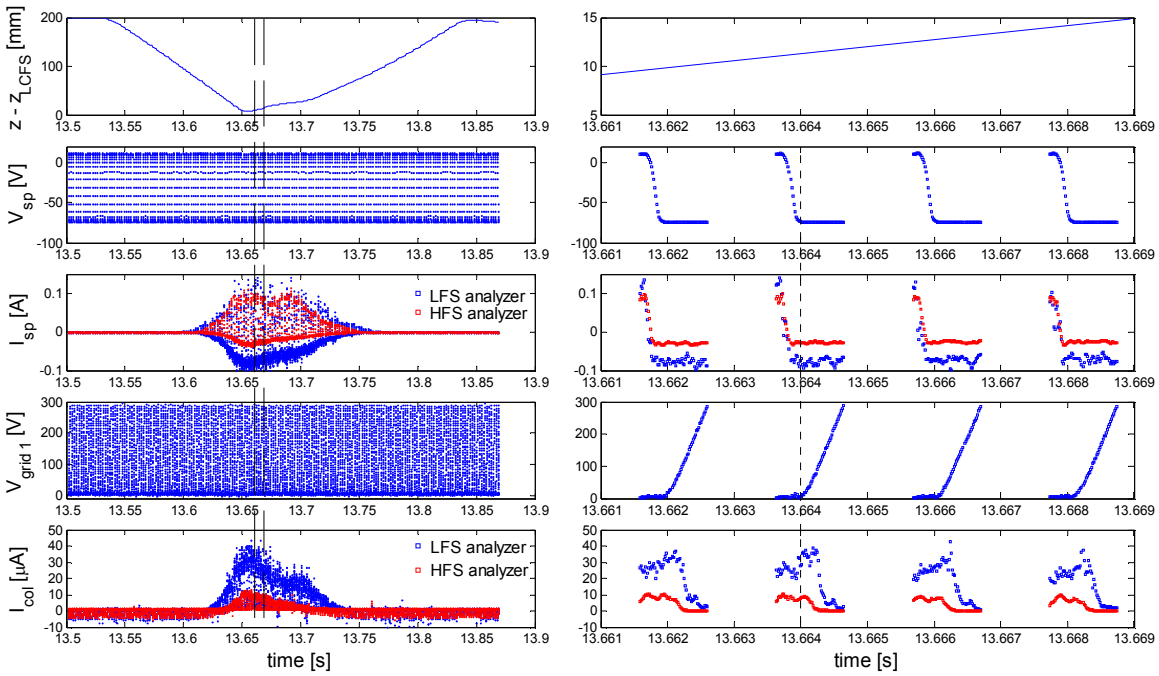

Figure 2.12. Left: RFA signals measured in one reciprocation. HFS (LFS) analyzer is facing the HFS (LFS) limiter target. From top to bottom: vertical distance from the LCFS, bias voltage applied to the slit plate, slit plate current, bias voltage applied to grid 1 and the collector current. Constant negative bias of -180 V was applied on grid 2. Currents measured by the LFS / HFS analyzer are plotted separately. Time slice of the RFA signals (vertical dashed line) is shown on right. Vertical dotted line separates the characteristic into two parts. T_i is measured in the second part of the characteristic. Data were measured in TS discharge #35880 at t=13.5 s (volume averaged density $\langle n_e \rangle = 2.2 \cdot 10^{19}\, m^{-3}$, $I_p = 1\, MA$, $B_t = 3.8\, T$, $R = 2.38\, m$, $a = 0.72\, m$, ohmic heating only).

Figure 2.12 illustrates the typical RFA signals measured in one reciprocation. Also plotted are the external bias voltages applied to the electrodes. A detail for $t = 13.661 - 13.669$ s shows four individual characteristics. The currents measured by the HFS (LFS) analyzer, which is the one facing the HFS (LFS) limiter target, are plotted separately.

The envelope of I_{sp} and I_{col} clearly follows the probe vertical distance from the LCFS, including the transient slow-down of the probe vertical movement during retraction (see figure 2.11). For $z - z_{LCFS} > 7$ cm both I_{sp} and I_{col} are negligible. (the offset on I_{col} measured far from the LCFS which is due to the cable capacitance is

subtracted during the data analysis.) The envelope of the RFA signals compared to the probe distance from the LCFS gives rough idea about the SOL width.

The detail of I_{sp} signal shows that the current to the slit plate saturates around $V_{sp} = -20\,\mathrm{V}$, meaning that the maximum bias voltage applied to the slit plate (-75 V) is sufficient to repel all thermal electrons.

The asymmetry of the HFS / LFS currents is believed to be due to the parallel flow in the SOL which is directed towards the LFS analyzer for the standard plasma configuration in Tore Supra (i.e. $R = 2.39\,\mathrm{m}$, $a = 0.72\,\mathrm{m}$, plasma contact point at the TPL, figure 1.15). The LFS analyzer thus receives larger ion currents. In addition, I_{col} measured by the HFS analyzer drops faster with V_{grid1} that I_{col} measured by the LFS analyzer, meaning that the effective ion temperature T_i^* at the HFS analyzer is lower compared to the LFS analyzer. The asymmetry in T_i^* roughly follows the ion current asymmetry, which is consistent with the kinetic model of Valsaque [Valsaque 2002] (section 2.2).

Because of the asymmetry in T_i^* it would be preferential to bias grid 1 of each analyzer separately with different maximum V_{grid1}, $V_{\max}$. As seen in figure 2.12 the collector current measured by the HFS-analyzer drops to zero already at about $V_{grid1} \approx 150\,\mathrm{V}$, so that the points on the *I-V* characteristics measured for higher V_{grid1} are sampled just at noise level and does not contribute to the fit Eq.(2.2). In turn, the LFS analyzer (which is here characterized by higher T_i^*) would require even larger $V_{\max}$ than that used in #35880 to repel all ions. Separate biasing of grid 1 for each analyzer is not possible because of the hardware restrictions.

Each characteristic is sampled for about 1 ms. Individual characteristics are separated by a window of about 1 ms during which the RFA signals are not measured (in addition, no data are collected between individual reciprocations), providing the time resolution of about 2 ms. The separation of the individual characteristics is used in order to reduce the volume of the data measured in one discharge. For the reciprocation shown in figure 2.12 (as well as for most RFA reciprocations) the number of data points per single characteristic is 64. The integration time between the individual data points is 16 μs, meaning that the RFA cannot measure any events characterized by smaller timescale.

The spatial resolution of the RFA is defined by the radial extension of the probe collection area increased by the radial displacement of the probe during the measurement of a single *I-V* characteristic. The vertical displacement of the RFA during the measurement of a single *I-V* characteristic is about 1 mm, except at the target position where the probe velocity is zero. Since the RFA is located close to the top of the plasma, the vertical displacement is nearly perpendicular to the magnetic flux surface. For the slit plate measurements (i.e. T_e, j_{sat}, and V_f) the collection area is defined by $S_{orifice}$ (figure 2.6). For the collector measurements (i.e. T_i, V_s and I_0) the collection area is defined by the area of the slit plate aperture, $S_{aperture} = hw$, (section 2.3.1.1). The orifice and the aperture dimensions are respectively 7 mm × 3 mm and 5 × 30 μm. As mentioned in section 2.3.1.1, both the vertical and the horizontal orientation of the orifice and the aperture was used for TS RFA. For the vertical orientation the radial resolution of the

RFA is approximately 8 mm for T_e, j_{sat}, and V_f, and about 6 mm for T_i and V_s. For the horizontally oriented orifice and aperture the radial resolution is about 4 mm for T_e, j_{sat}, and V_f, and about 1 mm for T_i and V_s. Both the radial separation of T_i and T_e measurements as well as the radial resolution of the probe are much smaller than the typical SOL temperature and density *e*-folding lengths in Tore Supra.

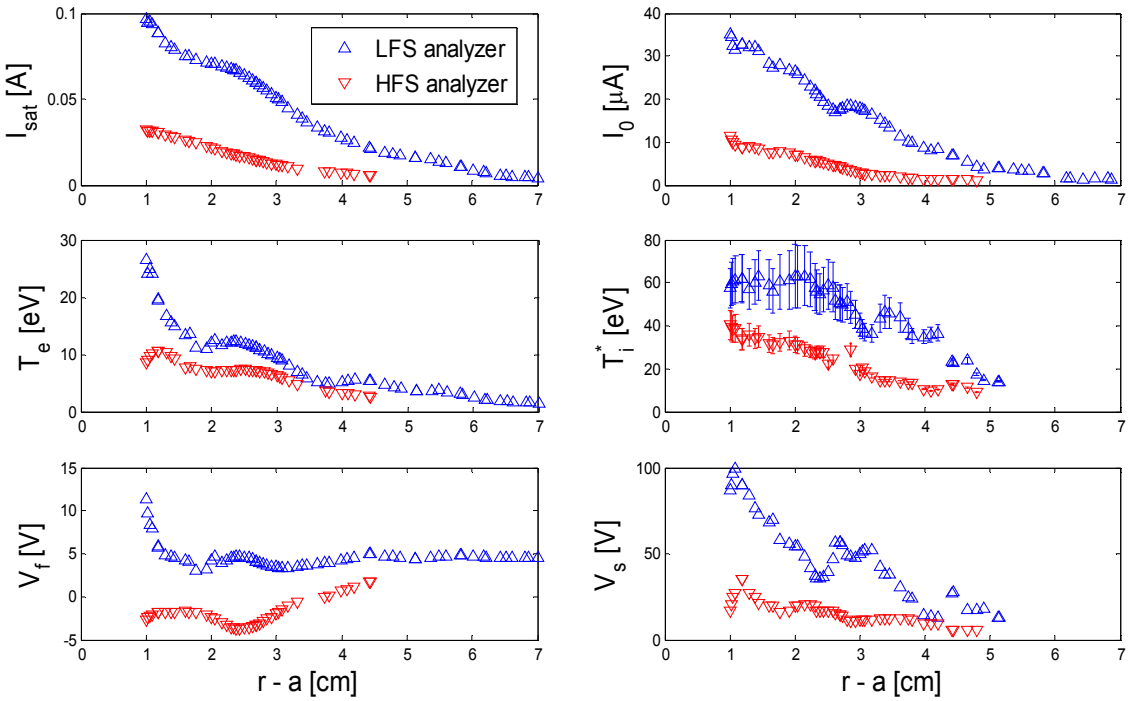

Figure 2.13. Radial profiles of the electron temperature T_e, the ion saturation current I_{sat}, the floating potential V_f, the maximum ion current at the collector I_0, the effective ion temperature T_i^* and the sheath potential V_s obtained from the RFA data shown in figure 2.12. The profiles measured by the HFS and the LFS analyzer are plotted separately.

Figure 2.13 shows the radial profiles of T_e, I_{sat}, V_f, I_0, T_i^* and V_s, measured by the HFS and the LFS analyzers, obtained from the data shown in figure 2.12. T_e, I_{sat}, V_f were obtained from the standard analysis of the LP characteristics measured by the slit plate. I_0, T_i^* and V_s were obtained from the fit Eq.(2.2) to the collector *I-V* characteristics (I_{col} against V_{grid1}). The error bar of T_i^* represents the confidence interval of fit. Some details about the error on T_i^* and V_s arising from the application of the nonlinear least squares fit are addressed in section 2.3.

Typical values of I_{sat} are almost by four orders of magnitude larger than I_0. This is partially because of the large difference in the collection area of the slit plate and the aperture (see above). However, as seen from figure 2.13 the collector receives only about

3-5% of the ion current that would be received by the collector if only a simple geometrical projection of $S_{aperture}$ plays a role (i.e. $I_0 \cong I_{sat} S_{aperture} / S_{orifice}$). Additional reduction of the ion current is due to the attenuation of ion flux on the front protective plate attached to the slit plate, figure 2.6, as well due to the transmission of ions through the slit plate and through the grids. These effects are studied in detail in section 2.3.

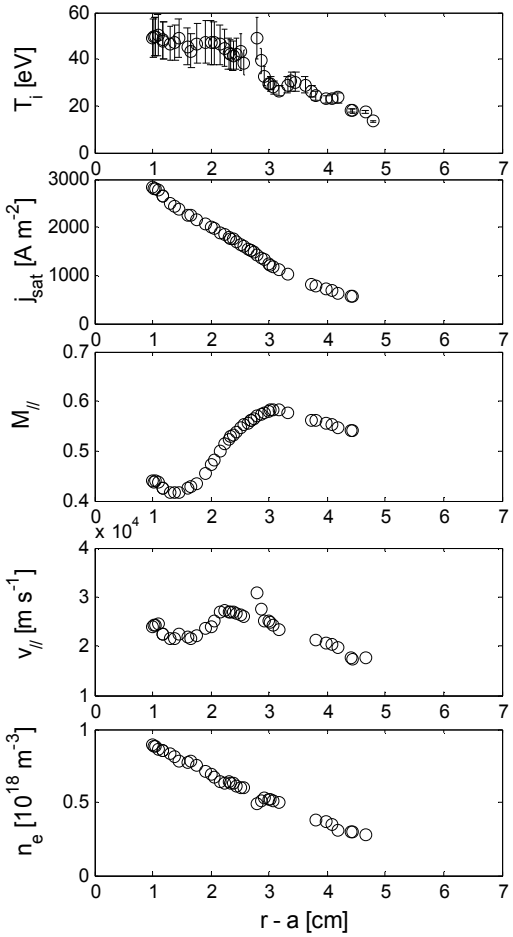

Figure 2.14. Radial profiles of the SOL parameters calculated from the RFA measurements shown in figure 2.13 (TS #35880 at t=13.7 s). From top to bottom: unperturbed ion temperature T_i, ion saturation current density j_{sat}, parallel Mach number $M_{//}$, parallel flow velocity $v_{//}$ and the electron density n_e.

Due to the parallel plasma flow [Hutchinson 1987] the radial profiles of I_{sat} and I_0 are strongly asymmetric. In addition, similar asymmetry is seen in the effective ion temperature T_i^* and the sheath potential V_s and can be explained by the disturbing effect of the probe combined with the plasma flow past the probe (see section 2.2 and [Valsaque 2002]). However, while the asymmetries in I_{sat}, I_0, T_i^* and V_s are understood, the asymmetry in T_e, which is also seen in figure 2.13 (as well as in most other LP measurements in TS), is not well understood. The difference in T_e on each side of the Mach probes was addressed only recently [LaBombard 2004, Dejarnac 2007]. However, a model that could explain the asymmetry in T_e is not yet available. Thus T_e is calculated as a mean value of the HFS and LFS analyzer measurements $(T_e^{HFS} + T_e^{LFS})/2$.

Additional important SOL parameters that can be calculated from the RFA measurements are:

- unperturbed ion temperature $T_i = (T_i^{HFS} + T_i^{LFS})/2$ (section 2.2 and [Valsaque 2002]),
- ion saturation current density $j_{sat} = \sqrt{I_{sat}^{HFS} \cdot I_{sat}^{LFS}} / S_{orifice}$ (Eq.(7) in [Dejarnac 2007])
- parallel Mach number $M_{//} \cong 0.4 \ln(I_{sat}^{LFS} / I_{sat}^{HFS})$ [Hutchinson 1991] (here the positive $M_{//}$ means that the flow is directed towards the HFS target[9]),
- parallel flow velocity $v_{//} = M_{//} c_s$ with $c_s = \sqrt{e(T_i + T_e)/m_i}$ being the ion sound speed,
- electron density $n_e \cong j_{sat} / (0.35 e c_s)$ [Hutchinson 1987].

These parameters are plotted in figure 2.14.

Returning to the bias voltage applied to grid 1, a wide range of T_i and V_s in the Tore Supra SOL requires an optimization of the voltage range for given plasma conditions. In general, the maximum voltage applied to grid 1, $V_{\max}$, should be low enough so that the major part of the *I-V* characteristic is sampled above the noise level of I_{col}, but yet high enough to capture the exponentially decaying slope of the *I-V* characteristic. This implies the optimal value of $V_{\max}$ of about $V_s + 3T_i$. For ohmic and additionally heated plasmas, the optimal value of $V_{\max} = 200 - 500\,\mathrm{V}$ (figure 2.15, left), depending on applied heating power and plasma density. For detached discharges, where T_i is only a few eV, the optimal value of $V_{\max}$ was found to be an order of magnitude smaller (figure 2.15, right).

[9] It should be noted that the there is no unified convection for the sign of the parallel flow. In e.g. [Erents 2004, Asakura 2007, Pitts 2007] the flow is defined as positive when it is directed towards the HFS target (i.e. anticlockwise poloidal direction). In e.g. [Gunn 2007] the convection is opposite, following the poloidal projection of the flow (i.e. the flow is positive when it is in the clockwise poloidal direction for the right-handed toroidal coordinate system for which the poloidal angle is also in the clockwise direction) rather than ***B***-aligned coordinate system.

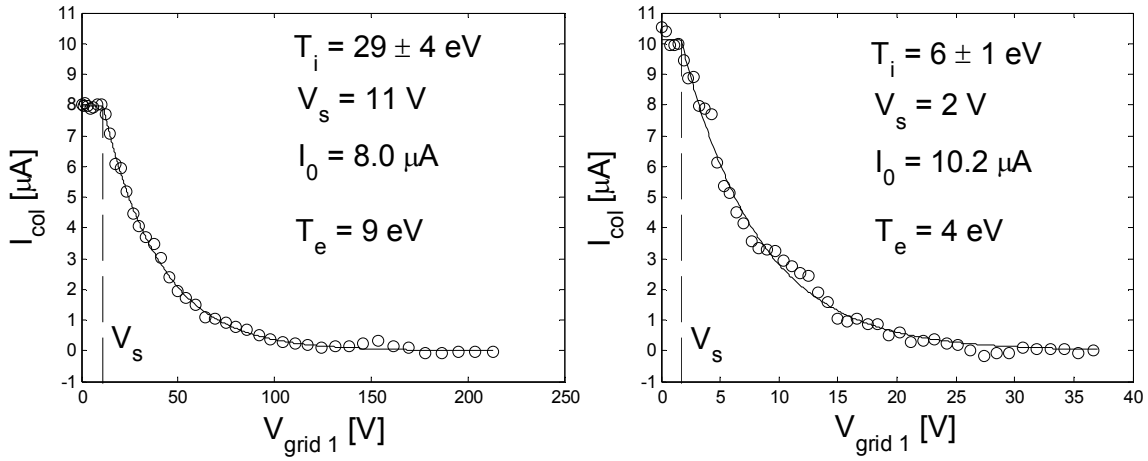

Figure 2.15. Typical RFA I-V characteristics for two different maximum bias voltages applied on grid 1. Left: attached ohmic plasma (TS discharge #42455 from group 1 at t =5.0 s, $\langle n_e \rangle = 1.25 \cdot 10^{19}\ \mathrm{m}^{-3}$, 6 mm outside the LCFS). Right: detached ohmic plasma (TS discharge #42463 from group 2 at t = 7.2 s, $\langle n_e \rangle = 2.3 \cdot 10^{19}\ m^{-3}$, 3 mm inside the LCFS). T_i, V_s, and I_0 were obtained from the fit Eq.(2.2) to the I-V characteristic. T_e was measured by the slit plate working as a Langmuir probe. All parameters were measured by the analyzer facing the HFS.

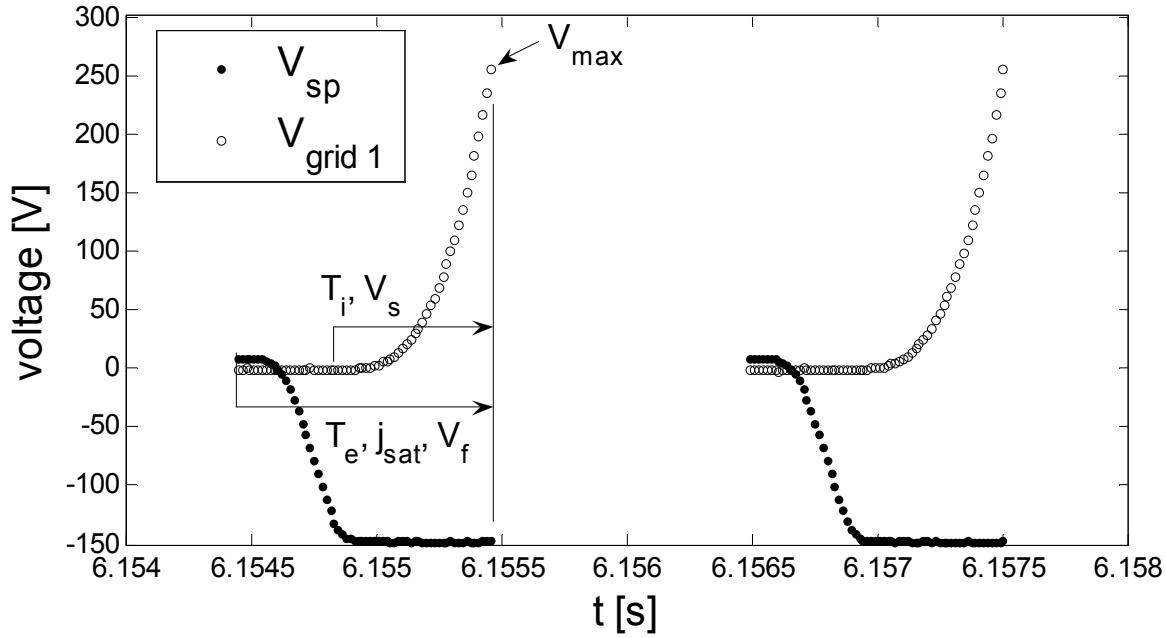

Figure 2.16. Time traces of the bias voltage applied on the slit plate V_{sp} and V_{grid1} (TS #42456, discharge). Also indicated is the part of each waveform used for the measurements of T_e, j_{sat}, and V_f (slit plate) and T_i and V_s (grid 1). $V_{\max} = \max(V_{grid1})$.

As a further optimization, a quadratic waveform instead of the usually applied simple linear sweep (e.g. [Kimura 1979, Wan 1986, Raychaudhuri 1999, Pitts 2003, Nedzelskiy 2006]) was used for V_{grid1} in order to acquire more points of the *I-V* characteristic at the steepest slope of I_{col}, figure 2.16. In addition, in order to account for the radial variation of T_i and V_s, a real-time feedback on based on the RFA probe position was developed to modulate $V_{\max}$ during the reciprocation (figure 2.17). A more refined approach would also likely to account for the upstream-downstream asymmetry of T_i and use different $V_{\max}$ for each side of the RFA: somewhat higher (lower) for the upstream (downstream) analyzer where the effective T_i tends to be higher (lower). This would, however, require additional 0-1000M Kepco power supply which is not available in Tore Supra.

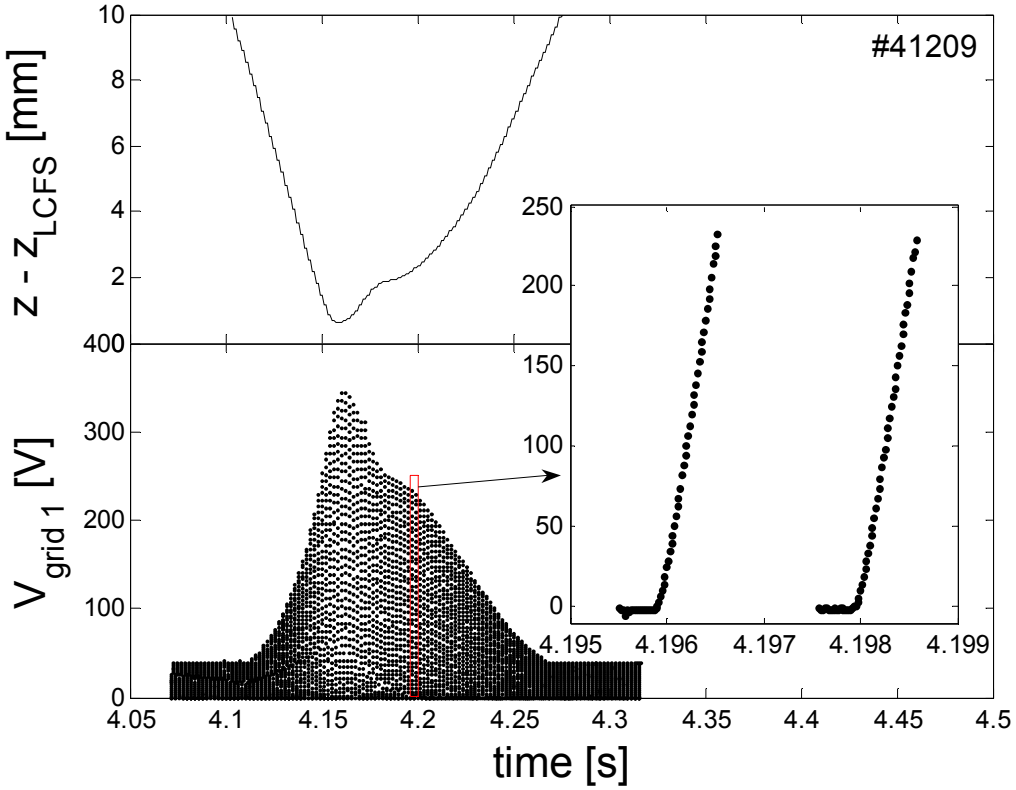

Figure 2.17. Above: distance of the RFA from the LCFS during reciprocation. Below: Bias voltage applied to grid 1, V_{grid1}. A real-time feedback based on the RFA probe position is used to modulate the maximum voltage applied to grid 1.

2.4. Instrumental study of the Tore Supra RFA

The theory of the RFA operation is so straightforward that it is tempting to assume that the response of the real RFA is the same as that of an idea device. However, since an independent experimental validation of RFA T_i measurements on a large fusion reactor is not yet available due to a lack of simultaneous measurements with other relevant diagnostics, in this section, the instrumental effects and their influence on RFA measurements (T_i in particular) are studied. Some results from the following sections are compiled in the paper published in the Review of Scientific Instruments [Kocan 2008c] (see annex to chapter 2).

Following the ion path from the entrance of the CFC protective housing to the collector, we study separately the following processes:

(i) Attenuation of the ion flux on the CFC protective housing and its influence on j_{sat} measurements (section 2.4.1).
(ii) Attenuation of the ion flux on front protective plate of the slit plate and its influence on T_i measurements (section 2.4.2).
(iii) Ion transmission through the entrance slit and its influence on T_i measurements (section 2.4.3).
(iv) Effect of the positive space charge inside the RFA cavity and its influence on T_i measurements (section 2.4.4).
(v) Influence of the negatively biased grid on T_i measurements (section 2.4.5).

Experimental and theoretical investigations of the instrumental effects in RFA were already reported elsewhere. Some of the topics mentioned above were addressed e.g. in [Pánek 2004] (i), [Nachtrieb 2000, Matthews 1984, Wan 1986, Pitts 1991, Pitts 1996] (iii), [Molvik 1981, Wan 1986, Matthews 1985] (iv) and [Matthews 1985] (v). In this section we introduce several improvements and arrive at some new conclusions with respect to the earlier studies.

In (i) we take into account specific geometry of the orifice of the Tore Supra RFA protective housing. Moreover, compared to [Pánek 2004] where the attenuation was studied only by particle simulations, we combine the experimental data, particle simulations and a simple theoretical model based on the scaling of the magnetic pre-sheath thickness to quantify the attenuation effect. We conclude that the attenuation of the ion flux on the CFC protective housing is responsible for an underestimation of j_{sat} measured by the Tore Supra RFA by up to a factor of ~2.

(ii) is similar to (i). The attenuation of the ion current on the protective plate is studied by means of PIC simulations. We conclude that the actual protective plate geometry of Tore Supra RFA attenuates strongly the incident ion current (factor of 1.7 – 3 for the range of parameters studied here). We propose an alternative protective plate geometry to reduce this effect. However, even for the actual protective plate geometry the effect of the attenuation on T_i measurements is negligible for the typical external slit plate bias voltages.

In (iii) we partially follow some ideas originally proposed by Nachtrieb [Nachtrieb 2000]. What is new is the quantitative evaluation of the effect of the slit transmission on T_i as a function of the slit plate thickness, ion-to-electron temperature ratio and the angle of the slit plate misalignment with respect to the magnetic field vector **B**. We show that the selective ion transmission through the RFA slit plate is responsible for an overestimation of T_i by less than 14%, even for a relatively thick slit plate. We therefore conclude that, providing that the signal level is sufficient, thicker slit plates are preferable since they reduce, e.g., the risk of melting during off-normal events, and the effect of the positive space charge inside the RFA cavity. In addition, improving upon [Nachtrieb 2000], we apply more general approach in the evaluation of the relative slit transmission factor and compare the theoretical calculation with the particle simulations and experimental data for different slit plate thicknesses and slit lengths. We demonstrate that the relative slit transmission factor is almost independent of the misalignment of the slit with respect to **B**. Therefore, taken that the electrons are transmitted into the analyzer by optical transmission because of much smaller Larmor radii compared to ions, a slightly tilted slit plate (by an angle defined by the slit width-to-thickness ratio) could be used as effective method for preventing the electrons to enter the analyzer independently of the bias voltage applied to the slit plate.

In (iv) the formula derived in [Nachtrieb 2000] was used to calculate the modification by positive space charge of the vacuum potential between the slit plate and grid 1. We conclude that for the typical ion currents measured by Tore Supra RFA the potential between the slit plate and grid 1 is dominated by the vacuum potential and space charge effects are therefore negligible.

In (v) we show that (in contrast to what was suggested in [Pitts 2003]) the transmission of the negatively biased grid is close to optical and its influence on T_i measurements is negligible.

Finally, the error on V_s and T_i arising from the application of the standard fitting procedure (Eq.(2.2)) to the RFA *I-V* characteristics is studied for the first time. We show that the application of the standard fitting procedure leads to an overestimation of T_i by up to ~10% and to the overestimation of V_s by up to $0.3T_e$. Because the measurements of the collector current are necessarily subject to noise and the parallel ion velocity distributions are not exponential for a certain range of velocities, these errors are largely unavoidable. It is concluded that in order to reduce the error on T_i the upper limit of the range of the collector currents included in the fit (Eq.(2.2)) should be as small as possible (within the limits given by the collector current signal-to-noise ratio).

Some issues concerning the reliability of T_i measurements are not addressed in this section, the most important of them being the influence of impurity ions in the SOL. As the analysis of the RFA current-voltage (*I-V*) characteristics assumes Maxwellian singly charged ions, impurities with higher charge states can affect the measurement of T_i. Separation of the components of the analyzed ion flux by charge state and temperature has been proposed in [Pitts 1991]. However, the model needs to specify the fractions of the total flux carried by ions with a given charge state as well as their temperatures. Such measurements are not available.

2.4.1. Attenuation of the ion flux on the CFC protective housing

This study was motivated by the experimental observation that the parallel ion saturation current density measured by the RFA, $j_{\mathrm{sat}}^{\mathrm{RFA}}$, is systematically lower compared to that measured simultaneously by a so called the tunnel probe (TP) [Gunn 2002], $j_{\mathrm{sat}}^{\mathrm{TP}}$, figure 2.18. Typical radial profiles $j_{\mathrm{sat}}^{\mathrm{RFA}}$ and $j_{\mathrm{sat}}^{\mathrm{TP}}$, measured in very similar plasmas, are shown in figure 2.19. The difference between $j_{\mathrm{sat}}^{\mathrm{RFA}}$ and $j_{\mathrm{sat}}^{\mathrm{TP}}$ increases up to $j_{\mathrm{sat}}^{\mathrm{RFA}} / j_{\mathrm{sat}}^{\mathrm{TP}} \sim 2$ near the LCFS.

The electric field gradient in the magnetic pre-sheath (MPS) is known to deflect the ions near the surface towards its normal if the ion Larmor radius is larger than the Debye length [Riyopoulos 1996a]. In this case, the ion flux entering a tunnel whose axis is nearly parallel with the magnetic field is subject to attenuation and the transmitted ion current is lower than that entering the tunnel orifice. The attenuation has direct consequences for Langmuir probes measurements of j_{sat}. Probes are often inserted into a protective housing and the ion current is transmitted to the probe through a small hole in drilled into the housing.

In Tore Supra RFA the incident ion current can be attenuated on the inner walls of the CFC orifice through which the plasma flows towards the slit plate, figure 2.6. In turn, the TP has a collecting area clearly defined by the tunnel orifice and is, therefore, immune to the attenuation [Dejarnac 2007].

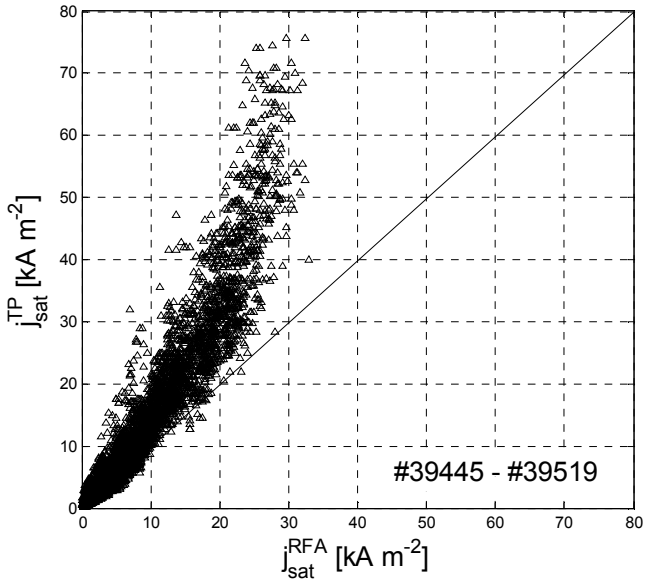

Figure 2.18. Comparison of the ion saturation current densities measured by the RFA and by the TP. Measurements were performed in the steady-state phase of the discharge. The RFA and TP measurements are separated by ~0.5 second. Each data point corresponds to the measurements at the same radial position in the SOL. The discharges are characterized by the toroidal magnetic field $B_t \cong 3.75\ T$*, total heating power* $P_{tot} \cong 0.8 \to 6.0\ MW$ *and the volume averaged density* $\langle n_e \rangle = 1.6 \to 3.6 \cdot 10^{19}\ m^{-3}$.

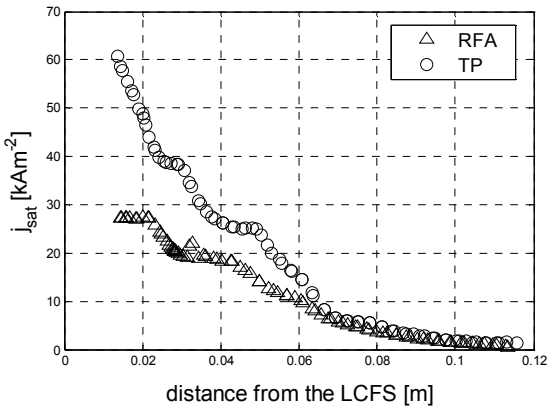

Figure 2.19. Radial profiles of the ion saturation current density j_{sat} measured by the RFA and the TP (TS discharge #39507 at t = 18 s, $B_t \cong 3.75$ T, Bt = 3.75 T, $P_{tot} \cong 4.7$ MW and $\langle n_e \rangle \cong 2.8 \cdot 10^{19}$ m^{-3}). The RFA and TP measurements are separated by ~0.5 second. Measurements were performed in a steady-state phase of the discharge.

In this section, the attenuation of ion flux on the CFC protective housing of the Tore Supra RFA is studied experimentally by comparing the RFA measurements of the ion saturation current density with those measured by the TP. In addition, the attenuation is studied by particle-in-cell simulations as well as a simple analytical model. It is shown that the attenuation of the ion flux is stronger at higher electron temperatures, which agrees with the theoretical scaling of the MPS thickness. The estimate of the attenuation factor can be used to calibrate the ion saturation current density measured by the RFA.

The attenuation effect was observed earlier in JET from large discrepancy between j_{sat} measured by the RFA [Pitts 2003] and that obtained from the turbulent transport probe (TTP) [Silva 2004]. The RFA j_{sat} was found to be a factor of 4 to 5 lower compared to that measured by the TTP, i.e. at least a factor of 2 stronger attenuation compared to that measured by Tore Supra RFA and the TP. Since the actual value of the attenuation factor depends on the probe geometry, this difference in the attenuation factor could be associated with the difference in the JET and Tore Supra RFA geometry. In addition, in contrast to the tunnel probe, TTP does not have a clearly defined collecting area so that the ion saturation current density measured by this probe could be overestimated, providing falsely high values of the attenuation factor for the RFA. In [Pánek 2004] the attenuation factor for JET RFA was evaluated using PIC simulations.

In section 2.4.1.1 we mention some well known conclusions from MPS theory and we propose a simple model that can be used for the estimation of the attenuation factor, based on the scaling for the MPS thickness. In section 2.4.1.2 we describe briefly the tunnel probe and make arguments why we consider the ion current density measured by the tunnel probe to be an accurate reference value. In section 2.4.1.3 the ion flux attenuation on Tore Supra protective housing is studied by means of PIC simulations. In section 2.4.1.4 the attenuation factor obtained experimentally is confronted with the results from the model and the PIC simulations.

2.4.1.1. Background of the ion current attenuation

The electric field gradient in the MPS and its effect on the ion trajectories has been extensively studied by many authors due to its important role in the plasma wall transition. In addition, new electrostatic probes for fast electron and ion temperature measurements such as the TP or its modification, the segmented tunnel probe (STP) [Kočan 1997], respectively, are based on the "demagnetization" of ions inside the MPS.

In the configuration with the magnetic field nearly parallel to the electrically conducting wall and the ion Larmor radius larger than the Debye length, the plasma-wall transition layer proves to have a double structure comprising a quasi-neutral MPS preceding the electrostatic Debye sheath [Chodura 1982]. In the MPS, the incoming ion flow turns from being sonic parallel to the magnetic field at the MPS entrance to being sonic parallel to the surface normal at the sheath edge. The thickness of the MPS, $L_{\mathrm{MPS}} \approx c_{\mathrm{e}} / \Omega_{\mathrm{i}}$, where $c_{\mathrm{e}}^2 = eT_{\mathrm{e}} / m_{\mathrm{i}}$ is the cold ion sound speed and Ω_{i} is the ion cyclotron frequency [Chodura 1982, Kim 1995, Gunn 1997]. In what follows we use the scaling $L_{\mathrm{MPS}} = 4.6(c_{\mathrm{e}} / \Omega_{\mathrm{i}})^{1.05}$ from [Gunn 1997] which is derived for slab geometry. For typical SOL electron temperatures the magnetic presheath thickness $L_{\mathrm{MPS}} = 0.2 \rightarrow 1\,\mathrm{mm}$.

Riyopoulos proved analytically that the positive electric field gradient in the MPS causes unstable particle motion across the magnetic field towards the surface [Riyopoulos 1996a, Riyopoulos 1996b]. This is true, however, only in the particular case of "demagnetized" sheath in which the ion Larmor radius r_{L} is larger to the typical scale length of the electric field gradient $E / \nabla E \propto \lambda_{\mathrm{D}}$ [Laframbois 1990], with λ_{D} being the Debye length.

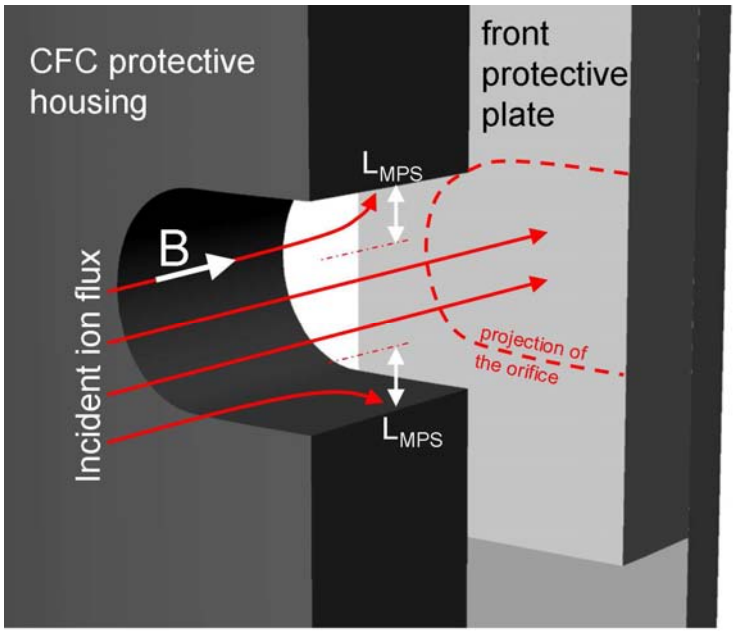

Figure 2.20. Schematic of the ion transmission through the CFC tunnel. The ion guiding centre trajectories are indicated by red arrows. The ions inside the magnetic pre-sheath are demagnetized, torn from the field lines and accelerated towards the surface. See also figures 2.6 and 2.21 for more details about the orifice dimensions.

In the Tore Supra SOL, the value of the "magnetization parameter" [Gunn 1997] $\zeta = r_{\mathrm{L}} / \lambda_{\mathrm{D}} = B^{-1}\sqrt{n_{\mathrm{e}} m_{\mathrm{i}} / \varepsilon_0}$ varies in the range of 2→8 so that the ions in the MPS are demagnetized. Consider the ions that follow the magnetic field lines towards the RFA and enter the orifice of the CFC protective housing. Inside the CFC tunnel, the ion flux can be divided into two parts. Those ions who enter the tunnel close to its axis with the distance from the tunnel wall of more than L_{MPS} continue unaffected along the magnetic field lines to the slit plate. On the other hand, the ions that enter the tunnel within about L_{MPS} about its surface are torn from the field lines and accelerated towards the tunnel surface, figure 2.20. Therefore, a large fraction of ions that enter the MPS does not reach the tunnel exit which makes the effective collection area of the RFA smaller. Let's assume that all ions that enter the MPS have a parallel transit time along the CFC tunnel longer than the transit time across the MPS (i.e. we assume that all ions that enter the MPS are collected by the tunnel). We assume, in addition, that the ion current density at the entrance of the CFC orifice is uniform. Under such conditions, the attenuation factor α can be expressed as a function of L_{MPS}:

$$\alpha_{\mathrm{model}} = \frac{A_{\mathrm{CFC\,RFA}}}{\widetilde{A}_{\mathrm{CFC\,RFA}}} = \frac{(r+1)^2 - 1}{(\widetilde{r}+1)^2 - 1}, \tag{2.4}$$

where $\widetilde{A}_{\mathrm{CFC\,RFA}}$ is the effective probe collection area, $r = \pi R/(L-2R)$, and $\widetilde{r} = \pi(R - L_{\mathrm{MPS}})/(L-2R)$ with R and L defined in figure 2.21.

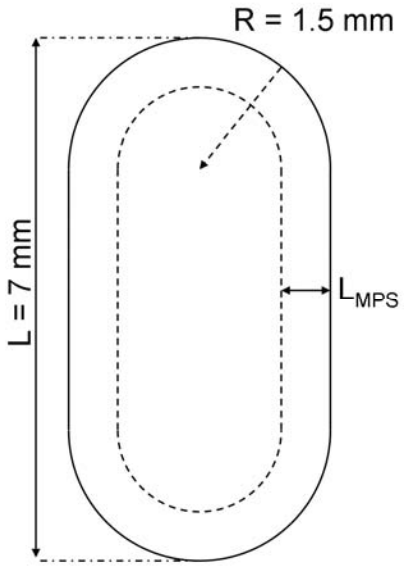

Figure 2.21. Full line: the area of the orifice drilled into the CFC protective housing. Dashed line: the effective area of the orifice. L_{MPS} is the magnetic pre-sheath thickness.

2.4.1.2. Tunnel probe

The TP used in Tore Supra consists of a hollow conducting tunnel, 3 mm in diameter and 5 mm deep, closed at one end by an electrically isolated conducting back plate. The tunnel axis is aligned with the magnetic field. The sum of the tunnel and the back plate currents gives the ion saturation current I_{sat}^{TP}. The probe is inserted into a protective housing made of CFC. The plasma is transmitted to the probe through a circular hole in the housing with a diameter of 7 mm giving $A_{\mathrm{CFC\,TP}} = 38.5\times10^{-6}\ \mathrm{m}^2$. The tunnel probe with the projection of the CFC orifice is shown in figure 2.22, right. For comparison, the projection of the CFC orifice on the RFA slit plate is also shown in figure 2.22, left. As seen from figure 2.22 the orifice of the TP protective housing is not perfectly aligned with the tunnel orifice and the distance of the orifice from the tunnel edge varies from about 1 to 3 mm. However, since the L_{MPS} in Tore Supra SOL is about 0.2 – 1 mm, it is unlikely that the TP measurements of j_{sat} are, in contrast to RFA, influenced by attenuation effect. We therefore argue that the collecting area of the TP is clearly defined by the area of the $A_{\mathrm{tunnel}} \cong 7.1\times10^{-6}\ \mathrm{mm}^2$, rather than by $A_{\mathrm{CFC\,TP}}$, i.e. $j_{\mathrm{sat}}^{\mathrm{TP}} = I_{\mathrm{sat}}^{\mathrm{TP}} / A_{\mathrm{tunnel}}$.

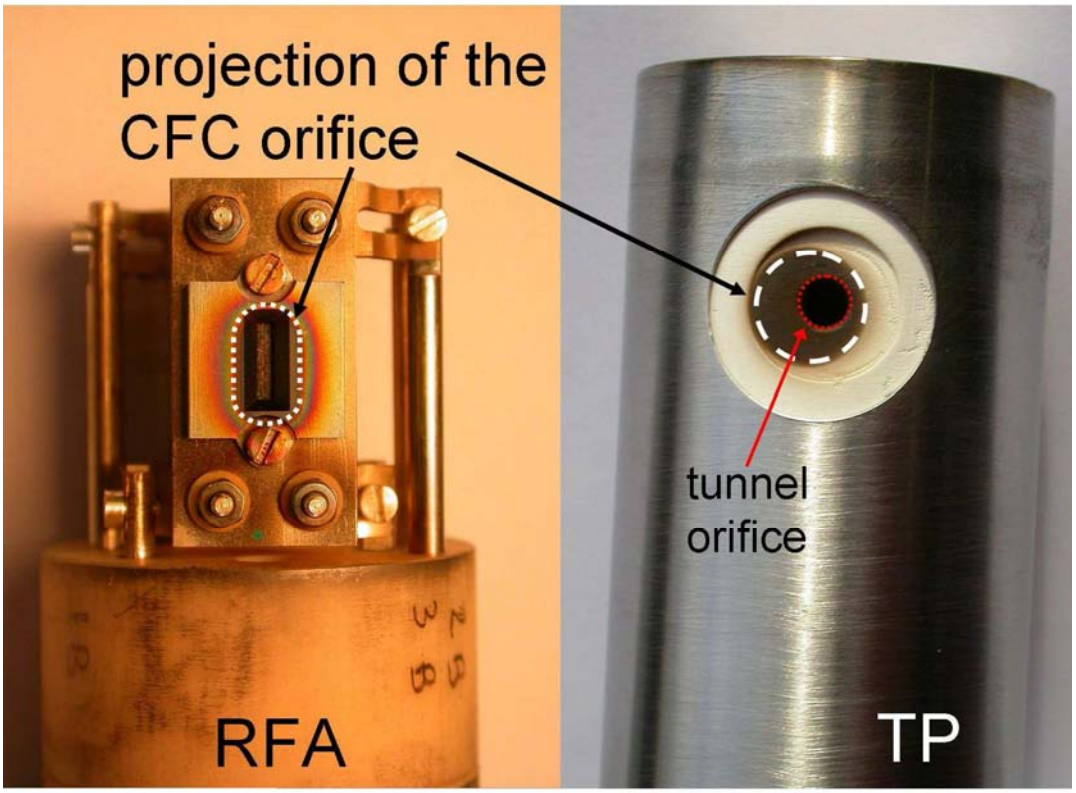

Figure 2.22. Left: RFA. Right: tunnel probe. Both probes are inserted into the protective housing made of CFC (not shown). The projection of the CFC orifice appears as a dark area of deposited carbon. In RFA the CFC orifice defines the probe collecting area. The collecting area of the tunnel probe is defined by the tunnel orifice.

2.4.1.3. Particle-in-cell simulations

In this section, the attenuation of ion flux in the tunnel of the RFA protective housing is studied by particle-in-cell (PIC) simulations. In contrast to the model proposed in section 2.3.1.2 which was based on a simple geometrical assumptions and does not account for the finite tunnel length (assuming that all ions entering the MPS inside the tunnel are absorbed), in the PIC simulations the magnetic pre-sheath inside the tunnel is solved self-consistently and the trajectories of individual particles are tracked.

The attenuation is studied by means of the PIC code XOOPIC [Verboncoeur 1995]. The cross-section of the tunnel is oval (figure 2.21) which implies three-dimensional geometry of the problem to solve. The XOOPIC code allows for simulations with only two spatial dimensions so that the geometry of the problem requires simplifications. We utilize the fact that in the Tore Supra SOL the typical $L_{\mathrm{MPS}} = 0.2 \rightarrow 1$ mm which is substantially smaller compared to the both orifice dimensions (figure 2.21). Therefore, the attenuation acts only in a thin layer above the inner walls of the tunnel and is not significantly influenced by the actual curvature of the tunnel walls. The attenuation factor will be, therefore, similar for a tunnel with a circular cross-section but with the circumference identical to that of the real oval orifice. Such circular orifice is axially symmetric and can be therefore modelled by XOOPIC code in a cylindrical geometry. The simulations were performed as follows. Ions and electrons were injected towards a tunnel with the length of $s = 3.5\,\mathrm{mm}$ and the radius of $r_{\mathrm{CFC}} = 2.8\,\mathrm{mm}$. The injection plane was positioned 1 mm in front of the tunnel orifice. The system was terminated by a slit plate, positioned 1 mm behind the tunnel exit, i.e. the real distance of the RFA slit plate from the CFC housing (about 4 mm) was reduced in order to make the simulations faster. This should have no influence on the particle trajectories inside the tunnel, as the Debye sheath potential drop in front of the slit plate was found to be substantially smaller than 1 mm so that it does not influence the electric field inside the tunnel. The potential difference between the injection plane and the tunnel was set to

$$\phi_{\mathrm{ph}} = \frac{T_{\mathrm{e}}}{2} \ln\left[2\pi \frac{m_{\mathrm{e}}}{m_{\mathrm{i}}} \left(1 + \frac{T_{\mathrm{i}}}{T_{\mathrm{e}}} \right) \right], \tag{2.5}$$

assuming that the protective housing is biased to the floating sheath potential with respect to plasma. The potential difference between the injection plane and the slit plate was set to

$$\phi_{\mathrm{sp}} = V_{\mathrm{sp}} + \frac{T_{\mathrm{e}}}{2} \ln\left[2\pi \frac{m_{\mathrm{e}}}{m_{\mathrm{i}}} \left(1 + \frac{T_{\mathrm{i}}}{T_{\mathrm{e}}} \right) \right], \tag{2.6}$$

where $V_{\mathrm{sp}} = -80\,\mathrm{V}$ is the slit plate external bias voltage (similar bias voltage for the RFA slit plate was used for the measurements of the experimental data addressed here). T_{i} and T_{e} are respectively the ion and electron temperatures at injection. Secondary electron emission from the protective housing and from the slit plate was neglected. The ions and

electrons were injected with full Maxwellian distributions and with the current densities j_i and $j_e = j_i\sqrt{m_d / m_e}$, where m_d and m_e are, respectively, the deuteron and electron mass. The magnetic field vector **B** was aligned with the injection plane normal and its absolute value was set to 3.75 T. This is close to the value of the magnetic field for the discharges in which the data shown in figure 2.18 were measured and thus allows direct comparison of the PIC simulations and experiment. The simulation domain is illustrated in figure 2.23.

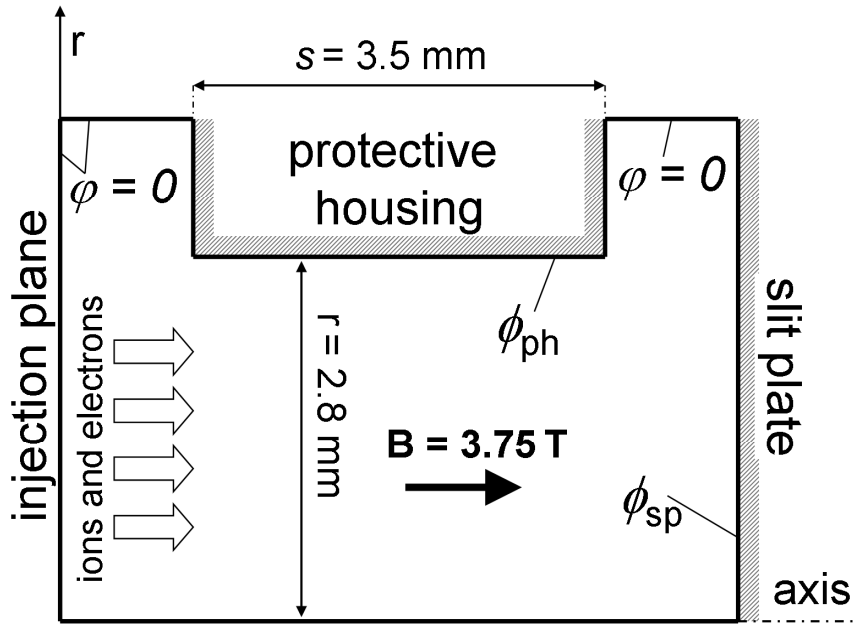

Figure 2.23. Simulation domain used for studying the attenuation effect by means of XOOPIC code. Ions and electrons are injected from left towards the slit plate. The ratio of the injected ion current to the ion current measured at the slit plate provides the value of the attenuation factor.

Each simulation was left to run to a steady-state. Consequently, the total current to the slit plate, I_{sp}, was measured during approximately one ion transit time. The attenuation factor α_{PIC} was calculated as

$$\alpha_{PIC} = j_i A_{model} / I_{sp}. \tag{2.7}$$

The simulations were reproduced for different combinations of j_i, T_e, and T_i typical for Tore Supra SOL. The results – α_{PIC} obtained for each set of the input parameters – are listed in table 2.1. α_{PIC} is almost independent on j_i and weakly dependent on T_i. The most dominant dependence is on T_e which is consistent with the scaling of the L_{MPS}. The results from PIC simulations for different T_e and T_i are compared with the experimental data in the following section.

j_i [kAm^{-2}]	T_i [eV]	T_e [eV]	α_{PIC}
5	20	5	1.39 ± 0.16
5	20	10	1.39 ± 0.23
5	50	10	1.57 ± 0.16
10	50	10	1.56 ± 0.16
10	50	20	1.68 ± 0.25
10	100	10	1.75 ± 0.27
10	100	20	1.84 ± 0.31
10	100	30	2.26 ± 0.44
20	100	10	1.77 ± 0.24
20	100	20	1.84 ± 0.29
20	100	30	2.22 ± 0.40
20	100	40	3.12 ± 1.05
50	100	40	3.06 ± 0.63

Table 2.1. Attenuation factor α_{PIC} obtained form the PIC simulations for different sets of the injected ion current density and ion and electron temperatures. α_{PIC} was calculated from Eq. (2.7). The confidence interval for α_{PIC} accounts for the fluctuations of I_{sp}.

2.3.1.4. Comparison of experimental data, theory and PIC simulations

Figure 2.24 compares the attenuation factor α measured experimentally with the theoretical model Eq.(2.4) and XOOPIC simulations, Eq. (2.7). Experimental value of the attenuation factor is calculated as $\alpha_{exp} = j_{sat}^{TP} / j_{sat}^{RFA}$. α is plotted as a function of the electron temperature (which is case of α_{exp} is T_e measured by the RFA). Since α_{PIC} was found to be almost independent of j_i, XOOPIC simulations for fixed T_e and T_i and different j_i are replaced by a single averaged value.

A linear least-squares fit to experimental data gives the approximate value:

$$\alpha_{exp}^{fit} \cong 0.823 + 0.032 T_e . \tag{2.8}$$

As seen from figure 2.24, the standard deviation of α_{exp} is relatively large so that α_{exp}^{fit} gives only very approximate value of the attenuation factor. α_{exp}^{fit} can be used to calibrate the RFA measurements, i.e. $j_{sat}^{RFA\,calib} = \alpha\, j_{exp}^{fit}(T_e) j_{sat}^{RFA}$.

The model and the simulations agree surprisingly well, taken the extreme simplicity of the model and the relative complexity of the self-consistent PIC simulations. Slight differences between α_{PIC} and α_{model} could be explained by the fact that the scaling of L_{MPS} used for the calculation of α_{model} is valid for slab geometry whereas the PIC simulations are performed for a circular tunnel. Both the model and the simulations predict α which is by about 50% larger compared to α_{exp}. One possible explanation for this discrepancy could be secondary electron emission from the RFA slit plate due to ion

impact. Since every secondary electron released from the slit plate is detected as a collected ion, the emission could lead to an overestimation of j_{sat}^{RFA}, hence the underestimation of α_{exp}. The ion current to the back plate of the tunnel probe can be influenced by the secondary electron emission as well. However, in the Tore Supra TP the ion current to the tunnel is higher than the back plate current so that the influence of the secondary electron emission on j_{sat}^{TP} is very small.

Assuming that the difference in the attenuation factor predicted by theory (or by XOOPIC) and α_{exp} is due to the ion-induced secondary electron emission from the slit plate, the secondary electron emission coefficient δ for the slit plate can be estimated from the comparison of α_{exp} with α_{PIC} or α_{model}. Taking α_{PIC} as an example, $\alpha_{PIC}/\alpha_{exp} = (I_0/I_{sp})/\left[I_0/I_{sp}(1+\delta)\right]$ (where I_0 is the ion current at the entrance of the CFC orifice) so that $\delta = \alpha_{PIC}/\alpha_{exp} - 1 \approx 0.4$. Since the plasma wetted area of the slit plate comprises the nickel slit plate as well as the Inconel front protective plate (figure 2.22), δ is an effective secondary electron emission coefficient of the slit plate. $\delta \approx 0.4$ is reasonably close to the values found for e.g. carbon or molybdenum (see e.g. figure 8.3.4 in [Pitts 1991].

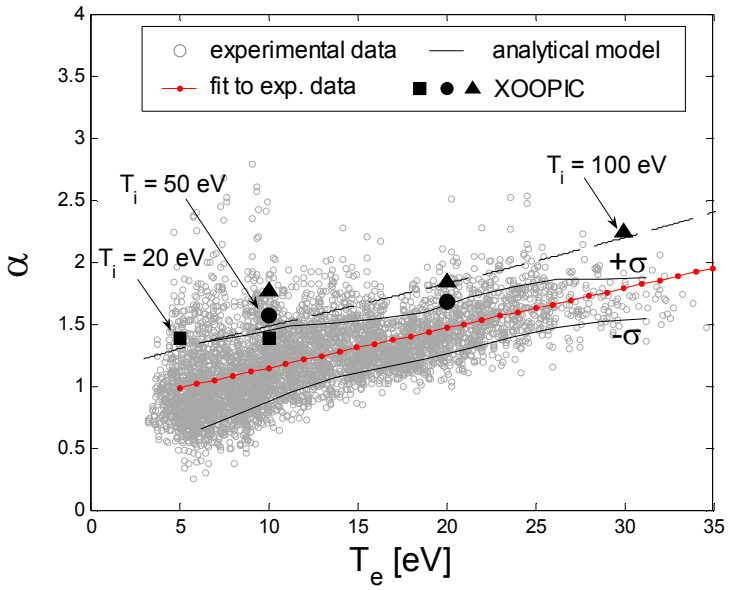

Figure 2.24. Attenuation factor α measured from the TP-to-RFA j_{sat}, obtained from a simple theoretical model (Eq. (2.4)) and from XOOPIC simulations (Eq. (2.7)). α is plotted as a function of electron temperature. Also plotted is the linear least-squares fit to experimental data (Eq. (2.8)). Full line indicates the standard deviation ($\pm\sigma$) of the experimental data.

Finally, it is worth mentioning that the effect of the ion current attenuation on the CFC protective housing studied in the previous section on the parallel ion energy distribution (and hence T_i inferred from the analyzer) can be most likely neglected. The attenuation can be in principle selective in the parallel ion velocities. However, the ions

flowing towards the slit plate aperture (i.e. the ones whose parallel energy distribution is measured by the analyzer) are about 1.5 mm far from the tunnel walls which is a distance larger than the L_{MPS}. Therefore, the ions flowing through the tunnel towards the aperture are most likely unaffected by the attenuation and its effect on T_i measurements can be neglected. Simulations should be carried out in order to verify this hypothesis.

2.4.2. Attenuation of the ion flux on the protective plate

As shown in figure 2.6, the aperture of the TS RFA is preceded by the front protective plate which serves as a heat sink. The ions flow towards the aperture through the rectangular window in the protective plate. Since the aperture is only 0.5 mm from the walls (which is a distance comparable to the magnetic pre-sheath thickness in TS SOL, see section 2.4.1.1), the ion flux to the aperture can be subject to attenuation similar to the one addressed in the previous section. Since the protective plate is in electrical contact with the slit plate, the attenuation caused by the protective plate does not affect the measurements of j_{sat}. However, because of selective parallel ion loss, it could affect T_i measurements as well as the transmission factor of the slit plate evaluated from experimental data, Eq. 2.3. The latter could be affected because the ion current actually received by the aperture can be smaller than j_{sat} multiplied by the aperture area which is one of the assumptions in Eq. 2.3.

The attenuation of ion flux on the protective plate is studied by means of the PIC code SPICE (Sheath Particle In CEll) [Dejarnac 2007]. Originally, the SPICE code was developed for studying the flow of plasma into gaps between the limiter and divertor tiles. SPICE allows for 2d3v simulations in Cartesian coordinates. The code implements a standard leapfrog method for particle advancing, and uses first order (*cloud-in-cell*) weighting [Birdsall 1985].

Two different protective plate geometries are assumed in the simulations:

- actual geometry of the TS RFA protective plate referred to as “A”,
- alternative knife edge geometry referred to as “B”.

The simulation domains for both A and B are shown in figure 2.25, right. The Cartesian coordinate system is used. The simulation domain is aligned with the *x*-*z* plane (with *x* being the direction aligned with **B**). *y*-direction is ignored in the simulations. The absorbing walls of the protective plate as well as the slit plate are set at the potential defined by Eq.(2.6), which includes the external slit plate bias voltage V_{sp} as well as the natural sheath potential drop. The “plasma” boundaries (i.e. the injection plane and the boundaries attached to it) are set to $\varphi = 0$. The boundaries attached to the injection plane are periodic. The length of the system in the *z*-direction as well as the distance of the injection plane from the protective plate are set large enough to avoid perturbations generated by the chamfered edges as well as to allow for a Debye sheath potential drop in front of the wall, respectively. The magnetic field B = 3.5 T is uniform and directed towards the slit plate. The ions ($m_i = m_D$) are injected with a parallel velocity distribution calculated from the kinetic model of Chung and Hutchinson [Chung 1988] for zero drift

velocity. The ion velocity distribution in both perpendicular directions is Maxwellian. Electrons are injected with fully Maxwellian distribution. The ion temperature, electron temperature, and electron density are set to $T_i = 40$ eV, $T_e = 20$ eV, and $n_e = 10^{18}$ m^{-3}, respectively. For each geometry, simulations were performed for three different values of the external slit plate bias voltage $V_{sp} = 0$, -100 and -200 V. Each simulation is left to run to a steady state before collecting the time averaged quantities.

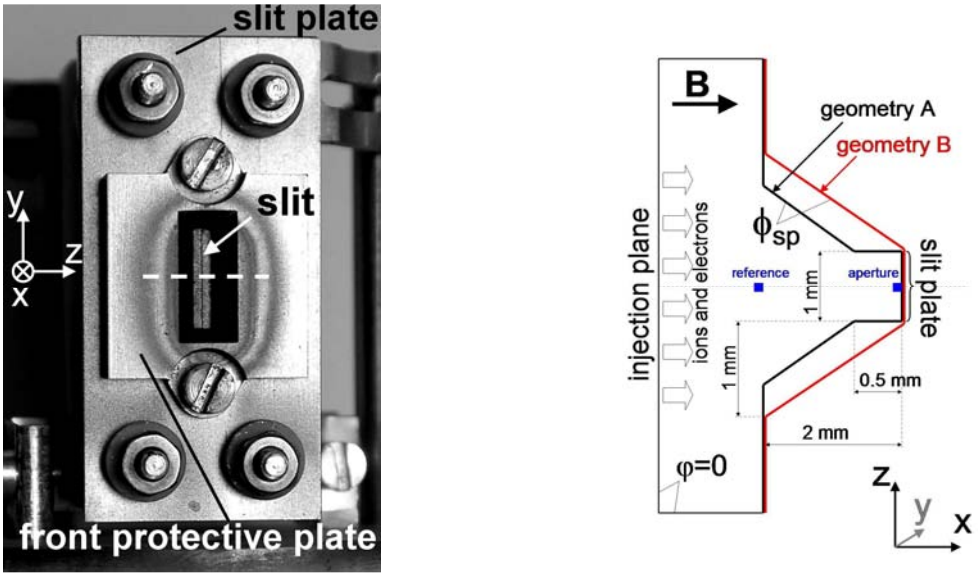

Figure 2.25. Left: Photograph of the front protective plate and the slit plate of Tore Supra RFA. The ions are transmitted to the slit through a rectangular window in the protective plate. Horizontal dashed line indicates the cut through the protective plate which is modeled by PIC simulations. Right: simulation domain used for studying the ion current attenuation on the protective plate walls for two different protective plate geometries A (actual) and B (alternative). Third dimension in the y-direction was neglected. Ion energy distributions were monitored in the positions marked by blue squares. Ion current distribution along the slit plate was also measured.

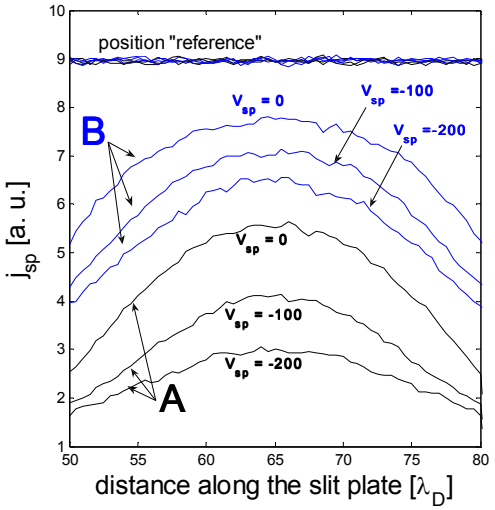

Figure 2.26. Ion current profiles along the slit plate for two different protective geometries A and B (figure 2.25) and for three different values of the external slit plate bias voltages. Also shown is the current profile at the reference position (figure 2.25).

Figure 2.26 shows the ion current profile along the slit plate (which is the 1 mm long region between the protective plate walls, figure 2.25) for different V_{sp} and for geometries A and B. The ion current in the middle of the profile I_{ap} corresponds to the current received by the aperture. Also plotted for comparison is the "reference" ion current profile monitored at the entrance of chamfered edges of the protective plate, figure 2.25. The reference current profile is flat, unaffected by the attenuation. The attenuation factor $\alpha_{protplate} = I_{ref} / I_{ap}$, with I_{ref} being the ion current in the middle of the reference profile. For geometry A, I_{ap} is a relatively strong function of the bias voltage: for $V_{sp} = 0 \rightarrow -200$ V I_{ap} decreases by more than a factor of 2 and the attenuation factor $\alpha_{protplate} \cong 1.6 \rightarrow 3$, figure 2.27. For geometry B I_{ap} is less sensitive to V_{sp} and the absolute attenuation factor is also lower ($\alpha_{protplate} \cong 1.1 \rightarrow 1.4$ for $V_{sp} = 0 \rightarrow -200$).

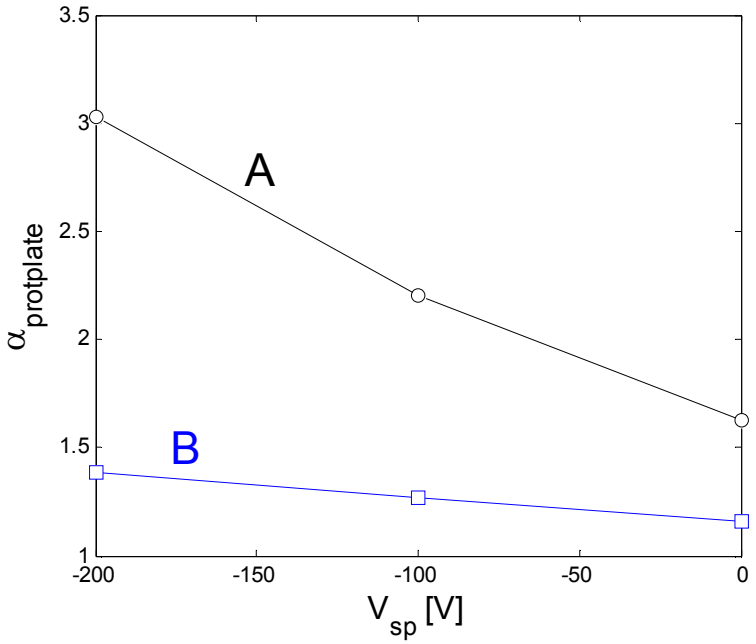

Figure 2.27. Attenuation factor calculated from the ratio of the reference current to the aperture current $\alpha_{protplate} = I_{ref} / I_{ap}$ measured in the centre of the profiles plotted in figure 2.26. $\alpha_{protplate}$ is plotted against the external bias voltage applied to the slit plate V_{sp}. Values for two different protective plate geometries A (actual) and B are shown.

Figure 2.28 shows the stream lines of ions for geometries A and B and for different bias voltages V_{sp}. Streamlines were calculated by tracing the trajectory of a point with the initial position near the injection plane through the field of the ion velocities v_x and v_z averaged over the saturated state. Figure 2.28 clearly demonstrates that some of the ions originally flowing towards the slit plate are deflected towards the protective plate walls. The deflection (curvature of the stream lines) is stronger for higher

V_{sp}, which coincides with the decrease of the slit plate current (figure 2.26) and increase of the attenuation factor (figure 2.27).

Since the parallel ion energy loss due to attenuation could be selective (ions with a certain range of $v_{//} = v_x$ could be preferably removed from the parallel ion energy distribution), the attenuation could also affect the ion energy distribution measured by the collector. To study the effect of the attenuation on T_i we used the method which is described in detail in section 2.4.3.1: for each simulation, the *I-V* characteristics were reconstructed from the parallel ion energy distribution measured (i) at the reference position which is unaffected by attenuation and at the aperture entrance (see schematic in figure 2.25). The characteristics were fit using Eq.(2.2) to obtain the effective parallel ion temperature of the distribution. The ratio of the effective ion temperature at the aperture entrance to the one at the reference position, $r_T = T_{i\,eff}^{ap} / T_{i\,eff}^{ref}$, measures the degree of the disturbance of the parallel ion energy distribution due to attenuation. r_T and is plotted against V_{sp} in figure 2.29. For $V_{sp} = 0 \rightarrow -100$ V $r_T \approx 1$, meaning that the parallel ion distribution is almost unaffected by the attenuation. For $V_{sp} = -200$ the ion temperature measured at the aperture entrance is by about 8% higher compared to the reference value for geometry A and almost equal to the original temperature for geometry B.

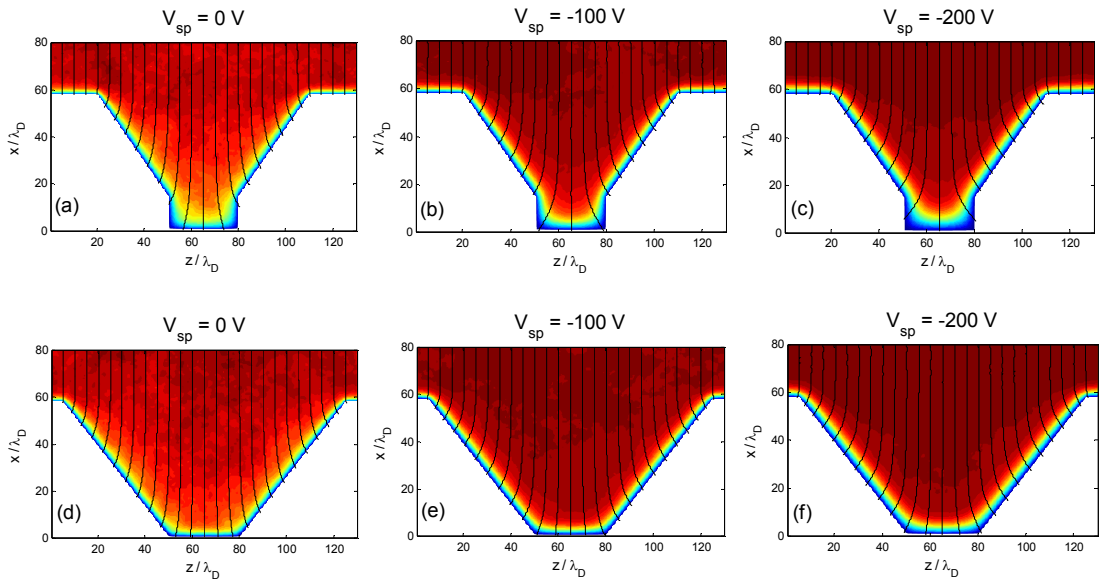

Figure 2.28. Stream lines of ions for geometries A (a-c) and B (d-f) and for different external slit plate bias voltages V_{sp}. Streamlines were calculated by tracing the trajectory of a point with the initial position near the injection plane through the field of the average ion velocities v_x and v_z measured in the saturated state. Also plotted is the steady-state potential distribution in the simulation domain.

It is important to mention that the V_{sp} used for the RFA measurements is higher than -200 volts for all measurements and higher than -100 volts for most measurements. For such voltages the influence of the protective plate on T_i measurements can be neglected (higher overestimation of T_i is expected to be due to the selective slit transmission, section 2.4.3, as well as the fitting of the *I-V* characteristics, section 2.4.6). In addition, for higher densities than those studied here the attenuation effect will be weaker as the Debye shielding will be more effective (i.e. the effective layer from which the ions are deflected towards the protective plate will be thinner).

To conclude, the actual geometry of the RFA protective plate strongly attenuates the ion current flowing towards the slit plate aperture. Attenuation factors of $1.6 \rightarrow 3$ were obtained from the simulations for the external slit plate bias voltages $V_{sp} = 0 \rightarrow -200$ V typically used for RFA operation. The attenuation is stronger for higher bias as more ions are deflected towards the walls of the protective plate. This could explain the disagreement between the experimentally measured and the calculated relative slit plate transmission factor (section 2.4.3.4). Alternative knife edge geometry of the protective plate is characterized by lower attenuation which is also less sensitive to the bias voltage. From the limited data set studied here the effect of the attenuation on T_i measurements seems to be stronger for the actual protective plate geometry compared to the alternative knife edge geometry. However, even for the actual geometry the increase of effective ion temperature for bias voltages typically applied in experiment can be neglected.

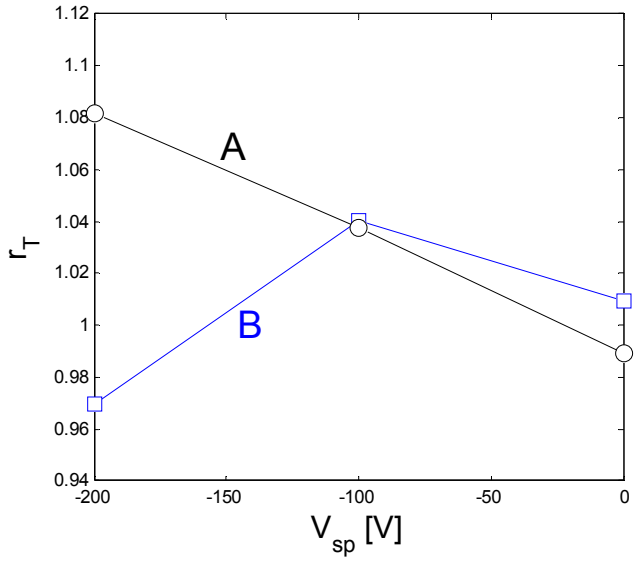

Figure 2.29. The ratio of the effective ion temperature at the aperture entrance to the one at the reference position, $r_T = T_{ieff}^{ap} / T_{ieff}^{ref}$, plotted against the external slit plate bias voltage V_{sp}. The values for two different protective plate geometries A and B are shown. The effective ion temperatures were obtained from the parallel ion energy distribution using the method described in section 2.4.3.1. r_T measures the degree of the disturbance of the parallel ion energy distribution due to attenuation.

2.4.3. Ion transmission through the entrance slit

In this section we focus on the following questions: To what degree is the inferred ion temperature influenced by selective ion transmission through the slit (the transmission probability of an individual ion depends on its parallel speed)? Does selective ion transmission vary with the slit plate thickness? As different slit plate thicknesses have been used for the Tore Supra RFA, the latter question concerns the comparability of the results from different experimental campaigns.

Experimental and theoretical studies aimed at the choice of appropriate RFA slit dimensions were reported in [Matthews 1984, Pitts 1991, Pitts 1996]. The particularity of our work is in the evaluation of the ratio of ion temperature after and before the slit transmission, r_T, as a function of τ, slit plate thickness s, and the angle of the slit plate misalignment with respect to the magnetic field vector **B,** α_{mis}. We combine the kinetic model of Chung and Hutchinson [Chung 1988], with the one originally proposed by Nachtrieb [Nachtrieb 2000], including some adjustments concerning the slit geometry and ion velocity distribution function. In addition to the model, the slit transmission is studied by PIC simulations and from experimental data. The procedure used here can be applied for similar problems where charged particles are transmitted through a thin aperture.

2.4.3.1 Theoretical model of ion transmission through the slit

In this section, ion transmission through the slit is studied by means of a simple analytical model. Our aim is (a) to derive the expression for the relative slit transmission factor, and (b) to evaluate the influence of the slit transmission on the parallel ion velocity distribution. The first enables to estimate the magnitude of the ion current transmitted to the RFA cavity and thus to calculate its relative importance to e.g. gas breakdown or space charge limit. Similar calculations have been made by [Matthews 1985]. The latter allows to inspect the influence of the selective ion transmission on T_i.

We partially follow the original model of Nachtrieb [Nachtrieb 2000], but the dimensions and the shape of the slit are adjusted to the ones of the Tore Supra RFA. In [Nachtrieb 2000], the parallel ion velocity distribution was approximated by shifted Maxwellian velocity distribution. We apply a more general approach by approximating the parallel ion velocity distribution by δ-function. As shown below, this enables to evaluate the slit transmission factor for an arbitrary ion velocity distribution.

The model (see schematic in figure 2.30) is based on the assumption that $r_L >> w$, which is well satisfied in the SOL of Tore Supra. Under these conditions, most ion trajectories within the slit can be approximated by straight lines. The electric field inside the slit is assumed to be zero. An incident ion is transmitted only if its ratio of perpendicular-to-parallel velocities v_z / v_x satisfies the condition:

$$v_z / v_x \le \begin{cases} (w/2 + z)/s + \tan\alpha_{mis} & \text{for } v_z < 0 \\ (w/2 - z)/s - \tan\alpha_{mis} & \text{for } v_z > 0. \end{cases} \qquad (2.9)$$

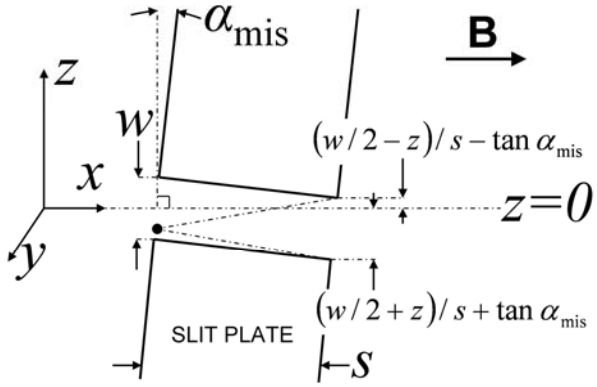

Figure 2.30. Scheme of the theoretical model of the ion transmission through the slit. The position of an ion at the slit entrance is illustrated by a black dot. The pitch angles correspond to the critical ion velocity ratios $\pm v_z/v_x$. w and s are respectively the slit width and the slit plate thickness (not to scale). The model is valid for small α_{mis}.

$\alpha_{mis}=0$ corresponds to perfect probe head alignment with **B**. Condition (2.9) is valid for small α_{mis}. The slit boundaries in the *y*-direction are considered to be infinitely far from the slit axis. The model neglects (a) the ions with $r_L < 0.5w$ that would pass through the slit even if they didn't satisfy the condition (2.9), and (b) the ions with the velocities $v_y/v_x \geq h/s \approx 50$ (for $s=100\,\mu$m) that would be absorbed on the slit boundaries in the *y*-direction. For typical ion temperature $T_i = 50$ eV, (a) represents only ≈ 0.04 of the total ion population. Case (b) can also be neglected, since v_x and v_y are both of the same order given by the ion thermal velocity $v_T = \sqrt{eT_i/m_i}$.

Assume that the ions at the slit entrance are Maxwellian in the perpendicular directions and monoenergetic in the parallel direction,

$$f(v'_x, v_y, v_z) = \frac{n}{2\pi v_T^2}\delta(v'_x - v_x)\exp\left(-v_y^2 - v_z^2\right). \tag{2.10}$$

The relative slit transmission factor ξ_r^δ is given by the ratio of the transmitted to the incident ion flux,

$$\xi_r^\delta(v_x) = \frac{\langle\Gamma_{tr}\rangle}{\Gamma_{in}} = \frac{w^{-1}\int_{-w/2}^{w/2} dz\,\Gamma_{tr}(z)}{\Gamma_{in}} = w^{-1}\int_{-w/2}^{w/2} dz\,\frac{\int_{b_1(v_x,z)}^{b_2(v_x,z)} dv_z e^{-v_z^2}}{\int_{-\infty}^{\infty} dv_z e^{-v_z^2}} \cong \frac{1}{\sqrt{\pi}}\left[\frac{v_x w}{s}\left(1-\tan^2\alpha_{mis}\right) - \frac{1}{6}\left(\frac{v_x w}{s}\right)^3\right], \tag{2.11}$$

where $b_1 = v_x\left[(w/2+z)/s + \tan\alpha_{mis}\right]$, $b_2 = v_x\left[(w/2-z)/s - \tan\alpha_{mis}\right]$ and $w < s$. The velocities are normalized to $\sqrt{2}v_T$. The relative slit transmission factor for an arbitrary ion velocity distribution function is given by

$$\xi_{\mathrm{r}} = \frac{\int_0^{\infty} dv_{\mathrm{x}} v_{\mathrm{x}} \xi_{\mathrm{r}}^{\delta}(v_{\mathrm{x}}) f(v_{\mathrm{x}})}{\int_0^{\infty} dv_{\mathrm{x}} v_{\mathrm{x}} f(v_{\mathrm{x}})}. \tag{2.12}$$

Values of ξ_{r} similar to the ones given by Eqs. (2.11) are obtained for parallel ion velocity distribution functions at the slit entrance that are either Maxwellian with a shift of $v_0 = \sqrt{Z_{\mathrm{i}}\phi / T_{\mathrm{i}}}$ (with $\phi = |V_{\mathrm{s}} + V_{\mathrm{sb}}|$), ξ_r^{Maxw}, or box function with $v_{\mathrm{x}} \in [v_0; \sqrt{1+v_0^2}]$, ξ_r^{box}. ξ_r^{δ}, ξ_r^{Maxw} and ξ_r^{box} for three different slit plate thicknesses are compared in figure 2.31.

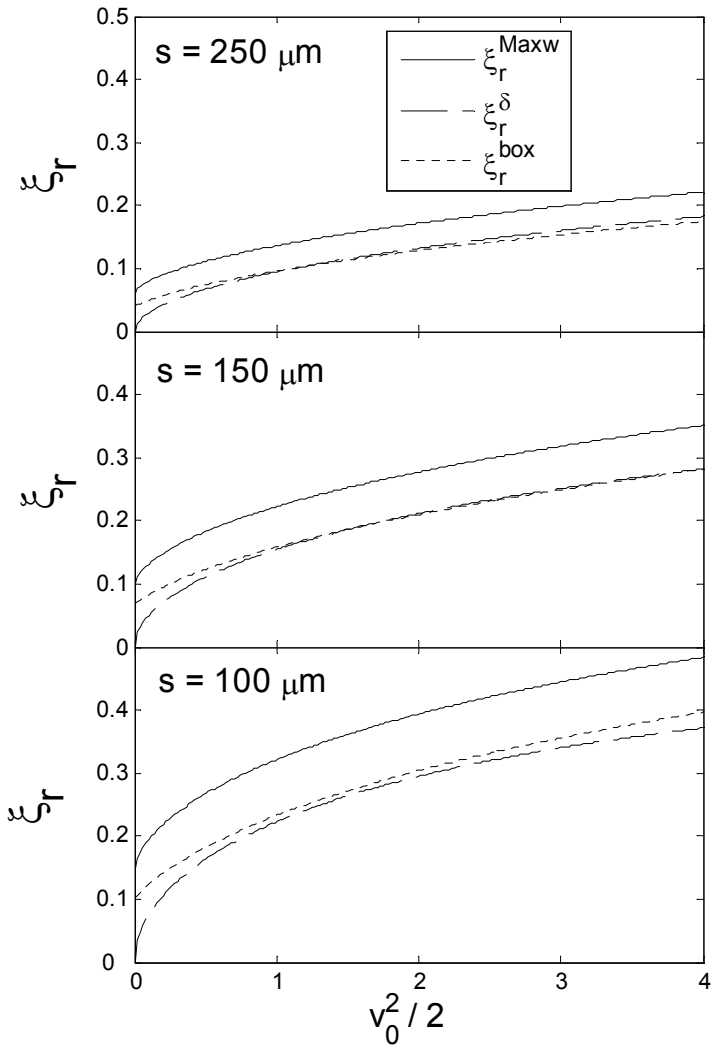

Figure 2.31. Relative slit transmission factor, ξ_r, calculated for three different slit thicknesses, s, and parallel ion velocity distribution functions at the slit entrance. $v_0^2 / 2$ is the potential drop in front of the slit plate normalized to ion temperature.

The influence of selective slit transmission on T_i can be quantified using the following procedure: The parallel ion velocity distribution function at the sheath edge in front of the probe is given by the kinetic model of Chung and Hutchinson [Chung 1988] for a certain value of $\tau = T_i / T_e$. The ions are accelerated through the sheath potential ϕ, $v_x^2 \to v_x^2 + v_0^2$, so that the resulting distribution $f_{se}(v_x)$ corresponds to the one at the slit entrance. The transmitted distribution is $f_{tr}(v_x) = f_{se}(v_x) \cdot \xi_r^\delta(v_x)$, with ξ_r^δ given by Eq. (2.11). The procedure is illustrated in figure 2.32; f_{se}, f_{tr}, and ξ_r^δ are calculated for $T_i = 100\,\text{eV}$, $T_e = 20\,\text{eV}$, $V_{sb} = -80\,\text{V}$ (which corresponds to $\tau = 5$ and $v_0 = 1.12$), $w = 30$ µm, $\alpha_{mis} = 0$, and for $s = 30$, 100, and 300 µm. ξ_r^δ increases with v_x, so that the slowest ions in the distribution are preferentially filtered. Next, the parallel ion current i_{col} is calculated as

$$i_{col}(v_{min}) \propto \int_{v_{min}}^{10 v_T} dv_x v_x f_{tr}(v_x), \tag{2.13}$$

with $v_{min} = 0 \to \max(v_x)$. Within the normalization factor, i_{col} coincides with the collector current, Eq. (2.1), and v_{min}^2 is analogous to V_{grid1} / T_i. In figure 2.32, i_{col} is plotted against v_{min}^2. The characteristics are calculated from f_{se} and f_{tr} and plotted in figure 2.33.

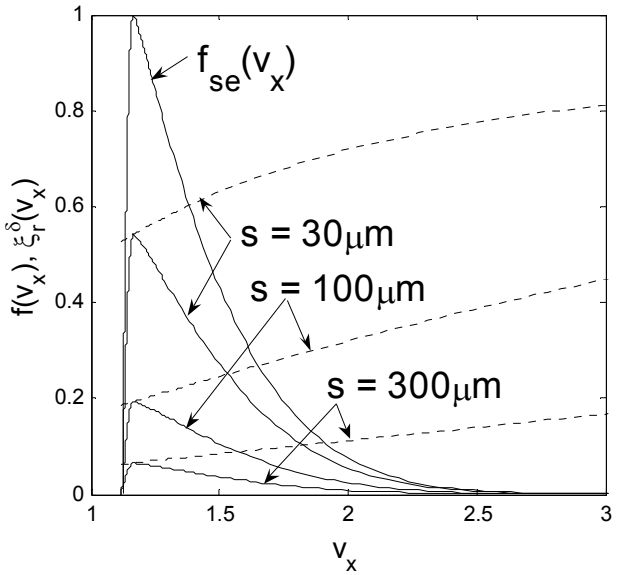

Figure 2.32. Parallel ion velocity distribution functions at the slit entrance $f_{se}(v_x)$ and after the slit transmission $f_{tr}(v_x)$ (full curves) at $s = 30$, 100, and 300 µm. ξ_r^δ is the corresponding relative slit transmission factor (dashed curves) given by Eq. (6). f_{se}, f_{tr}, and ξ_r^δ are calculated for $T_i = 100\,eV$, $T_e = 20\,eV$, $V_{sb} = -80\,V$ (i.e. $\tau = 5$ and $v_0 = 1.12$), $w = 30$ µm and $\alpha_{mis} = 0$. v_x is normalized to $\sqrt{2} v_T$.

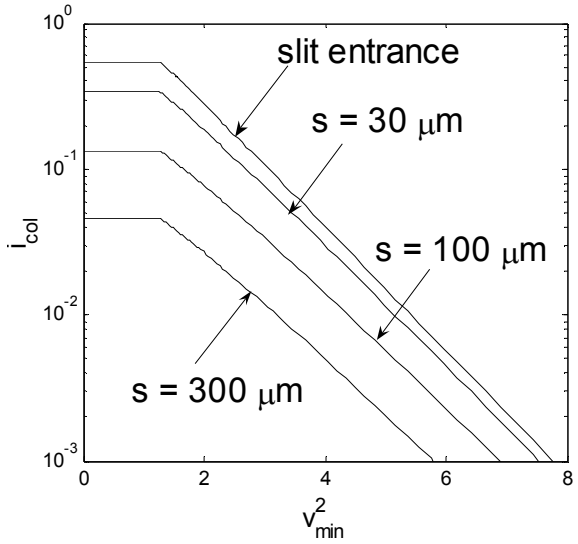

Figure 2.33. i_{col} *is plotted against* v_{min}^2*, calculated (Eq. (8)) from* f_{se} *and* f_{tr} *'s, stated in Fig. 7. t indicates the slit thickness.* i_{col} *coincides with the collector current, Eq. (2), and* v_{min}^2 *is analogous to* $V_{\mathrm{grid1}}/T_{\mathrm{i}}$ *. The slope of the characteristics for* $\ln(i_{\mathrm{col}})-4<\ln(i_{\mathrm{col}})<\ln(i_{\mathrm{col}})-1$ *gives the ratio of* T_{i} *after and before the slit transmission* r_{T}*.*

The ratio of the ion temperatures after and before the slit transmission, r_{T}, is obtained from a fit to the decaying part of the characteristic,

$$i_{\mathrm{col}} = \exp[-(v_{\mathrm{min}}^2 - v_{\mathrm{min}}^{*\,2})/r_{\mathrm{T}}], \tag{2.14}$$

which is analogous to Eq. (2.2). $v_{\mathrm{min}}^{*2} = \phi/T_{\mathrm{i}}$. As the characteristics are not exponential in their upper part and very small currents are not measurable in experiment, the range of i_{col} needs to is restricted by e.g. $\ln(i_{\mathrm{col}})-4<\ln(i_{\mathrm{col}})<\ln(i_{\mathrm{col}})-1$ [Valsaque 2002].

r_{T} calculated for different τ, s, and α_{mis} will be given in section 2.4.3.3. ξ_{r} is compared with experimental values in section 2.4.3.4.

2.4.3.2. PIC simulations of the ion transmission through the slit

As in the section 2.3.2, the PIC code SPICE has been used to study the ion transmission through the RFA slit. Contrary to the theoretical model, the PIC simulations include the self-consistent electrostatic field.

A schematic of the simulation model is illustrated in figure 2.34. Deuterons and electrons are injected towards the wall representing the slit plate, located several tens of λ_D away from the injection plane. The x axis coincides with the injection plane normal. The z axis is parallel to the injection plane. The wall contains a gap with a width $w = 30\,\mu\mathrm{m}$ and the total length $s = 360\,\mu\mathrm{m}$. The gap axis is positioned at $z = 0$. The third

dimension of the slit in the *y*-direction, $h = 5\,\text{mm}$ in the real situation, is considered to be infinitely long. The magnetic field of 3.5 T is inclined at α_{mis} with respect to the injection plane normal.
The potential difference between the injection plane and the wall ϕ_{PIC} is given by the Eq.(2.6) with $V_{\text{sp}} = -80\,\text{V}$. Secondary electron emission from the slit plate is neglected. The velocity distribution of the injected ions and electrons is the same like in the simulations described in section 2.3.2.

	T_{i} [eV]	T_{e} [eV]	n_{e} [10^{18} m^{-3}]	α_{mis} [°]
(a)	30	10	0.7	0
(b)	100	20	1.5	0
(c)	20	5	5	0
(d)	100	20	1.5	3

Table 2.2. Input parameters used in the PIC simulations of the ion transmission through the slit. From left to right: ion and electron temperatures and plasma density at injection, the inclination of the magnetic field with respect to the injection plane normal.

Four simulations for different combinations of the input parameters (table 2.2) were performed. Simulations (a) and (b) represent the typical SOL plasma parameters of Tore Supra, with $w \cong \lambda_{\text{D}}$. Simulation (c) was aimed at studying the extreme case of $w \cong 4\lambda_{\text{D}}$. Simulations (a)-(c) represent the case of a perfect probe head alignment with respect to **B**. Simulation (d) corresponds to the case of the probe head misalignment of 3° with respect to **B**.

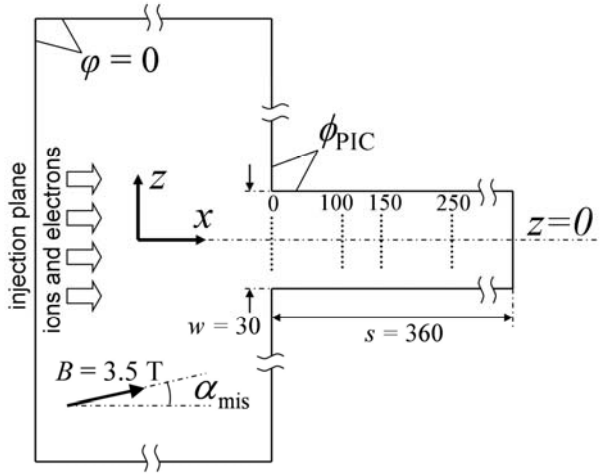

Figure 2.34. Schematic of the SPICE simulations of the ion transmission through the slit. Distances are indicated in microns (not to scale). Ions and electrons are injected towards the wall containing a slit. The boundaries perpendicular to the injection plane are periodic. Ion distribution functions are measured at the positions indicated by dotted lines with respect to the distance from the slit entrance.

Each simulation was left to run to a steady state. The ion velocity distributions in all three directions were measured at the slit entrance, and 100, 150, and 250 microns deep inside the slit. The relative slit transmission factor for a given slit thickness $\xi_{\mathrm{r(i)}}^{\mathrm{PIC}}$ was calculated from the ion velocity distribution functions as:

$$\xi_{\mathrm{r(i)}}^{\mathrm{PIC}} = \frac{\Gamma_{//\mathrm{i}}}{\Gamma_{//0}} = \frac{\int_0^{\infty} dv_{\mathrm{x}} v_{\mathrm{x}} \int_{-\infty}^{\infty} dv_{\mathrm{y}} \int_{-\infty}^{\infty} dv_{\mathrm{z}} f_i(v_{\mathrm{x}}, v_{\mathrm{y}}, v_{\mathrm{z}})}{\int_0^{\infty} dv_{\mathrm{x}} v_{\mathrm{x}} \int_{-\infty}^{\infty} dv_{\mathrm{y}} \int_{-\infty}^{\infty} dv_{\mathrm{z}} f_0(v_{\mathrm{x}}, v_{\mathrm{y}}, v_{\mathrm{z}})}, \tag{2.15}$$

where the subscript i indicates a depth inside the slit (i.e. the slit thickness, 100, 150 or 250 μm) and the subscript "0" indicates the position at the slit entrance.

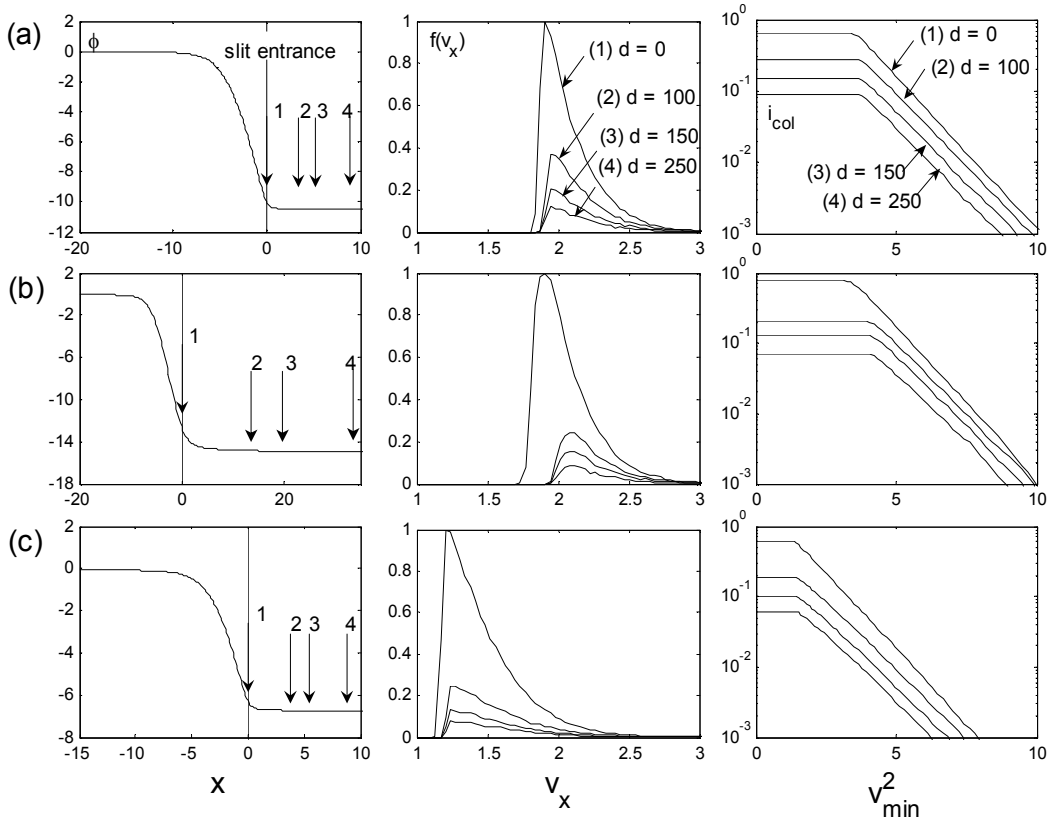

Figure 2.35. Results from PIC simulations (a)-(c). First column: radial profiles of the potential φ calculated along the slit axis ($z = 0$). φ is normalized to T_{e}. The distance from the slit entrance x is normalized to λ_{D}. The arrows indicate the positions of measurements of the parallel ion velocity distribution functions $f(v_{\mathrm{x}})$. Second column: $f(v_{\mathrm{x}})$ measured at different positions inside the slit with respect to the slit entrance, d [μm]. $f(v_{\mathrm{x}})$ is normalized to the maxima of $f(v_{\mathrm{x}})$ measured at $d = 0$. v_{x} is normalized to $\sqrt{2}v_{\mathrm{T}}$. Third column: parallel ion current i_{col} calculated from $f(v_{\mathrm{x}})$, Eq.(2.13), plotted against v_{min}^2.

Figure 2.35 compiles the results from the SPICE simulations for perfect probe head alignment with respect to B. Each row corresponds to one simulation, (a)-(c), characterized by the parameters stated in table 2.2. The first column in figure 2.35 shows the radial profiles of the electrostatic potential $\varphi(x, z=0)$. φ is normalized to T_e. The distance from the right boundary of the simulation system, x, is normalized to λ_D. The slit entrance is indicated by a vertical line. The arrows indicate the positions of measurements of $f(v_x)$. For simulations (a) and (c) (where $w \cong \lambda_D$) φ reaches its minimum value within approximately $\sim\lambda_D$ inside the slit. For simulation (b) ($w \cong 4\lambda_D$) the equipotential surface corresponding to ϕ_{PIC} is not perfectly parallel to the front face of the slit plate but penetrates $\sim 4\lambda_D$ inside the slit. φ does not reach its minimum at the slit entrance. This gives rise to a perpendicular electric field $\approx 2eV_{res}(d)/w$. $V_{res}(d) = \varphi(d, z=0) - \phi_{PIC}$ is the residual voltage and d is the position inside the slit with respect to the slit entrance. The influence of a perpendicular electric field on ion transmission is discussed in the next section. The second column in figure 2.35 shows $f(v_x)$, scanned at different d (in μm). The $f(v_x)$ are normalized to the maxima of $f(v_x)$ measured at $d = 0$. Parallel ion velocity v_x is normalized to $\sqrt{2}v_T$. Due to V_{res}, the $f(v_x)$ measured at $d > 0$ are somewhat narrower and shifted to higher velocities, compared to the ones measured at the slit entrance. The third column of figure 2.35 shows the characteristics (i_{col} versus v_{min}^2) calculated from $f(v_x)$, Eq. (2.13). A fit, Eq. (2.14), to the decaying part of the characteristics gives r_T. In the next section, r_T from the PIC simulations is compared with the one obtained from the theoretical model.

2.4.3.3. Deformation of I-V characteristics

Figure 2.36 shows the ratio r_T, calculated from the theoretical model (section 2.3.3.1) for $w = 30$ μm. r_T is plotted as a function of s for $s = 30 \rightarrow 300$ μm. r_T is evaluated for $\tau = 1 \rightarrow 5$ and for two different values of $\alpha_{mis} = 0$ and 10°. The results from the model are juxtaposed to the ones obtained from PIC simulations (a)-(c).

r_T obtained from the model increases with s and τ. The increase of r_T with s is most significant for $s < 100$ μm. For $s > 100$ μm, r_T increases only by ~2%. $\partial r_T / \partial \tau$ is a decreasing function of τ. For $100 \le s \le 250$ μm, $r_T \cong \ln(2.83\tau^{0.05})$. PIC simulations and the model predict very similar values of r_T. This indicates that the influence of the perpendicular electric field inside the slit $2eV_{res}/w$ on selective ion transmission does not play an important role, even at $w \cong 4\lambda_D$. For $s = 250$ μm the agreement between the model and PIC simulations is somewhat worse. In this case, the particle statistics in the PIC simulation are less reliable due to relatively low number of ions deep inside the slit. Within the range of r_T plotted in figure 2.36, the overestimation of T_i is less than 14%.

The slit plate misalignment has only a small influence on ion transmission. The values of r_T for $\alpha_{mis} = 0$ and $\alpha_{mis} = 10°$ are very similar. In addition, simulation (d) for

$\alpha_{mis} = 3°$ gives practically the same r_T (not plotted in figure 2.36) as simulation (b) for $\alpha_{mis} = 0$ (the difference is much less than 1%). This negative result can be explained as follows: The slit plate misalignment tilts the loss cone of perpendicular-to-parallel ion velocities in the v_z-direction by α_{mis}. However, since the parallel and perpendicular ion velocities are de-correlated, each value of v_z contains the full set of parallel velocities v_x. Therefore, ξ_r is only a weak function of α_{mis}.

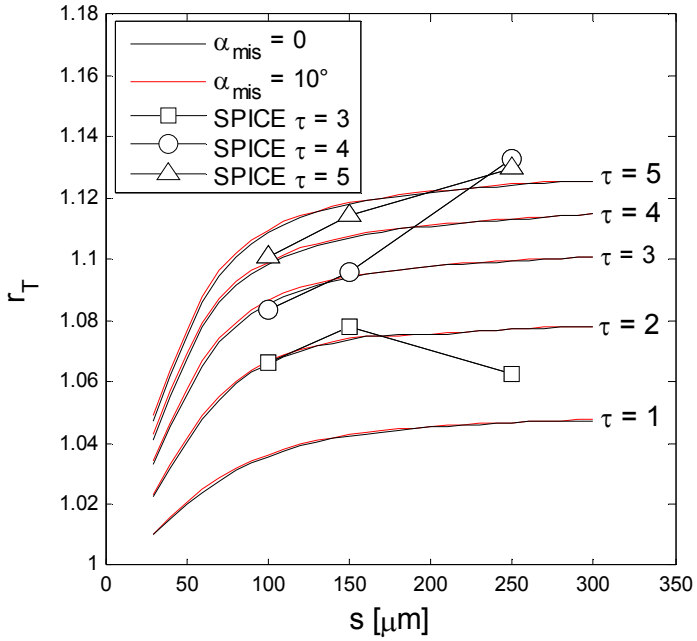

Figure 2.36. Ratio of ion temperature after and before slit transmission r_T calculated from the theoretical model (section 2.3.3.1) and from PIC simulations (a)-(c) for $w = 30$ μm. r_T is plotted against the slit plate thickness s. r_T from the model is evaluated for $\tau = 1 \rightarrow 5$ and for two different values of α_{mis} = 0 and 10°.

2.4.3.4. The relative slit transmission factor

Figure 2.37 shows the relative slit transmission factor, ξ_r, calculated from the experimental data (Eq.(2.3)), theoretical model (Eq. (2.11)), and PIC simulations (Eq. (2.15)), for $w = 30$ μm, $\alpha_{mis} = 0$, and for three different slit thicknesses of 250, 150, and 100 μm. ξ_r is plotted as a function of $v_0^2/2$. Experimental values of $v_0^2/2$ have been calculated from measurements of V_s and T_i. The experimental data measured for two slit lengths $h = 3$ mm and $h = 5$ mm and the slit plate thickness of 100 μm are compared in figure 2.37. ξ_r is independent of the slit length, meaning that the chamfered opening of the front protective plate (figure 2.6) at both ends of the slit does not affect strongly the ion transmission. PIC simulations and the model predict nearly the same ξ_r which is,

however, up to a factor of 2 higher than the experimental data. Both the theory and the simulations predict the increase of ξ_r with $v_0^2/2$, whereas ξ_r^{exp} is nearly independent of $v_0^2/2$. The discrepancy might be caused by the fact that the measurement of j_{+sat} and I_{col} can be, respectively, influenced by (i) ion induced secondary electron emission from the plasma facing surface of the slit plate and by (ii) the attenuation of ion flux on the inner walls of the front and rear protective plates (figure 2.6). The latter can be caused either by absorption of ions whose trajectories intersect the rear protective plate or by deflection of ions towards the inner walls of the front protective plate as shown in section 2.4.2). Both (i) and (ii) (neglected in Eq.(2.3)) have the tendency to decrease ξ_r^{exp}.

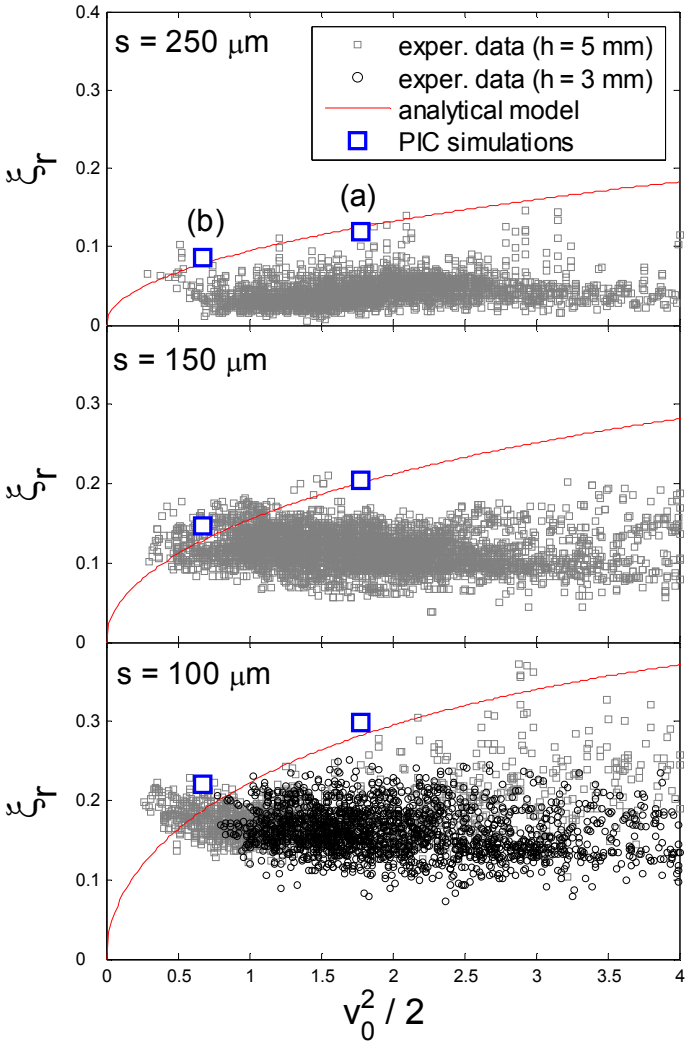

Figure 2.37. Relative slit transmission factor ξ_r for different slit plate thickness s obtained from the experimental data (Eq. 2.3), the model (Eq. 2.11), and the SPICE simulations (Eq. 2.16) represented by simulations (a) and (b), see table 2.2. ξ_r is plotted as a function potential drop in front of the slit plate (including the natural sheath voltage and the applied bias) normalized to ion temperature, $v_0^2/2$.

Interesting is the comparison of the difference between the modeled and the experimentally measured relative transmission factor with the attenuation factor of the ion flux on the protective plate predicted by SPICE simulations (section 2.3.2). For example, the simulation performed for $V_{bias} = -100\,\mathrm{V}$, $T_i = 40\,\mathrm{eV}$ and $T_e = 20$ eV, which corresponds to $v_0^2/2 \cong 2.6$, predicts the attenuation of the incident ion current by a factor of ~2.2 (figure 2.26). This is in a very good quantitative agreement with the difference between the modeled and the experimentally measured ξ_r at a given value of $v_0^2/2$, meaning that the attenuation of the ion current on the protective plate could explain a large portion of the discrepancy between the model and experimental data seen in figure 2.37.

2.4.4. Space charge effects

In the Tore Supra RFA, the voltage applied to grid 1 V_{grid1} is assumed to be the highest potential in the system. Under this assumption, grid 1 reflects those transmitted ions with the parallel kinetic energy lower than $Z_i e V_{grid1}$, where Z_i is the ion charge. However, if the maximum of the potential in the system is not defined by V_{grid1} but, for example, by the maxima of the superposition of the vacuum electrostatic potential and the positive space charge potential, the analysis of the *I-V* characteristics provides incorrect values of the ion temperature and the sheath potential.

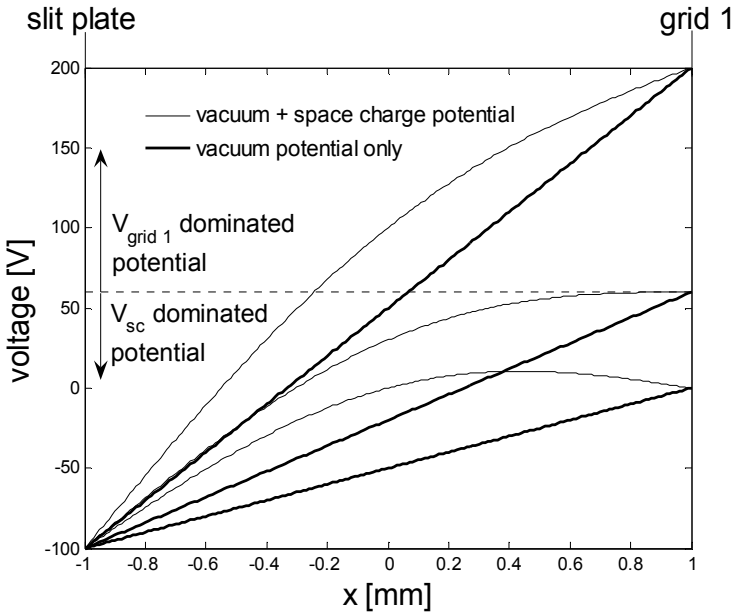

Figure 2.38. The potential between the slit plate and grid 1 for three different voltages applied to grid 1. The slit plate voltage is $V_\mathrm{s} + V_\mathrm{sb} = -100\,V$*, including the external bias and the natural sheath potential drop. The space charge potential is approximated by* $V_{sc} = V_0 \cos(\pi x / 2a)$ *with the amplitude* $V_0 = 50\,V$*. The potential in the system is dominated by the space charge for* $V_{grid1} < 60\,V$*.*

Figure 2.38 illustrates two different potential structures in the space in front of grid 1, i.e. between the grid 0 (which is attached to the rear of the protective plate, section 2.3.1.1) and grid 1: (i) the vacuum potential which increases linearly between grid 0 and grid 1 up to the maximum value given by V_{grid1}, and (ii) the superposition of the vacuum electrostatic potential and the positive space charge potential V_{sc} approximated here by $V_{sc} = V_0 \cos(\pi x / 2a)$ with $V_0 = 50\,\mathrm{V}$. For (ii) and $V_{grid1} < V_{crit}$ (with $V_{crit} \cong 60\,\mathrm{V}$), the ions are reflected by the space charge rather than by grid 1. If $V_{crit} > |V_s|$, a fit (x) to the experimental I-V characteristic will provide falsely low I_0 as well as falsely higher T_i compared to that measured in the vacuum-potential-dominated system. Figure 2.38 also illustrates that the amplitude of the space charge potential V_0 must be relatively large (at least several tens of volts) to dominate V_{grid1} as the increase of the vacuum potential between the slit plate and grid 1 is relatively steep even for $V_{grid1} = 0\,\mathrm{V}$.

If the number of ion and electron charges inside the analyzer were equal, quasi-neutrality would prevent the formation of the positive space charge structure between the electrodes. However, since most of the electrons are repelled by the slit plate so that the transmitted flux consists almost exclusively of ions, it is obvious to ask which potential – V_{grid1} or the superposition of the vacuum electrostatic potential and the positive space charge potential – dominates the system.

In this section we use the model from [Nachtrieb 2000] to estimate for typical Tore Supra parameters and the RFA geometry the amplitude of the positive space charge potential between grid 0 and grid 1. The ions could be reflected by the space charge potential between grid 1 and the collector as well. However, taken the reduction of the ion current by the grid transmission, it is reasonable to assume that the effect of the space charge potential between grid 1 and the collector is much lower.

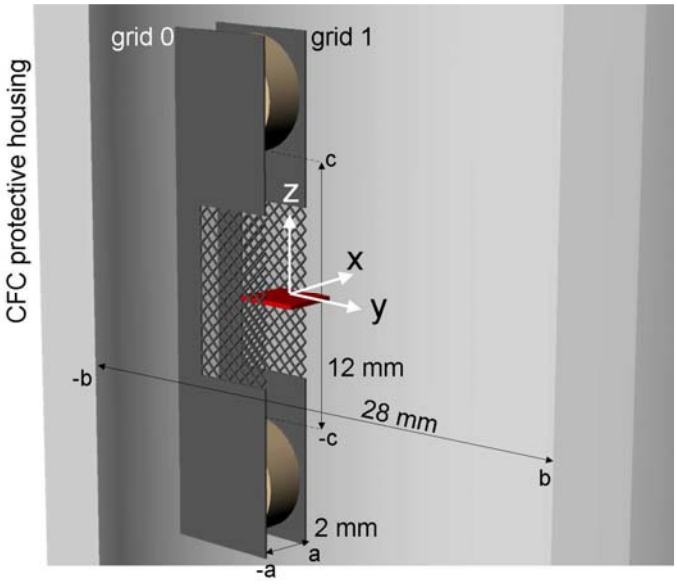

Figure 2.39. Schematic of the geometry cavity used for the calculation of the space charge potential between grid 0 and grid 1. The cavity dimensions are approximately determined by the free space between the grids. The block of the positive space charge with the dimensions given by the grid separation and the slit plate aperture area is illustrated by a red box.

As shown by Nachtrieb [Nachtrieb 2000], the approximate value of the electrostatic potential due to a rectangular beam of positively charged species propagating between two grounded surfaces can be found by integrating the product of the Green function and the beam charge density over the volume of a rectangular cavity inside which the beam propagates. In case of the Tore Supra RFA, the cavity dimensions between grid 0 and grid 1 are approximately defined as follows (figure 2.39): The length of the cavity which coincides with *x* direction is defined by the separation of grid 0 and grid 1, $x = \pm a$, with a = 1mm. Here grid 0 is positioned at $x = -a$ and grid 1 at $x = +a$. The width of the cavity is given roughly by the distance between the inner walls of the CFC protective housing, $y = \pm b$, with $b = 14$ mm. Finally, let the height of the cavity be defined by the separation of the top and the bottom of the alumina spacers placed between the grids, $z = \pm c$, with $c = 6$ mm. In the rectangular approximation which neglects the ion Larmor radii, the space charge extends along the magnetic field lines between the grids, $-A < x < A$, with $A = a = 1$ mm, The width and the height of the space charge are defined by the area of the slit plate aperture. Since the calculation below will be performed for the slit plate aperture with the length of 3 mm, $-B < y < B$ with $B = 1.5$ mm). $-C < z < C$ with $C = 15$ μm. The space charge potential along $y = z = 0$ and $-a < x < a$ is then given by [Nachtrieb 2000]:

$$\frac{V_{sc}(x,0,0)}{\rho/\varepsilon_0} = \sum_{l,m,n}^{\infty} \frac{8\cos k_l x}{k_l^2 + k_m^2 + k_n^2} \frac{(-1)^l}{k_l a} \frac{\sin k_m B}{k_m b} \frac{\sin k_n C}{k_n c}, \tag{2.16}$$

where $k_l = (l + \frac{1}{2})\pi / a$, $k_m = (m + \frac{1}{2})\pi / b$, $k_n = (n + \frac{1}{2})\pi / c$ and the ion current density $\rho \cong I^* / (v_T 4BC)$ (with I^* being the ion current flowing between grid 0 and grid 1). Eq.(2.16) can be written as

$$V_{sc}(x,0,0) = \frac{I_0}{\sqrt{T_i}} KS, \tag{2.17}$$

where I_0 is the collector current for $V_{\text{grid1}} = 0 \to |V_s|$, $K = \left(4\xi_{opt}^2 \varepsilon_0 BC\sqrt{e/m_i}\right)^{-1}$ (with ξ_{opt} being the grid transmission factor, section 2.3.1.1) and *S* is the summation term in (2.16). From (2.17) it follows that the effect of the space charge scales with $I_0 / \sqrt{T_i}$. The highest $I_0 / \sqrt{T_i}$ is reached for thin slit plate used in high plasma densities characterized by low ion temperatures.

The experimental values of $\sqrt{T_i}$, plotted against I_0, measured by the RFA equipped with the 100 microns thick slit plate (which is the thinnest slit plate used for Tore Supra RFA) with the slit plate aperture length of 3 mm are shown in figure 2.40. The data were measured by a LFS analyzer (which received larger currents due to upstream-downstream asymmetries in the discharge configurations studied here). The plasma was heated ohmically to reach relatively low values of T_i. For the discharges plotted in figure 2.40 the volume-averaged densities $\langle n_e \rangle = 0.9 \to 3 \cdot 10^{19}$ m^{-3}

($\langle n_e \rangle = 3 \cdot 10^{19}$ is close to the maximum value in Tore Supra). The diagonal line in figure 2.40 corresponds to $I_0 / \sqrt{T_i} = 10^{-5}$ [A eV$^{1/2}$]. Most experimental points lie above the diagonal line and are thus characterized by lower $I_0 / \sqrt{T_i}$.

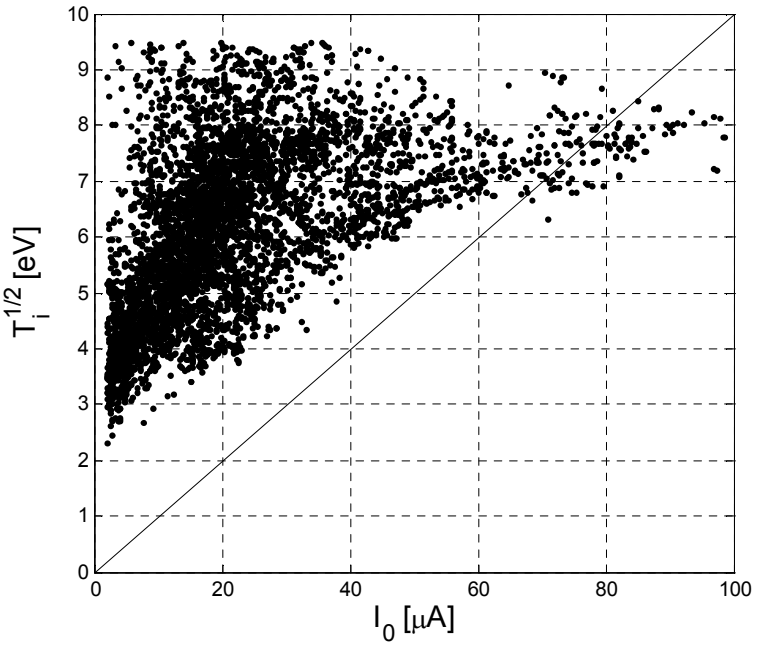

Figure 2.40. $\sqrt{T_i}$ plotted against the collector current I_0 measured for $V_{\text{grid1}} = 0 \rightarrow |V_s|$. Most experimental points lie above the diagonal line corresponding to $I_0 / \sqrt{T_i} = 10^{-5}$ A eV$^{1/2}$ and are thus characterized by lower $I_0 / \sqrt{T_i}$. The data were measured in ohmic plasmas characterized by the volume-averaged density $\langle n_e \rangle = 0.9 \rightarrow 3.0 \cdot 10^{19}$ m^{-3} (TS discharges #42670-#42674, #42681-#42683, #42436-#42452, #42939-#42648). The RFA was equipped with 100 μm thick slit plate with the aperture length of 3 mm.

Figure 2.41 shows the profile of the positive electrostatic space charge potential $V_{sc}(x,0,0)$ between grid 0 and grid 1 obtained from Eq.(2.17). $V_{sc}(x,0,0)$ is evaluated for the cavity / beam dimensions stated above, $m_i = m_D$ and for $I_0 / \sqrt{T_i} \cong 10^{-5}$ [A / (eV)$^{1/2}$]. The amplitude of $V_{sc}(x,0,0)$, $V_{sc}(0,0,0)$, is above 13 volts. Figure 2.41 also shows the electrostatic vacuum potential as well as the superposition of the space charge potential and the vacuum potential for the slit plate voltage $\varphi = V_{sp} + V_s = -100\,\text{V}$ (which is about a highest value in Tore Supra RFA given the typical values of V_{sp} and V_s) and $V_{grid1} = 0\,\text{V}$. Clearly, the maxima of the potential in the system is given by V_{grid1}, meaning that the influence of the positive space charge is negligible for the typical ion current densities inside the RFA cavity. In addition, the model from [Nachtrieb 2000] can be considered as a "worst case scenario" since it neglects the radial divergence of the ion beam due to

finite ion Larmor radii and positive space charge effects, as well as the presence of electrons inside the cavity that were not repelled by the slit plate. These effects have the tendency to decrease further the influence of the positive space charge.

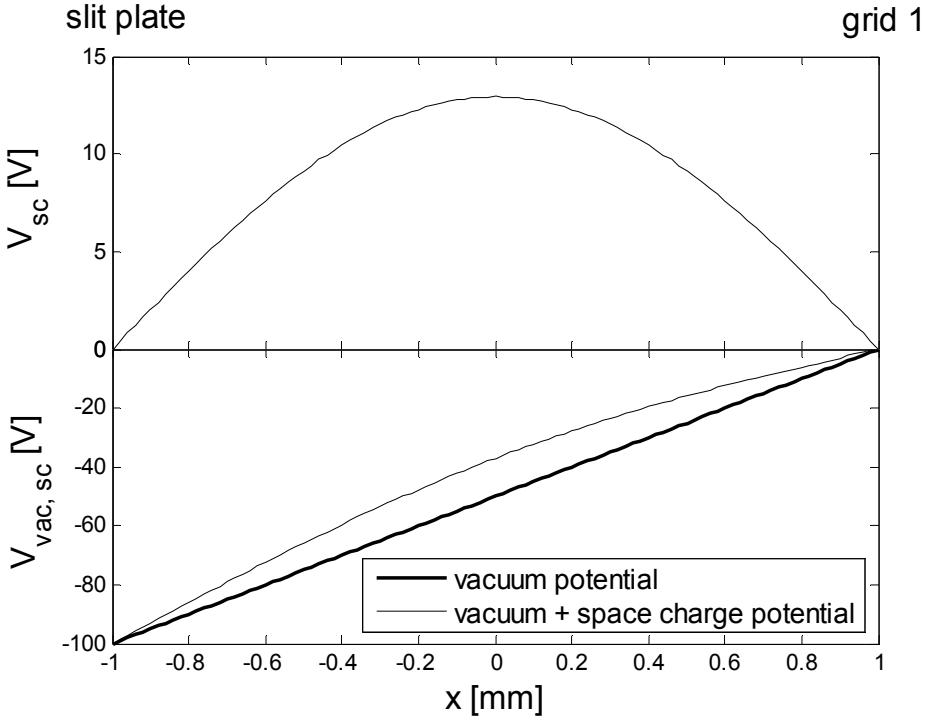

Figure 2.41. Profile of the positive electrostatic space charge potential between grid 0 and grid 1 for $y = z = 0$, $V_{sc}(x,0,0)$. $V_{sc}(x,0,0)$ *was calculated for* $I_0 / \sqrt{T_i} \cong 10^{-5}$ *[A eV],* $V_{sp} + V_s = -100$ *V,* $V_{grid\,1} = 0$ *V,* $a = 1$ *mm,* $b = 14$ *mm,* $c = 6$ *mm,* $A = 1$ *mm,* $B = 1.5$ *mm and* $C = 15\,\mu$*m using Eq. (2.18).*

2.4.5. Influence of the negatively biased grid

As mentioned in section 2.2, the negatively biased grid 2 is used to repel the plasma electrons that enter the RFA cavity, and to suppress the secondary electron currents. At the same time, grid 2 constitutes a final obstacle for ions before they reach the collector. In this section the influence of grid 2 on T_i measurements is analyzed.

In [Pitts 2003] it was suggested that the transmission factor of grid 2 could be modified by the deflection of ion trajectories passing close to the grid wires, which might increase the effective grid wire diameter

$$\Delta_{\text{eff}} = \Delta(1 + V_{\text{grid2}} / E_0)^{1/2}, \tag{2.18}$$

where E_0 is the initial ion energy infinitely far from the wire and Δ the grid wire diameter. Expression (2.18) is derived from single-particle orbital theory for a single

circular wire and $B = 0$ [Mott-Smith 1926]. In the real situation, however, a grid is composed of a large number of equally spaced wires. The resulting electric field is nearly planar everywhere except very close to individual wires, i.e. the perpendicular component of the electric field which is responsible for ion deflection in Eq.(2.18) is very small (see also figure 2.42). We show below that the grid transmission is very close to optical.

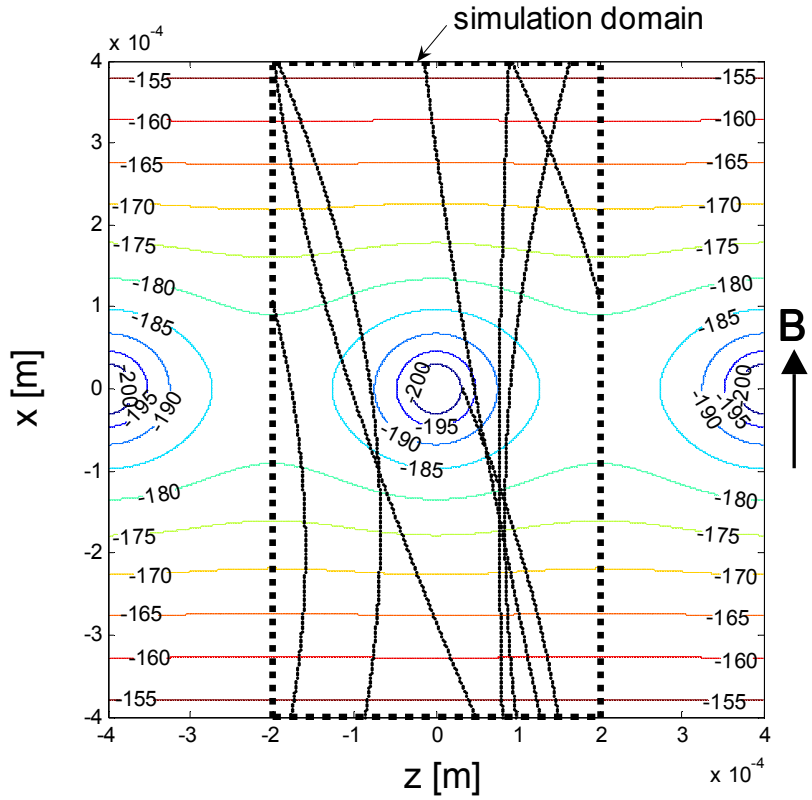

Figure 2.42. Vacuum potential around an infinitely long array of circular wires of diameter $\Delta = 63\ \mu m$, biased to $V_{\text{grid}\,2} = -200\ V$ and separated by 2 mm from another arrays of wires biased to $V_{\text{grid}\,1} = 0\ V$ (Eqs.(2.19-2.21)). Individual wires are separated by the distance $D = 0.4\ mm$. The simulation domain with a single wire in the centre and periodic boundary conditions is indicated by thick dashed lines. Also shown are the trajectories of ions with $E_{//\text{i}} = 250\ eV$ and perpendicular ion energy $E_{\perp\text{i}}$ is chosen randomly from a Maxwellian distribution with characteristic energy of 50 eV.

The effect of negative grid bias on ion trajectories was evaluated by means of two-dimensional Monte Carlo simulations. The simulation domain consists of a rectangular box containing a single wire positioned in the centre, figure 2.42. The width of the system equals the distance between the grid wires D. The boundary conditions are periodic. The electric field inside the system corresponds to the vacuum electric field due to an infinitely long array of the circular wires of diameter $\Delta = 63\ \mu m$, biased to $V_{\text{grid}\,2}$ and separated by $d = 2\ mm$ from another grid biased to $V_{\text{grid}\,1}$. (In reality, the grid wire cross section is rectangular but it is assumed here that the effect of the electric field close to the wire corners on the particle trajectories is negligible. In addition, the simulations

for circular wires allow direct comparison with the single-particle orbital theory, Eq. (2.18), which is also derived for a wire with a circular cross section.) The analytical solution for the vacuum potential in such configuration reads [Lefaucheux 2006]:

$$V(x,z)=\frac{\beta}{2}\ln\left[2\cosh\left(\frac{2\pi}{D}x\right)-2\cos\left(\frac{2\pi}{D}z\right)\right]+\gamma\,, \tag{2.19}$$

where

$$\beta=\frac{V_{grid\,2}-\frac{1}{2}V_{grid\,1}}{\ln\left|2\sin\left(\frac{\Delta\pi}{2D}\right)\right|-\frac{\pi d}{D}}, \tag{2.20}$$

$$\gamma=\frac{\frac{V_{grid\,1}}{2}\ln\left|2\sin\left(\frac{\Delta\pi}{2D}\right)\right|-\frac{\pi d}{D}V_{grid\,2}}{\ln\left|2\sin\left(\frac{\Delta\pi}{2D}\right)\right|-\frac{\pi d}{D}} \tag{2.21}$$

where $d=2\,\mathrm{mm}$ is the distance between grids. The vacuum potential for $V_{\mathrm{grid}\,2}=-200\,\mathrm{V}$ and $V_{\mathrm{grid}\,1}=0\,\mathrm{V}$ is illustrated in figure 2.42. The injection plane is positioned 0.4 mm in front of the wire to ensure a practically planar electric field there. Since the local ion density close to the grid wires is $<10^{15}\,\mathrm{m}^{-3}$, the influence of ion space charge on the vacuum potential is neglected (following e.g. [Nachtrieb 2000], it can be shown that for such densities the contribution of the space charge to vacuum potential is ~1 V). In each simulation the orbits of 10^5 deuterons are calculated. The parallel ion energy at injection $E_{//\mathrm{i}}$ is fixed. The perpendicular ion energy $E_{\perp\mathrm{i}}$ is chosen randomly from a Maxwellian distribution. The initial position of ions along the injection plane is random. The time step is kept below 1/20 of the ion transit time through the distance Δ. In order to allow the variation of the time step during the integration process, the ions are advanced by the midpoint Runge-Kutta method [Press 1992]:

$$\begin{aligned}
&t_m=t_n+\Delta t/2,\;\; z_m=z_n+v_n\Delta t/2,\;\; v_m=v_n+a_n\Delta t/2\\
&a_n=a(t_n,z_n,v_n),\;\; a_m=a(t_m,z_m,v_m)\\
&z_{n+1}=z_n+v_m\Delta t,\;\; v_{n+1}=v_n+a_m\Delta t,
\end{aligned} \tag{2.22}$$

with all symbols having their usual meaning. Ion trajectories inside the simulation domain are illustrated in figure 2.42. Those ions whose trajectories intersect the wire are absorbed. Those reaching the upper boundary of the system positioned behind the wire are considered to be transmitted. Assuming that the electric field in the grid wire corners does not influence the transmission, the effect of four grid wires can be combined to produce the total grid transmission factor $\xi_{\mathrm{grid}\,2}(E_{//\mathrm{i}},E_{\perp\mathrm{i}},V_{\mathrm{grid}\,2})=(N_{\mathrm{trans}}/N_{\mathrm{inj}})^2$. N_{trans} and N_{inj} are respectively the total number of the transmitted and injected ions.

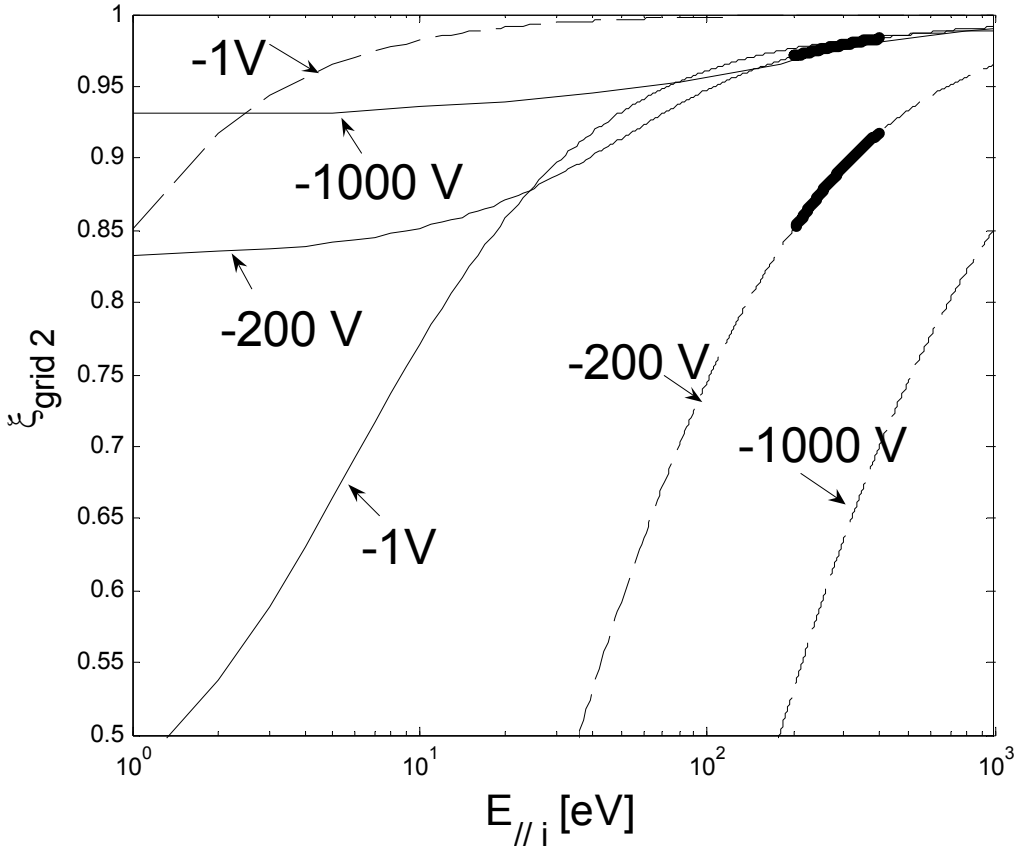

Figure 2.43. Transmission factor of the negatively biased grid 2, $\xi_{\mathrm{grid}\,2}$, calculated for fixed perpendicular ion energy $E_{\perp \mathrm{i}} = 50$ eV and three different values of the grid bias voltage $V_{\mathrm{grid}\,2} = -1$, -200 and -1000 V. $\xi_{\mathrm{grid}\,2}$ is normalized to the optical transmission factor of the grid ξ_{opt} and plotted as a function of the parallel ion energy $E_{//\mathrm{i}}$. Results from Monte Carlo simulations (full curves) simulations are compared with the ones calculated from the single-particle orbital theory (dashed curves), Eq. (2.19). For $V_{\mathrm{grid}\,2} = -200$ V, a range of the typical parallel ion energies at the distance $D = 0.4$ mm in front of the grid 2 is highlighted by thicker lines.

The simulations were reproduced for different combinations of $E_{//\mathrm{i}} = 1 \to 10^3$ eV, $E_{\perp \mathrm{i}} = 1 \to 10^3$ eV, and $V_{\mathrm{grid}\,2} = 0 \to -10^3$ V. Figure 2.43 illustrates $\xi_{\mathrm{grid}\,2}$ calculated for fixed value of $E_{\perp \mathrm{i}} = 50$ eV, and for three different values of $V_{\mathrm{grid}\,2} = -1, -200$, and -1000 V. $\xi_{\mathrm{grid}\,2}$ is normalized to ξ_{opt}. $\xi_{\mathrm{grid}\,2}$ increases with $E_{//\mathrm{i}}$ and tends to ξ_{opt} for stronger grid bias. This is because the field in front of the grid is basically planar, and the ions gain large parallel energy before coming into the zone of influence of the wire. For single-particle orbital theory the tendency is opposite. Realistic parallel ion energies 0.4

mm in front of the grid 2 for $V_{\text{grid}1} = 0$ V and $V_{\text{grid}2} = -200$ V, $E_{//\text{i}} = T_{\text{i}} + e|V_{\text{s}}| + 160$ eV, are plotted by a thick line in figure 2.43. Within this range, $\xi_{\text{grid}2} \cong \xi_{\text{opt}}$. For comparison, the grid transmission factors derived from the single-particle orbital theory, Eq.(2.18), are also shown. The fact that for realistic parallel ion energies $\xi_{\text{grid}2} \cong \xi_{\text{opt}}$ independently of $V_{\text{grid}2}$ can be easily understood: since the typical ion Larmor radius is comparable to the grid wire separation D, the approximate condition for $\xi_{\text{grid}2} \cong \xi_{\text{opt}}$ is given by $\Delta / v_{//} < D/(r_{\text{L}}\omega_{\text{L}})$, where ω_{L} is the ion Larmor frequency. Due to acceleration of ions in the sheath and in front of grid 2, $E_{//\text{i}}$ at the grid is larger than $E_{\perp\text{i}}$ ($E_{//\text{i}} \cong E_{\perp\text{i}} + 3T_{\text{e}} - eV_{\text{grid2}}$), so that $t_{//} < D/(r_{\text{L}}\omega_{\text{L}})$ for any $V_{\text{grid}2} < 0$.

The influence of the grid transmission on ion temperature was quantified using the procedure similar to the one described in section 2.3.3.1; $f(v_{//})$ at the sheath edge in front of the probe were calculated from [Chung 1988] for various values of τ. To account for the potential drop between the sheath edge and grid 2, the distributions were shifted in the parallel direction by $e|V_{\text{s}} + V_{\text{grid}2}|$ eV. Consequently, the distributions were transformed by the following operation: $f(E_{//\text{i}}) = f(E_{//\text{i}}) \cdot \xi_{\text{grid}2}(E_{//\text{i}})$, with $\xi_{\text{grid}2}(E_{//\text{i}})$ calculated for $E_{\perp\text{i}} = 50$ eV and $V_{\text{grid}2} = -200$ V. Finally, I-V characteristics were constructed from the parallel velocity distribution functions, and fit by Eq.(2.2). From these results it follows that the negatively biased grid accounts for an increase of T_{i} of less than 1% (for single-particle orbital theory, T_{i} increases 2 – 4 %). Since for typical parallel ion energies $\xi_{\text{grid}2}$ is independent on $V_{\text{grid}2}$, the same result is obtained for $V_{\text{grid}2} = 0 \rightarrow -1000$ V. These results are substantiated by RFA measurements in Tore Supra, performed on a shot-to-shot basis in similar ohmic plasmas. Between the shots, $V_{\text{grid}2}$ was varied in a range of $-10 \rightarrow -600$ V. Other parameters were kept constant ($I_{\text{p}} = 0.6$ MA, $\bar{n}_{\text{e}} = 1.4 \cdot 10^{19}$ m^{-3}). As an example, radial profiles of T_{i} measured for $V_{\text{grid}2}$ = -10, -150, -250, and -550 V are shown in figure 2.44; despite the variation of $V_{\text{grid}2}$, T_{i} is constant within the error bars. It is worth noticing that for $V_{\text{grid}2} = -10$ V the secondary electrons in the RFA are not fully repelled. However, the secondary electron current from the collector is merely an offset on I_{col}, and the one from the rear of the slit plate is reduced by the transmission of electrons through the grids.

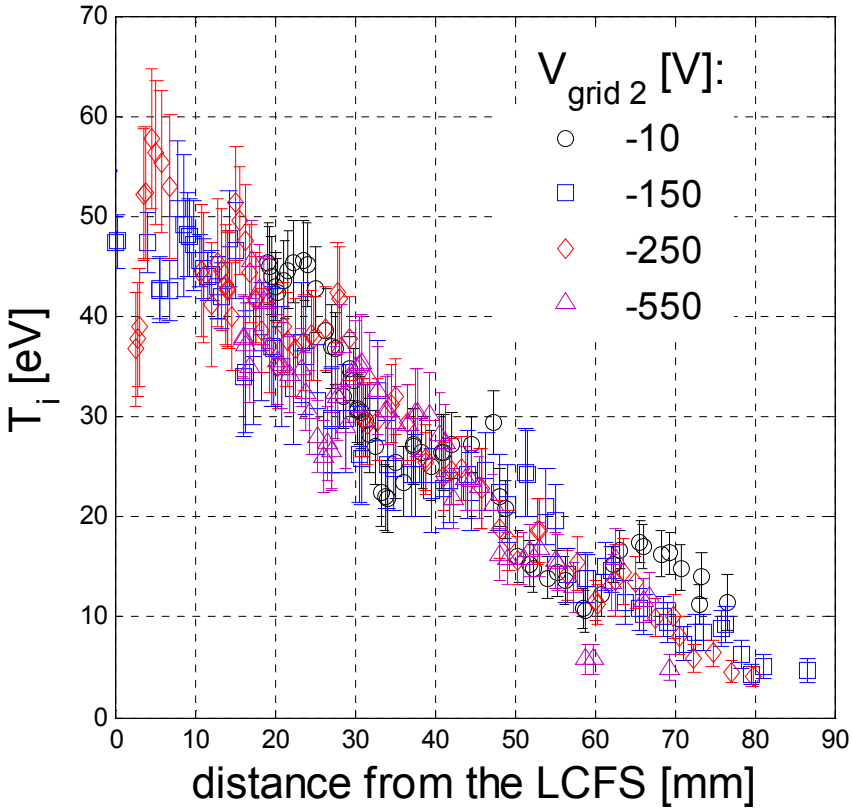

Figure 2.44. SOL ion temperature profiles measured by the Tore Supra RFA in similar ohmic discharges. Bias voltage applied on grid 2 $V_{grid\,2}$ was varied between the shots. Other parameters were constant (I_p = 0.6 MA, central line averaged density $\bar{n}_e = 1.4 \cdot 10^{19}\ m^{-3}$). T_i is independent of $V_{grid\,2}$.

2.4.6. Some remarks on the error on V_s and T_i due to the fit to the measured RFA *I-V* characteristics

2.4.6.1. Introduction

As discussed in section 2.2, the analysis of the RFA *I-V* characteristics assumes that the collector current I_{col} is constant up to a certain value of the bias voltage applied to grid 1 $V_{grid\,1}$ and decreases exponentially with $V_{grid\,1}$ for higher voltages. Exponential fit to the slope of the *I-V* characteristic gives T_i. The part of the *I-V* characteristics with almost constant I_{col} is related to the parallel acceleration of ions in the sheath potential in front of the RFA slit plate. The maximum $V_{grid\,1}$ in the flat-top phase of I_{col} gives the floating sheath potential V_s. In practice, V_s can be obtained from the intersection of the horizontal line at I_0 (which is the maximum collector current measured at $V_{grid\,1} = 0$) with the exponential fit (Eq.(2.2)).

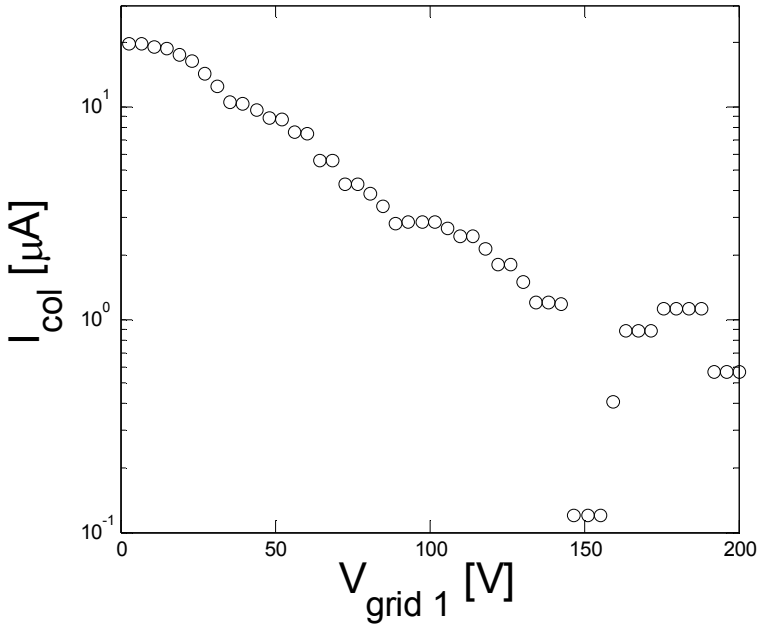

Figure 2.45. RFA I-V characteristic measured at $r - a \cong 2.5\,cm$ by the analyzer facing the LFS (TS discharge #42403).

However, it is often observed experimentally (figure 2.45) that the transition between the flat-top phase and the decaying part of the characteristic is relatively smooth and comprises a relatively wide range of $V_{grid\,1}$. Referring to the kinetic model of Chung and Hutchinson [Chung 1988], such a smooth transition might be related to the fact that the parallel ion velocity distributions $f(v_x)$ at the sheath edge are not exponential at low v_x, figure 2.46. This has a direct implication for the measurements of both T_i and V_s. First, since the exponential fit to the decaying part of the characteristic is influenced mainly by highest values of I_{col}, the measurements of T_i can be overestimated if the range of I_{col} included in the fit comprises also the non-exponential "rounded" part. Therefore, the range of I_{col} that enters the fit needs to be restricted to $I_{col} < I^*$. In order to ensure that only the exponential part of the *I-V* characteristic is included in the fit Valsaque *et al* [Valsaque 2002] recommend $I^* = 0.1I_0$. Since this is close to the typical noise level of the typical collector signal, it could hardly be applied to experimental data. Therefore, values like, for example, $I^* = 0.5I_0$ seem to be a more reasonable compromise (an additional reason for omitting the collector current above a certain value of I_{col} are the impurity ions which affect mainly the upper part of the slope, section 7.1.1 in [Pitts 1991]). The problem of the non-exponential part of the characteristic concerns the measurements of V_s as well. Since the transmission between the flat-top phase and the exponentially decreasing part of the characteristic is smooth it is not exactly clear where the sheath potential is on the experimental characteristic.

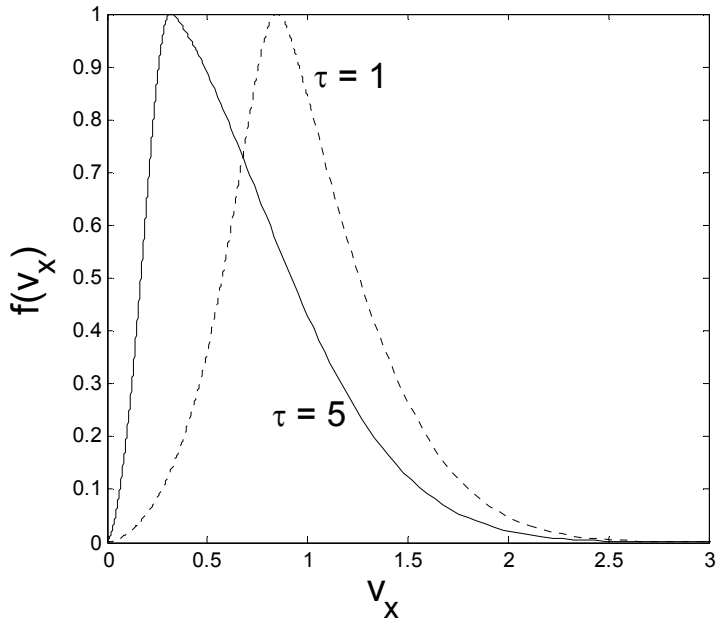

Figure 2.46. Parallel ion velocity distribution at the sheath edge calculated from the kinetic model of Chung and Hutchinson [Chung 1988] for zero parallel flow velocity v_0 and two values of the ion-to-electron temperature ratio $\tau = 1$ and $\tau = 5$. The parallel velocity v_x is normalized to $\sqrt{2}v_T$ with $v_T = \sqrt{eT_i / m_i}$ being the ion thermal velocity.

In this section the errors on V_s and T_i arising purely from the application of the standard fitting procedure to the RFA *I-V* characteristics is studied for a first time. We analyse the artificial *I-V* characteristics constructed from the parallel ion velocity distributions at the sheath edge given by the kinetic model of Chung and Hutchinson [Chung 1988] which is the best theory available. We show that the application of the standard fitting procedure leads to an overestimation of T_i by up to ~10 per cent and to the overestimation of V_s by up to $0.3T_e$. The error on V_s was found to be smaller for higher the ion-to-electron temperature ratio τ. By coincidence, the sheath theory also predicts the decrease of V_s with τ (Eq.(1.9)). This should be taken into account when comparing V_s measured by RFA with theory as systematic errors on V_s may partially account for the observed dependences of V_s on τ. Because the measurements of the collector current are necessarily subjected to noise and the parallel ion velocity distributions are not exponential for a certain range of velocities, these errors are largely unavoidable. We show that less restrictive condition for the upper limit of the collector current included in the fit generally leads to smaller overestimation of V_s but larger overestimation of T_i and vice versa. This, in addition to the fact that the upper part of the characteristic is most influenced by impurities, implies that the upper limit of I_{col} included in the fit should be as small as possible (within the limits given by the collector current signal-to-noise ratio) when T_i is the main quantity of interest.

2.4.6.2. Analysis of the artificial I-V characteristics

We study the error on V_s using the procedure described in section 2.4.3.1, i.e. we construct the RFA *I-V* characteristics from the parallel ion velocity distributions at the sheath edge $f(v_x)$ with $f(v_x)$ calculated from the kinetic model of Chung and Hutchinson [Chung 1988]. For simplicity we assume zero parallel drift velocity v_0. We include $f(v_x)$ calculated for the ion-to-electron temperature ratio τ in the range of 1 – 5. $f(v_x)$ for $\tau = 1$ and $\tau = 5$ are illustrated in figure 2.46. Like in section 2.4.3.1, v_x is normalized to $\sqrt{2}v_T$ with $v_T = \sqrt{eT_i / m_i}$ being the ion thermal velocity. The "collector current" i_{col} is calculated from $f(v_x)$ using Eq.(2.13) and is normalized to one. Consequently, the characteristics (i_{col} against $v_{\min}^2$ with $v_{\min}^2$ being the analogous to V_{grid1} / T_i) are analyzed using the fitting procedure normally applied to experimental data. It is particularly important to note that since $f(v_x)$ are evaluated at the sheath edge, V_s is zero. Therefore, V_s obtained from the fit provides an estimate of the error on the sheath potential (normalized to T_i) introduced by the standard fitting routine for the *I-V* characteristics.

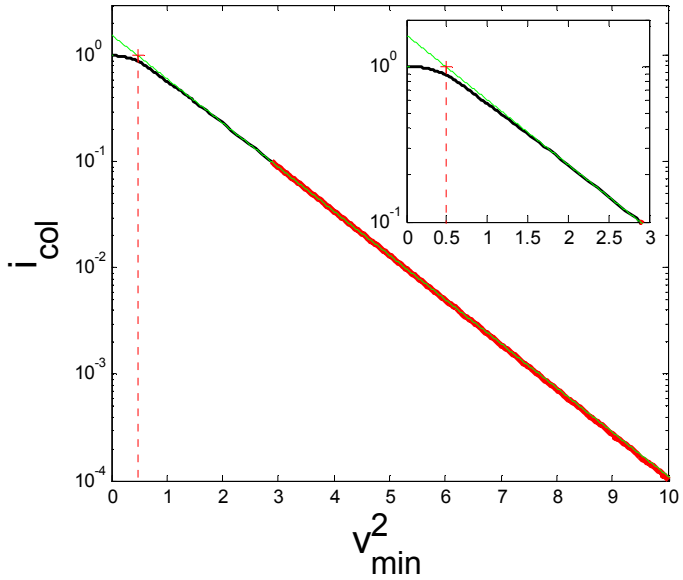

Figure 2.47. i_{col} calculated (Eq.(2.13)) from the parallel ion velocity distribution at the sheath edge obtained from the kinetic model of Chung and Hutchinson [Chung 1988] for the parallel drift velocity $v_0 = 0$ and the ion-to-electron temperature ratio $\tau = 1$. i_{col} is plotted against $v_{\min}^2$ which is analogous to V_{grid1} / T_i. A fit (Eq.(2.14)) to $10^{-4} < i_{col} < 10^{-1}$ (referred to as "ideal" restriction, thick red line) is indicated by green line. The intersection of the fit with $i_{col} = 1$ (indicated by red cross) gives the error on the sheath potential normalized to ion temperature $\Delta V_s / T_i \cong 0.5$.

We apply two different restrictions for the range of i_{col} included in the exponential fit to the artificial *I-V* characteristics (Eq.(2.14)). First, we follow the proposal of Valsaque *et al* [Valsaque 2002] and we restrict i_{col} by $10^{-4} < i_{col} < 10^{-1}$. Such restriction ensures that only the exponential part of the characteristic is included in the fit and is referred to as "ideal" restriction. Second, we apply the restriction more relevant to experimental data, i.e. $i_{col} < 5 \cdot 10^{-1}$ (this is referred to as "realistic" restriction). In addition, in order to simulate the effect of the noise on the collector signal, the realistic restriction is also applied to the characteristics with normally distributed random numbers with zero mean and standard deviation of 0.05 (simulating 5% noise on the collector signal) added to the each value of i_{col}. The latter is referred to as "noisy realistic" case.

A fit to the *I-V* characteristic for the range of i_{col} entering the fit given by the ideal restriction is illustrated in figure 2.47. The characteristic is calculated from $f(v_x)$ for $\tau = 1$. The range of i_{col} included in the fit is indicated by thick red line. The intersection of the exponential fit with $i_{col} = 1$, marked with small cross, gives the error on the sheath potential $v_{\min}^2 = \Delta V_s / T_i \cong 0.5$ which is a significant fraction of the ion temperature. Note also that the decrease of i_{col} with $v_{\min}^2$ becomes exponential just at about $i_{col} \approx 0.3 - 0.5$.

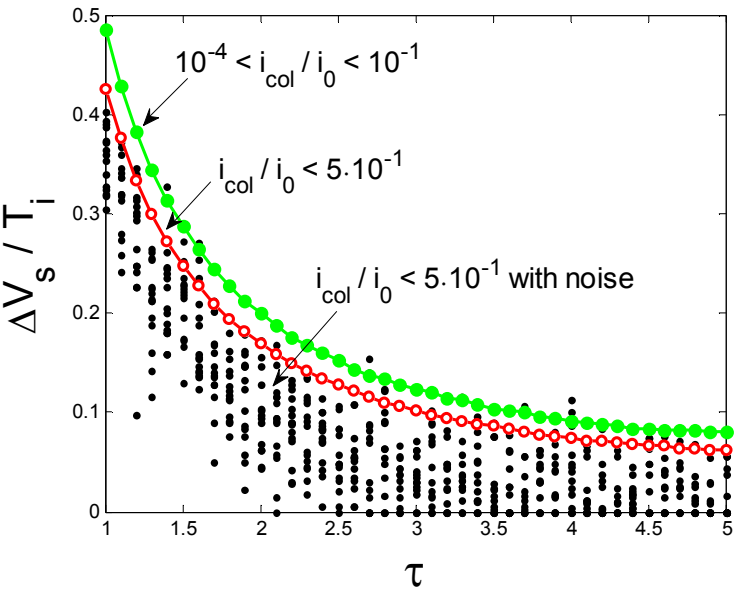

Figure 2.48. The error on the sheath potential produced by the fit $\Delta V_s / T_i$ plotted against the ion-to-electron temperature ratio. Three different methods for the restriction of the collector current entering the fit (Eq.(2.14)) are compared. —●— : ideal restriction (no noise on I-V characteristics, $10^{-4} < i_{col} < 10^{-1}$ included in the fit, —θ— : realistic restriction (no noise, $i_{col} < 5 \cdot 10^{-1}$ included in the fit), • : noisy realistic restriction (normally distributed random number with mean 0 and standard deviation 0.05 added to i_{col}, $i_{col} < 5 \cdot 10^{-1}$ included in the fit.

Applying the same procedure for the *I-V* characteristics calculated for $\tau = 1-5$ and analyzed using ideal, realistic, and noisy realistic restrictions for the range of i_{col} included in the fit produces the data plotted in figure 2.48. For the noisy realistic case the calculation was run several times to obtain better statistics. $\Delta V_s / T_i$ decreases with the increase of τ. This is because for higher τ $f(v_x)$ starts to decrease exponentially at lower v_x (see figure 2.46) so that the non-exponential "rounded" part of the *I-V* characteristic comprises smaller range of $v_{\min}^2$. The realistic restriction leads to somewhat lower error on V_s than the ideal restriction. This is because some points on the non-exponential part of the characteristic are included in the fit which makes the slope of the fit less steep. The price paid for this is in the overestimation of T_i by $7 \to 5\,\%$ for $\tau = 1 \to 5$. With the noise added to the realistic restriction the error on V_s becomes even

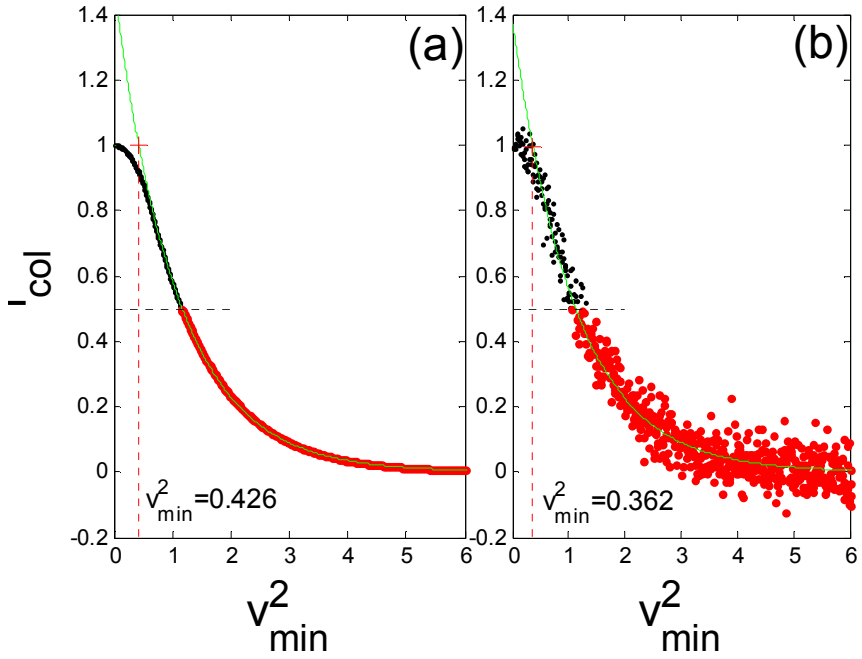

Figure 2.49. Exponential fit to the theoretical I-V characteristics calculated (Eq.(2.13)) from the parallel ion velocity distribution at the sheath edge obtained from the kinetic model of Chung and Hutchinson [Chung 1988] for the parallel drift velocity $v_0 = 0$ and the ion-to-electron temperature ratio $\tau = 1$. Two restrictions for the range of i_{col} included in the fit are compared: (a) realistic restriction (no noise, $i_{col} < 5 \cdot 10^{-1}$ included in the fit), (b) noisy realistic restriction (normally distributed random number with mean 0 and standard deviation 0.05 added to i_{col}, $i_{col} < 5 \cdot 10^{-1}$ included in the fit). The data included in the fit are indicated by red dots. The intersection of the fit with $i_{col} = 1$ (indicated by red cross and vertical dashed line) gives the error on the sheath potential normalized to ion temperature.

smaller. The reason why this is so is illustrated in figure 2.49: by cutting all points above $i_{col} = 5 \cdot 10^{-1}$, the highest values of i_{col} associated to the lowest values of $v_{\min}^2$ included in the fit are removed. Since the fit is influenced mainly by the currents associated to lowest $v_{\min}^2$, the final slope of the fit gets less steep so that $\Delta V_s / T_i$ is lower. Again, smaller overestimation of V_s is paid by larger overestimation of T_i ($12 \to 8\,\%$ for $\tau = 1 \to 5$). For the noisy realistic case (which is probably closest to experimental measurements) and for the range of τ typically measured in the SOL the error on $V_s \approx 0.05 \to 0.1\, T_i$, i.e. about $1-10$ volts in absolute value. Multiplying $\Delta V_s / T_i$ by τ the gives the error on V_s normalized to T_e, figure 2.50. Such normalization seems to be more appropriate as $\Delta V_s / T_i$ seems to be much less dependent on τ for $\tau > 2$ which is typically measured in the SOL. In this range of τ, the error on V_s is up to 30% of T_e for the noisy realistic restriction.

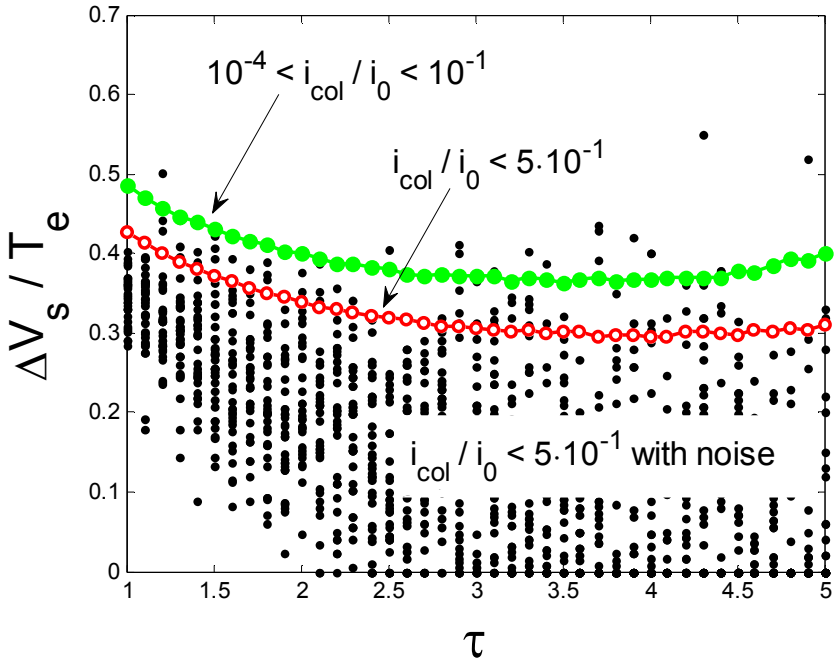

Figure 2.50. $\Delta V_s / T_e$ plotted against the ion-to-electron temperature ratio. Three different methods for the restriction of the collector current entering the fit (Eq.(2.14)) are compared. —●— : ideal restriction (no noise, $10^{-4} < i_{col} < 10^{-1}$ included in the fit), —o— : realistic restriction (no noise, $i_{col} < 5 \cdot 10^{-1}$ included in the fit), • : noisy realistic restriction (normally distributed random number with mean 0 and standard deviation 0.05 added to i_{col}, $i_{col} < 5 \cdot 10^{-1}$ included in the fit).

Annex

REVIEW OF SCIENTIFIC INSTRUMENTS **79**, 073502 (2008)

On the reliability of scrape-off layer ion temperature measurements by retarding field analyzers

M. Kočan,[1,a)] J. P. Gunn,[1] M. Komm,[2] J.-Y. Pascal,[1] E. Gauthier,[1] and G. Bonhomme[3]
[1]*CEA, IRFM, F-13108 Saint-Paul-lez-Durance, France*
[2]*Association Euratom-IPP.CR, Institute of Plasma Physics, Za Slovankou 3, 18200 Prague, Czech Republic*
[3]*Université Henri Poincaré, Nancy I, BP 239, 54506 Vandoeuvre-lès-Nancy Cedex, France*

(Received 27 March 2008; accepted 15 June 2008; published online 15 July 2008)

The retarding field analyzer (RFA) is one of the only widely accepted diagnostics for measurements of ion temperature T_i in the tokamak scrape-off layer. In this paper we analyze some instrumental effects of the RFA and their influence on T_i measurements. It is shown that selective ion transmission through the RFA slit is responsible for an overestimation of T_i by less than 14%, even for a relatively thick slit plate. Therefore, thicker slit plates are preferable, since they reduce, e.g., the risk of melting during off-normal events, and the effect of positive space charge inside the cavity. The influence of the electron repelling grid, as well as misalignment of the slit with respect to the magnetic field on T_i measurements are negligible. © *2008 American Institute of Physics.*
[DOI: 10.1063/1.2955465]

I. INTRODUCTION

Ion-to-electron temperature ratio $\tau=T_i/T_e$ plays an important role in the tokamak scrape-off layer (SOL). Its value determines, e.g., the relative importance of the conducted ion and electron heat fluxes, classical drift flows compared to turbulence driven flows, the amount of heat convected to a surface, etc.

Measurements of SOL T_i are rare. Novel electrostatic probes for T_i measurements have been successfully used on small experimental fusion reactors in the past.[1–6] However, the most widely accepted diagnostic for SOL T_i measurements is the retarding field analyzer (RFA). The ions are transmitted through a thin slit into the analyzer and their parallel velocity distribution is analyzed by means of a retarding electric field applied to a grid. The RFA has been used in a plasma with[7–14] or without[15,16] magnetic field. A bidirectional probe head equipped with two RFAs based on the earlier joint european torus (JET) design[13] is routinely used on the Tore Supra tokamak.

Our study was motivated by recent RFA measurements performed in Tore Supra, which systematically give high values $\tau=2-7$. Such high values of τ have been reported before, e.g., in Refs. 6 and 11. An independent experimental validation of RFA T_i measurements on a large fusion reactor is not yet available due to a lack of simultaneous measurements with other relevant diagnostics. Therefore, the main aim of this paper is to verify the reliability of RFA measurements using a theoretical model and particle-in-cell (PIC) simulations.

In this paper we address the following questions concerning the interpretation of RFA measurements: To what degree is the inferred ion temperature influenced by selective ion transmission through the slit (the transmission probability of an individual ion depends on its parallel speed)? Does selective ion transmission vary with the slit plate thickness? As different slit plate thicknesses have been used for the Tore Supra RFA, the latter question concerns the comparability of the results from different experimental campaigns.

Experimental and theoretical studies aimed at the choice of appropriate RFA slit dimensions were reported in Refs. 8, 11, and 12. The particularity of our work is in the evaluation of the ratio of ion temperature after and before the slit transmission, r_T, as a function of τ, slit plate thickness s, and the angle of the slit plate misalignment with respect to the magnetic field vector $\mathbf{B}$, α_{mis}. We combine the kinetic model of Chung and Hutchinson,[17] with the one originally proposed by Nachtrieb,[18] including some adjustments concerning the slit geometry and ion velocity distribution function. In addition to the model, the slit transmission is studied by PIC simulations and from experimental data. Moreover, we show that the influence of the negatively biased electron repelling grid on T_i measurements is negligible. The procedure used here can be applied for similar problems where charged particles are transmitted through a thin aperture.

Some issues concerning the reliability of T_i measurements are not addressed in this paper, the most important of them being the influence of impurity ions in the SOL. As the analysis of the RFA current-voltage (I-V) characteristics assumes Maxwellian singly charged ions, impurities with higher charge state can affect the measurements of T_i. Separation of the components of the analyzed ion flux by charge state and temperature was proposed in Ref. 11. However, the model needs to specify the fractions of the total flux carried by ions with a given charge state as well as their temperatures. Such measurements are not available.

In this paper, the ion and electron temperatures are stated in electron volts, and the indication "parallel" or "perpendicular" relates to $\mathbf{B}$.

[a)]Author to whom correspondence should be addressed. Tel.: 33-(0)4 42 25 36 08. FAX: 33-(0)4 25 49 90. Electronic mail: martin.kocan@cea.fr.

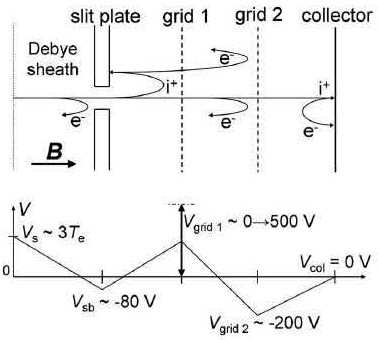

FIG. 1. Main components of the RFA and the biasing scheme applied for ion temperature measurements.

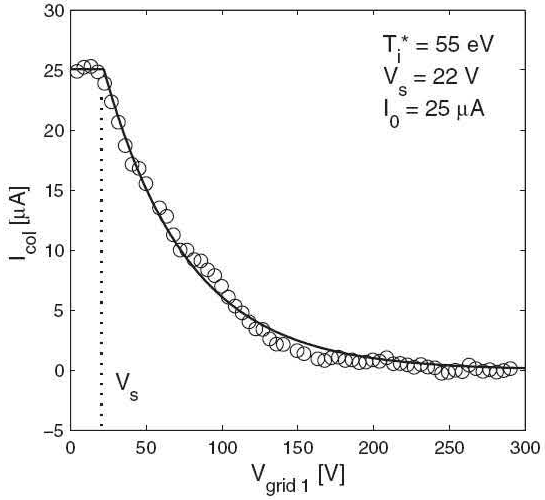

FIG. 2. Typical RFA *I-V* characteristic. Current to the collector, I_{col}, is plotted against the bias voltage of grid 1, $V_{grid\ 1}$. For $V_{grid\ 1}<|V_s|$, I_{col} remains constant since all ions are shifted toward higher energies due to the Debye sheath potential drop in front of the slit plate, V_s. A fit to the decaying part of the characteristic gives the effective ion temperature T_i^*.

In Sec. II, the RFA principle is discussed. In Sec. III, some details of the Tore Supra RFA are addressed. Section IV deals with selective ion transmission through the RFA slit and its influence on T_i. The influence of the negatively biased electron repelling grid on ion temperature is studied in Sec. V. Conclusions are given in Sec. VI.

II. RFA PRINCIPLE

The schematic of the analyzer and the biasing scheme are shown in Fig. 1. The operational principle of T_i measurements by the RFA can be briefly summarized as follows.

A fraction of the incident ion flux is transmitted through the slit. The slit plate is biased negatively to repel most of the thermal electrons. The transmitted ions are retarded in the electric field created by a swept positive voltage applied to grid 1, $V_{grid\ 1}$. A constant negative bias is applied on grid 2, $V_{grid\ 2}$, to repel the remaining fast electrons from the tail of the distribution and to suppress the secondary electrons emitted from the collector or from the rear of the slit plate due to ion impact. $V_{grid\ 2}$ is the lowest voltage in the system. The collector measures the ion current, I_{col}. Figure 2 shows a typical *I-V* characteristic. For a certain range of $V_{grid\ 1}=0 \rightarrow |V_s|$ the collector current remains at I_0; all ions gain a parallel energy of $eZ_i|V_s|$ (with eZ_i being the ion charge and V_s the sheath potential) in the collisionless Debye sheath. For $V_{grid\ 1}>|V_s|$ the current to the collector starts to decrease. Assuming that fuel ions of charge eZ_i dominate the incident flux, I_0 can be expressed as (see, e.g., Ref. 13)

$$I_{col} = A_{slit} eZ_i \int_u^\infty dv_\parallel v_\parallel \xi f(v_\parallel), \tag{1}$$

where A_{slit} is the slit area, ξ is the total transmission factor that includes the transmission of the slit and the grids, $u=\sqrt{2eZ_iV_{grid\ 1}/m_i}$ (with m_i being the ion mass), and $f(v_\parallel)$ is the parallel ion velocity distribution.

Far from the probe, the ions are assumed to be characterized by a Maxwellian distribution, with a well defined temperature T_i. However, in the vicinity of the probe the

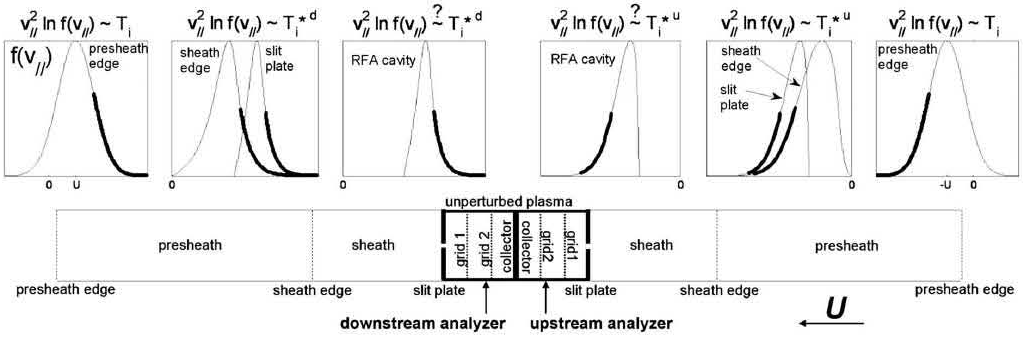

FIG. 3. Schematic of the RFA inserted into the plasma. The probe consists of two identical analyzers mounted back to back. In the unperturbed plasma the parallel ion velocity distribution is Maxwellian with well defined temperature T_i. T_i is given by the decaying part of the distribution, shown schematically by a thick line. In the presheath the Maxwellian distribution gets distorted both on the upstream (u) side (where flow velocity U is directed toward the probe) and on the downstream (d) side (where U is directed away from the probe). The effective ion temperature $T_i^{*u}>T_i^{*d}$, with $T_i \cong (T_i^{*u}+T_i^{*d})/2$ (Ref. 19). Inside the analyzer the distribution can be further influenced by instrumental effects (selective ion transmission through the slit) so that the measured temperature can differ from T_i^*.

plasma is perturbed by the shadowing effect induced by the probe itself, which depends significantly on the bulk ion flow past the probe. $f(v_\parallel)$ is distorted from Maxwellian and an exponential fit to the high-energy tail of the *I-V* characteristic yields an effective ion temperature T_i^*. Except when the parallel flow velocity $\mathbf{U}=0$, $T_i^* \neq T_i$. In addition, as shown by Valsaque *et al.*,[19] the effective ion temperatures measured on the two sides of the probe are different. Figure 3 shows a schematic of the RFA inserted into the plasma. The probe consists of two analyzers mounted back to back, aligned with $\mathbf{U}$. The Maxwellian distribution gets distorted in the presheath, both on the upstream (u) side (where $\mathbf{U}$ is directed toward the probe) and on the downstream (d) side (where $\mathbf{U}$ is directed away from the probe), with $T_i^{*u} > T_i^{*d}$. An accurate estimation of T_i is given by $T_i \cong (T_i^{*u}+T_i^{*d})/2$, as shown theoretically in Ref. 19 and demonstrated experimentally in Refs. 7 and 20. T_i^* can be obtained by the RFA from a fit to the decaying part of the *I-V* characteristics and (Fig. 2)

$$I_{\mathrm{col}} = I_0 \exp\left[-\frac{Z_i}{T_i^*}(V_{\mathrm{grid1}} - |V_s|)\right]. \quad (2)$$

In this paper it is assumed, for simplicity, $\mathbf{U}=0$, so that $T_i^{*u}=T_i^{*d}=T_i$.

III. TORE SUPRA RFA

Tore Supra[21] is a large tokamak with a plasma of circular cross-sectional (major radius $R=2.4$ m and minor radius $a=0.72$ m) whose last closed flux surface is defined by its intersection with the bottom toroidal pump limiter. The maximum plasma current and toroidal magnetic field are $I_p<2$ MA and $B_\Phi<4$ T, respectively, both are oriented in the negative toroidal direction, i.e., clockwise viewed from above. Typical values of SOL electron and ion temperatures, plasma density, Debye length, and ion Larmor radius are $T_e=5\rightarrow100$ eV, $T_i=5\rightarrow200$ eV, $n_e=10^{17}\rightarrow10^{19}$ m^{-3}, $\lambda_D=20\rightarrow30$ μm, and $r_L=150\rightarrow800$ μm, respectively.

The design of Tore Supra RFA is based on the one that was originally used in JET.[13] The RFA is located in a top port at poloidal angle $\theta=79°$ with respect to the outer midplane. The probe is mounted on a fast reciprocating drive which allows several insertions into the plasma during a single discharge (up to 14 until now). Plasma is scanned up to 3 cm inside the last closed flux surface. The probe is used to measure T_i, T_e, V_s, the parallel ion saturation current density $j_{+\mathrm{sat}}$, and the floating potential V_f. T_e, $j_{+\mathrm{sat}}$, and V_f are measured by the slit plate working as a Langmuir probe. Measurements of T_i and V_s, and T_e, $j_{+\mathrm{sat}}$, and V_f are separated by $\sim$0.5 ms. Figure 4 shows the usual bias waveforms applied on the slit plate and grid 1, as well as the currents to the slit plate and to the collector. The database from six experimental campaigns consists of more than 600 radial profiles of T_i, V_s, T_e, $j_{+\mathrm{sat}}$, and V_f measured in discharges with Ohmic or rf heating up to 8 MW.

The alignment of the probe head with the magnetic field is achieved by rotating the slit axis (see Fig. 5) in the horizontal plane by 7° with respect to the toroidal magnetic field, an angle optimized for edge safety factor $q=rB_\Phi/(RB_\theta)\approx3$ operation. Here r, R, B_Φ, and B_θ are tokamak major and minor radii and local toroidal and poloidal magnetic fields, respectively.[22] Since q varies between the discharges as well as over the probe reciprocation, alignment within about 3° is guaranteed.

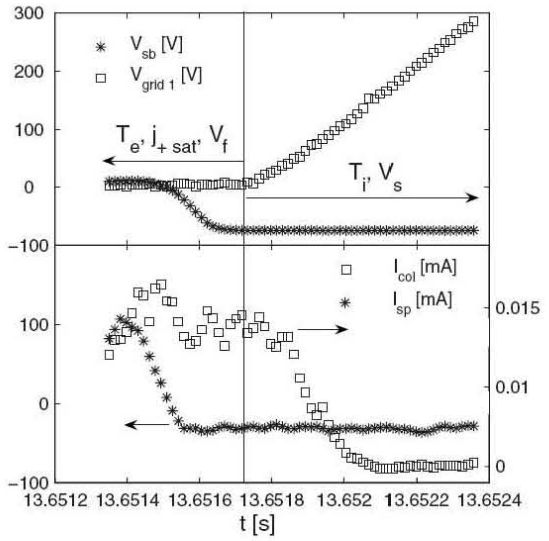

FIG. 4. Above: typical bias waveforms applied to the slit plate and to grid 1 for Tore Supra RFA. Below: current to the collector and the slit plate current, I_{sp}. Vertical line separates the waveform into two parts. In the first part of the waveform, T_e, $j_{+\mathrm{sat}}$, and V_f are measured by the slit plate working as a Langmuir probe. T_i and V_s are measured in the second part of the waveform.

The probe head (Fig. 5, left) is protected by a housing with outer diameter of 40 mm made from carbon fiber composite (CFC). The thickness of the housing is 3.5 mm. Plasma is transmitted to slit plate through an orifice, $A_{\mathrm{orifice}}=19.6\times10^{-6}$ m^2, drilled into the CFC housing. The dimensions of the orifice are indicated in Fig. 5.

The slit plate (Fig. 5, right) is made of a thin nickel foil and pressed between two Inconel protective plates. A rectangular slit with length $h=5$ mm and width $w=30$ μm is laser cut into the foil. Nickel foils with three different thicknesses $s=250$, 150, and 100 μm have been used in consecutive experimental campaigns. The temperature rise of the slit plate itself is estimated to be $150\rightarrow700$ °C for a 40 ms pulse at 10 MW/m^2. The melting point of nickel is 1453 °C. The probe has been exposed to heat flux densities up to 30 MW/m^2 for $\sim$10 ms, without any damage on the slit plate. Since the ion current transmitted to the probe cavity is relatively low (<0.1 mA for $s=100$ μm), the influence of positive space charge inside the cavity on T_i is negligible. Using the slab-geometry model for the transmitted ion beam from Ref. 18, it can be shown that for such currents the vacuum potential ($\sim10^2$ V) dominates the space charge potential ($\sim$1 V). The space charge becomes important for $s<50$ μm. In addition, the slab-geometry model can be considered as a "worst-case scenario" since it neglects the defocusing of the ion beam, as well as the presence of electrons inside the cavity, both having the tendency to decrease further the influence of the space charge.

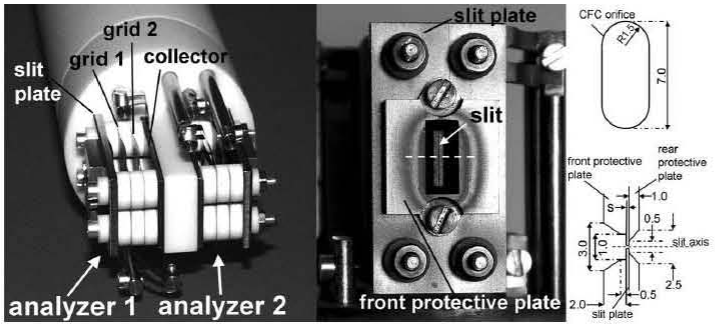

FIG. 5. Tore Supra RFA. Left: the probe head with two identical analyzers mounted back to back. Right: plasma facing components of each analyzer consist of the front protective plate and the slit plate. The "shadow" of the CFC orifice, which is visible on the protective plate, defines the plasma wetted area, A_{orifice}. Orifice dimensions are stated upper right. Horizontal dashed line through the slit indicates a cut of the slit plate which is given lower right (not in scale).

The grids are made of nickel. Individual grid currents are not measured. Grid wires with width of $\Delta=63\ \mu$m are separated by $D=0.4$ mm, giving an optical transmission factor of the grid $\xi_{\text{opt}}=(D-\Delta)^2/D^2\cong 0.71$. In addition to the principal grids 1 and 2, another grid (not shown in the schematic of Fig. 1) is attached to the rear Inconel protective plate of the slit plate in order to render the electric field behind Inconel plate as planar as possible. This technique has been used, e.g., in Ref. 7. The collector is made of copper. The grids and the collector are separated by 2 mm, a distance given by spatial restrictions.

Taking the absorption of ions on the grid wires into account, the relative transmission factor of the slit plate can be calculated from the experimentally measured quantities as

$$\xi_r^{\text{exp}}=\frac{I_0}{j_{+\text{sat}}hw\xi_{\text{opt}}^3}. \tag{3}$$

For all three grids, the transmission factor is assumed to be equal to ξ_{opt}. There might be some uncertainty in ξ_r^{exp} due to, e.g., ion induced secondary electron emission from the slit plate, which if nonzero would cause $j_{+\text{sat}}$ to be overestimated (and thus underestimate ξ_r^{exp}). In our study, the secondary electron emission from the slit plate is neglected.

IV. TRANSMISSION OF IONS THROUGH THE SLIT

A. Theoretical model of ion transmission through the slit

In this section, ion transmission through the slit is studied by means of a simple analytical model. Our aim is (a) to derive the expression for the relative slit transmission factor and (b) to evaluate the influence of the slit transmission on parallel ion velocity distribution. The first enables to estimate the magnitude of the ion current transmitted to the RFA cavity and thus to calculate its relative importance to e.g. gas breakdown or space charge limit. Similar calculations were made in Ref. 23. The latter allows to inspect the influence of the selective ion transmission on T_i.

We partially follow the original model of Nachtrieb,[18] but the dimensions and the shape of the slit are adjusted to the ones of the Tore Supra RFA. In Ref. 18, the parallel ion velocity distribution was approximated by shifted Maxwellian velocity distribution. We apply more general approach by approximating the parallel ion velocity distribution by δ-function. As shown below, this enables to evaluate the slit transmission factor for an arbitrary ion velocity distribution.

The model (see schematic in Fig. 6) is based on the assumption that $r_L \gg w$, which is well satisfied in the SOL of Tore Supra. Under these conditions, most ion trajectories within the slit can be approximated by straight lines. The electric field inside the slit is assumed to be zero. An incident ion is transmitted only if its ratio of perpendicular-to-parallel velocities v_z/v_x satisfies the condition

$$v_z/v_x \leqslant \begin{cases} (w/2+z)/s+\tan\alpha_{\text{mis}} & \text{for } v_z<0 \\ (w/2-z)/s-\tan\alpha_{\text{mis}} & \text{for } v_z>0 \end{cases}. \tag{4}$$

$\alpha_{\text{mis}}=0$ corresponds to perfect probe head alignment with **B**. Condition (4) is valid for small α_{mis}. The slit boundaries in the y direction are considered to be infinitely far from the slit axis. The model neglects (a) the ions with $r_L<0.5w$ that would pass through the slit even if they did not satisfy condition (4) and (b) the ions with the velocities $v_y/v_x \geqslant h/s \approx 50$ (for $s=100\ \mu$m) that would be absorbed on the slit boundaries in the y direction. For typical ion temperature $T_i=50$ eV, (a) represents only ≈ 0.04 of the total ion population. Case (b) can also be neglected since v_x and v_y are both of the same order given by the ion thermal velocity $v_T=\sqrt{eT_i/m_i}$.

Assume that the ions at the slit entrance are Maxwellian in the perpendicular directions and monoenergetic in the parallel direction

$$f(v_x',v_y,v_z)=\frac{n}{2\pi v_T^2}\delta(v_x'-v_x)\exp(-v_y^2-v_z^2). \tag{5}$$

The relative slit transmission factor ξ_r^{δ} is given by the ratio of the transmitted to the incident ion flux

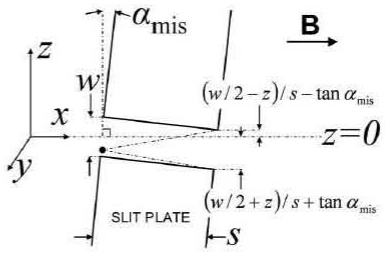

FIG. 6. Scheme of the theoretical model of the ion transmission through the slit. The position of an ion at the slit entrance is illustrated by a black dot. The pitch angles correspond to the critical ion velocity ratios $\pm v_z/v_x$. w and s are the slit width and the slit plate thickness (not to scale), respectively. The model is valid for small α_{mis}.

$$\xi_r^{\delta}(v_x) = \frac{\langle \Gamma_{tr} \rangle}{\Gamma_{in}} = \frac{w^{-1}\int_{-w/2}^{w/2} dz \Gamma_{tr}(z)}{\Gamma_{in}}$$
$$= w^{-1}\int_{-w/2}^{w/2} dz \frac{\int_{b_1(v_x,z)}^{b_2(v_x,z)} dv_z e^{-v_z^2}}{\int_{-\infty}^{\infty} dv_z e^{-v_z^2}} \cong \frac{1}{\sqrt{\pi}}\left[\frac{v_x w}{s}(1 - \tan^2 \alpha_{mis}) - \frac{1}{6}\left(\frac{v_x w}{s}\right)^3\right], \quad (6)$$

where $b_1 = v_x[(w/2+z)/s + \tan \alpha_{mis}]$, $b_2 = v_x[(w/2-z)/s - \tan \alpha_{mis}]$, and $w < s$. The velocities are normalized to $\sqrt{2}v_T$. The relative slit transmission factor for an arbitrary ion velocity distribution function is given by

$$\xi_r = \frac{\int_0^{\infty} dv_x v_x \xi_r^{\delta}(v_x) f(v_x)}{\int_0^{\infty} dv_x v_x f(v_x)}. \quad (7)$$

Values of ξ_r similar to the ones given by Eq. (6) are obtained for parallel ion velocity distribution functions at the slit entrance that are either Maxwellian with a shift of $v_0 = \sqrt{Z_i \phi / T_i}$ (with $\phi = |V_s + V_{sb}|$) or box function with $v_x \in [v_0; \sqrt{1+v_0^2}]$.

The influence of selective slit transmission on T_i can be quantified using the following procedure. The parallel ion velocity distribution function at the sheath edge in front of the probe is given by the kinetic model of Chung and Hutchinson[17] for a certain value of $\tau = T_i/T_e$. The ions are accelerated through the sheath potential ϕ, $v_x^2 \rightarrow v_x^2 + v_0^2$, so that the resulting distribution $f_{se}(v_x)$ corresponds to the one at the slit entrance. The transmitted distribution is $f_{tr}(v_x) = f_{se}(v_x)\xi_r^{\delta}(v_x)$, with ξ_r^{δ} given by Eq. (6). The procedure is illustrated in Fig. 7; f_{se}, f_{tr}, and ξ_r^{δ} are calculated for $T_i = 100$ eV, $T_e = 20$ eV, $V_{sb} = -80$ V (which corresponds to $\tau = 5$ and $v_0 = 1.12$), $w = 30$ μm, $\alpha_{mis} = 0$, and for $s = 30$, 100, and 300 μm. ξ_r^{δ} increases with v_x so that the slowest ions in the distribution are preferentially filtered. Next, the parallel ion current i_{col} is calculated as

$$i_{col}(v_{min}) \propto \int_{v_{min}}^{10 v_T} dv_x v_x f_{tr}(v_x), \quad (8)$$

with $v_{min} = 0 \rightarrow \max(v_x)$. Within the normalization factor, i_{col} coincides with the collector current, Eq. (1), and v_{min}^2 is analogous to $V_{grid\,1}/T_i$. In Fig. 8, i_{col} is plotted against v_{min}^2. The characteristics are calculated from f_{se} and f_{tr} and plotted in Fig. 7. The ratio of the ion temperatures after and before the slit transmission, r_T, is obtained from a fit to the decaying part of the characteristic

$$i_{col} = \exp[-(v_{min}^2 - v_{min}^{*2})/r_T], \quad (9)$$

which is analogous to Eq. (2). $v_{min}^{*2} = \phi/T_i$. As the characteristics are not exponential in their upper part and very small currents are not measurable in experiment, the range of i_{col} needs to is restricted by, e.g., $\ln(i_{col}) - 4 < \ln(i_{col}) < \ln(i_{col}) - 1$.[19]

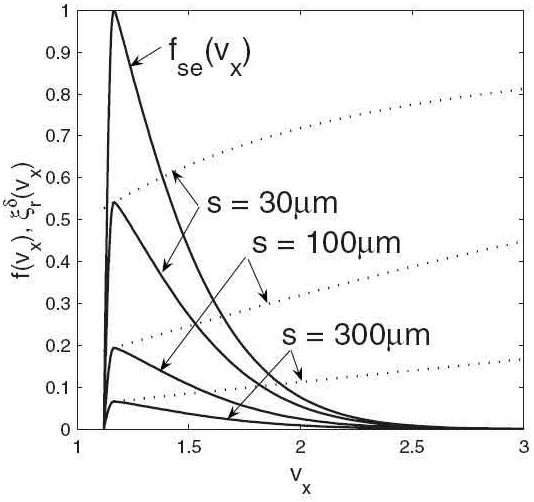

FIG. 7. Parallel ion velocity distribution functions at the slit entrance $f_{se}(v_x)$ and after the slit transmission $f_{tr}(v_x)$ (full curves) at $s = 30$, 100, and 300 μm. ξ_r^{δ} is the corresponding relative slit transmission factor (dotted curves) given by Eq. (6). f_{se}, f_{tr}, and ξ_r^{δ} are calculated for $T_i = 100$ eV, $T_e = 20$ eV, $V_{sb} = -80$ V (i.e., $\tau = 5$ and $v_0 = 1.12$), $w = 30$ μm, and $\alpha_{mis} = 0$. v_x is normalized to $\sqrt{2}v_T$.

r_T calculated for different τ, s, and α_{mis} will be given in Sec. IV C. ξ_r is compared to experimental values in Sec. IV D.

B. PIC simulations of the ion transmission through the slit

PIC code SPICE (Sheath Particle In CEll) (Ref. 24) has been used to study the ion transmission through the RFA slit.

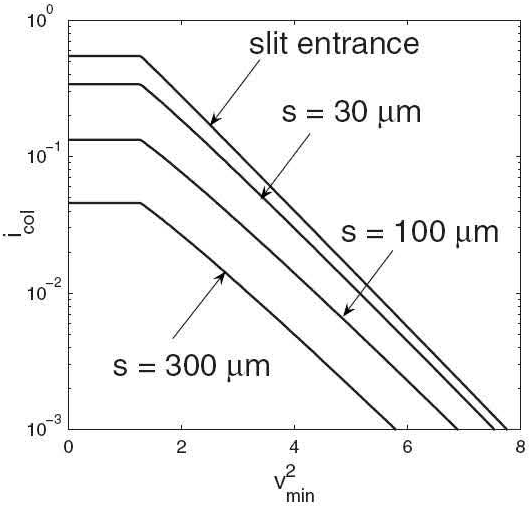

FIG. 8. i_{col} is plotted against v_{min}^2, calculated [Eq. (8)] from f_{se} and f_{tr}'s, stated in Fig. 7. s indicates the slit thickness. i_{col} coincides with the collector current, Eq. (2), and v_{min}^2 is analogous to $V_{grid\,1}/T_i$. The slope of the characteristics for $\ln(i_{col}) - 4 < \ln(i_{col}) < \ln(i_{col}) - 1$ gives the ratio of T_i after and before the slit transmission r_T.

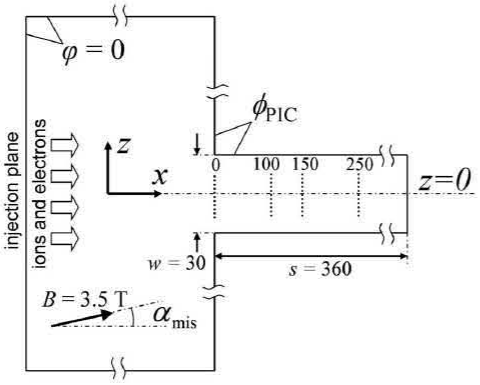

FIG. 9. Schematic of the SPICE simulations of the ion transmission through the slit. Distances are indicated in microns (not to scale). Ions and electrons are injected towards the wall containing a slit. The boundaries perpendicular to the injection plane are periodic. Ion distribution functions are measured at the positions indicated by dotted lines with respect to the distance from the slit entrance.

Contrary to the theoretical model, the PIC simulations include the self-consistent electrostatic field.

Originally, the SPICE code was developed for studying the flow of plasma into gaps between the limiter and divertor tiles. SPICE allows for $2d3v$ simulations in Cartesian coordinates. The code implements a standard leapfrog method for particle advancing and uses first order (*cloud-in-cell*) weighting.[25]

A schematic of the simulation model is illustrated in Fig. 9. Deuterons and electrons are injected toward the wall representing the slit plate, located several tens of λ_D away from the injection plane. The x axis coincides with the injection plane normal. The z axis is parallel to the injection plane. The wall contains a gap with a width $w=30$ μm and the total length $s=360$ μm. The gap axis is positioned at $z=0$. The third dimension of the slit in the y direction, $h=5$ mm in the real situation, is considered to be infinitely long. The magnetic field of 3.5 T is inclined at α_{mis} with respect to the injection plane normal.

The potential difference between the injection plane and the wall is set to

$$\phi_{\text{PIC}} = V_{\text{sb}} + \frac{T_e}{2}\ln\left[2\pi\frac{m_e}{m_i}\left(1+\frac{T_i}{T_e}\right)\right], \tag{10}$$

where $V_{\text{sb}}=-80$ V and T_i and T_e are the ion and electron temperatures at injection, respectively. The second term represents the floating sheath potential. Secondary electron emission from the slit plate is neglected.

The ions are injected with a parallel velocity distribution calculated from the kinetic model of Chung and Hutchinson.[17] The ion velocity distribution in both perpendicular directions is Maxwellian. The electrons are injected with a full Maxwellian distribution.

Four simulations for different combinations of the input parameters (Table I) were performed. Simulations (a) and (b) represent the typical SOL plasma parameters of Tore Supra, with $w\cong\lambda_D$. Simulation (c) was aimed at studying the extreme case of $w\cong 4\lambda_D$. Simulations (a)–(c) represent the case of a perfect probe head alignment with respect to **B**. Simulation (d) corresponds to the case of the probe head misalignment of 3° with respect to **B**.

TABLE I. Input parameters used in the PIC simulations of the ion transmission through the slit. From left to right: ion and electron temperatures and plasma density at injection, the inclination of the magnetic field with respect to the injection plane normal.

	T_i (eV)	T_e (eV)	$n_e(10^{18}$ m$^{-3})$	α_{mis} (deg)
(a)	30	10	0.7	0
(b)	100	20	1.5	0
(c)	20	5	5	0
(d)	100	20	1.5	3

Each simulation was left to run to a steady state. The ion velocity distributions in all three directions were measured at the slit entrance, and 100, 150, and 250 μm deep inside the slit. The relative slit transmission factor for a given slit thickness $\xi^{\text{PIC}}_{r(i)}$ was calculated from the ion velocity distribution functions as

$$\xi^{\text{PIC}}_{r(i)} = \frac{\Gamma_{\parallel i}}{\Gamma_{\parallel 0}} = \frac{\int_0^\infty dv_x v_x \int_{-\infty}^\infty dv_y \int_{-\infty}^\infty dv_z f_i(v_x,v_y,v_z)}{\int_0^\infty dv_x v_x \int_{-\infty}^\infty dv_y \int_{-\infty}^\infty dv_z f_0(v_x,v_y,v_z)}, \tag{11}$$

where the subscript i indicates a depth inside the slit (i.e., the slit thickness, 100, 150, or 250 μm) and the subscript "0" indicates the position at the slit entrance.

Figure 10 compiles the results from the SPICE simulations for perfect probe head alignment with respect to **B**. Each row corresponds to one simulation, (a)–(c), characterized by the parameters stated in Table I. The first column in Fig. 10 shows the radial profiles of the electrostatic potential $\varphi(x,z=0)$. φ is normalized to T_e. The distance from the slit entrance, x, is normalized to λ_D. The slit entrance is indicated by a vertical line. The arrows indicate the positions of measurements of $f(v_x)$. For simulations (a) and (c) (where $w\cong\lambda_D$) φ reaches its minimum value within approximately $\sim\lambda_D$ inside the slit. For simulation (b) ($w\cong 4\lambda_D$) the equipotential surface corresponding to ϕ_{PIC} is not perfectly parallel to front face of the slit plate but penetrates $\sim 4\lambda_D$ inside the slit. φ does not reach its minimum at the slit entrance. This gives rise to the perpendicular electric field $\approx 2eV_{\text{res}}(d)/w$. $V_{\text{res}}(d)=\varphi(d,z=0)-\phi_{\text{PIC}}$ is the residual voltage and d is the position inside the slit with respect to the slit entrance. The influence of the perpendicular electric field on ion transmission is discussed in the next section. The second column in Fig. 10 shows $f(v_x)$, scanned at different d (in microns). The $f(v_x)$ are normalized to the maxima of $f(v_x)$ measured at $d=0$. Parallel ion velocity v_x is normalized to $\sqrt{2}v_T$. Due to V_{res}, the $f(v_x)$ measured at $d>0$ are somewhat narrower and shifted to higher velocities, compared to the ones measured at the slit entrance. The third column of Fig. 10 shows the characteristics (i_{col} versus v^2_{min}) calculated from $f(v_x)$ [Eq. (8)]. A fit, Eq. (9), to the decaying part of the characteristics gives r_T. In the next section, r_T from the PIC simulations is compared to the one obtained from the theoretical model.

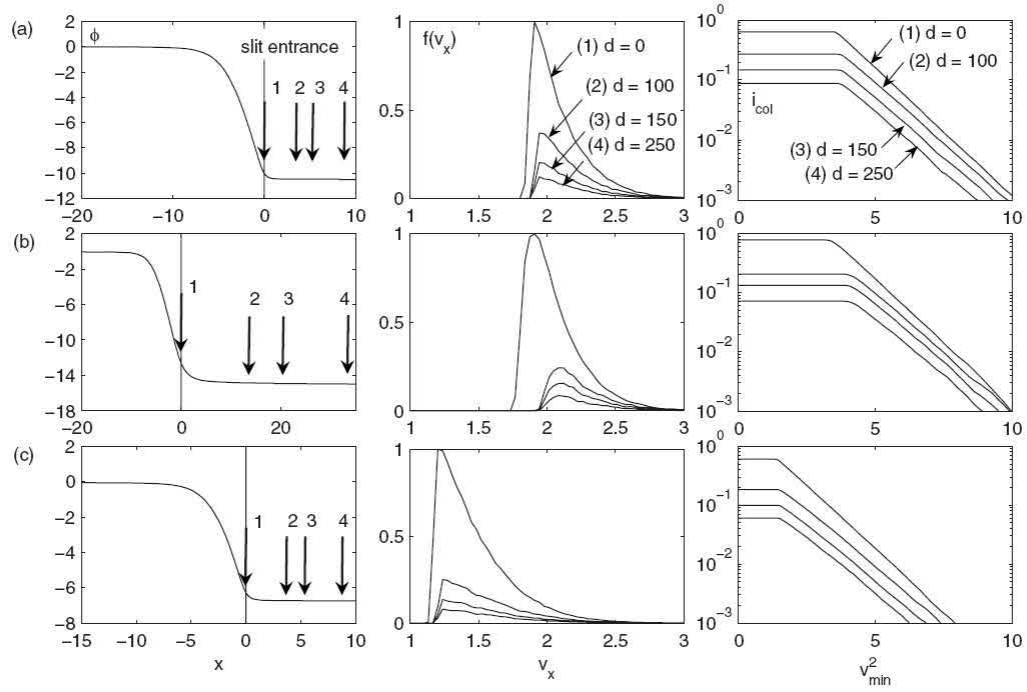

FIG. 10. Results from PIC simulations (a)–(c). First column: radial profiles of the potential φ calculated along the slit axis ($z=0$). φ is normalized to T_e. The distance from the slit entrance x is normalized to λ_D. The arrows indicate the positions of measurements of the parallel ion velocity distribution functions $f(v_x)$. Second column: $f(v_x)$ measured at different positions inside the slit with respect to the slit entrance, d (in microns). $f(v_x)$ is normalized to the maxima of $f(v_x)$ measured at $d=0$. v_x is normalized to $\sqrt{2}v_T$. Third column: parallel ion current i_{col} calculated from $f(v_x)$, Eq. (8), plotted against v^2_{min}.

C. Deformation of *I-V* characteristics: Comparison of the model and PIC simulations

Figure 11 shows the ratio r_T, calculated from the theoretical model (Sec. IV A) for $w=30$ μm. r_T is plotted as a function of s for $s=30\rightarrow300$ μm. r_T is evaluated for $\tau=1\rightarrow5$ and for two different values of $\alpha_{mis}=0$ and 10°. The results from the model are juxtaposed to the ones obtained from PIC simulations (a)–(c).

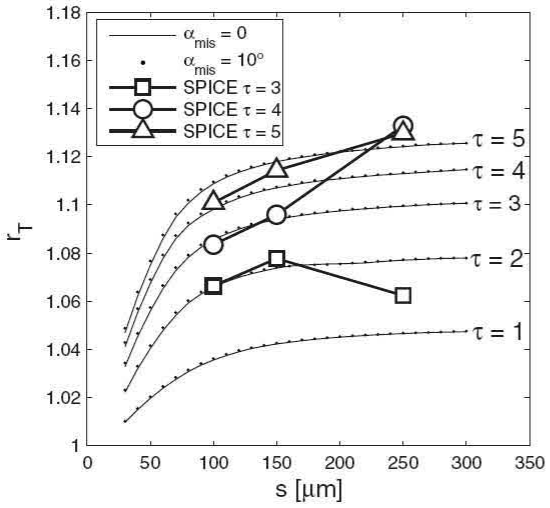

FIG. 11. Ratio of ion temperature after and before slit transmission r_T calculated from the theoretical model (Sec. IV A) and from PIC simulations (a)–(c) for $w=30$ μm. r_T is plotted against the slit plate thickness s. r_T from the model is evaluated for $\tau=1\rightarrow5$ and for two different values of $\alpha_{mis}=0$ and 10°.

r_T obtained from the model increases with s and τ. The increase in r_T with s is most significant for $s<100$ μm. For $s>100$ μm, r_T increases only by $\sim2\%$. $\partial r_T/\partial\tau$ is a decreasing function of τ. For $100\leqslant s\leqslant250$ μm, $r_T\cong\ln(2.83\tau^{0.05})$. PIC simulations and the model predict very similar values of r_T. This indicates that the influence of the perpendicular electric field inside the slit $2eV_{res}/w$ on selective ion transmission does not play an important role, even at $w\cong4\lambda_D$. For $s=250$ μm the agreement between the model and PIC simulations is somewhat worse. In this case, the particle statistics in the PIC simulation are less reliable due to relatively low number of ions deep inside the slit. Within the range of r_T plotted in Fig. 11, the overestimation of T_i is less than 14%.

The slit plate misalignment has only a small influence on ion transmission. The values of r_T for $\alpha_{mis}=0$ and $\alpha_{mis}=10°$ are very similar. In addition, simulation (d) for $\alpha_{mis}=3°$ gives practically the same r_T (not plotted in Fig. 11) as simulation (b) for $\alpha_{mis}=0$ (the difference is much less than 1%). This negative result can be explained as follows: The slit plate misalignment tilts the loss cone of perpendicular-to-parallel ion velocities in the v_z direction by α_{mis}. However, since the parallel and perpendicular ion velocities are de-correlated, each value of v_z contains the full set of parallel velocities v_x. Therefore, ξ_r is only a weak function of α_{mis}.

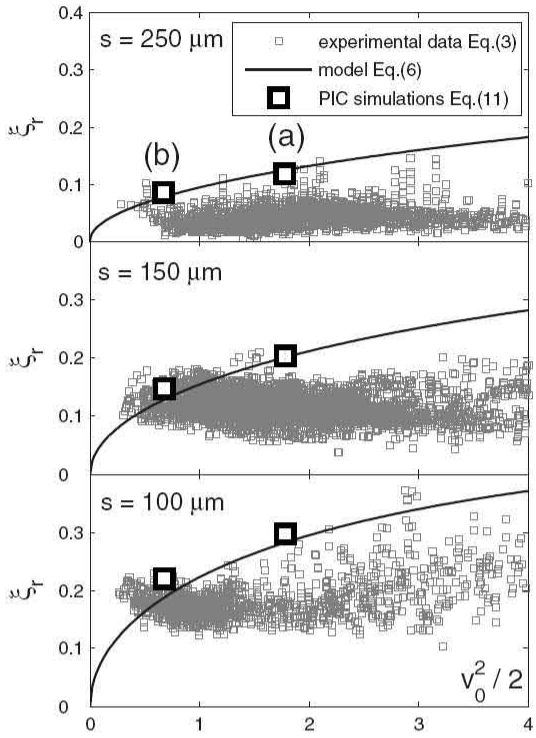

FIG. 12. Relative slit transmission factor ξ_r obtained from the experimental data, the model, and the SPICE simulations [represented by simulations (a) and (b), see Table I] for different slit plate thickness s. ξ_r is plotted as a function of the potential drop in front of the slit plate (including the natural sheath voltage and the applied bias) normalized to ion temperature, $v_0^2/2$.

D. The relative slit transmission factor

Figure 12 shows the relative slit transmission factor, ξ_r, calculated from the experimental data [Eq.(3)], theoretical model [Eq. (6)], and PIC simulations [Eq. (11)] for $w=30$ μm, $\alpha_{\text{mis}}=0$, and for three different slit thicknesses of 250, 150, and 100 μm. ξ_r is plotted as a function of $v_0^2/2$. Experimental values of $v_0^2/2$ have been calculated from measurements of V_s and T_i. PIC simulations and the model predict nearly the same ξ_r which is, however, up to a factor of 2 higher than the experimental data. Both the theory and the simulations predict the increase in ξ_r with $v_0^2/2$ whereas ξ_r^{exp} is nearly independent of $v_0^2/2$. The discrepancy might be caused by the fact that the measurement of $j_{+\text{sat}}$ and I_{col} can be influenced by (i) ion induced secondary electron emission from the plasma facing surface of the slit plate and by (ii) the attenuation of ion flux on the inner walls of the front and rear protective plates (Fig. 5, right bottom), respectively. The latter can be caused either by absorption of ions whose trajectories intersect the rear protective plate or by deflection of ions towards the inner walls of the front protective plate (similar effect has been studied by PIC simulations in Ref. 26). Both (i) and (ii) (neglected in our study) have the tendency to decrease ξ_r^{exp}.

V. INFLUENCE OF THE NEGATIVELY BIASED GRID ON T_i

As mentioned in Sec. II, the negatively biased grid 2 is used to repel the plasma electrons that enter the RFA cavity and to suppress the secondary electron currents. At the same time, grid 2 constitutes a final obstacle for ions before they reach the collector. In this section the influence of grid 2 on T_i measurements is analyzed.

In Ref. 7 it was suggested that the transmission factor of grid 2 could be modified by the deflection of ion trajectories passing close to the grid wires, which might increase the effective grid wire diameter

$$\Delta_{\text{eff}} = \Delta(1 + V_{\text{grid2}}/E_0)^{1/2}, \tag{12}$$

where E_0 is the initial ion energy infinitely far from the wire and Δ the grid wire diameter. Expression (12) is derived from single-particle orbital theory for a single cylindrical wire and $B=0$.[27] In the real situation, however, a grid is composed of a large number of equally spaced wires. The resulting electric field is nearly planar everywhere except very close to individual wires, i.e., the perpendicular component of the electric field which is responsible for ion deflection in Eq. (12) is very small. We show below that the grid transmission is very close to optical.

The effect of negative grid bias on ion trajectories was evaluated by means of two-dimensional Monte Carlo simulations. The simulation domain consists of a rectangular box containing a single wire positioned in the centre. The width of the system equals the distance between the grid wires D. The boundary conditions are periodic. The electric field inside the system corresponds to the vacuum electric field due to an infinitely long array of the wires of diameter $\Delta=63$ μm, biased to $V_{\text{grid 2}}$. The injection plane is positioned 0.4 mm in front of the wire to ensure practically planar electric field there. Since the local ion density close to grid wires is $<10^{15}$ m^{-3}, the influence of ion space charge on the vacuum potential is neglected (following e.g., Ref. 18, it can be shown that for such densities the contribution of the space charge to vacuum potential is ~ 1 V). In each simulation the orbits of 10^5 deuterons are calculated. The parallel ion energy at injection $E_{\|i}$ is fixed. The perpendicular ion energy $E_{\perp i}$ is chosen randomly from a Maxwellian distribution. The initial position of ions along the injection plane is random. The time step is kept below 1/20 of the ion transit time through the distance Δ. In order to allow the variation of the time step during the integration process, the ions are advanced by the midpoint Runge–Kutta method.[28] Those ions whose trajectories intersect the wire are absorbed. Those reaching the upper boundary of the system positioned behind the wire are considered to be transmitted. Assuming that the electric field in the grid wire corners does not influence the transmission, the effect of four grid wires can be combined to produce the total grid transmission factor $\xi_{\text{grid 2}}(E_{\|i}, E_{\perp i}, V_{\text{grid 2}}) = (N_{\text{trans}}/N_{\text{inj}})^2$. N_{trans} and N_{inj} are the total number of the transmitted and injected ions, respectively.

The simulations were reproduced for different combinations of $E_{\|i}=1\rightarrow 10^3$ eV, $E_{\perp i}=1\rightarrow 10^3$ eV, and $V_{\text{grid 2}}=0\rightarrow -10^3$ V. Figure 13 illustrates $\xi_{\text{grid 2}}$ calculated for fixed value

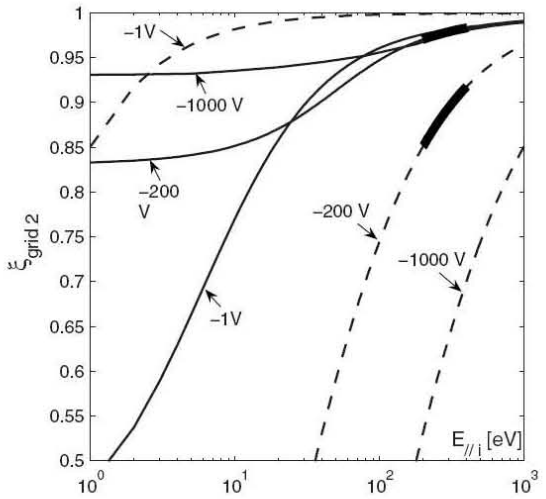

FIG. 13. Transmission factor of the negatively biased grid 2, $\xi_{\text{grid 2}}$, calculated for fixed perpendicular ion energy $E_{\perp i}$=50 eV and three different values of the grid bias voltage $V_{\text{grid 2}}$=−1, −200, and −1000 V. $\xi_{\text{grid 2}}$ is normalized to the optical transmission factor of the grid ξ_{opt} and plotted as a function of the parallel ion energy $E_{\|i}$. Results from Monte Carlo simulations (full curves) are compared to the ones calculated from the single-particle orbital theory (dashed curves), Eq. (12). For $V_{\text{grid 2}}$=−200 V, a range of the typical parallel ion energies at the distance D=0.4 mm in front of the grid 2 is highlighted by thicker lines.

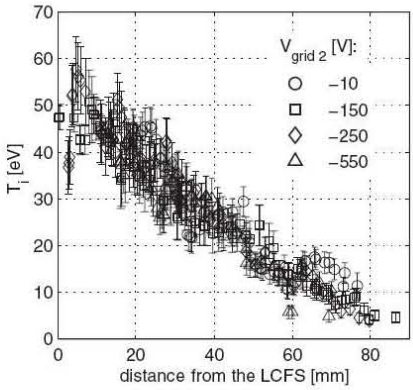

FIG. 14. SOL ion temperature profiles measured by the Tore Supra RFA in similar ohmic discharges. Bias voltage applied on grid 2 $V_{\text{grid 2}}$ was varied between the shots. Other parameters were constant (I_p=0.6 MA, $\bar{n}_e$=1.4 $\times 10^{19}$ m^{-3}).

of $E_{\perp i}$=50 eV and for three different values of $V_{\text{grid 2}}$=−1, −200, and −1000 V. $\xi_{\text{grid 2}}$ is normalized to ξ_{opt}. $\xi_{\text{grid 2}}$ increases with $E_{\|i}$ and tends to ξ_{opt} for stronger grid bias. This is because the field in front of the grid is basically planar and the ions gain large parallel energy before coming into the zone of influence of the wire. For single-particle orbital theory the tendency is opposite. Realistic parallel ion energies 0.4 mm in front of the grid 2 for $V_{\text{grid 1}}$=0 V and $V_{\text{grid 2}}$=−200 V, $E_{\|i}=T_i+e|V_s|+160$ eV, are plotted by a thick line in Fig. 13. Within this range, $\xi_{\text{grid 2}} \cong \xi_{\text{opt}}$. For comparison, the grid transmission factors derived from the single-particle orbital theory, Eq. (12), are also shown. The fact that for realistic parallel ion energies $\xi_{\text{grid 2}} \cong \xi_{\text{opt}}$ independently of $V_{\text{grid 2}}$ can be easily understood since the typical ion Larmor radius is comparable to the grid wire separation D, the approximate condition for $\xi_{\text{grid 2}} \cong \xi_{\text{opt}}$ is given by $\Delta/v_{\|} < D/(r_L \omega_L)$, where ω_L is the ion Larmor frequency. Due to acceleration of ions in the sheath and in front of grid 2, $E_{\|i}$ at the grid is larger than $E_{\perp i}$ ($E_{\|i} \cong E_{\perp i}+3T_e-eV_{\text{grid 2}}$), so that $\Delta/v_{\|} < D/(r_L \omega_L)$ for any $V_{\text{grid 2}} < 0$.

The influence of the grid transmission on ion temperature was quantified using the procedure similar to the one described in Sec. IV A; $f(v_{\|})$ at the sheath edge in front of the probe were calculated from Ref. 17 for various values of τ. To account for the potential drop between the sheath edge and grid 2, the distributions were shifted in the parallel direction by $e|V_s+V_{\text{grid 2}}|$. Consequently, the distributions were transformed by the following operation: $f(E_{\|i}) = f(E_{\|i}) \cdot \xi_{\text{grid 2}}(E_{\|i})$, with $\xi_{\text{grid 2}}(E_{\|i})$ calculated for $E_{\perp i}$ =50 eV and $V_{\text{grid 2}}$=−200 V. Finally, I-V characteristics were constructed from the parallel velocity distribution functions, and fit by Eq. (9). From these results it follows that the negatively biased grid accounts for an increase in T_i of less than 1% (for single-particle orbital theory, T_i increases 2%–4%). Since for typical parallel ion energies $\xi_{\text{grid 2}}$ is independent on $V_{\text{grid 2}}$, the same result is obtained for $V_{\text{grid 2}}$=0→−1000 V. These results are substantiated by RFA measurements in Tore Supra, performed on a shot-to-shot basis in similar Ohmic plasmas. Between the shots, $V_{\text{grid 2}}$ was varied in a range of −10→−600 V. Other parameters were kept constant (I_p=0.6 MA, $\bar{n}_e=1.4\times10^{19}$ m^{-3}). As an example, radial profiles of T_i measured for $V_{\text{grid 2}}$=−10, −150, −250, and −550 V are shown in Fig. 14; despite the variation of $V_{\text{grid 2}}$, T_i is constant within the error bars. It is worth noticing that for $V_{\text{grid 2}}$=−10 V the secondary electrons in the RFA are not fully repelled. However, the secondary electron current from the collector is merely an offset on I_{col} and the one from the rear of the slit plate is reduced by the transmission of electrons through the grids.

VI. SUMMARY AND CONCLUSIONS

The RFA is one of the only applied diagnostics for measurements of SOL T_i. The probe measures the effective parallel ion temperature, from which the information about that in ambient plasma can be derived.[19] However, this is true only if instrumental effects do not affect the measurements.

In this paper, selective ion transmission through the RFA slit plate and its influence on T_i measurements was analyzed by an analytical model and by two-dimensional PIC simulations. Contrary to the former, the latter method included the self-consistent electrostatic field. Both methods gave very similar results, indicating that the electric field just inside the slit does not play an important role with regards to the selective ion transmission, even for slit width up to $w \cong 4\lambda_D$.

For given slit dimensions, the slit transmission factor increases with parallel ion velocity so that the slowest ions in the distribution are preferentially removed. The selective ion transmission is proportional to ion-to-electron temperature ratio τ and the slit thickness s. For relatively thick slit plate (s=300 μm), however, selective ion transmission accounts

for an overestimation of T_i by less than 14%. Thick slit plates (i.e., $s/w > 1$) can therefore be used to advantage since they reduce, e.g., the risk of melting during off-normal events, the neutral gas pressure inside the RFA cavity that can lead to electrical breakdown, and the positive space charge. The influence of the slit plate misalignment with respect to **B** on T_i measurements was proved to be negligible, at least for $\alpha_{\text{mis}} < 10°$ which is well above the maximum expected value ($\sim 3°$).

The influence of the negatively biased electron repelling grid on T_i measurements was analyzed by Monte Carlo simulations. It was shown that the ions are transmitted optically, independently of the bias voltage on the grid. The increase in T_i due to grid transmission is less than 1%.

ACKNOWLEDGMENTS

This work was partly supported by the Grant Agency of the Academy of Sciences of the Czech Republic Grant No. GAAV KJB100430602.

[1] P. Staib, J. Nucl. Mater. **93**, 351 (1980).
[2] I. Katsumata, Contrib. Plasma Phys. **36S**, 73 (1996).
[3] S. V. Ratynskaia, V. I. Demidov, and K. Rypdal, Rev. Sci. Instrum. **73**, 4232 (2002).
[4] N. Ezumi, J. Nucl. Mater. **313**, 696 (2003).
[5] D. G. Chavers and F. R. Chang-Díaz, Rev. Sci. Instrum. **73**, 3500 (2002).
[6] M. Kočan, R. Pánek, J. Stöckel, M. Hron, J. P. Gunn, and R. Dejarnac, J. Nucl. Mater. **363–365**, 1436 (2007).
[7] R. A. Pitts, R. Chavan, S. J. Davies, S. K. Erents, G. Kaveney, G. F. Matthews, G. Neill, J. E. Vince, and I. Duran, Rev. Sci. Instrum. **74**, 4644 (2003).
[8] G. F. Matthews, J. Phys. D **17**, 2243 (1984).
[9] A. S. Wan, T. F. Yang, B. Lipschultz, and B. LaBombard, Rev. Sci. Instrum. **57**, 1542 (1986).
[10] R. A. Pitts, Phys. Fluids B **3**, 2871 (1991).
[11] R. A. Pitts, Ph.D. thesis, University of London, 1991.
[12] R. A. Pitts, Contrib. Plasma Phys. **36**, 87 (1996).
[13] H. Y. Guo, G. F. Matthews, S. J. Davies, S. K. Erents, L. D. Horton, R. D. Mond, and P. C. Stangeby, Contrib. Plasma Phys. **36**, 18 (1996).
[14] G. F. Matthews, R. A. Pitts, G. M. McCracken, and P. C. Stangeby, Nucl. Fusion **31**, 1495 (1991).
[15] S. Stephanakis and W. H. Bennett, Rev. Sci. Instrum. **39**, 1714 (1968).
[16] R. L. Stenzel, R. Williams, R. Agüero, K. Kitazaki, A. Ling, T. McDonald, and J. Spitzer, Rev. Sci. Instrum. **53**, 1027 (1982).
[17] K.-S. Chung and I. H. Hutchinson, Phys. Rev. A **38**, 4721 (1988).
[18] R. Nachtrieb, Ph.D. thesis, Massachusetts Institute of Technology, 2000.
[19] F. Valsaque, G. Manfredi, J. P. Gunn, and E. Gauthier, Phys. Plasmas **9**, 1806 (2002).
[20] R. A. Pitts, I. Ďuran, S. K. Erents, J. Horáček, G. F. Matthews, and the JET-EFDA contributors, 30th EPS Conference on Contr. Fusion and Plasma Phys., St. Petersburg, 7–11 July 2003 (unpublished), ECA, Vol. 27A, P-2.84.
[21] J. Jacquinot and G. T. Hoang, Plasma Sources Sci. Technol. **6**, 2101 (2004).
[22] J. Wesson, *Tokamaks*, 2nd ed. (Oxford University Press, Oxford, 1997).
[23] G. F. Matthews, Ph.D. thesis, University of Oxford, 1985.
[24] R. Dejarnac and J. P. Gunn, J. Nucl. Mater. **363–365**, 560 (2007).
[25] C. K. Birdsall and A. B. Langdon, *Plasma Physics via Computer Simulation* (McGraw-Hill, New York, 1985).
[26] R. Pánek, R. A. Pitts, J. P. Gunn, and S. K. Erents, Czech. J. Phys. **54**, 150 (2004).
[27] H. M. Mott-Smith and I. Langmuir, Phys. Rev. **28**, 727 (1926).
[28] W. H. Press, S. A. Teukolsky, W. T. Vetterling, and B. P. Flannery, *Numerical Recipes in Fortran 77* (Cambridge University Press, Cambridge, 1992), Chap. 16.

Chapter 3

Experimental results

In this chapter, selected experimental results are presented in the form of papers published (or submitted for publication) during the thesis. The main diagnostic in all experiments is the RFA.

In order to motivate the reader for this chapter we refer to section 1.4.1, in which the importance of SOL T_i measurements, the experimental results related to SOL T_i reported from different tokamaks, and some ideas for further work were discussed.

In the first two papers [Kočan 2008, Kočan 2008b] measurements of both T_i and T_e in an ohmic helium density scan in the Tore Supra SOL are reported. It is shown that the usual assumption of equal SOL temperatures due to equipartition is not satisfied in the Tore Supra SOL, confirming the results obtained in other tokamaks, but demonstrated on a smaller dataset (see references in section 1.4.1). The link between T_i and T_e measured in the SOL and the temperatures measured inside the LCFS by charge exchange recombination spectroscopy, Thomson scattering, and electron cyclotron emission diagnostics, is discussed. The first continuous T_i / T_e profile from the edge of the confined plasma into the SOL is constructed using data from several tokamaks. It is shown that T_i / T_e increases with radius, with $T_i / T_e > 1$ already in the edge of the confined plasma.

In the third paper [Kočan 2009b] a previously unobserved strong increase of SOL T_i with the intensity of the toroidal magnetic field B_t is reported. The only other parameter which is found to be also correlated with the B_t is the core electron

temperature (core ion temperature is not available for the discharges analyzed in this paper). SOL T_e is found to be practically decoupled from core electron temperature.

The fourth paper [Kočan 2009c] is aimed at the study of the dependence of SOL parameters (such as T_i, T_e, j_{sat} and n_e) on the plasma density and the radiated power fraction, including detached plasmas. SOL ion temperature is measured for the first time in a detached plasma. The influence of the radiated power fraction on SOL T_i and T_e measured experimentally is compared with the results obtained from a simple power balance model.

Finally, in the last paper [Kočan 2009], the first evidence of a poloidal asymmetry of the radial ion and electron energy transport is reported. Implications for ITER start-up phase are discussed. Correlation of the asymmetries of SOL T_i and T_e measured on each side of the RFA with changes of the parallel Mach number $M_{//}$, important for validating kinetic Mach probe theory, are briefly addressed.

Edge ion-to-electron temperature ratio in the Tore Supra tokamak

M Kočan[1], J P Gunn[1], J-Y Pascal[1], G Bonhomme[2], C Fenzi[1], E Gauthier[1] and J-L Segui[1]

[1] CEA, IRFM, F-13108 Saint-Paul-lez-Durance, France
[2] Nancy-Université, BP 239, 54506 Vandœuvre-lès-Nancy Cedex, France

E-mail: martin.kocan@cea.fr

Received 29 July 2008, in final form 2 October 2008
Published 6 November 2008
Online at stacks.iop.org/PPCF/50/125009

Abstract

Both ion and electron temperatures in the scrape-off layer (SOL) of the Tore Supra tokamak were measured by a retarding field analyzer during an ohmic density scan. SOL T_i was found to be higher than T_e by a factor of 4–7. The ion-to-electron temperature ratio τ decreases with increasing density. Core T_i and T_e measurements in Tore Supra combined with a multi-machine database of τ measurements show that $\tau > 1$ also in the edge of the confined plasma and increases with radius.

(Some figures in this article are in colour only in the electronic version)

1. Introduction

The ion temperature T_i in the tokamak scrape-off layer (SOL) is of key importance for modelling plasma–surface interaction processes such as physical sputtering, reflection and impurity release [1] and estimation of the amount of the heat flux deposited on the divertor tiles and main chamber walls. These are critical parameters for designing tokamak plasma facing components.

While the SOL electron temperature T_e is easily accessible by simple Langmuir probes, T_i can be measured only by complex particle analyzers or, indirectly, by, for example, charge-exchange recombination spectroscopy (CXRS) or from the post-mortem analysis of ion deposition profiles on collector probes. Measurements of T_i were obtained in tokamaks such as Alcator C-mod [2], ASDEX Upgrade [3, 4], CASTOR [5], DITE [6–11], JET [12, 13], JFT-2M [14], JT-60U [15], TEXTOR [16–18], TFR 600 [19] and recently in Tore Supra [20] showing that $T_i > T_e$ in the SOL but also in the edge of the confined region. This is in contrast to what is often assumed in models ($T_i = T_e$). For example, in order to be consistent with this assumption, experimentally measured edge temperature profiles in [21] were arbitrarily shifted radially to make the two temperatures agree.

0741-3335/08/125009+10$30.00

Both SOL T_i and T_e were measured by a retarding field analyzer (RFA) during an ohmic density scan in the Tore Supra tokamak [22]. We show that the assumption of equal SOL temperatures due to equipartition is not justified in Tore Supra, confirming results of a similar study performed in the DITE [9, 10]. T_i and T_e measured in the SOL are compared with the ones measured inside the last closed flux surface (LCFS) by CXRS, Thomson scattering (TS) and electron cyclotron emission (ECE) diagnostics. In addition, our results are compared with a multi-machine database of the measurements of the ion-to-electron temperature ratio. To our knowledge this is the first time that a global study using data from several machines has attempted to construct a continuous T_i/T_e profile from the edge into the SOL.

The paper is organized as follows. The experiment is described in section 2. The operational principle of the RFA is addressed in section 3. Experimental results are shown and discussed in section 4. Conclusions are given in section 5.

2. Experimental set up

Tore Supra is a large tokamak with a plasma of circular cross-section whose LCFS is defined by its intersection with the bottom toroidal pump limiter.

SOL T_i and T_e were measured by a RFA ([23] and references therein). For comparison, T_e was measured simultaneously by a tunnel probe (TP) [24]. RFA and TP were separated toroidally by 120°. Both probes were mounted on a fast reciprocating drive located in top ports at a poloidal angle $\theta = 79°$ with respect to the outer midplane. The fast reciprocating drive allows several insertions of the probe during a single discharge (up to 15 until now) up to 3 cm inside the LCFS.

The discharges were characterized by plasma current $I_p = 0.5$ MA and toroidal magnetic field $B_t = 3.8$ T. Major and minor radii were $R = 2.38$ m and $a = 0.72$ m, respectively, giving a safety factor at the LCFS $q_a = 10$. The central line-averaged density $\bar{n}_e \cong 0.7 \rightarrow 4.2 \times 10^{19}\,\mathrm{m}^{-3}$ (corresponding to a Greenwald density fraction $\bar{n}_e/\bar{n}_e^{GW} = 0.23 \rightarrow 1.37$, where $\bar{n}_e^{GW} = I_p/(\pi a^2)$ [$10^{20}\,\mathrm{m}^{-3}$, MA, m]) was varied on shot-to-shot basis. Feedback control on gas puffing was used to keep the density constant during probe reciprocation. A database consisting of 90 reciprocations (corresponding to 14 discharges performed in a single experimental session) was assembled. Helium was used as the working gas, since it provides a higher density limit than deuterium. All discharges were ohmically heated.

3. Tore Supra RFA

The design of the Tore Supra RFA is based on the one that was originally used in JET [12]. Technical details of the probe were addressed in [23]. The probe is used to measure T_i, T_e, the sheath potential V_s, the parallel ion saturation current density j_{+sat} and the floating potential V_f. T_e, j_{+sat} and V_f are measured by the slit plate working as a Langmuir probe (see [23]). Measurements of T_i and V_s and T_e, j_{+sat} and V_f are separated by ~0.5 ms. The database from six experimental campaigns consists of more than 3000 probe reciprocations in discharges with ohmic or RF heating up to 8 MW.

The schematic of the analyzer and the biasing scheme are shown in figure 1. The operational principle of T_i measurements by the RFA can be briefly summarized as follows.

The probe head is aligned with the magnetic field. A fraction of the incident ion flux is transmitted through the slit. The slit plate is biased negatively to repel most of the thermal electrons. The transmitted ions are retarded in the electric field created by a swept positive voltage applied to grid 1, $V_{grid\ 1}$. A constant negative bias is applied on grid 2, $V_{grid\ 2}$, to repel the

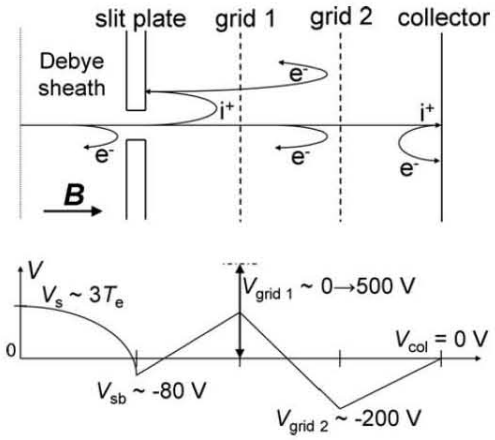

Figure 1. Main components of the RFA and the biasing scheme applied for ion temperature measurements.

remaining fast electrons from the tail of the distribution and to suppress the secondary electrons emitted from the collector or from the rear of the slit plate due to ion impact. $V_{\text{grid 2}}$ is the lowest voltage in the system. The collector measures the ion current, I_{col}. Figure 2 shows a typical current–voltage (I–V) characteristic. For a certain range of $V_{\text{grid 1}} = 0 \rightarrow |V_s|$ the collector current remains at I_0; all ions gain a parallel energy of $eZ_i|V_s|$ (with eZ_i being the ion charge) in the collisionless Debye sheath. For $V_{\text{grid 1}} > |V_s|$ the current to the collector starts to decrease. Assuming that fuel ions of charge eZ_i dominate the incident flux, I_0 can be expressed as (e.g. [12])

$$I_{\text{col}} = A_{\text{slit}} eZ_i \int_u^\infty \mathrm{d}v_\parallel v_\parallel \xi(v_\parallel) f(v_\parallel), \tag{1}$$

where A_{slit} is the slit area, $\xi(v_\parallel)$ is the total transmission factor that includes the transmission of the slit and the grids, $u = \sqrt{2eZ_i V_{\text{grid 1}}/m_i}$ (with m_i being the ion mass) and $f(v_\parallel)$ is the parallel ion velocity distribution. Assuming, in addition, that $f(v_\parallel)$ is Maxwellian, T_i can be obtained by the RFA from a fit to the decaying part of the I–V characteristics, figure 2:

$$I_{\text{col}} = I_0 \exp\left[-\frac{Z_i}{T_i}(V_{\text{grid 1}} - |V_s|)\right]. \tag{2}$$

T_i was calculated assuming that the SOL plasma is dominated by He^{2+} ions, i.e. $Z_i = 2$. Ions with different charge-to-mass ratios affect T_i inferred from RFA [9, 10] (but also from any other probe). These can be either singly charged helium ions He^+ (overestimating T_i) or impurities (mainly carbon and oxygen in Tore Supra) which have a tendency to underestimate T_i. At high densities, for which SOL $T_e < 10$ eV, the relative abundance of He^+ can exceed that of He^{2+} [9]. The effect of impurities is expected to play an important role at lowest $\bar{n}_e$ where their concentration relative to He^{2+} is highest. Separation of the components of the ion flux to the analyzer by charge state and temperature has been proposed in [10]. However, the model needs to specify the fractions of the total flux carried by ions with a given charge state as well as their temperatures. Such measurements are not available. Indeed, it is reasonable to expect some underestimation (overestimation) of T_i at lowest (highest) $\bar{n}_e$.

Instrumental effects which account for overestimation of T_i by 4–12% [23] were taken into account in the analysis.

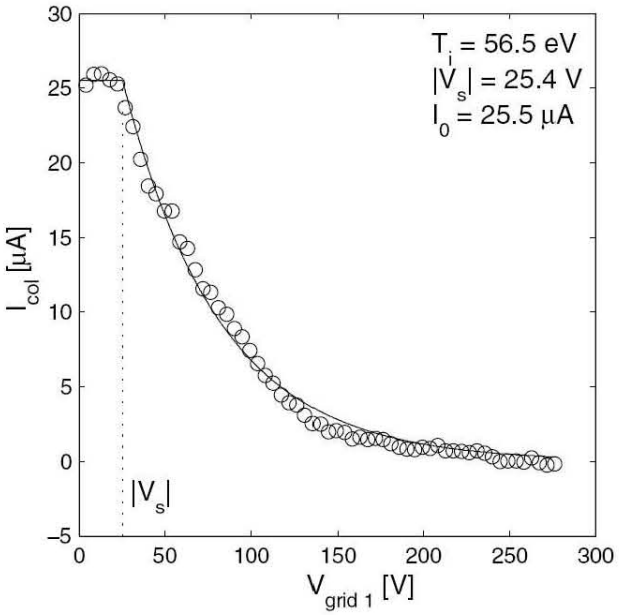

Figure 2. Typical RFA I–V characteristic measured 2.8 cm outside the LCFS (Tore Supra discharge #35880 at $t = 3.7$ s). Current to the collector, $I_{\rm col}$, is plotted against the bias voltage of grid 1, $V_{\rm grid\ 1}$. For $V_{\rm grid\ 1} < |V_{\rm s}|$, $I_{\rm col}$ remains constant, since all ions are shifted towards higher energies due to the Debye sheath potential drop in front of the slit plate, $V_{\rm s}$. A fit to the decaying part of the characteristic gives the ion temperature $T_{\rm i}$.

4. Experimental results

4.1. Scaling of SOL temperatures with the plasma density

Figure 3 shows SOL $T_{\rm i}$ and $T_{\rm e}$ as well as their ratio $\tau = T_{\rm i}/T_{\rm e}$ measured by the RFA, plotted as a function of $\bar{n}_{\rm e}$. For better statistics, measurements are averaged over a window of 1 cm, localized between 2 and 3 cm outside the LCFS. TP values of $T_{\rm e}$ are in good agreement with those measured by RFA.

$T_{\rm i}$ decreases by a factor ∼3 with the increase in $\bar{n}_{\rm e} = 1 \rightarrow 4.2 \times 10^{19}\,{\rm m}^{-3}$. Within the same range of $\bar{n}_{\rm e}$, $T_{\rm e}$ decreases by a factor of ∼2. The decrease in temperatures with density can be due to the fact that $\bar{n}_{\rm e}$ increases approximately two times faster than the total plasma energy content $E_{\rm dia} \propto nT$ obtained from diamagnetic measurements (figure 4(*a*)). For $\bar{n}_{\rm e} = 0.7 \rightarrow 1.2 \times 10^{19}\,{\rm m}^{-3}$ the ion-to-electron temperature ratio increases ($\tau = 4 \rightarrow 7$). For $\bar{n}_{\rm e} = 1 \rightarrow 2.8 \times 10^{19}\,{\rm m}^{-3}$, $\tau = 7 \rightarrow 4$. For $\bar{n}_{\rm e} > 2.8 \times 10^{19}\,{\rm m}^{-3}$, $\tau \cong 4$. In order to verify the reproducibility of $T_{\rm i}$ and $T_{\rm e}$ measurements, $\bar{n}_{\rm e}$ was steadily decreased during the experiment ($\bar{n}_{\rm e} \cong 3.8 \rightarrow 0.7 \times 10^{19}\,{\rm m}^{-3}$, light symbols in figure 3(*a*)) and last discharges were reproduced at high densities ($\bar{n}_{\rm e} = 3.2 \rightarrow 4.2 \times 10^{19}\,{\rm m}^{-3}$, heavy symbols). The temperatures measured in the initial and in the final phase of experiment are very similar. It is worth noting that $T_{\rm i}$ in helium plasma is up to a factor of 2 higher compared with $T_{\rm i}$ measured in deuterium plasma at similar conditions [20]. A similar result was obtained in the DITE tokamak and was attributed to the difference in the rate by which the ions lose their energy by charge-exchange collisions with neutrals in edge plasma [10] (in deuterium the reaction cross section can be up to an order of magnitude higher compared with helium). The electron temperature measured in

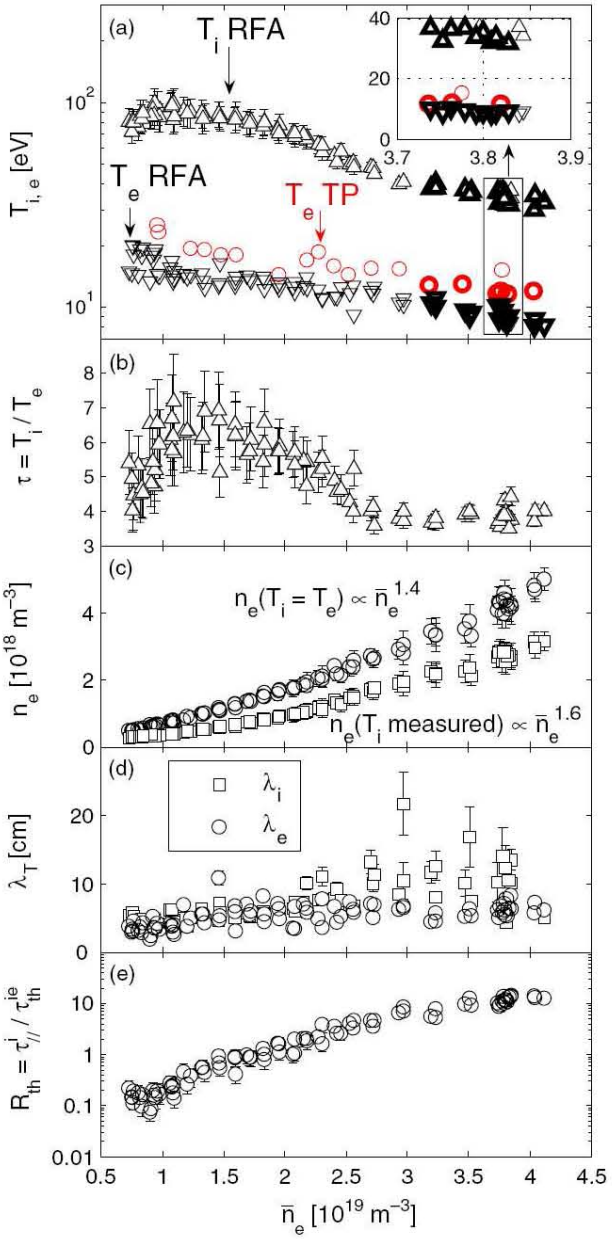

Figure 3. (*a*) SOL T_i measured 2–3 cm outside the LCFS by RFA. SOL T_e measured by RFA and TP. Light symbols: high-to-low density scan. Heavy symbols: measurements of T_i and T_e reproduced at high density. (*b*) Ion-to-electron temperature ratio τ. (*c*) SOL electron density calculated from RFA measurements of T_i, T_e and $j_{+\mathrm{sat}}$. n_e calculated for $T_\mathrm{i} = T_\mathrm{e}$ is also plotted for comparison. (*d*) Ion and electron e-folding lengths evaluated 1–5 cm outside the LCFS. (*e*) Ratio of the ion parallel SOL transit time to the ion–electron thermalization time R_th evaluated at the LCFS. Data are plotted against the central line-averaged density $\bar{n}_\mathrm{e}$.

helium was found to be higher by up to 25% compared with those measured in deuterium [20]. The statistical error on T_i increases monotonically with the decrease in $\bar{n}_\mathrm{e}$, up to ~20% at lowest densities, which can be due to the fact that the RFA signal level (I_col) is proportional to density.

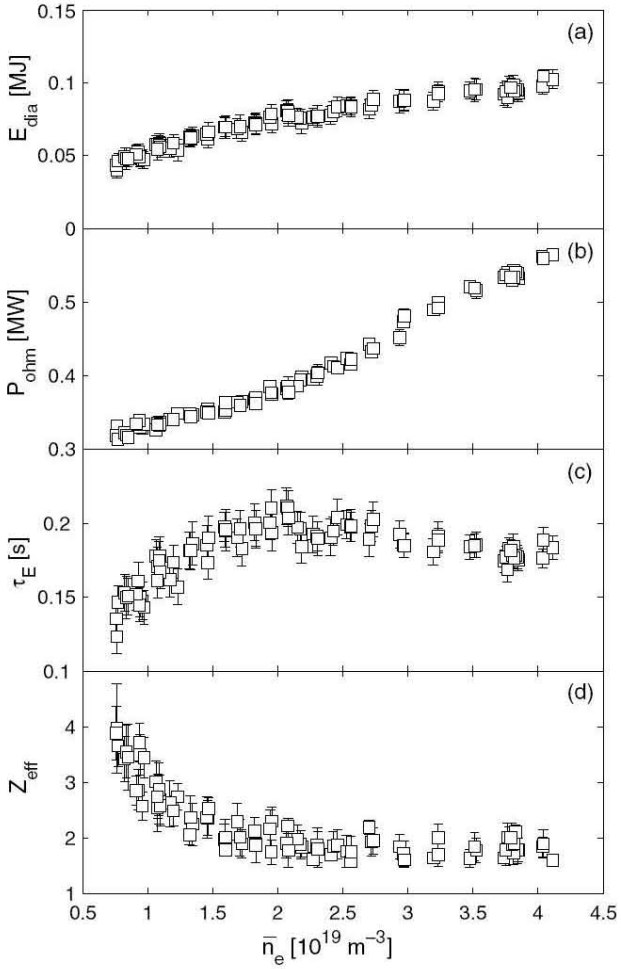

Figure 4. Plasma parameters during the RFA reciprocations. From top to bottom: total plasma energy obtained from diamagnetic measurements E_{dia}, the ohmic power P_{ohm}, the energy confinement time $\tau_E = E_{dia}/(P_{ohm} - \partial E_{dia}/\partial t)$ and the central line-averaged effective ion charge Z_{eff}. The data are plotted against the central line-averaged density $\bar{n}_e$.

The electron density calculated from RFA measurements of T_i, T_e and j_{+sat}, $n_e = j_{sat}/[0.35e^{1.5}\sqrt{(T_i + T_e)/m_i}]$ [25], is plotted in figure 3(*c*). n_e is evaluated over a window of 1 cm, localized between 2 and 3 cm outside the LCFS. Also plotted in figure 3(*c*) is the electron density calculated assuming $T_i = T_e$. The latter is nearly two times higher than the former.

Figure 3(*d*) shows the ion (λ_i) and electron (λ_e) temperature *e*-folding lengths evaluated from the data measured 1–5 cm outside the LCFS. Both λ_i and λ_e increase with density. At low densities ($\bar{n}_e < 2 \times 10^{19}$ m^{-3}) the *e*-folding lengths are comparable ($\lambda_i/\lambda_e = 1.1 \pm 0.6$). At higher densities the ion temperature *e*-folding length is longer ($\lambda_i/\lambda_e = 1.5 \pm 0.8$). The difference in the *e*-folding lengths could be explained by the difference in the parallel losses of ions and electrons on open field lines, given by the difference in the ion and electron heat transmission coefficient, $\gamma_e/\gamma_i \propto 1/\tau_t$ [26], where τ_t is the ion-to-electron temperature ratio at the target. Assuming that τ_t behaves with the density in a similar way as τ, the parallel electron losses relative to the ion losses are expected to be highest at high densities, so that $\lambda_i > \lambda_e$.

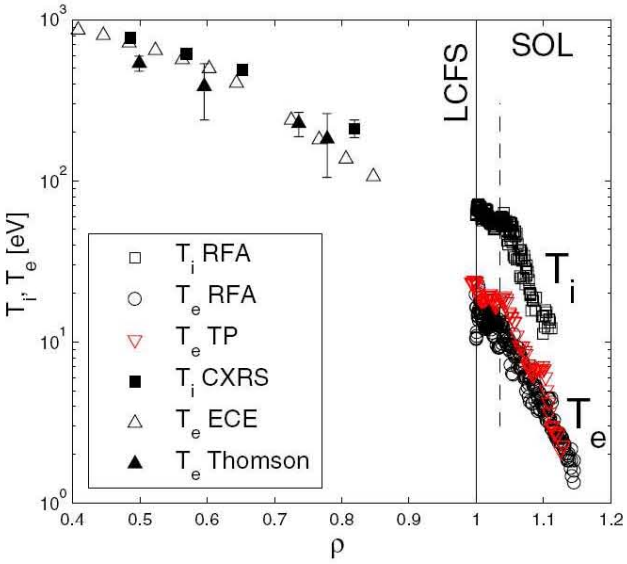

Figure 5. Ion and electron temperature profiles measured during a steady-state phase of a single discharge characterized by $\bar{n}_e = 2.5 \times 10^{19}\,\mathrm{m}^{-3}$. Temperatures are plotted against the distance from the plasma centre normalized to minor radius, $\rho = r/a$. Inside the LCFS the temperatures are measured by ECE and TS diagnostics (T_e) and by CXRS (T_i). In the SOL the temperatures are measured by RFA (T_i and T_e) and by TP (T_e). The dashed line indicates the position of the outboard modular limiter.

Thermal coupling of SOL ions and electrons was estimated from the ratio of the ion parallel SOL transit time to the ion–electron thermalization time, $R_{th} = \tau_\parallel^i/\tau_{th}^{ie}$, where $\tau_\parallel^i \propto L_\parallel/\sqrt{T_i + T_e}$ and $\tau_{th}^{ie} \propto T_e^{3/2}/n_e$. Here $L_\parallel \approx q_a \pi R \approx 75\,\mathrm{m}$ is the parallel connection length and n_e is the electron density. $R_{th} < 1$ implies thermally decoupled ions and electrons. $R_{th} \gg 1$ implies strong thermal coupling at which the ion and electron temperatures are expected to converge. R_{th} was evaluated at the LCFS radius from extrapolated RFA data. Figure 3(*e*) shows R_{th} plotted against $\bar{n}_e$. R_{th} varies from 0.1 up to 15 at highest densities. For $R_{th} > 1$, τ decreases with the increase in R_{th}. For $R_{th} > 5$, τ remains at a constant value of 4, i.e. far from full thermalization. The saturation of τ at highest densities could be explained by the overestimation of T_i (by up to a factor of 2) due to an increase in He^+/He^{2+} with $\bar{n}_e$ (section 3). This could partially explain why $\tau \cong 4$ at the highest densities at which both temperatures are expected to converge due to strong thermal coupling. In addition, the filtering effect of the sheath which tends to remove the fastest electrons from the distribution thus reducing effective SOL T_e may strengthen the tendency for $\tau > 1$ even at highest densities.

4.2. Radial profiles of T_i, T_e and τ

Figure 5 shows the radial profiles of T_i and T_e measured inside the LCFS and in the SOL during one of the discharges described in section 2 ($\bar{n}_e = 2.5 \times 10^{19}\,\mathrm{m}^{-3}$). The electron temperature inside the LCFS was measured by ECE and TS diagnostics. The ion temperature inside the LCFS was obtained from CXRS. SOL temperatures were measured by RFA and TP. The locations of individual measurements are shown in figure 6. For better statistics, the data from three RFA reciprocations during a steady-state phase of the discharge are superimposed in figure 5. The temperatures are plotted against the distance from the plasma centre normalized

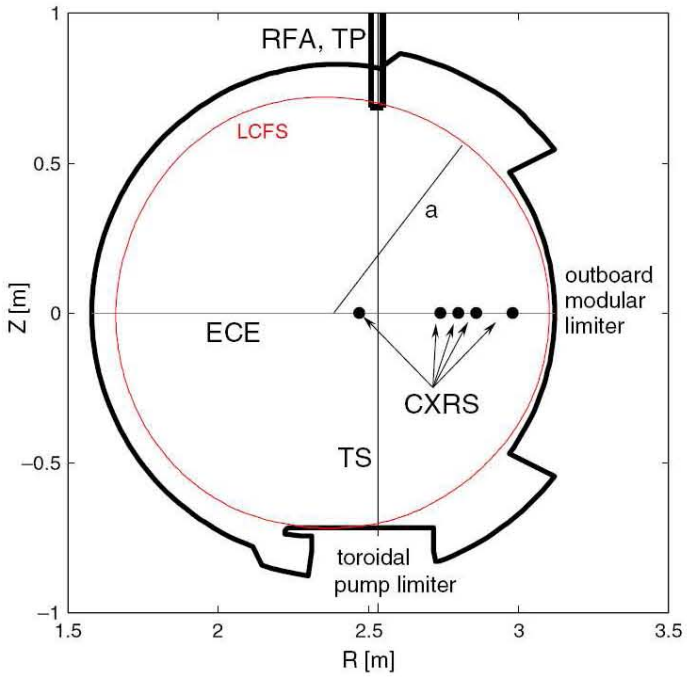

Figure 6. Poloidal cross-section of Tore Supra plasma and the location of individual temperature measurements shown in figure 5. The LCFS is defined by the intersection of plasma with the toroidal pump limiter.

to the minor radius $\rho = r/a$. At $\rho = 0.6$ $\tau \cong 1$. At $\rho = 0.82$ $\tau \cong 2$. At the LCFS $\tau \cong 4$. No temperature measurements are available in the region $0.82 < \rho < 1$. It must be noted that T_i was measured by CXRS during the injection of the neutral beam (required for CXRS operation, but not aimed at heating the plasma in Tore Supra) with the power of 0.4 MW in addition to the ohmic power (figure 4(*b*)), whereas all other measurements plotted in figure 5 comes from the ohmic phase of the discharge. For a given discharge the increase in electron temperature during the beam injection in the region of the dominant neutral beam power deposition (i.e. $0.7 < \rho < 0.8$) is about 30 eV compared with T_e measured during the ohmic phase. Therefore, it is reasonable to expect at least the same increase for T_i.

Figure 7 compiles the measurements of the ion-to-electron temperature ratio in ohmic (light symbols) and additionally heated L-mode plasmas (heavy symbols) from different tokamaks. The figure combines measurements in limiter as well as in divertor configuration for a wide range of main plasma parameters. τ is taken from [3, 4, 7, 9–11, 13–15, 17, 18, 20] and plotted against ρ. The ion temperature was measured either by probes [7, 9–11, 13, 14, 20] or by CXRS [3, 4, 15, 17, 18]. Due to ambiguous definition of the probe position with respect to the LCFS, the measurements of τ reported, for example, in [2] ($\tau = 1.7 \rightarrow 7$ in the SOL, Alcator C-mod), [5] ($\tau = 1 \rightarrow 2.7$ in the SOL, CASTOR), [12] ($\tau = 1.5 \rightarrow 3$ in the SOL, JET) and [16] ($\tau = 8.7$ in the shadow of the limiter, TEXTOR) are not included in figure 7. The results from our study are shown to be consistent with the multi-machine database. As seen from figure 7, τ increases with radius. The ohmic and additionally heated discharges produce similar values of τ. $\tau = 0.8 \rightarrow 2.5$ in the region $0.8 < \rho < 1$ (referred to as 'edge'). In the SOL τ is always greater than unity ($\tau = 1.5 \rightarrow 10$). The spread of the data points is relatively large (especially in the SOL) and can be caused by the variation of the

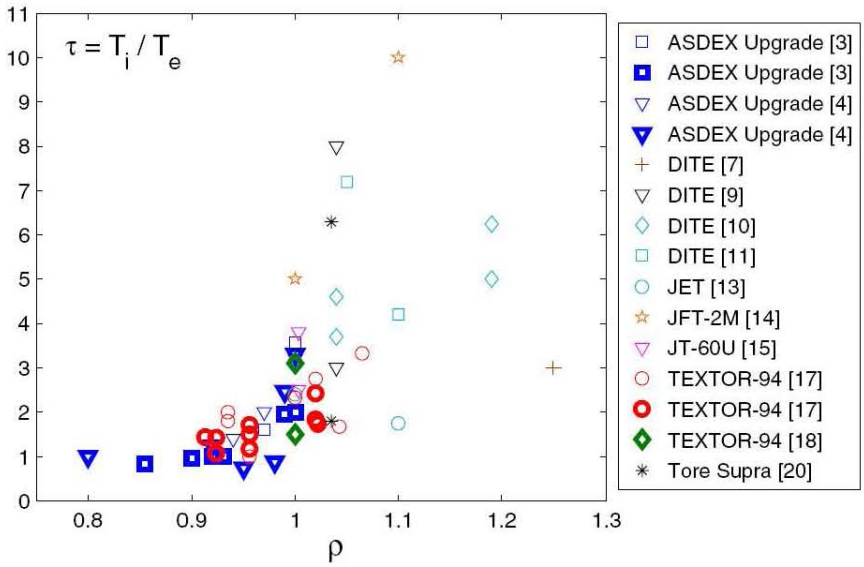

Figure 7. Measurements of the ion-to-electron temperature ratio in different tokamaks. τ is plotted against the distance from the plasma centre normalized to minor radius, $\rho = r/a$.

main plasma parameters, poloidal location of the measurements, plasma shape, difference in the measurement techniques, etc.

5. Conclusions and summary

Both ion and electron temperatures in the SOL of the Tore Supra tokamak were measured by a RFA during an ohmic density scan in helium plasma. SOL T_i was found to be by a factor of 4–7 higher than T_e. The ion temperature decreases faster with density than electron temperature. At low densities the SOL temperature e-folding lengths are comparable. At high densities the ion temperature e-folding length is a factor of 1.5 longer than the electron temperature e-folding length. This is qualitatively consistent with the difference in the ion and electron parallel losses on open field lines.

A continuous $\tau = T_\mathrm{i}/T_\mathrm{e}$ profile from the edge into the SOL was constructed using data from several machines. τ increases with radius, with $\tau > 1$ already in the edge of the confined plasma ($\rho > 0.8$), which is consistent with Tore Supra measurements of SOL and edge T_i and T_e. The experimental data included in the multi-machine database are characterized by a large spread of τ values caused by different operating conditions, plasma shape, poloidal location of the measurements and, possibly, due to a difference in the measurement techniques. Therefore, a single value of τ cannot be suggested for theoretical modelling. Instead, measurements of both T_i and T_e are necessary for every particular case. Also it is important for the validation of Ti measurements to obtain overlapping CXRS and RFA profiles.

From the present experimental data there is good evidence that the energy of SOL ions exceeds that of electrons, both in limited and diverted tokamak plasmas. Whether this also holds for particles arriving at the wall surface or at the target plates remains unknown, since direct measurements of T_i in the far SOL and at the target plates are not available. Some progress in this direction has been made recently by Pitts [27], demonstrating experimentally that during ELM events the ions arrive at the non-divertor components with impact energies

that would provide non-negligible erosion rates in future tungsten-wall machines. Therefore, high priority should be given to the development of diagnostics for measurement of ion energies in the far SOL and at the target plates.

Acknowledgments

The authors wish to thank Drs X Garbet, T Hoang and P Lotte for useful comments. This work, supported by the European Communities under the contract of Association between EURATOM and CEA, was carried our within the framework of the European Fusion Development Agreement. The views and opinions expressed herein do not necessarily reflect those of the European Commission.

References

[1] Kirschner A, Philipps V, Winter J and Kögler U 2000 *Nucl. Fusion* **40** 989
[2] Wan A S, Yang T F, Lipschultz B and LaBombard B 1986 *Rev. Sci. Instrum.* **57** 1542
[3] Reich M, Wolfrum E, Schweinzer J, Ehmler H, Horton L D, Neuhauser J and ASDEX Upgrade Team 2004 *Plasma Phys. Control. Fusion* **46** 797
[4] Reich M, Wolfrum E, Horton L D, Schweinzer J, Neuhauser J and ASDEX Upgrade Team 2004 *31st EPS Conf. on Plasma Physics (London, 28 June–2 July 2004)*
[5] Kočan M, Pánek R, Stöckel J, Hron M, Gunn J P and Dejarnac R 2007 *J. Nucl. Mater.* **363–365** 1436
[6] Erents S K and Stangeby P C 1982 *J. Nucl. Mater.* **111–112** 165
[7] Stangeby P C, McCracken G M, Erents S K, Vince J E and Wilden R 1983 *J. Vac. Sci. Technol.* A **1** 1302
[8] Pitts R A, McCracken G M and Matthews G F 1989 *J. Nucl. Mater.* **162–164** 568
[9] Matthews G F, Pitts R A, McCracken G M and Stangeby P C 1991 *Nucl. Fusion* **31** 1495
[10] Pitts R A 1991 *PhD Thesis* University of London
[11] Pitts R A 1996 *Contrib. Plasma Phys.* **36** 87
[12] Guo H Y, Matthews G F, Davies S J, Erents S K, Horton L D, Mond R D, Stangeby P C 1996 *Contrib. Plasma Phys.* **36** 81
[13] Pitts R A, Chavan R, Davies S J, Erents S K, Kaveney G, Matthews G F, Neill G, Vince J E and Ďuran I 2003 *Rev. Sci. Instrum.* **74** 4644–57
[14] Uehara K, Tawakami T, Amemiya H, Höthker K, Cosler A and Bieger W 1998 *Nucl. Fusion* **38** 1665
[15] Asakura N, Koide Y, Itami K, Shimizu K, Tsuji-Iio S, Sakurai S and Sakasai A 1997 *J. Nucl. Mater.* **241–243** 559
[16] Höthker K, Belitz H-J, Bieger W and Amemiya H 1990 *Rev. Sci. Instrum.* **61** 114
[17] Huber A, Pospieszczyk A, Unterberg B, Brix M, Mertens Ph, Philipps V and Schweer B 2000 *Plasma Phys. Control. Fusion* **42** 569
[18] Kreter A 2001 *PhD Thesis* Düsseldorf University
[19] Staudenmaier G, Staib P and Poschenrieder W 1980 *J. Nucl. Mater.* **121–126** 121
[20] Kočan M *et al* 2008 Measurements of scrape-off layer ion-to-electron temperature ratio in Tore Supra ohmic plasmas *J. Nucl. Mater.* submitted
[21] Saarelma S *et al* 2005 *Plasma Phys. Control. Fusion* **47** 713
[22] Jacquinot J and Hoang G T 2004 *Plasma Sci. Technol.* **6** 2101
[23] Kočan M, Gunn J P, Komm M, Pascal J-Y, Gauthier E and Bonhomme G 2008 *Rev. Sci. Instrum.* **79** 073502
[24] Gunn J P *et al* 2002 *Czech. J. Phys.* **52** 1107
[25] Hutchinson I H 1987 *Phys. Fluids* **30** 3777
[26] Stangeby P C 2000 *The Plasma Boundary in Magnetic Fusion Devices* (Bristol: Institute of Physics Publishing) p 649
[27] Pitts R A, Fundamenski W, Erents S K, Andrew Y, Loarte A, Silva C and JET-EFDA contributors 2006 *Nucl. Fusion* **46** 82

35th EPS Conference on Plasma Phys. Hersonissos, 9 - 13 June 2008 ECA Vol.32, P-1.006 (2008)

Measurements of ion temperature in the scrape-off layer of Tore Supra

M. Kočan[1], J. P. Gunn[1], T. Gerbaud[1], J.-Y. Pascal[1], G. Bonhomme[2], C. Fenzi[1], E. Gauthier[1], O. Meyer[1], J.-L. Segui[1]

[1] *CEA, IRFM, F-13108 Saint-Paul-lez-Durance, France*
[2] *Université Henri Poincaré, Nancy I, BP 239, 54506 Vandoeuvre-lès-Nancy Cedex, France*

1. Introduction

The ion temperature T_i in the tokamak scrape-off layer (SOL) is of key importance for modelling plasma surface interaction processes such as physical sputtering, reflection and impurity release [1], estimation of the amount of the heat flux deposited on the divertor tiles and main chamber walls by the ELM filaments [2], etc. These are critical parameters for designing tokamak plasma facing components.

While the SOL electron temperature T_e is easily accessible by simple Langmuir probes, T_i can be measured only by complex electrostatic particle analyzers or, indirectly, by charge exchange recombination spectroscopy. Consequently, due to lack of systematic T_i measurements, the models usually assume that SOL ions are in thermal equipartition with electrons (i.e. $T_i = T_e$) [3]. This is in contrast to what was measured recently in tokamaks TEXTOR [4], ASDEX [5] and CASTOR [6] or much earlier in DITE [7-9] and JT60 [10] (i.e. $T_i > T_e$).

This paper reports on measurements of SOL T_i and T_e during an ohmic density scan in Tore Supra tokamak. We show that the assumption of equal SOL temperatures due to equipartition is not justified, even at the highest densities for which ions and electrons are expected to be fully thermalized due to strong thermal coupling. The correlation between density fluctuations level and electron heat diffusivity in the edge plasma is analyzed.

2. Experimental set up

SOL temperatures were measured by a reciprocating probe system located in a top port at poloidal angle $\theta = 79°$ with respect to the outer midplane. The system was equipped with a retarding field analyzer (RFA) ([11] and references therein). The ions are transmitted through a thin slit into the analyzer and their parallel velocity distribution is analyzed by means of a retarding electric field applied to a grid, providing measurements of T_i. T_e is measured by operating the RFA slit plate as a single Langmuir probe. Temperatures can be measured up to 3 cm inside the last closed flux surface (LCFS) with a typical spatial resolution of ~1-2 mm and a temporal resolution of ~1 ms. Measurements of T_i and T_e are separated by ~0.5 ms.

The central-line-averaged density $\overline{n}_e \cong 0.7 \rightarrow 4.2 \cdot 10^{19}\,\mathrm{m}^{-3}$ was varied on a shot-to-shot basis. Feedback control on gas puffing was used to keep the density constant during each probe reciprocation. A database consisting of 90 reciprocations was assembled. The discharges were characterized by plasma current $I_p = 0.5\,\mathrm{MA}$ and toroidal magnetic field $B_t = 3.8\,\mathrm{T}$. Major and minor radii $R = 2.38\,\mathrm{m}$ and $a = 0.72\,\mathrm{m}$ respectively. Helium was used as a working gas, since it provides higher density limit than deuterium. All discharges were ohmic.

T_i was calculated assuming that SOL plasma is dominated by He^{2+} ions. Ions with different charge-to-mass ratios affect T_i inferred from RFA [8, 9]. These can be singly charged helium ions He^+ (overestimating T_i), or impurities (mainly carbon and oxygen)

which have a tendency to underestimate T_i. At high densities, for which $T_e < 10$ eV, the relative abundance of He^+ can exceed that of He^{2+} [8]. The effect of impurities is expected to play an important role at lowest $\overline{n}_e$ where their concentration relative to He^{2+} is highest. Separation of the components of the ion flux to the analyzer by charge state and temperature has been proposed [9]. However, the model needs to specify the fractions of the total flux carried by ions with a given charge state as well as their temperatures. Such measurements are not available. Indeed, it is reasonable to expect some underestimation (overestimation) of T_i at lowest (highest) $\overline{n}_e$. The instrumental effects which accounts for overestimation of T_i by 4-12% [11] were taken into account.

3. Results and discussion

Figures 1a and 1b show SOL T_i and T_e as well as their ratio $\tau = T_i / T_e$ measured by RFA, plotted as a function of $\overline{n}_e$. For better statistics the data are averaged over 2-3 cm outside the LCFS. For comparison, the simultaneous measurements of T_e by tunnel probe (TP) [12] installed in second reciprocating drive are also shown in Fig. 1a. RFA and TP are separated toroidally by 120°. TP values of T_e are in a good agreement with those measured by RFA.

T_i decreases by a factor ~3 with the increase of $\overline{n}_e = 1 \rightarrow 4.2 \cdot 10^{19}$. Within the same range of $\overline{n}_e$, T_e decreases by a factor of ~2. The decrease of temperatures with density can be due to the fact that $\overline{n}_e$ increases approximately two times faster than the total plasma energy content ($\propto nT$) obtained from diamagnetic measurements. For $\overline{n}_e = 0.7 \rightarrow 1.2 \cdot 10^{19}\,\mathrm{m}^{-3}$, $\tau = 4 \rightarrow 7$. For $\overline{n}_e = 1 \rightarrow 2.8 \cdot 10^{19}\ \mathrm{m}^{-3}$, $\tau = 7 \rightarrow 4$. For $\overline{n}_e > 2.8 \cdot 10^{19}\ \mathrm{m}^{-3}$, $\tau \cong 4$. In order to verify the reproducibility of T_i and T_e measurements, $\overline{n}_e$ was steadily decreased during experiment ($\overline{n}_e \cong 3.8 \rightarrow 0.7 \cdot 10^{19}\,\mathrm{m}^{-3}$, light symbols in Fig. 1a) and last discharges were repeated at high densities ($\overline{n}_e = 3.2 \rightarrow 4.2 \cdot 10^{19}\,\mathrm{m}^{-3}$, heavy symbols). The temperatures measured in the initial and in the final phase of experiment are very similar. It is worth noting that T_i in helium plasma is up to a factor of 2 higher compared to T_i measured in deuterium plasma at similar conditions. Similar result was obtained in DITE tokamak and was attributed to the difference in the rate by which the ions lose their energy by charge-exchange collisions with neutrals in edge plasma [9] (in deuterium the reaction cross section can be up to an order of magnitude higher compared to helium). T_e measured in helium was found to be higher by up to 25% compared to those measured in deuterium. The statistical error on T_i increases monotonically with the decrease of $\overline{n}_e$, up to 20% at lowest densities, which is due to the fact that the RFA signal level is proportional to density.

The ion temperature e-folding length (7 ± 3 cm) close to the LCFS was found to be about a factor of 1.4 longer than the electron temperature e-folding length (5 ± 2 cm).

Thermal coupling of SOL ions and electrons was estimated from the ratio of the ion parallel transit time to the ion-electron thermalization time, $R_{th} = \tau^i_{//} / \tau^{ie}_{th}$, where $\tau^i_{//} \propto L_{con} / \sqrt{T_i + T_e}$ and $\tau^{ie}_{th} \propto T_e^{3/2} / n_e$. Here $L_{con} \approx q\pi R$ (with q being the safety factor at the LCFS) is the parallel connection length and n_e is the local electron density. $R_{th} < 1$ implies thermally decoupled ions and electrons. $R_{th} >> 1$ implies strong thermal coupling at which the ion and electron temperatures are expected to converge. R_{th} was evaluated at the LCFS radius from extrapolated RFA data. Fig. 1c shows R_{th} plotted against $\overline{n}_e$. R_{th} varies from 0.1 up to

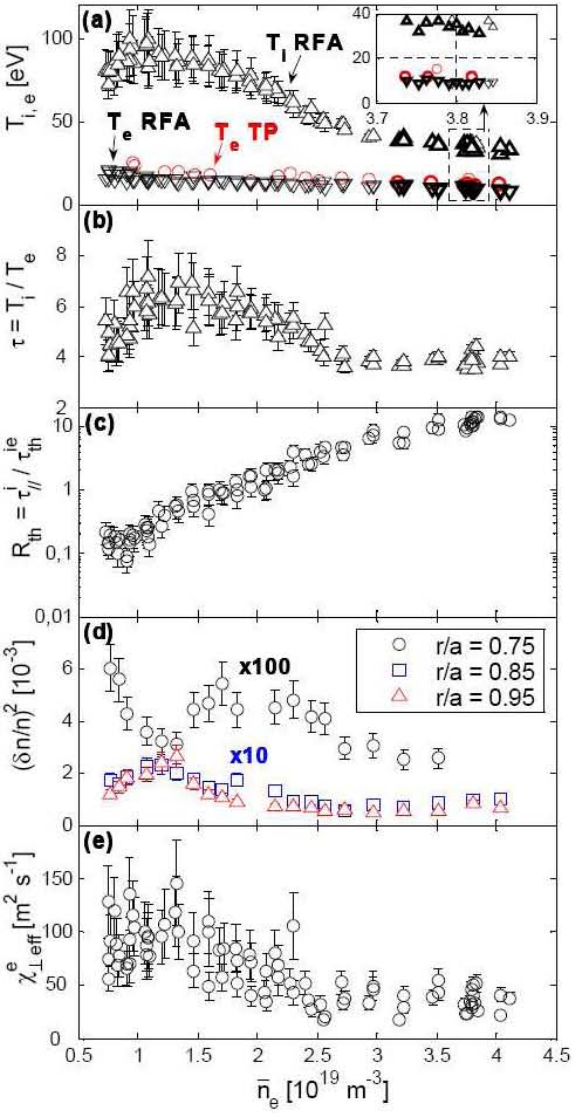

Fig. 1. (a) T_i measured by RFA. T_e measured by RFA and TP. Light symbols: high-to-low density scan. Heavy symbols: measurements of T_i and T_e repeated at high density. (b) Ion-to-electron temperature ratio τ. (c) Ratio of the ion parallel transit time to the ion-electron thermalization time R_{th}. (d) Density fluctuation level $(\delta n/n)^2$. (e) The effective cross-field electron heat diffusivity $\chi^e_{\perp eff}$ at the LCFS evaluated from RFA data and main plasma parameters. Data are plotted against the central-line averaged density $\bar{n}_e$.

15 at highest densities. For $R_{th} > 1$, τ decreases with the increase of R_{th}. For $R_{th} > 5$, τ remains at constant value of 4, i.e. far from full thermalization. The saturation of τ at highest densities can be explained by the balance between ion-electron collisions (which tends to decrease τ) and the tendency for $T_e < T_i$ on open field lines due to higher parallel thermal conductivity of electrons compared to that of ions ($\chi^e_{//} / \chi^i_{//} \propto \sqrt{m_{He}/m_e}\,\tau^{-5/2}$). On the other hand, the saturation of τ might also be explained by the overestimation of T_i (by up to a factor of 2) due to an increase of He^+/He^{2+} with $\bar{n}_e$.

The properties of the electron heat transport in edge plasma were analyzed by comparing the effective cross-field electron heat diffusivity $\chi^e_{\perp eff}$ with the density fluctuation level $(\delta n/n)^2$ obtained from reflectometry [13]. $\chi^e_{\perp eff}$ was evaluated combining RFA data and the main plasma parameters. $\chi^e_{\perp eff} = q_e/(en_e\nabla T_e)$ where q_e is the electron heat flux density at the LCFS and e is the elementary charge. Assuming poloidally and toroidally uniform q_e, $q_e \cong (P_{ohm} - P_{rad})/4\pi^2 aR$ with P_{ohm} and P_{rad} being the ohmic heating power and the radiated power inside the LCFS, respectively. Power lost by electrons due to ion-electron collisions inside the LCFS P_{ei} (typically less than $0.2\,P_{ohm}$ at the LCFS [14]), as well as the other electron power losses and gains, were neglected. n_e and ∇T_e were obtained from RFA data measured 2-3 cm outside the LCFS. Since the electron density and temperature increases towards the LCFS, $\chi^e_{\perp eff}$ is likely to be about one order of magnitude higher compared to electron heat diffusivity at the LCFS. Figures 1d and 1e show $(\delta n/n)^2$ at $r/a = 0.75$, 0.85 and 0.95, as well as $\chi^e_{\perp eff}$, plotted against $\bar{n}_e$. The fluctuation level increases strongly with radius ($\delta n/n$ up to 3-5% at

$r/a = 0.95$). $\chi^{e}_{\perp eff}$ decreases with the increase of density up to $\overline{n}_e = 2.5 \cdot 10^{19}\,\mathrm{m}^{-3}$, and than saturates. The saturation of $\chi^{e}_{\perp eff}$ coincides with the saturation of the energy confinement time obtained from diamagnetic measurements. The difference between $\chi^{e}_{\perp eff}$ measured at high and low $\overline{n}_e$ is expected to be even larger if P_{ei} is included in q_e, as P_{ei} is an increasing function of density. The change of $(\delta n/n)^2$ at $r/a = 0.95$ and 0.85 with density is correlated with similar variation of $\chi^{e}_{\perp eff}$ (the Person correlation coefficient is 0.78 and 0.77, respectively). At $r/a = 0.75$ the correlation is only 0.24. This suggests that at low densities the edge turbulence increases which leads to strong increase of electron heat diffusivity. Since $\chi^{e}_{\perp eff}$ and $(\delta n/n)^2$ are not evaluated at the same radial position, a certain self similarity between the radial profiles of $\chi^{e}_{\perp eff}$ and $(\delta n/n)^2$ is assumed.

4. Summary

Ion and electron temperatures in the SOL of Tore Supra tokamak were measured by a retarding field analyzer in ohmic density scan. SOL T_i was found to be by a factor of 4-7 higher than T_e. The ion-to-electron temperature ratio decreases with the increase of density and saturates at high densities. At low densities the edge turbulence increases significantly and leads to a strong increase of electron heat diffusivity. The saturation of the electron heat diffusivity coincides with the saturation of the energy confinement time. Similar observations has been already reported in [15, 16].

Acknowledgements

The authors wish to thank Drs X. Garbet, T. Hoang and R. Guirlet for useful comments.

References

[1] A. Kircher *et al.*, Nucl. Fusion **40** (2000) 989.
[2] W. Fundamenski *et al.*, Plasma Phys. Contr. Fusion **48** (2006) 109.
[3] C. S. Pitcher, P. C. Stangeby, Plasma Phys. Contr. Fusion **39** (1997) 779.
[4] A. Huber *et al.*, Plasma Phys Control. Fusion **42** (2000) 569.
[5] M. Reich *et al.*, Plasma Phys. Control. Fusion **46** (2004) 797.
[6] M. Kočan *et al.*, J. Nucl. Matter. **363-365** (2007) 1436.
[7] S. K. Erents, P. C. Stangeby, J. Nucl. Mater. **111-112** (1982) 165.
[8] G. F. Matthews *et al.*, Nucl. Fusion **31** (1991) 1495.
[9] R. A. Pitts, Ph.D. thesis, University of London, 1991.
[10] N Asakura *et al.*, J. Nucl. Mater. **241-243** (1997) 559.
[11] M. Kočan *et al.*, accepted for publication in Rev. Sci. Instrum. (2008).
[12] J. P. Gunn *et al.*, Czech. J. Phys. **52** (2002) 1107.
[13] T. Gerbaud *et al.*, Proc. 8th Int. Reflectometer Workshop (St. Petersburg, 2007).
[14] E. E. Simmet, Plasma Phys. Contr. Fusion, **38** (1996) 689.
[15] X. Garbet *et al.*, Nucl. Fusion **32** (1992) 2147.
[16] T. Hoang et al., Nucl. Fusion **38** (1998) 117.

Contents lists available at ScienceDirect

Journal of Nuclear Materials

journal homepage: www.elsevier.com/locate/jnucmat

Measurements of scrape-off layer ion-to-electron temperature ratio in Tore Supra ohmic plasmas

M. Kočan [a,*], J.P. Gunn [a], J.-Y. Pascal [a], G. Bonhomme [b], P. Devynck [a], I. Ďuran [c], E. Gauthier [a], P. Ghendrih [a], Y. Marandet [d], B. Pegourie [a], J.-C. Vallet [a]

[a] CEA, IRFM, F-13108 Saint-Paul-lez-Durance, France
[b] Nancy Université, BP 239, 54506 Vandoeuvre-lès-Nancy cedex, France
[c] Institute of Plasma Physics, Association EURATOM/IPP.CR, Prague 18200, Czech Republic
[d] CNRS/Université de Provence, Centre Saint Jérôme, case 232, F-13397 Marseille cedex 20, France

ARTICLE INFO

PACS:
52.40.Hf
52.70.−m

ABSTRACT

The scrape-off layer (SOL) ion (T_i) and electron (T_e) temperatures were measured in ohmic plasmas of the Tore Supra tokamak for a wide range of main plasma parameters. T_i increases strongly with the intensity of the toroidal magnetic field B_t, whereas T_e is nearly unaffected. The ion-to-electron temperature ratio $\tau = T_i/T_e \propto B_t^{2.5}$ and is a weak function of plasma density and plasma current. Close to the last closed flux surface $\tau = 2 \rightarrow 6$ so that equipartition is never reached. The SOL ion temperature e-folding length is about 30% greater than the electron temperature e-folding length meaning that τ increases with radius in the SOL.

1. Introduction

Ion (T_i) and electron (T_e) temperatures are key parameters of the scrape-off layer (SOL). They determine e.g. the amount of the heat flux convected to a surface, the relative importance of classical drift flows compared to turbulence driven flows, and physical sputtering rates. These are critical plasma parameters that constrain the design of plasma facing components in tokamaks.

While SOL T_e can be easily measured by Langmuir probes, SOL T_i is accessible only by complex electrostatic particle analyzers or, indirectly and with larger uncertainty, by e.g. charge exchange recombination spectroscopy (CXRS) [1–4], post mortem analysis of the ion deposition profiles on collector probes [5], or bolometers combined with Langmuir probes [6]. Consequently, due to the lack of systematic measurements, simple models (such as the famous two-point model [7]) assume that ions and electrons in the SOL are thermally well coupled (i.e. $T_i = T_e$). SOL measurements of T_i and T_e obtained in limiter [2,5,6,8] as well as divertor [1,3,4,9] tokamaks revealed ion-to-electron temperature ratios $\tau = T_i/T_e > 1$, which indicates that SOL ions and electrons can be thermally decoupled. However, systematic measurements of τ are sparse [10].

This paper reports on the measurements of τ in Tore Supra ohmic plasmas by a retarding field analyzer (RFA) [11]. Improving upon earlier studies, a more statistically significant database of SOL T_i and T_e is obtained for wide ranges of different plasma parameters. In addition, we report on a previously unobserved strong dependence of SOL T_i on the intensity of the toroidal magnetic field B_t. It is shown that in the SOL of Tore Supra the assumption of equal temperatures due to equipartition is not justified.

2. Experimental set-up

Tore Supra [12] is a large tokamak with a plasma of circular cross-section whose last closed flux surface (LCFS) is defined by its intersection with the bottom toroidal pump limiter. The RFA is mounted on a fast reciprocating drive which allows several insertions into the plasma during a single discharge (up to 15 until now) with a frequency of 1 Hz. Instrumental effects which lead to an overestimation of T_i by 4–12% [11] are taken into account. T_i is calculated assuming that fuel ions dominate the SOL plasma. T_e is measured by operating the RFA slit plate as a single Langmuir probe. Individual measurements of T_i and T_e are separated by ~0.5 ms. Each reciprocation provides a radial profile of T_i and T_e, typically up to 1–2 cm outside the LCFS, with a spatial resolution of about 1–2 mm and a temporal resolution of about 2 ms. The database obtained in six years of RFA operation consists of more than 600 radial profiles of SOL T_i and T_e measured in discharges with ohmic or RF heating up to 8 MW.

Fig. 1 illustrates radial profiles of SOL T_i and T_e measured by the RFA. In order to demonstrate good reproducibility of the measurements, data from 24 probe reciprocations (corresponding to 21 discharges measured in a time span of two years with 16 discharges

* Corresponding author.
E-mail address: martin.kocan@cea.fr (M. Kočan).

0022-3115/$ - see front matter © 2009 Elsevier B.V. All rights reserved.
doi:10.1016/j.jnucmat.2009.01.294

being measured during a single experimental session) in very similar plasmas are superimposed in one graph. Also shown in Fig. 1 is T_e measured inside the LCFS by electron cyclotron emission (ECE) and Thomson scattering (TS) diagnostics. Temperatures are plotted against the distance from plasma centre normalized to minor radius $\rho = r/a$.

One hundred and twenty-five probe reciprocations obtained from 79 discharges are analyzed. The range of the main plasma parameters is: $\bar{n}_e = 1.3 - 4.5 \cdot 10^{19}\ m^{-3}$, I_p = 0.75–1.2 MA, Z_{eff} = 1.2–4.3, and B_t = 2.4, 3.1 and 3.8 T. Here $\bar{n}_e$ is the central-line-averaged density, I_p is the plasma current, and Z_{eff} is the central-line-averaged effective ion charge calculated from visible bremsstrahlung radiation. The Greenwald density fraction $\bar{n}_e/\bar{n}_e^{GW} = 0.22 \rightarrow 0.63$, where $\bar{n}_e^{GW} = I_p/(\pi a^2)$ ($10^{20}\ m^{-3}$, MA, m). Major and minor radii R = 2.39 m and a = 0.72 m, respectively. The working gas is deuterium. All database discharges are analyzed in a steady-state phase.

3. Results and discussion

Fig. 2 shows T_i, T_e and τ plotted as a function of $\bar{n}_e$. For better statistics, measurements are averaged over a window of 1 cm, localized between 2 and 3 cm outside the LCFS. The width of the window is shorter than the typical ion and electron e-folding lengths (see below) so that it is reasonable to assume constant temperatures within the averaging region. Data are divided into three groups, characterized by different value of B_t. T_i increases with B_t, while the variation of T_e with B_t is insignificant. As a consequence, τ increases with B_t. Comparison of T_i measured at constant I_P = 0.75 MA and different B_t = 2.4 and 3.1 T (or at B_t = 3.1 T and different I_p) shows that the increase of T_i is due to an increase of B_t rather than of I_p. It should be noted that the variation of B_t (at fixed I_p) changes the degree of the probe head misalignment to the total magnetic field vector (with which the probe is supposed to be ideally perfectly aligned). For the database discharges the maximum misalignment due to B_t variation is less than 2°. As shown in [11], such misalignment should not affect T_i measurements. For B_t = 3.1 T and I_p = 0.75 MA both T_i and T_e decrease with $\bar{n}_e$. For other values of B_t and I_p the range of densities is too small to identify clear trends. The same applies for the dependence of SOL temperatures on I_p, as the data points measured at fixed B_t and $\bar{n}_e$ are characterized by a relatively small range of the plasma current. τ = 2 → 6 so that equipartition is never reached. An unconstrained non-linear least-square fit to the experimental values of τ with equal weight given to each point gives:

$$\tau = 0.095\, \bar{n}_e^{0.28\pm0.1} I_p^{0.08\pm0.1} Z_{eff}^{0.19\pm0.07} B_t^{2.5\pm0.2}. \quad (1)$$

The only significant dependence is on B_t. The Pearson correlation coefficient of the fit is 0.89. Experimental τ is plotted against the fit in Fig. 3.

The only other parameter found thus far that strongly correlates with B_t is the core electron temperature. In Fig. 4, the measurements of SOL T_i and T_e are plotted against the electron temperature measured by ECE diagnostics at ρ = 0, $T_e(0)$. For the database discharges an empirical scaling $T_e(0) \propto B_t I_p/\bar{n}_e$ is found. Taken that in the steady-state $\tau_E = W_{dia}/P_{ohm} \propto nT/P_{ohm}$ and $P_{ohm} \propto I_p$, the increase of $T_e(0)$ with B_t roughly follows the empirical saturated ohmic energy confinement time scaling $\tau_E \propto B_t^{0.6\pm0.2}$ found in Tore Supra [13]. Here W_{dia} is the plasma energy obtained from diamagnetic measurements and P_{ohm} is the ohmic heating power. The correlation of SOL T_i with $T_e(0)$ is strong, whereas SOL T_e is practically independent of $T_e(0)$. Since the systematic measurements of core ion temperature $T_i(0)$ are not available in Tore Supra, we do not have any direct evidence how τ behaves in the core. We speculate that due to collisional coupling $T_i(0)$ increases similarly to $T_e(0)$, and that T_i in the SOL is simply related to $T_i(0)$ through radial

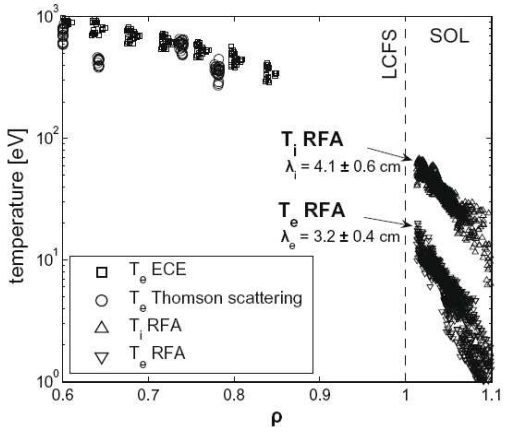

Fig. 1. Radial profiles of SOL T_i and T_e measured by RFA in 24 reciprocations characterized by similar plasma parameters, juxtaposed to T_e measured by ECE and Thomson scattering diagnostics. λ_i and λ_e are, respectively, the SOL ion and electron temperature e-folding lengths. $\bar{n}_e = 2.5 - 3 \cdot 10^{19}\ m^{-3}$, I_p = 0.9–1.1 MA, and B_t = 3.8 T.

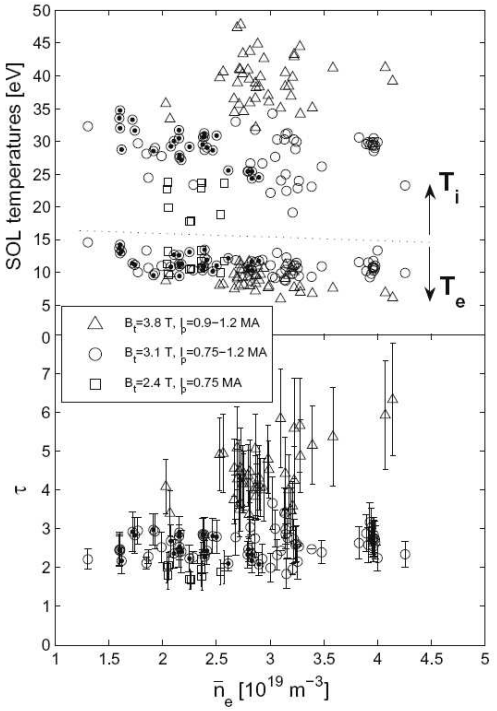

Fig. 2. Above: T_i and T_e measured 2–3 cm outside the LCFS, plotted as a function of the central-line-averaged density (dots: B_t = 3.1 T, I_p = 0.75 MA). Error bars are not plotted for clarity, but are typically 5–10%. Below: ion-to-electron temperature ratio τ. The error on τ is due to statistical errors on T_i and T_e.

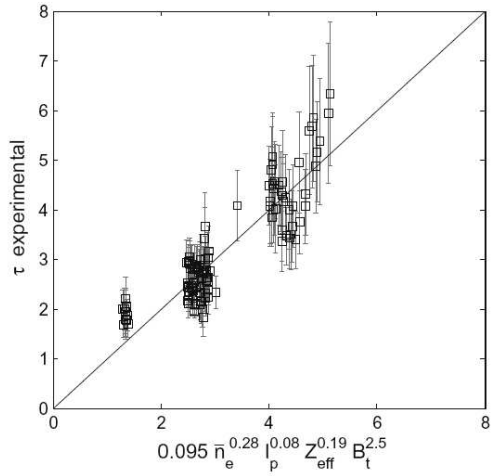

Fig. 3. Experimental values of τ plotted against the scaling law.

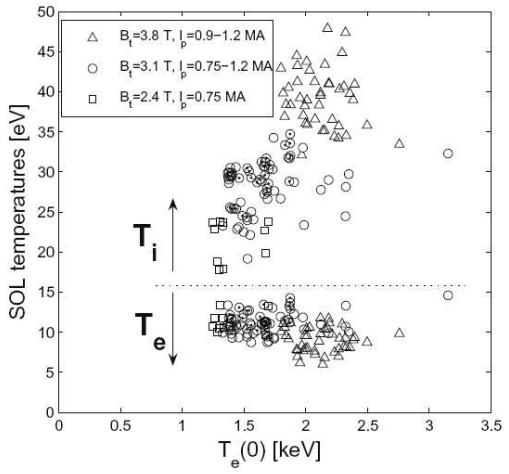

Fig. 4. SOL T_i and T_e measured 2–3 cm outside the LCFS plotted against the electron temperature $T_e(0)$ measured by ECE diagnostics at $\rho = 0$.

transport. A mechanism that would decouple the SOL electrons from the $T_e(0)$ needs to be identified.

It is worth noting that the database discharges were performed over a long time span that covers several experimental campaigns separated by e.g. boronization, machine opening, re-installation of the probe itself, so that the experimental conditions (in particular the charge state distribution and the amount of impurities in the SOL) could have changed. However, due to the lack of relevant measurements, it is not possible to quantify their effect on SOL temperatures. This can contribute to data scatter and confuse the scaling. In addition, as the analysis of the RFA current–voltage characteristics assumes Maxwellian deuterons, impurities with different charge-to-mass ratio can cause T_i inferred from RFA being underestimated. Separation of the components of the analyzed ion flux by charge state and temperature has been proposed in [10]. However, the model needs to specify the fractions of the total flux carried by ions with a given charge state as well as their temperatures. Such measurements are not available. The insertion of the probe into the plasma can itself modify the parameters being measured. The probe disturbance is expected to be significant if the ambipolar probe collection length L_{col} is larger than the magnetic connection length along the field line from the probe to the limiter L_{con}. For database discharges $L_{con} \cong 25 \rightarrow 40$ m. $L_{col} \cong d^2 c_s / 8 D_\perp$ [14] where $d = 0.04$ m is the probe diameter, $c_s = \sqrt{e(Z_i T_i + T_e)/m_i}$ is the isothermal ion sound speed (with T_i and T_e in electron volts) and $D_\perp$ is the anomalous ambipolar cross field diffusion coefficient. Assuming $D_\perp = 1\ m^2\ s^{-1}$, $L_{con} \cong 10$ m so that finite connection length effects do not need to be considered.

The ion and electron temperature e-folding lengths for the database discharges, $\lambda_i \equiv T_i/|\nabla T_i|$ and $\lambda_e \equiv T_e/|\nabla T_e|$, respectively, has been evaluated from the data measured 1–4 cm outside the LCFS. The scatter of λ_i and λ_e values is relatively large without any clear trend. The average ion temperature e-folding length for the whole dataset, $\langle \lambda_i \rangle$, is by about 30% longer than $\langle \lambda_e \rangle$ ($\langle \lambda_i \rangle = 6.1 \pm 3.3$ cm, $\langle \lambda_e \rangle = 3.7 \pm 1.4$ cm), which implies that τ increases with radius in the SOL. The difference in the ion and electron temperature e-folding lengths can be easily understood as the energy removal at the sheath edge is smaller for ions than for electrons [15]. Other ion energy losses in the SOL due to e.g. ion-electron and ion-neutral collisions are negligible, as the ion-electron thermal coupling and the ion-neutral collisionality are small in the deuterium SOL plasma in Tore Supra.

Returning to general observation that T_i exceeds T_e in the SOL, this is usually explained by a filtering effect of the sheath which tends to remove fastest electrons from the distribution thus reducing effective SOL T_e [16]. Although the sheath effect can strengthen the tendency for $T_i > T_e$ in the SOL, there is increasing experimental evidence that, except at highest densities, in ohmic as well as in L-mode plasma $T_i > T_e$ a few centimetres inside the LCFS where no sheath effects exist. Values of $\tau = 3 \rightarrow 5$ at the LCFS were reported in [3,4,17,18], meaning that in some cases the sheath plays only a subsidiary role in strengthening the tendency for $T_i > T_e$ in the SOL. Similar results were obtained by Tore Supra RFA reciprocating up to the LCFS [19]. In addition, sheath filtering is governed by parallel transport, so it certainly cannot explain the strong variation of τ with B_t. Whether the fast drop of T_e compared to T_i in the edge plasma arises due to the difference in e.g. ion and electron heat/particle transport, volumetric power losses (like charge-exchange reactions, interaction of electrons with impurity ions and neutrals, etc.) is not well understood. More insight could be obtained from a simple radial transport model, provided that the relevant edge plasma parameters (e.g. ion and electron temperatures, effective ion charge, volumetric loss and source terms) are reasonably well known. Unfortunately, large uncertainties in such parameters (or lack of measurements thereof) lead to an error on the calculated variables of interest (e.g. edge profiles of the ion and electron cross-field heat diffusivities) which is much larger than their variation within the input parameter range.

4. Summary

The scrape-off layer ion and electron temperatures in a large number of ohmically heated plasmas were measured by a retarding field analyzer in the Tore Supra tokamak. T_i was found to be a strong function of the toroidal magnetic field B_t. SOL T_e is nearly independent of B_t. Variation of SOL T_i and T_e with B_t are not understood. The only other parameter found thus far which also correlates with B_t is the core electron temperature. The SOL ion temperature e-folding length is by about 30% greater than the electron temperature e-folding length so that τ increases with radius in

the SOL. For 2–3 cm outside the LCFS the ion-to-electron temperature ratio $\tau = T_i/T_e \propto B_t^{2.5}$. Close to the LCFS $\tau = 2 \rightarrow 6$. This implies that e.g. the SOL plasma density calculated for $\tau = 1$ can by overestimated by a factor of $1.2 \rightarrow 1.9$, heat flux density conducted by ions (which is negligible for $\tau = 1$) is comparable or higher than the one conducted by electrons, the relative importance of the classical drift driven flows calculated by replacing T_i by T_e can be significantly underestimated compared to turbulence driven flows.

Simultaneous measurements of core and SOL T_i for a wider range of B_t and in diverted plasmas are needed in order to validate the scaling. Also important for the validation of SOL T_i and T_e measurements is to obtain overlapping profiles measured by RFA and by CXRS and TS or ECE, respectively.

References

[1] N. Asakura et al., J. Nucl. Mater. 241–243 (1997) 559.
[2] A. Huber et al., Plasma Phys. Control. Fusion 42 (2000) 569.
[3] M. Reich et al., Plasma Phys. Control. Fusion 46 (2004) 797.
[4] M. Reich et al., in: 31st EPS Conference on Plasma Physics, London, 28 June–2 July 2004.
[5] G. Staudenmaier, P. Staib, W. Poschenrieder, J. Nucl. Mater. 93 & 94 (1980) 121.
[6] P.C. Stangeby et al., J. Vac. Sci. Technol. A1 (1983) 1302.
[7] C.S. Pitcher, P.C. Stangeby, Plasma Phys. Control. Fusion 39 (1997) 779.
[8] G.F. Matthews et al., Nucl. Fusion 31 (1991) 1495.
[9] R.A. Pitts et al., Rev. Sci. Instrum. 74 (2003) 4644.
[10] R.A. Pitts, PhD thesis, University of London, 1991.
[11] M. Kočan et al., Rev. Sci. Instrum. 79 (2008) 073502.
[12] J. Jacquinot, G.T. Hoang, Plasma Sci. Technol. 6 (2004) 2101.
[13] X.L. Zou et al., Controlled fusion and plasma physics, in: Proceedings of 22nd European Conference, Bournemouth, 1995, vol. 19C, Part I, European Physical Society, Geneva, 1995, p. 41.
[14] P.C. Stangeby, J. Phys. D 18 (1985) 1547.
[15] P.C. Stangeby, The Plasma Boundary in Magnetic Fusion Devices, Institute of Physical Publishing, Bristol and Philadelphia, 2000. p. 160.
[16] P.C. Stangeby, The Plasma Boundary in Magnetic Fusion Devices, Institute of Physical Publishing, Bristol and Philadelphia, 2000. p. 96.
[17] A. Kreter, PhD thesis, Düsseldorf University, 2000.
[18] K. Uehara et al., Nucl. Fusion 38 (1998) 1665.
[19] M. Kočan, J.P. Gunn, J.-Y. Pascal, G. Bonhomme, C. Fenzi, E. Gauthier, J.-L. Segui, Plasma Phys. Control. Fusion 50 (2008) 125009.

Confidential: not for distribution. Submitted to IOP Publishing for peer review 6 May 2009

Influence of the plasma density and the radiated power fraction on the Tore Supra scrape-off layer

M Kočan, J P Gunn, P Tamain [1], O Meyer, J-Y Pascal, J-L Segui and J-C Vallet

CEA, IRFM, F-13108 Saint-Paul-lez-Durance, France.

[1] EURATOM/UKAEA Fusion Association, Culham Science Centre, Oxfordshire OX14 3DB, UK

E-mail: martin.kocan@cea.fr

Abstract. The scrape-off layer (SOL) ion and electron temperatures, T_i and T_e, electron density n_e, and the ion saturation current density j_{sat} are studied in Tore Supra deuterium plasma for a wide range of densities $\langle n_e \rangle$ and radiated power fractions f_{rad}, including detached plasma. In ohmic plasma for low $\langle n_e \rangle$ and f_{rad}, $T_i / T_e \cong 3-4$ and $T_i \cong 50$ eV at the last closed flux surface. At highest $\langle n_e \rangle$ and f_{rad} as well as in detached plasma, $T_i \cong T_e$, both only a few electron volts. Detachment is also associated with the drop of both j_{sat} and n_e as well as the flattening of the radial profiles from the SOL to the edge of the confined plasma, which is consistent with earlier Langmuir probe measurements [McCracken G M *et al* 1987 *J. Nucl. Mater.* **145-147** 181]. At constant $\langle n_e \rangle$ an increase of f_{rad} by about ~30% coincides with a decrease of SOL T_i by almost a factor of 2, whereas SOL T_e is much less affected. A strong drop of T_i but also a substantial decrease of T_e with the increase of f_{rad} is obtained from a simple power balance model of the temperatures in the edge of the confined plasma.

PACS 52.25.Fi, 52.25.Xz, 52.55.Fa, 52.70.-m, 52.70.Ds

1. Introduction

One of the options for the ohmic plasma start-up phase in the current ITER design consists of two limiter modules located at the low-field side. The limiters will define the plasma last closed flux surface (LCFS) for about 30 seconds before the X-point divertor configuration is established [1]. The start-up plasma will be, therefore, characterized by the configuration close to that of the large circular tokamaks. Because of their small plasma-wetted area, the limiters will receive relatively large heat loads. Modelling activities have been recently focused on the estimation of the power crossing the LCFS as well as the resulting power load distribution on ITER limiters (e.g. [2, 3]). Taking into account the usual uncertainties in code predictions, the difference between the predicted heat flux densities to the ITER start-up limiters (<6 MW m^{-2} [2]) and their engineering limit (8 MW m^{-2} [4]) appears to be considerably small. Therefore, the modellers ask for further SOL measurements that could help to validate the codes [3].

In this work we study the scrape-off layer (SOL) ion and electron temperatures, electron density and the ion saturation current density for a broad range of core plasma density and radiated power fraction, including detached plasmas, in the large circular limiter tokamak Tore Supra [5]. The SOL parameters are measured by a retarding field analyzer (RFA) [6]. We focus mainly on ohmic discharges which are characterized by relatively low SOL heat fluxes and thus allow for probe measurements up to the LCFS.

Improving upon earlier studies (e.g. [7-11]), we show more systematic measurements of the SOL T_i which is an essential parameter for interpretation of the Langmuir probe measurements and modelling. Only a very limited database of SOL T_i is available (see [11] and references therein). In addition, the paper reports on first measurements of SOL T_i in detached plasma as well as previously unreported variation of SOL T_i with the radiated power. The paper also addresses some improvements of the RFA probe operation.

In order to avoid confusion, the "detachment" refers here to a steady state with poloidally symmetric radiation shifted inside the LCFS by about 30 cm, or 60% of the minor radius. The 'attached' plasma, in turn, refers to the state with poloidally asymmetric radiation localized just above the plasma contact point.

In this paper the temperatures are stated in electron volts and the indication "parallel" relates to the magnetic field vector B.

The paper is organized as follows. The main plasma parameters of the discharges studied in this paper are stated in section 2. The principle of the RFA probe is briefly described in section

3. Experimental results and simple power-balance modeling of the edge temperatures are discussed in section 4. Summary and conclusions are given in section 5.

2. Experimental database

The database studied in this paper comprises three different plasma configurations, labeled as discharge groups 1 – 3. Table 1 indicate the major (R) and minor (a) radii, the safety factor at the last closed flux surface (LCFS) (q_a), the toroidal magnetic field at R (B_t), the volume-averaged plasma density ($\langle n_e \rangle$), the radiated power fraction (f_{rad}) and the number of RFA measurements (comprising, in some cases, several RFA reciprocations in similar plasmas) for each discharge group. Also indicated are the plasma state (attached or detached) and the contact point. All discharges are heated ohmically and are characterized by plasma current $I_p = 0.6$ MA. At this value of I_p the database of RFA measurements covers a broad range of $\langle n_e \rangle$ at almost constant B_t. Figure 1 shows the poloidal cross sections of the plasma for each discharge group.

group	R [m]	a [m]	q_a	B_t [T]	$\langle n_e \rangle$ [10^{19} m^{-3}]	f_{rad}	number of measurements	state	contact point
1	2.39	0.72	8.0	3.82	1.02 – 1.74	0.57 → 0.76	6	A	TPL / APL
2	2.35	0.68	7.3	3.73	2.34, 2.82	~1	2	D	TPL
3	2.26	0.69	8.2	4.05	0.61 – 4.04	0.46 → ~1	12	A / D	BL

Table 1. Main plasma parameters for discharge groups 1 – 3 during the RFA measurements. A / D indicates attached / detached plasma. BL is the high-field-side bumper limiter, TPL is the toroidal pump limiter and APL is the antenna protection limiter located on the low-field side.

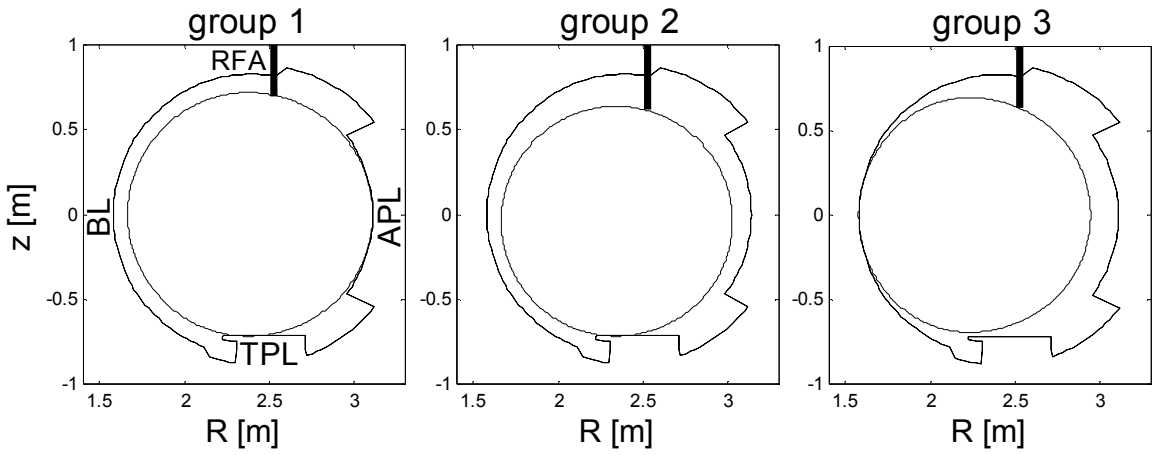

Figure 1. Plasma poloidal cross section for discharge groups 1 – 3. BL is the bumper limiter, TPL is the toroidal pump limiter and APL is the antenna protection limiter. Vertical line indicates the RFA position.

f_{rad} is calculated as P_{rad}/P_{ohm}, where P_{ohm} is the ohmic input power and $P_{rad}=(P_{rad}^{h}+P_{rad}^{v})/2$ (with P_{rad}^{h} and P_{rad}^{v} being the radiated power measured separately by the horizontal bolometric cameras located on the low-field side and the vertical bolometric cameras located on the top of the torus). As P_{rad}^{h} and P_{rad}^{v} are not identical because of the difference in the positions as well as the number of the viewing lines for the vertical and the horizontal cameras (for the discharges studied here $P_{rad}^{h}/P_{rad}^{v}=0.96\rightarrow 1.24$), f_{rad} provides only approximate value of the radiated power fraction. Figure 2 shows f_{rad} plotted against $\langle n_e \rangle$ for all discharges from groups 1 – 3.

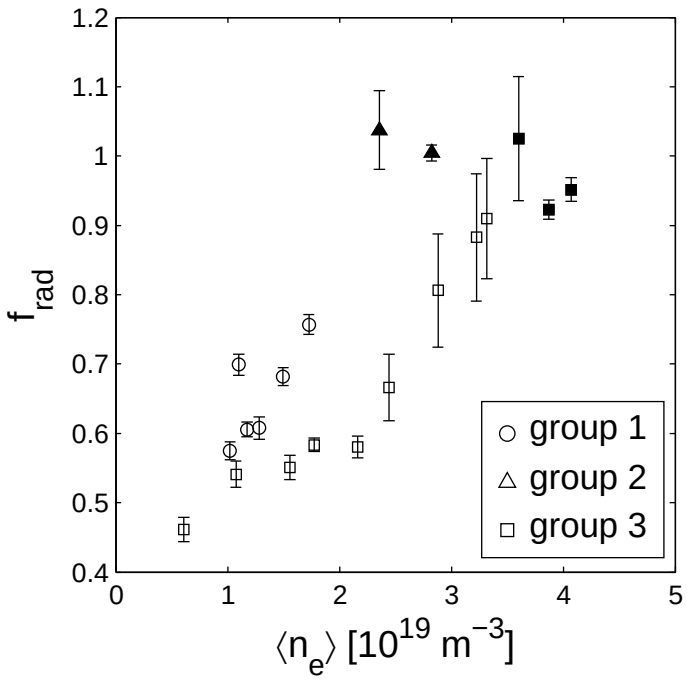

Figure 2. Radiated power fraction f_{rad} at the time of the RFA measurement plotted against the volume-averaged density $\langle n_e \rangle$ for discharge groups 1-3. Detached discharges are indicated by full symbols. The error bar represents the standard deviation of f_{rad} for the time of the probe reciprocation (~1 s).

From discharge groups 1 – 3, only group 3 comprises both attached and detached states and a wide range of densities. Unfortunately, the measurements of T_i in detached state are not available for group 3, because the RFA operation was not optimized for detached plasma (see sections 3 and 4) at the time of the measurements. Although characterized by identical I_p and similar B_t and q_a, individual discharge groups are characterized by different plasma configuration as well as the contact point (which is known to have a controlling influence on the scrape-off layer (SOL) properties [12]) and are, therefore, labeled separately throughout this paper.

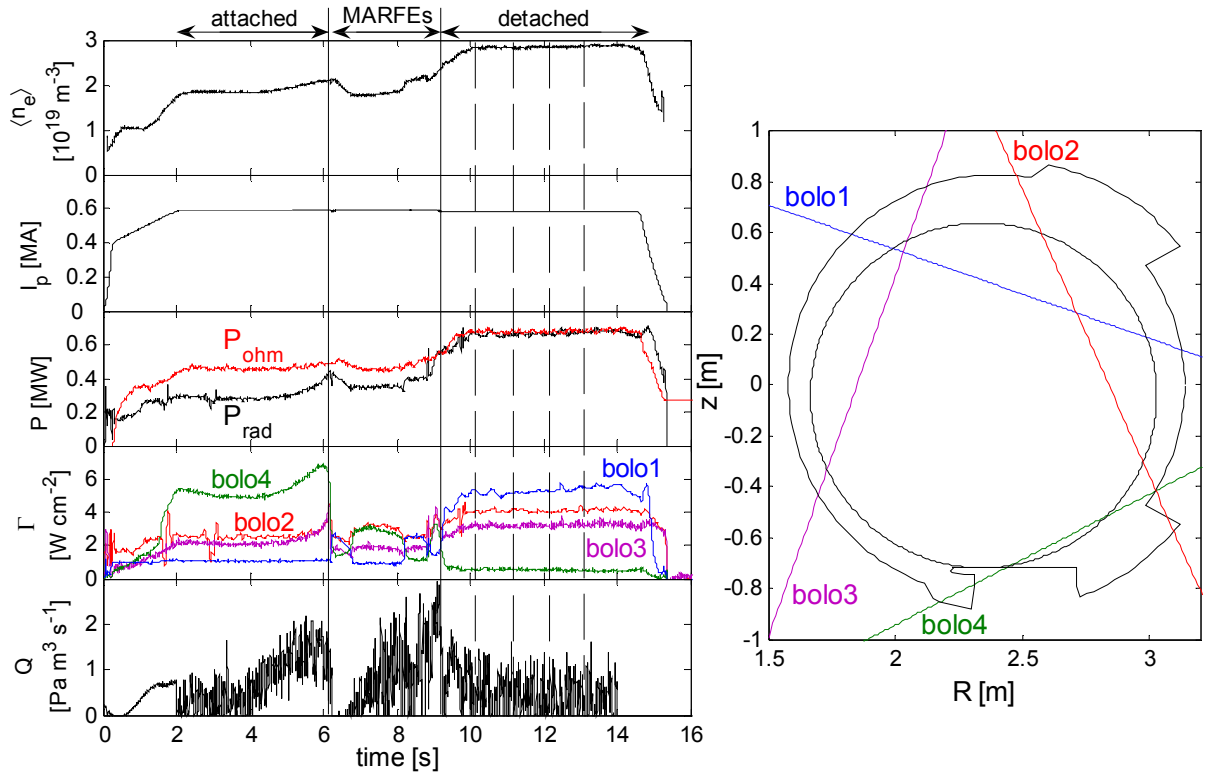

Figure 3. Right: Time traces of the volume-averaged density $\langle n_e \rangle$, plasma current I_p, ohmic power P_{ohm}, total radiated power P_{rad}, line integrated plasma emissivity Γ measured by selected bolometric viewing lines (left), and the gas injection rate Q for TS discharge #42406 from group 2. Steady-state detached phase, characterized by an inward shift of the radiating zone, is reached at t~10 s. Vertical dashed lines indicate RFA measurements.

In our experiments a limiter detachment [13] was reached by increasing the plasma density at constant I_p. A steady-state detached phase, often preceded by MARFEs, was identified visually by two CCD cameras viewing the plasma through a tangential port, and quantitatively by bolometer arrays. Figure 3 illustrates the transition from attached to detached state in TS discharge #42406 from the discharge group 2. The gas injection rate Q was controlled in real time by feedback on f_{rad} to reach $f_{rad} \approx 1$. The plasma was attached for $2 < t < 6.2$ s, followed by a MARFEing phase for $6.2 < t < 9.2$ s, finally detaching for $9.2 < t < 14.6$ s. As indicated by the measurements of line-integrated plasma emissivity, the radiating zone is peaked just above plasma contact point in the attached phase and moves inside the LCFS by about 30 cm and becomes poloidally symmetric in the detached phase (such variation of the plasma emissivity

was seen in other tokamaks [7, 14, 15]). Vertical dashed lines in figure 3 indicate four RFA reciprocations.

For discharges from group 3 the detachment is reached at $\langle n_e \rangle = 3.6 \cdot 10^{19}$ m^{-3}, whereas for discharge group 2 the detachment is reached already at $\langle n_e \rangle = 2.34 \cdot 10^{19}$ m^{-3}, indicating a lower density limit. From the limited dataset studied here it is not clear whether the difference in the density limit is because of the plasma configuration, or if it is because the discharges from groups 2 and 3 are separated by five years so that the charge state distribution and the amount of impurities in the plasma have changed.

3. Retarding field analyzer

The retarding field analyzer (RFA) is the most widely accepted diagnostic for SOL T_i measurements and has been successfully used in several magnetic fusion devices (e.g. [6, 11, 16-27]).

Technical details of the Tore Supra RFA, which is based on an earlier JET design [21], as well as the influence of the instrumental effects on T_i measurements were addressed in [6]. The RFA is mounted on a fast reciprocating drive located in a top port at $R = 2.53$ and moves vertically, figure 1. Real-time feedback based on magnetic measurements controls the probe position with respect to the LCFS during the reciprocation.

The RFA can be used to measure T_i, T_e, the sheath potential V_s, the ion saturation current density j_{sat} and the floating potential V_f. Its bi-directional capability allows also for the measurements of the parallel Mach number $M_{//}$. The unperturbed ion temperature is calculated as $T_i = (T_i^{HFS} + T_i^{LFS})/2$ [28] where the superscript HFS (LFS) indicates the analyzer facing the high-field side (low-field side) strike zone of the toroidal pump limiter. j_{sat} is calculated as $\sqrt{j_{sat}^{HFS} \cdot j_{sat}^{LFS}}$ (Eq.(7) in [29]). In what follows, the superscript HFS or LFS is dropped for clarity. It must be noticed that while the asymmetries on j_{sat} and T_i measured by each side of a bi-directional probe such as the RFA are understood to be due to the ion flow [28, 30, 31], the asymmetry on T_e, often measured by the RFA, is not well understood and is generally ignored in experiment, as it is also in this study. The difference in T_e on each side of the Mach probes was addressed only recently [29, 32]. However, a model that could explain the asymmetry in T_e is not

yet available. Thus T_e is also calculated as a mean value of the HFS and LFS analyzer measurements.

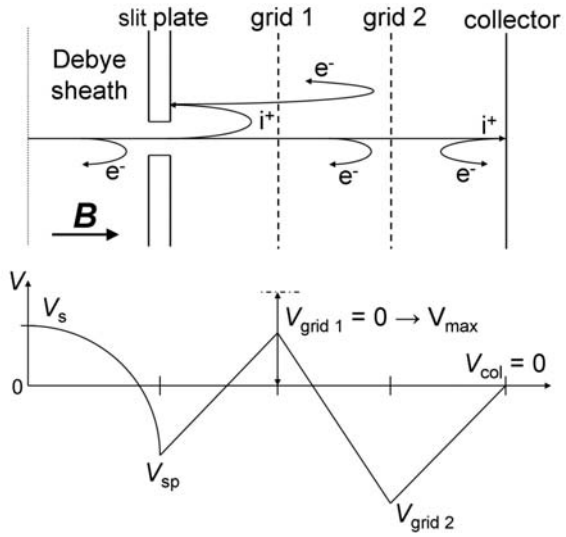

Figure 4. Principal components of the RFA and the biasing scheme applied for ion temperature measurements. All voltages refer to torus ground. V_{sp} is typically -90 → -150 V. $V_{grid\,2}$ is typically -200 V. $V_{\max}$ varies from 30 to 500 V, depending on the plasma conditions.

The schematic of the analyzer and the biasing scheme for T_i measurements are shown in figure 4 (alternative bias schemes aimed at the fast electrons measurements were used e.g. in [33]). The RFA is operated as follows. The probe is aligned with B. A Langmuir-probe bias waveform is applied to the slit plate, providing the measurements of T_e, j_{sat}, and V_f [6], figure 5.

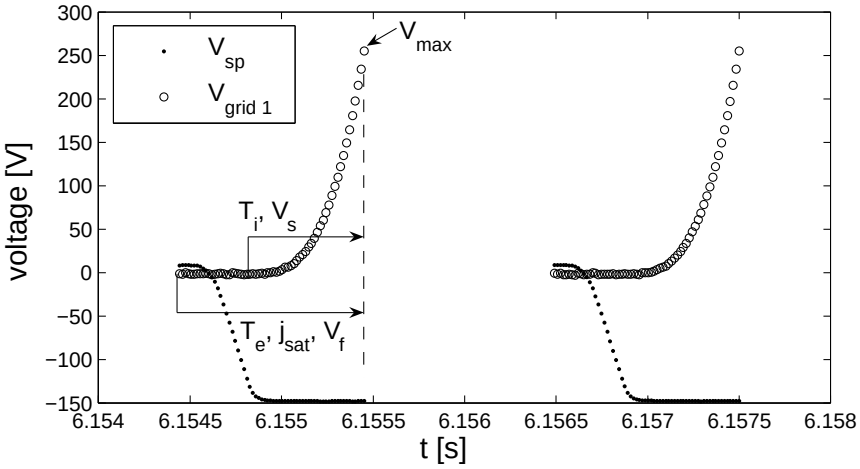

Figure 5. Time traces of the bias voltage applied on the slit plate V_{sp} and V_{grid1} (TS #42456, discharge group 1). Also indicated is the part of each waveform used for the measurements of T_e, j_{sat}, and V_f (slit plate) and T_i and V_s (grid 1). $V_{\max} = \max(V_{grid1})$. Individual waveforms are separated by 1 ms.

A fraction of the incident ion flux is transmitted through the slit. The ion transmission through the slit is selective and leads to an overestimation of T_i by 4–12% for the slit plate geometry used for Tore Supra RFA [6]. This effect is taken into account. Once the slit plate voltage is negative enough to repel most of the thermal electrons (typically -90 → -150 V), the voltage on grid 1, V_{grid1}, is swept from $0 \rightarrow V_{\max}$ (with $V_{\max} > 0$ and 0 referring to torus ground), figures 4 and 5, to obtain the ion current characteristic on the collector. A constant negative bias, lower than that applied on the slit plate, is applied on grid 2, V_{grid2}, in order to repel the remaining fast electrons not reflected by the slit plate and to suppress any secondary electrons emitted from the rear of the slit plate, grid 1 or collector. The collector is held at torus ground and measures the incident current, I_{col}.

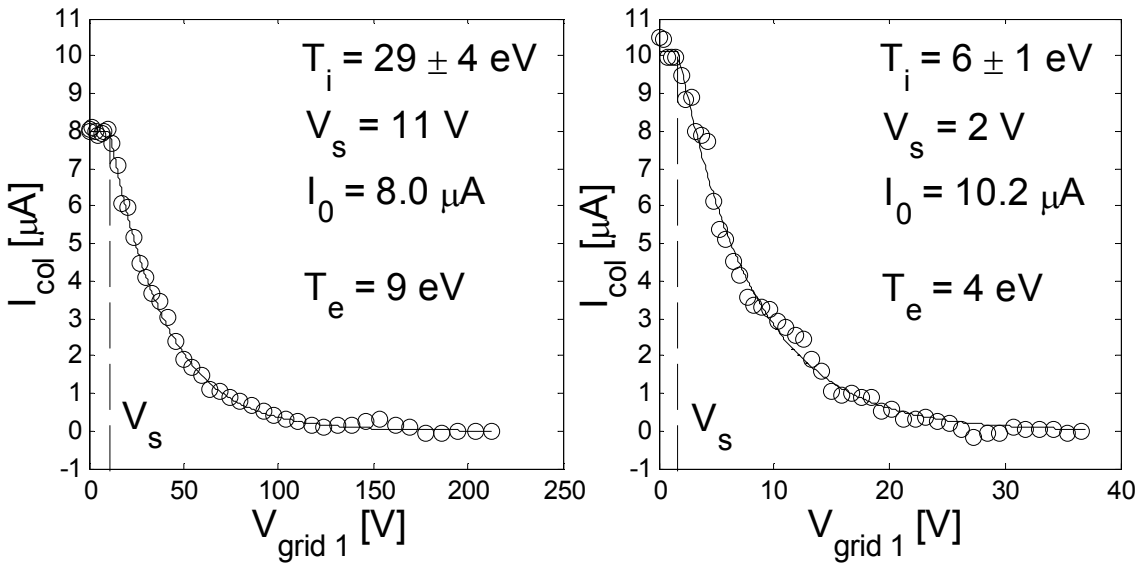

Figure 6. Typical RFA I-V characteristics for two different maximum bias voltages applied on grid 1. Left: attached plasma (TS discharge #42455 from group 1 at t =5.0 s, $\langle n_e \rangle = 1.25 \cdot 10^{19}$ m^{-3}*, 6 mm outside the LCFS). Right: detached plasma (TS discharge #42463 from group 2 at t = 7.2 s,* $\langle n_e \rangle = 2.3 \cdot 10^{19}\, m^{-3}$*, 3 mm inside the LCFS).* T_i*,* V_s*, and* I_0 *were obtained from the fit Eq.(2) to the I-V characteristic.* T_e *was measured by the slit plate working as a Langmuir probe. All parameters were measured by the analyzer facing the HFS.*

Figure 6 shows typical current-voltage (*I-V*) characteristics (I_{col} against V_{grid1}) measured by the RFA. For certain range of $V_{grid1} = 0 \rightarrow V_s$ the collector current is approximately constant since all ions gain a parallel energy of eZ_iV_s (with eZ_i being ion charge) in the collisionless Debye sheath in front of the slit plate. For $V_{grid1} > V_s$ the collector current decreases as the retarding potential begins to repel the slowest ions of the distribution. Assuming that fuel ions dominate the incident flux, I_{col} can be expressed as [21]:

$$I_{\mathrm{col}} = A_{\mathrm{slit}} eZ_i \int_u^\infty dv_{//} v_{//} \xi(v_{//}) f(v_{//}) \qquad (1)$$

where A_{slit} is the slit area, $\xi(v_{//})$ is the total transmission factor that includes the transmission of the slit and the grids, $u = \sqrt{2eZ_{\mathrm{i}}V_{\mathrm{grid1}} / m_{\mathrm{i}}}$ (with m_{i} being the ion mass) is the minimum ion

velocity needed to overcome the repulsive force of grid 1 biased to V_{grid1}, and $f(v_{//})$ is the parallel ion velocity distribution. Assuming, in addition, that $f(v_{//})$ is Maxwellian, T_i can be obtained from a fit to the decaying part of the *I-V* characteristic:

$$I_{\mathrm{col}} = I_0 \exp\left[-\frac{Z_\mathrm{i}}{T_\mathrm{i}} \left(V_{\mathrm{grid1}} - V_s \right) \right]. \tag{2}$$

Since V_{sp} and V_{grid1} are not swept simultaneously, figure 5, the measurements of T_e and T_i by Tore Supra RFA are separated by ~0.5 ms (during which the probe moves radially by less than 1 mm). In principle, one could sweep both electrodes simultaneously and use only grid 2 to repel the electrons from the collector. However, repelling most of the thermal electrons by the slit plate may prevent the ionization of the neutral gas inside the RFA cavity that could affect T_i measurements (see e.g. figure 4(b) in [34]).

The spatial resolution of the RFA is defined by the radial extension of the probe collection area increased by the radial displacement of the probe during the measurement of a single *I-V* characteristic. For T_e, j_{sat}, and V_f the collection area is defined by the orifice drilled into the CFC protective housing, through which the plasma flows towards the slit plate. For T_i and V_s the collection area is defined by the slit plate aperture. The orifice and the aperture dimensions are respectively 7 mm × 3 mm and 5 mm × 30 μm. For discharge groups 1 and 2 both the orifice and the aperture were oriented horizontally and for group 3 vertically. The vertical displacement of the RFA during the measurement of a single *I-V* characteristic is about 1 mm, except at the target position where the probe velocity is zero. Since the RFA is located close to the top of the plasma, the vertical and the radial displacement are almost identical. Therefore, for discharge groups 1 and 2 the radial resolution is about 4 mm for T_e, j_{sat}, and V_f, and about 1 mm for T_i and V_s. For discharge group 3 the radial resolution of the RFA is approximately 8 mm for T_e, j_{sat}, and V_f, and about 6 mm for T_i and V_s. As shown in Sec. 4, both the radial separation of T_i and T_e measurements as well as the radial resolution of the probe are much smaller than the typical SOL temperature and density *e*-folding lengths.

Returning to the bias voltage applied to grid 1, a wide range of T_i reported in our study required an optimization of the voltage range for given plasma conditions. In general, the

maximum voltage applied to grid 1, $V_{\max}$, should be low enough so that the major part of the *I-V* characteristic is sampled above the noise level of I_{col}, but yet high enough to capture the exponentially decaying slope of the *I-V* characteristic. This implies the optimal value of $V_{\max}$ of about $V_s + 3T_i$. Since T_i and V_s are a priori unknown, $V_{\max}$ can only be adjusted for a given plasma conditions by repetitive measurements. For attached discharges, the optimal value of $V_{\max} = 200 - 500\,\mathrm{V}$ (figure 6, left), depending on applied heating power and plasma density. For detached discharges the optimal value of $V_{\max}$ was found to be an order of magnitude smaller (figure 6, right). Further optimization implemented for V_{grid1} in Tore Supra RFA include a real-time feedback on $V_{\max}$ based on the probe position with respect to the LCFS which accounts for the radial variation of T_i and V_s and a quadratic waveform instead of the usually applied simple linear sweep (e.g. [17, 20, 23-25]) in order to acquire more points of the *I-V* characteristic at the steepest slope of I_{col} (figure 5).

Finally, it is worth mentioning that j_{sat} from the RFA slit plate is found to be systematically lower than that measured simultaneously by a tunnel probe (TP) [35] in Tore Supra SOL (figure 7). A similar discrepancy was observed earlier in JET between j_{sat} measured by the RFA [24] and the turbulent transport probe [36]. In [37] this discrepancy was attributed to the attenuation of ion flux due to the deflection of ions in the magnetic pre-sheath above the RFA protective walls attached to the slit plate, and quantified using particle-in-cell (PIC) simulations. The attenuation decreases the effective probe collecting area, so that j_{sat} inferred from the ion saturation current measurements is smaller by a factor γ_{att} (referred to as attenuation factor). In the Tore Supra RFA the incident ion current can be attenuated in a similar way on the inner walls of the CFC orifice through which the plasma flows towards the slit plate (see [6]). The ratio of j_{sat} measured by the TP and the RFA provides an approximate value $\gamma_{att} \cong 0.82 + 0.03T_e \cong 1 \to 2$ (the TP has a collecting area clearly defined by the tunnel orifice [35] and is therefore immune to the attenuation [29]). The dependence of γ_{att} on T_e is consistent with the scaling of the magnetic pre-sheath thickness [38, 39]. Similar values of γ_{att} were found in unpublished PIC simulation study which reproduces [37] for Tore Supra RFA geometry. In this paper, the experimental values of j_{sat} are multiplied by γ_{att}.

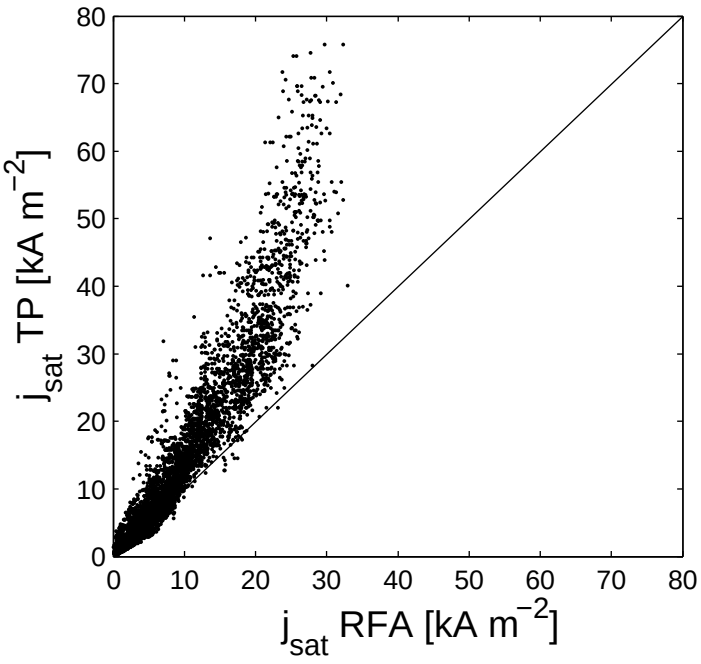

Figure 7. Comparison of the ion saturation current densities measured at the similar radii in the SOL simultaneously by the RFA and the TP (TS discharges #39445-39519).

4. Experimental results

4.1. Influence of the simultaneous variation of $\langle n_e \rangle$ and f_{rad} on the SOL parameters

Figure 8 illustrates the radial profiles of the SOL T_i and T_e and electron density n_e measured for discharges from groups 1 and 2. $n_e = j_{sat} / [0.35 e^{1.5} \sqrt{(T_i + T_e)/m_i}]$ [30] is evaluated only at the radii where the measurements of T_i, T_e and j_{sat} are available. Profiles are sorted according to the increasing $\langle n_e \rangle$ (which coincides with the increase of f_{rad}, figure 2). Columns 1 – 4 represent the measurements in attached plasmas, columns 5 – 6 represent the detached state. For comparison, T_e measured simultaneously by a Langmuir probe (LP) mounted on the second reciprocating drive separated from the RFA by 120° toroidally is also plotted in columns 3 and 4. T_e obtained from the LP is comparable to T_e from the RFA. Similar agreement was found in [11].

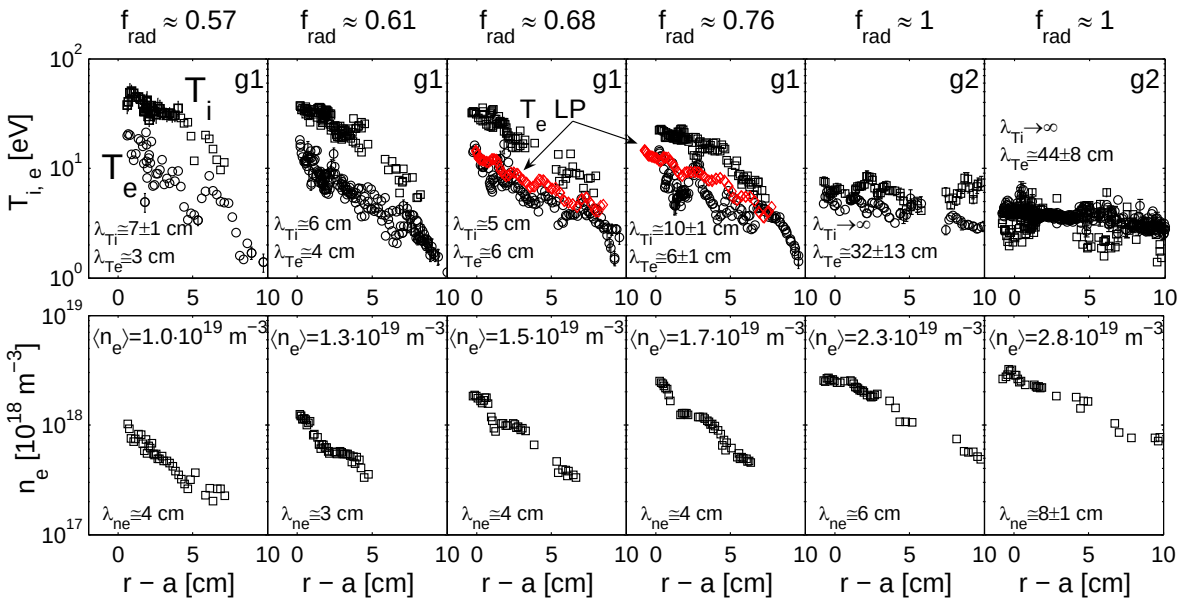

Figure 8. SOL T_i and T_e (top row) and n_e (bottom row) measured for different volume-averaged plasma densities $\langle n_e \rangle$ and radiated power fractions f_{rad} for selected discharges from groups 1 and 2. Columns 1 – 4: attached plasma. Columns 5 – 6: detached plasma. The profiles are plotted against the distance from the LCFS $r-a$ and sorted according to increasing $\langle n_e \rangle$ (which coincides with the increase of f_{rad}). Also indicated are the approximate values of the e-folding lengths evaluated 0 – 5 cm outside the LCFS (confidence intervals smaller than 1 cm are not stated).

Both, T_i and T_e decreases with the increase of $\langle n_e \rangle$ and f_{rad}. However, coherent variation of $\langle n_e \rangle$ and f_{rad} does not allow identifying individual influence of these parameters on SOL temperatures. Within the range of $\langle n_e \rangle$ and f_{rad} shown in figure 8, T_i decreases by more than an order of magnitude. T_e decreases only by a factor of ~3 (see also figure 10(a)). As a consequence, the ion-to-electron temperature ratio τ at the LCFS varies from ~3 to ~1 from lowest to highest $\langle n_e \rangle$ and f_{rad}. Within the same range of $\langle n_e \rangle$ and f_{rad}, the SOL density changes by a factor of 3 (see also figure 10(c)).

Also indicated in figure 8 are the temperature and density *e*-folding lengths (λ_{Ti}, λ_{Te}, λ_{ne}) evaluated 0 – 5 cm outside the LCFS. λ_{Ti} tends to be longer than λ_{Te}, which could be explained

by larger parallel electron losses relative to the ion losses, given by a difference in the sheath heat transmission coefficient of ions and electrons [40]. On the other hand, the radial profiles from column 3 indicate that such difference in the ion and electron temperature *e*-folding lengths might not be systematic. Detached discharges from group 2 are characterized by almost flat SOL temperature profiles as well as up to a factor of 2 longer λ_{ne} compared to attached discharges. This could be explained by two simultaneously acting effects. First, there is a difference in geometry between the attached discharges from group 1 and the detached discharges from group 2. For group 1 the contact point is on both the TPL and the APL whereas for group 2 the plasma is shifted away from the APL and the contact point is on the TPL only (figure 1). In such configuration the magnetic-field-aligned plasma filaments, or "blobs", initiated by a ballooning-type instability in the unfavourable curvature region on the LFS can propagate freely out to the wall, filling the available volume outside the LCFS. This could lead to a broad SOL, as demonstrated by Mach probe measurements in Tore Supra [12] as well as most divertor machines [41]. However, the flattening of the SOL profiles could be also associated with the plasma detachment, as shown by Langmuir probe measurements of T_e e.g. in DITE tokamak [7, 14].

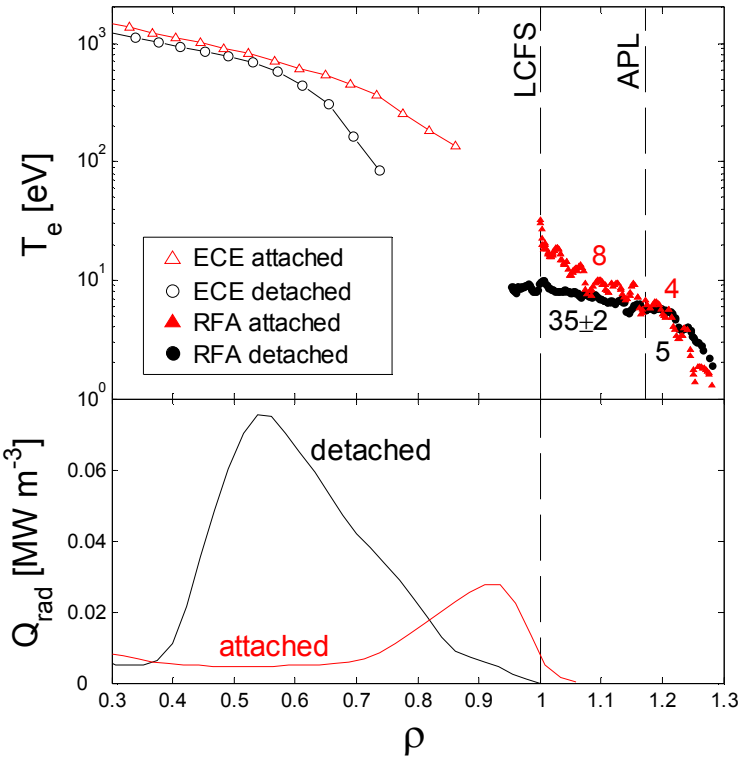

Figure 9. TS discharge #42959. Top: Electron temperature profiles measured by ECE and RFA diagnostics in attached and detached plasma. Numbers indicate the approximate values of the

SOL electron temperature e-folding lengths (in cm) for $\rho < 1.2$ *and* $\rho > 1.2$ *(confidence intervals smaller than 1 cm are not stated). Bottom: Poloidally averaged plasma emissivity* Q_{rad} *in attached and detached phase obtained from the tomografic reconstruction. Profiles are plotted against the distance from the plasma centre normalized to minor radius* $\rho = r/a$ *with a = 0.68 m. Vertical lines indicate the position of the LCFS and the antenna protection limiter (APL). Plasma configuration is identical to that of discharge group 2 shown in figure 1.*

In order to exclude the effect of the plasma geometry on the temperature *e*-folding lengths, a discharge with the configuration identical to that of group 2 but comprising both attached and detached phase was performed (TS discharge #42959). The RFA target position for the reciprocation in the detached phase was extended to 3.5 cm inside the LCFS to cover a broader range of radii. Radial profiles of SOL T_e measured by the RFA as well as the core T_e measured simultaneously by the electron cyclotron emission (ECE) diagnostic located at the outer midplane are shown in figure 9. The profiles are plotted against the distance from the plasma centre normalized to the minor radius $\rho = r/a \cong 0.55$ (with $a = 0.68$ m). Also plotted are the poloidally averaged plasma emissivity profiles Q_{rad}, obtained from the tomografic reconstruction of the bolometric data measured simultaneously with T_e. Transition to the detached state is associated with the steeping of the T_e profile around the maxima of Q_{rad}, followed by almost flat T_e profile just inside the LCFS and in the SOL for $\rho < 1.2$. The steepening of the T_e profile measured in the detached plasma in the region where the plasma radiates most strongly suggests that the electron heat diffusivity χ_e could increases with radius in this region. This is based on the assumption that the divergence of the conducted electron heat flux density $q_e = -e\chi_e n_e \nabla_r T_e$ is balanced by the radiative losses. Then, the steepening of the T_e profile should coincide with an increase of the electron heat diffusivity χ_e, with $\nabla_r \chi_e \approx 1\,\mathrm{m\ s^{-1}}$ (for this discharge the electron density $n_e \cong 3.2 \rightarrow 2.5 \cdot 10^{19}\ \mathrm{m^{-3}}$ for $\rho = 0.45 \rightarrow 0.7$). The electron power loss due to radiation can be also partially compensated by the gains due to equipartition term, making $\nabla_r \chi_e$ smaller. However, the equipartition term cannot be evaluated for this discharge as the ion temperature in the confined plasma was not measured. In attached state the maxima of Q_{rad} is located just inside the LCFS and the electron temperature gradient increases only little from the core to the SOL. In

detached state λ_{Te} for $1 < \rho < 1.2$ is more than a factor of 4 longer compared to that measured in attached state. Note also that λ_{Te} measured in attached state for $1 < \rho < 1.2$ is by 25% longer compared to that measured for discharge group 1 at similar density (column 4 in figure 8), which, as discussed above, could be explained by a difference in the plasma configuration. As seen in figure 9 in the shadow of the APL λ_{Te} becomes substantially shorter independently on plasma state, which may be related to shorter connection length. In detached phase the core electron temperature ($T_e(\rho = 0)_{det} \approx 1.4$ keV) is lower compared to attached state ($T_e(\rho = 0)_{att} \approx 1.9$ keV) because of the difference in the plasma density ($\langle n_e \rangle_{det} = 3.0 \cdot 10^{19}$ m^{-3}, $\langle n_e \rangle_{att} = 1.9 \cdot 10^{19}$ m^{-3}), following roughly the total pressure conservation (the total diamagnetic energy it the attached and detached state is $E_{att} \cong 9.6 \cdot 10^{-2}$ MJ and $E_{det} \cong 12 \cdot 10^{-2}$ MJ, respectively, so that $\langle n_e \rangle_{att} T_e(0)_{att} / \langle n_e \rangle_{det} T_e(0)_{det} \approx 0.86$ is close to $E_{att} / E_{det} \approx 0.80$, assuming that core T_i follows T_e). Also worth noting is that the SOL density profiles for this discharge were found to be characterized by similar λ_{ne} independently on the plasma state, which is consistent with the results reported from DITE [7]. Unfortunately, the measurements of SOL T_i by RFA are not available for this discharge due to the absence of the collector signal.

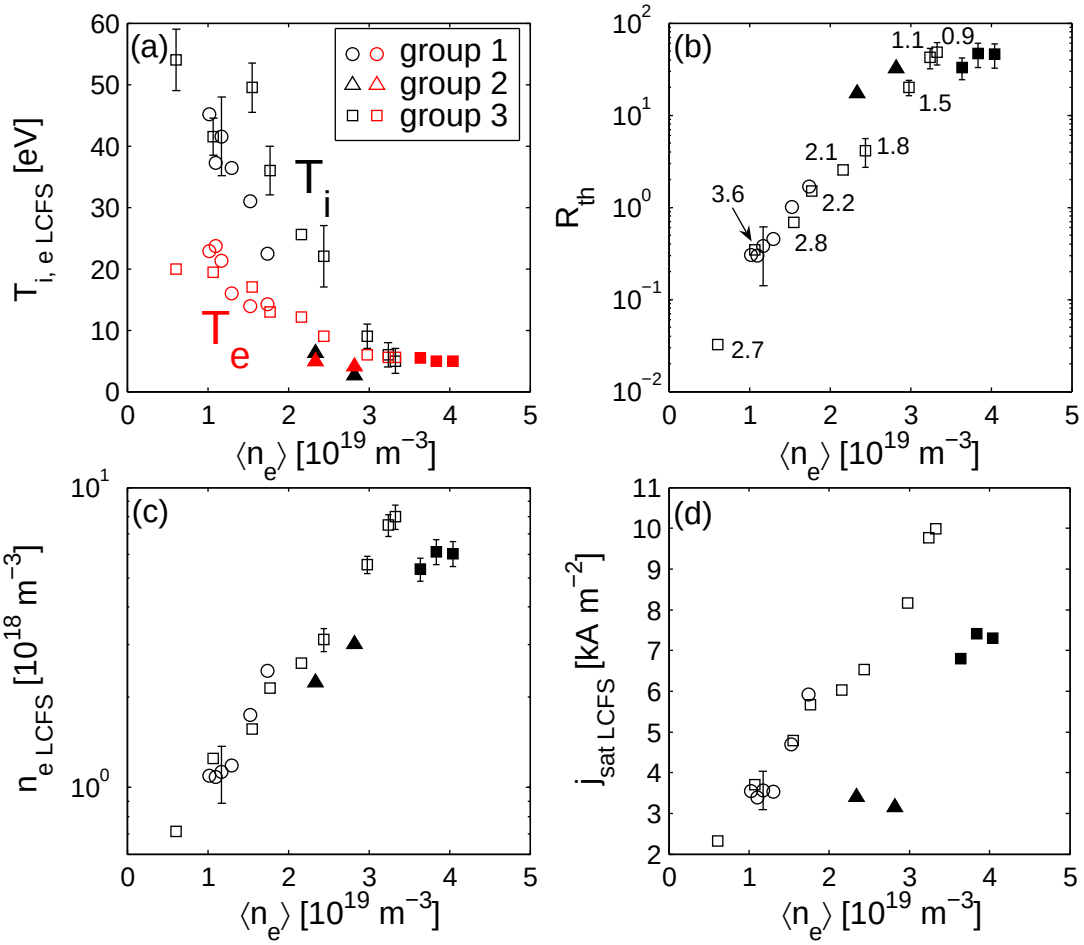

Figure 10. (a) SOL T_i and T_e at the LCFS. (b) The ratio of the ion transit time through the SOL to the ion-electron thermalization time R_{th} evaluated at the LCFS (numbers indicate the approximate value of the ion-to-electron temperature ratio 2 – 3 cm outside the LCFS for discharge group 3). (c) The electron density at the LCFS. (d) The ion saturation current density at the LCFS. All parameters are plotted against the volume-averaged density $\langle n_e \rangle$. Detached discharges are indicated by full symbols. For detached discharges from group 3 the measurements of T_i are not available and R_{th} is calculated assuming $T_i = T_e$.

Returning to the SOL ion-to-electron temperature ratio τ, the decrease of τ with the increase of density is intuitive as the increase of $\langle n_e \rangle$ strengthens the ion-electron collisional coupling. Figure 10(b) demonstrates this quantitatively and shows the ratio of the parallel ion transit time through the SOL to the ion-electron thermalization time evaluated at the LCFS

$R_{th} = \tau^{i}_{//} / \tau^{ie}_{th}$ for discharge groups 1–3. R_{th} is plotted against $\langle n_e \rangle$. Here $\tau^{i}_{//} \propto L_{//} / \sqrt{T_i + T_e}$, $\tau^{ie}_{th} \propto T_e^{3/2} / n_e$, and $L_{//}$ is the parallel connection length. Also indicated are the approximate values of the ion-to-electron temperature ratio τ evaluated 2 – 3 cm outside the LCFS. R_{th} is the average number of collisions with electrons suffered by each ion along its way through the SOL. Thermal equiparitition is, therefore, expected for $R_{th} >> 1$ (in fact, very strong collisionality might be needed in order to balance the cooling effect of the Debye sheath on electrons). $\tau \approx 1$ is reached just at $R_{th} > 30$.

For detached discharges from group 3 only an upper estimate of T_i is available, since the maximum bias voltage applied to grid 1 was fixed to 340 V and the RFA was equipped with thicker slit plate (250 μm compared to 100 μm for discharge groups 1 and 2). Such voltage and the plate thickness are too high to allow calculating the HFS-analyzer ion temperature T_i^{HFS}, Sec. 3, in detached plasma in TS. This is because the HFS analyzer is characterized by lower effective ion temperature and receives lower currents ($I_{col} < 3\,\mu A$ compared to $I_{col} < 10\,\mu A$ received by the LFS analyzer in detached discharges from group 3) for the plasma flows from the LFS to the HFS [28], which is the case of the discharges studied here. The LFS-analyzer ion temperature $T_i^{LFS} < 10\,eV$ at the LCFS provides an upper estimate of T_i for detached discharges from group 3. Therefore, for the detached discharges from group 3, R_{th} was calculated assuming $T_i = T_e \cong 5\,eV$ at the LCFS. This could lead to an overestimation of R_{th} by up to ~30%.

Interesting is the comparison of R_{th} and τ from the current study in the deuterium plasma with the ones calculated from the RFA measurements in the helium plasma [11]. For example, at $\langle n_e \rangle \cong 3 \cdot 10^{19}$ m^{-3} characterized here by $R_{th} \approx 20$ and τ close to one, in [11] $R_{th} \approx 10$ and $\tau \approx 4$ (the central-line-averaged density $\bar{n}_e \cong 4 \cdot 10^{19}$ m^{-3} in [11] corresponds to the volume-averaged density $\langle n_e \rangle \cong 3 \cdot 10^{19}$ m^{-3}). Since R_{th} is independent of ion mass and j_{sat} is similar in both experiments at $\langle n_e \rangle \cong 3 \cdot 10^{19}$ m^{-3}, lower value of R_{th} in [11] is mainly due to higher temperatures at the LCFS in the helium plasma. Higher T_i could be due to lower charge-exchange losses (the reaction cross section is by up to an order of magnitude smaller in helium compared to deuterium) [9] as well as lower radiative losses in the edge plasma (in [11] $f_{rad} \approx 0.6 - 0.7$ at $\langle n_e \rangle \cong 3 \cdot 10^{19}$ m^{-3}, i.e. ~30% lower). In addition, in [11] T_i was calculated

assuming pure He^{2+} plasma in Eq. 2. This assumption might not be valid at highest densities where the relative abundance of He^{+} can exceed He^{2+} [8] and could lead to an overestimation of T_i by up to a factor of 2.

Figures 10(c)-(d) shows the electron and the ion saturation current densities at the LCFS, n_{eLCFS} and $j_{satLCFS}$, plotted against $\langle n_e \rangle$ for discharge groups 1 – 3. For detached discharges from group 3 n_{eLCFS} was, due to the lack T_i measurements, calculated assuming $T_i = T_e$ (this assumption is justified by high ion-electron collisionality, as discussed in the previous paragraph and shown in figure 10(b)). For discharge groups 1 – 2 and for attached discharges from group 3, n_{eLCFS} increases monotonically with $\langle n_e \rangle$. $j_{satLCFS}$ follows the similar trend as n_{eLCFS}, although its increase with $\langle n_e \rangle$ is weaker, which is because of the decrease of temperatures with the increase of the plasma density. The transition from attached to detached state in group 3 is characterized by about 25 – 30% drop of n_{eLCFS} as well as $j_{satLCFS}$, indicating low degree of ionization in the plasma periphery. This is consistent with a very rough estimate of the ionization mean free path $\lambda_{mfp} \approx v_n / \left(n_e \langle \sigma v \rangle \right)$ (with $v_n = \sqrt{k_B T_n / m_D}$ being the mean velocity of the neutrals and $\langle \sigma v \rangle$ the ionization reaction rate [42]) of the deuterium neutrals released from the wall, assuming the temperature of the neutrals of $T_n = 500\,\mathrm{K}$ and radially constant edge electron temperature and density given by T_{eLCFS} and n_{eLCFS}, respectively. For detached discharges from group 3 ($T_{eLCFS} \cong 5\,\mathrm{eV}$, $n_{eLCFS} \cong 6 \cdot 10^{18}\,\mathrm{m^{-3}}$) $\lambda_{mfp} \approx 23\,\mathrm{cm}$, so that the probability of the neutral to be ionized in the SOL or just inside the LCFS is low. λ_{mfp} is also comparable to the inward shift of the radiating zone measured typically in detached plasma in Tore Supra (figure 9). Since $\langle \sigma v \rangle$ is a strong function of the electron temperature for the temperatures of the order of electron volts, the increase of T_{eLCFS} by a factor of 2 at fixed density leads to $\lambda_{mfp} \approx 3$ cm. Large difference in $j_{satLCFS}$ in attached and detached plasmas is seen also at $\langle n_e \rangle \cong 2.5 \cdot 10^{19}\,\mathrm{m^{-3}}$ by comparing the data from discharge groups 2 and 3 (however, the difference in the plasma configuration for discharge groups 2 and 3, figure 1, may also play a role here). In this particular case, the drop of $j_{satLCFS}$ coincides with almost similar drop of temperatures, so that n_{eLCFS} changes only little.

Figure 11 shows the total (ion and electron) heat transmission coefficient γ as well as the parallel heat flux density $q_{// LCFS}$ at the LCFS for discharge groups 1 – 3, calculated from the measurements shown in figure 10. γ and $q_{// LCFS}$ are plotted against the fraction of the input power entering the SOL, $f_{SOL} = 1 - f_{rad}$ ($f_{SOL} < 0$ is due to the inaccuracy in the measurements of f_{rad}). γ is calculated as [40]:

$$\gamma = \frac{2.5 T_{i\,LCFS}}{T_{e\,LCFS}} + 2 - 0.5 \ln\left[\left(2\pi \frac{m_e}{m_i}\right)\left(1 + \frac{T_{i\,LCFS}}{T_{e\,LCFS}}\right)\right], \tag{3}$$

assuming that the floating potential is small compared to V_s and the secondary electron emission can be neglected. $q_{// LCFS}$ is calculated as:

$$q_{// LCFS} = \gamma\, j_{sat\,LCFS} T_{e\,LCFS}\,. \tag{4}$$

Also shown for comparison in figure 11 is γ and $q_{// LCFS}$ calculated for $T_i = T_e$ (for detached discharges from group 3 the values overlap as the measurements of T_i are not available for these discharges and $T_i = T_e$ is assumed). Both γ as well as the $q_{// LCFS}$ increases with f_{SOL}, following roughly the power balance. In detached plasma $q_{// LCFS}$ is by a factor of ~3–5 lower compared to attached discharges with high f_{SOL}. At low f_{SOL} the assumption of equal temperatures does not affect strongly the values of γ and $q_{// LCFS}$. At high f_{SOL}, however, the assumption of equal temperatures leads to an underestimation of γ as well as the heat flux density at the LCFS by up to a factor of 1.6. Since the ion-to-electron temperature ratio typically increases with radius in the SOL (see e.g. figure 7 in [11]) because $\lambda_i > \lambda_e$, the heat flux density and the total integrated power in the SOL calculated only from T_e measurements can be underestimated by even larger factor.

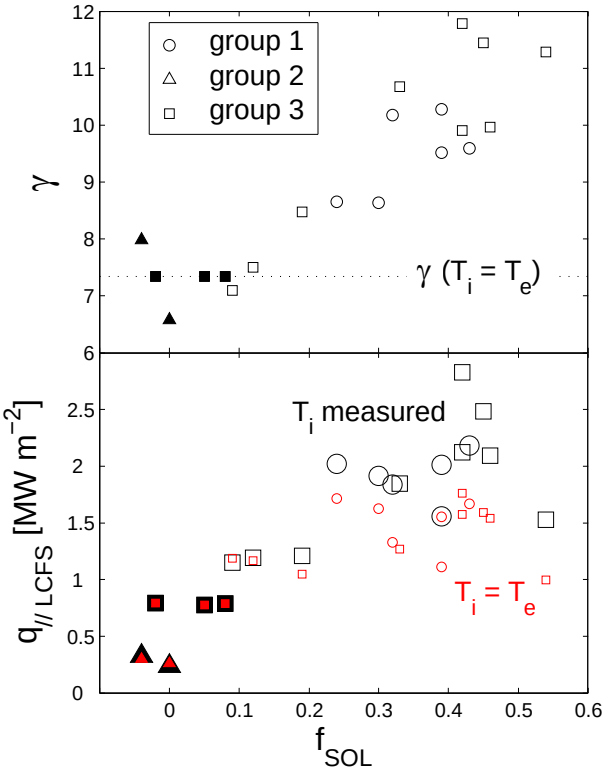

Figure 11. Top: total heat transmission coefficient γ calculated from the temperatures at the LCFS using Eq. (3). γ calculated assuming $T_i = T_e$ is also shown. Bottom: parallel heat flux density at the LCFS $q_{// LCFS}$ calculated from Eq.(4) using measured T_i (large symbols) and assuming $T_i = T_e$ (small symbols). Detached discharges are indicated by full symbols. For detached discharges from group 3 the measurements of T_i were not available and $T_i = T_e$ is assumed.

4.2. Correlation between f_{rad} and the SOL temperatures

The coherent variation of $\langle n_e \rangle$ and f_{rad} in the dataset studied in the previous section does not allow to identify the individual effects of these parameters on the SOL temperatures. Such coherent variation may also play a role in the earlier experiments aimed at the variation of SOL temperatures with the plasma density [8, 10, 11] in which the variation of SOL T_i and T_e was linked to the variation of plasma density and the influence of f_{rad} was not addressed. For example, within the range of $\langle n_e \rangle$ covered in [11] $f_{rad} = 0.45 \rightarrow 0.75$.

The extent of the database of the RFA measurements in Tore Supra allows selecting discharges with all parameters except f_{rad} being almost identical. One such example, a representative of systematic observations, is illustrated in figure 12. This figure shows the radial profiles of SOL T_i as well as T_e measured in the SOL and in the confined region at $f_{rad} = 0.64$ (TS discharges #42656–7) and $f_{rad} = 0.83$ (TS discharge #42655). Other plasma parameters were almost identical ($I_p = 1.0$ MA, $B_t = 3.8$ T, $q_a \cong 4.8$, $\langle n_e \rangle = 3.0 \cdot 10^{19}$ m^{-3}, $P_{heat} = P_{ohm} + P_{ICRH} = 0.8 + 0.9$ MW, attached state). Core T_e was measured by the Thomson scattering (ThS) and ECE diagnostics, respectively. Core T_i was not measured for these discharges but the profile from a similar discharge is shown for comparison. The plasma dimensions and the contact point were identical to that of the discharge group 1 (figure 1 and table 1). Higher f_{rad} in the discharge #42655 was due to higher concentration of oxygen and slightly higher concentration of metallic impurities (the concentration of carbon was similar in both case). For the discharge #42655 the central-line-averaged effective ion charge calculated from the visible bremsstrahlung radiation $Z_{eff} \cong 2.0$. For the discharges #42656-7 $Z_{eff} \cong 1.6$. TS discharge #42655 was proceed by pulses characterized by $I_p = 0.54$ MA and $q_a \cong 9$. Therefore, higher impurity concentration in #42655 could be explained by the variation of the edge safety factor which changes the location of the plasma-wall interaction.

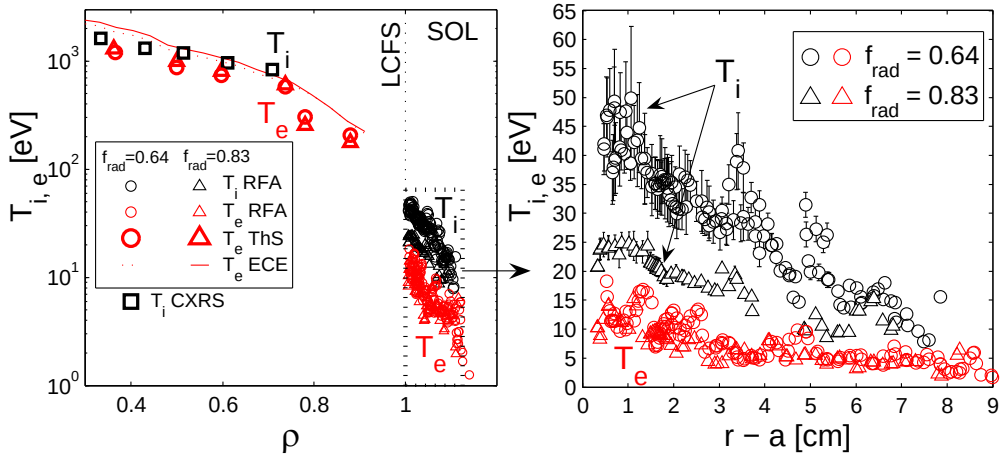

Figure 12. Radial profiles of ion and electron temperatures measured in two discharges characterized by different f_{rad}. Other plasma parameters were almost identical ($I_p = 1.0$ MA, $B_t = 3.8$ T, $\langle n_e \rangle = 3.0 \cdot 10^{19}$ m^{-3}, $P_{heat} = P_{ohm} + P_{ICRH} = 0.8 + 0.9$ MW). Inside the LCFS T_e is measured by the Thomson scattering (ThS) and electron cyclotron emission (ECE) diagnostics.

Left: Temperatures plotted against the distance from the plasma centre normalized to minor radius, $\rho = r/a$ *with* $a = 0.72$ *m. Core* T_i *was not measured for these discharges but the profile from a similar discharge #39598 is shown (* $I_p = 1.2$ *MA,* $B_t = 3.8$ *T,* $\langle n_e \rangle = 2.8 \cdot 10^{19}$ m^{-3}, $P_{heat} = P_{ohm} + P_{ICRH} = 1.0 + 0.8$ *MW). Right: SOL* T_i *and* T_e *measured by the RFA plotted against the distance from the LCFS.*

As seen from figure 12, the increase of f_{rad} coincides with the decrease of SOL T_i by almost a factor of 2, whereas SOL T_e is much less affected. In addition, core electron temperature changes only little with the increase of f_{rad} (the variation in much smaller than the difference in T_e measured by ThS and ECE). No temperature measurements are available just inside the LCFS. However, in order to connect the SOL profiles, both temperature gradients have to increase in this region.

The large variation of SOL T_i with f_{rad} and almost constant SOL T_e may be surprising as the variation of the radiated power is intuitively linked with the variation of SOL electron rather than ion temperature. Since P_{rad} comes mainly from line radiation due to the interaction of electrons with impurity ions and neutrals in the edge of the confined region, the increase of P_{rad} should lead to a lower edge T_e. SOL T_e is expected to simply follow the variation of edge T_e by radial transport. However, we argue that the drop of T_e in the edge of the confined region due to radiation strengthens the energy transfer from ions to electrons via collisional coupling ($Q_{ie} \propto (T_i - T_e) n_e^2 T_e^{-3/2}$). This may lead to the decrease the edge ion temperature. When T_e becomes very low relative to T_i, so that the cross-field heat flux in the electron channel becomes small, the radiative losses on electrons are, through equipartition term, compensated from the ion channel. Note that the decrease of SOL T_i by a factor of 2 coincides with a similar decrease of f_{SOL} (0.36 → 0.17), indicating that the power lost due to radiation comes really from the ion channel. The edge T_e is sustained at a low value, balanced between the radiative losses and gains due to equipartition. Other volumetric loss terms such as charge-exchange collisions of ions with neutrals, recombination and ionization could also play a role in the ion and electron power balance, but are typically much smaller compared to the radiative losses on electrons.

These qualitative arguments were verified by modelling the ion and electron temperature profiles in the edge of the confined plasma using power balance equations. Radiation and

equipartition were the only source terms taken into account in the model. Further approximations, forced by a lack of relevant measurements, were following. The cross-field heat transport, T_i, T_e, n_e and the radiated power density Q_{rad} were assumed to be poloidally and toroidally uniform, reducing the model to one dimension in the radial direction. Ion and electron heat diffusivities, χ_i and χ_e, were assumed to be constant. $n_i = n_e$ i.e. the effective ion charge in the plasma edge $Z_{eff} = 1$. Convective heat fluxes were neglected as the cross-field particle diffusivities are not measured in the edge plasma. Q_{rad} is known to be poloidally localized above the plasma contact point in the attached plasma. However, the assumption of the uniform Q_{rad} is justified by the fact that the electron transit time through the edge region (which is of the similar order as the energy confinement time, $\approx 0.1\,\mathrm{s}$) is at least by a factor of 10^4 longer compared to the time of one electron poloidal circumference ($\cong q\pi R / \sqrt{eT_e / m_e}$). On the other hand, we apply additional simplifying assumption that the radial profile of Q_{rad} is given, i.e. independent of local T_e and n_e.

Under these assumptions the ion and electron power balance equations in the cylindrical geometry read:

$$e\chi_i \frac{1}{r}\frac{d}{dr}\left(r n_e \frac{dT_i}{dr} \right) = -Q_{ie}, \tag{5}$$

and

$$e\chi_e \frac{1}{r}\frac{d}{dr}\left(r n_e \frac{dT_e}{dr} \right) = Q_{ie} - Q_{rad}. \tag{6}$$

The equations were solved numerically inside the region $\rho = r/a = 0.7 \to 1$, where the radiated power density is highest in TS attached plasma. The unknowns of the system were the temperature profiles. All the other fields were set as parameters. Incoming energy fluxes were imposed at the inner boundary ($\rho = 0.7$) by imposing the temperature gradients $\nabla_r T_{i,e}$. The proportionality between the temperature gradients and the local temperatures, $\nabla_r T_{i,e} = -T_{i,e} / \lambda_{i,e}$ (where $\lambda_{i,e}$ is the experimental decay length), was imposed at the outer boundary ($\rho = 1$) to

insure the continuity with the exponentially decaying profiles in the SOL. The non-linear system (5)-(6) was solved iteratively starting from an initial guess of the temperature profiles. For each iteration, the diffusion operators were inverted and the non-linear energy equipartition term Q_{ie} was computed as an explicit right-hand side from T_e and T_i obtained from the previous iteration. The iterative process was terminated when $\left(T_{e,i}^{n} - T_{e,i}^{n-1}\right) \Big/ T_{e,i}^{n-1} < 10^{-6}$ where n is the number of iterations.

The calculation was performed for discharges shown in figure 12. $n_e(r)$ was taken from reflectometry measurements. $\lambda_{Ti,Te} \approx 5$ cm was determined from RFA measurements. $\nabla_r T_{i,e}\Big|_{\rho=0.7} = -3$ keV m^{-1} was provided from ECE and charge exchange recombination spectroscopy (CXRS) measurements, respectively (CXRS measurements were not available for the discharges studied here and $\nabla_r T_{i,e}\Big|_{\rho=0.7}$ was taken from a similar discharge #39598, assuming that $\nabla_r T_{i,e}\Big|_{\rho=0.7}$ is independent of f_{rad}). $\chi_i = \chi_e = 2.8$ m^2 s^{-1}, leading to realistic temperatures at the LCFS, and $Q_{rad} = Q_0 \exp[(\rho - 1)/\lambda_{rad}]$ (with $\lambda_{rad} = 0.14$ m), approximately equal to the poloidally averaged plasma emissivity measured by bolometry, were assumed.

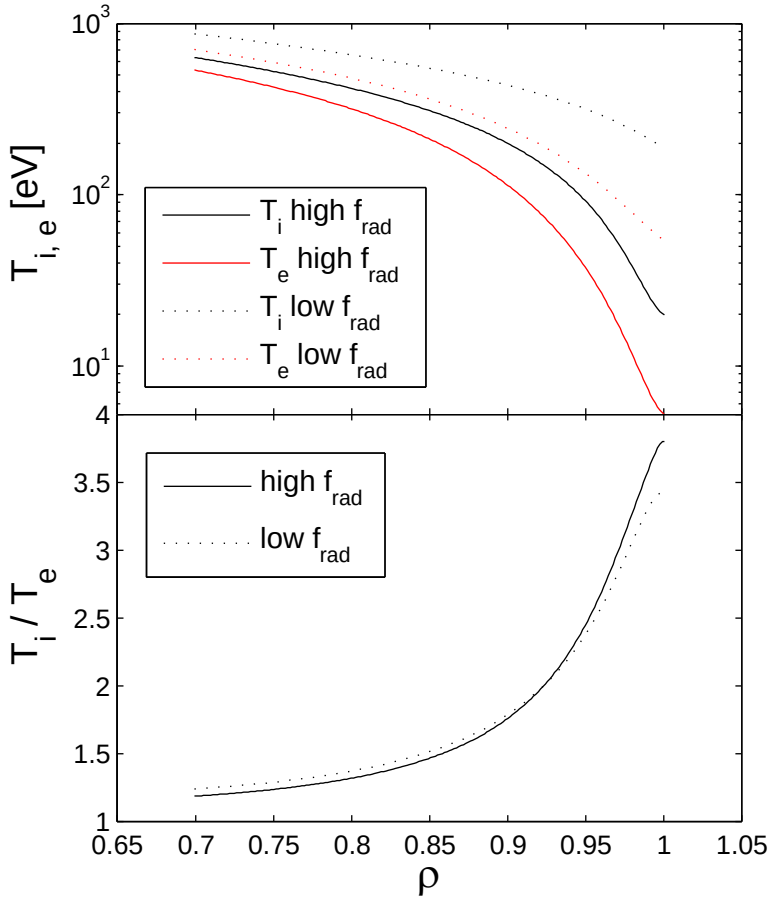

Figure 13. Radial profiles T_i and T_e (top) and T_i / T_e (bottom) in the edge of the confined region ($\rho = 0.7 \rightarrow 1$) calculated from the power balance model for two different values of the radiated power.

The results from two simulations (termed as "high" and "low", referring to f_{rad}) differing only in Q_0 ($Q_0^{high} = 1.9 \cdot 10^5$ W m^{-3}, $Q_0^{low} = 1.4 \cdot 10^5$ W m^{-3}) are compared in figure 13. The increase of the radiated power coincides with the decrease of T_i at the LCFS by 165 eV ($\sim 185 \rightarrow 20$ eV) and T_e by 49 eV ($\sim 54 \rightarrow 5$ eV). The temperatures at $\rho = 0.7$ are very close to experimental values ($T_{iCXRS} \approx 840$ eV, $T_{eThS} \approx 650$ eV, $T_{eECE} \approx 750$ eV, figure 12). In addition, T_e at $\rho = 0.7$ does not vary strongly with f_{rad} which is consistent with experimental observations. The edge ion-to-electron temperature ratio increases with radius (up to $T_i / T_e \approx 3.5$ at the LCFS) which is consistent with the measurements reported from different

tokamaks (see figure 7 in [11]). As mentioned above, the values of χ_i and χ_e were adjusted in order to obtain realistic LCFS temperatures. However, similar variation of the LCFS temperatures with f_{rad} was obtained from the simulations with different values χ_i and χ_e. Moreover, favorable values of edge χ_i and χ_e used in our calculation does not differ significantly from the ones suggested from more complex fluid models elsewhere. The model reproduces well the experimentally observed strong variation of T_i with f_{rad} and suggests that the drop of edge T_e due to radiation could significantly influence edge T_i due to ion-electron collisional coupling. On the other hand, the model also predicts relatively strong variation of the LCFS T_e with f_{rad} which is not seen in experiment (although the decrease of T_e with the increase of f_{rad} is much smaller in absolute values compared to T_i). This discrepancy indicates that some processes in the edge plasma and eventually in the SOL that could have a controlling influence on the electron temperature are not accounted in the model. In addition, Q_{rad} which is pre-defined in our model is in reality coupled with the local electron temperature and density and should be, therefore, modelled in a self-consistent way. The same arguments may apply for the heat diffusivities. In addition, it is known that the convective turbulent heat flux, neglected in our model, may be comparable to or larger than the conductive component [43].

5. Summary

Experimental studies of the SOL parameters in large circular limiter plasmas are needed to validate the models aimed e.g. at the estimation of the heat loads on the ITER start-up-phase limiters.

In this paper we studied in a large circular limiter tokamak Tore Supra the SOL ion and electron temperatures, T_i and T_e, electron density n_e and the ion saturation current density j_{sat} for a broad range of the plasma density $\langle n_e \rangle$ and the radiated power fractions f_{rad}, including detached plasmas.

In ohmic plasma for low $\langle n_e \rangle$ and f_{rad}, $T_i / T_e \cong 3-4$ and $T_i \cong 50\,\text{eV}$ at the LCFS. At highest $\langle n_e \rangle$ and f_{rad} as well as in detached plasma, $T_i \cong T_e$, both only a few electron volts. The decrease of T_i / T_e with $\langle n_e \rangle$ roughly follows the increase of the ion-electron collisionality in the SOL. In attached plasma, the LCFS j_{sat} and n_e increases monotonically with $\langle n_e \rangle$ except the

transition from attached to detached state which was found to be associated with 25 – 30% drop of the LCFS j_{sat} and n_e.

λ_{Ti} was found to be generally higher than λ_{Te} which is consistent with larger parallel electron losses relative to the ion losses in the SOL. The transition to detached state was found to be related with a strong flattening of the SOL temperature profiles and less than a factor of 2 increase of λ_{ne}.

The parallel heat flux density at the LCFS $q_{//LCFS}$ calculated from RFA measurements was found to be consistent with the power balance. In detached plasma $q_{//LCFS}$ was found to be a factor of ~3-5 lower compared to attached discharges characterized by $f_{SOL} = 1 - f_{rad} \approx 0.3 - 0.5$. In detached plasma ($T_i \cong T_e$) the lack of T_i measurements does not affect the calculation of the heat flux densities in the SOL. However, in attached plasma, the heat flux density as well as the total integrated power in the SOL, calculated assuming $T_i = T_e$, can be significantly underestimated because $T_i > T_e$ and $\lambda_{Ti} > \lambda_{Te}$ in the SOL.

SOL temperatures were also studied in the discharges with all parameters except the radiated power being fixed. The increase of f_{rad} by about ~30% was found to be associated with a decrease of SOL T_i by almost a factor of 2 but almost unaffected T_e in the SOL as well as in the core plasma. The decrease of SOL T_i coincides with a similar decrease of f_{SOL}, indicating that the power lost due to radiation comes mainly from the ion channel. A simple power balance model, with the radiation and equipartition being the only volumetric loss terms included, was employed to study the dependence of T_i and T_e on f_{rad} in the edge of the confined region. The model reproduces well a strong decrease of the LCFS T_i with the increase of the radiated power and shows that the power loss on electrons in the edge plasma can be, through ion-electron collisional coupling, compensated from the ion channel and strongly influence the edge T_i. The model also reproduces small variation of the core electron temperature with f_{rad} as well as the steepening of the temperature profiles just inside the LCFS suggested from the comparison of the core and the SOL measurements. However, the model fails in reproducing almost constant LCFS T_e independently of the radiated power. Although the modeled LCFS T_e varies much less than T_i in the absolute values with the increase of the radiated power, it decreases by a similar factor. We do not have any other explanation for this discrepancy except that the processes that would

decouple the edge and the SOL electrons are not accounted in our simple model. In the next step, 2D code which comprises both the edge plasma and the SOL, resolves the processes such as the radiation in a self-consistent way and includes additional volumetric loss terms such as the charge-exchange losses, recombination and ionization, needs to be employed to study the edge temperatures.

In general, we have demonstrated that the reciprocating probes in Tore Supra access the SOL parameters, in particular the ion temperature, for a broad range of the plasma conditions. This allows e.g. characterizing the heat flux densities in the SOL without using simplifying (and often underestimating) assumptions on SOL T_i. These results suggest that it could be interesting to further investigate detached plasma operation, and the significant increase in SOL spreading with the contact point on the HFS, to develop alternative start-up scenarios for ITER.

Acknowledgements

The authors would like to thank Drs. F. Clairet and C. Fenzi for providing the reflectometry and the CXRS measurements, respectively. The authors are grateful to Dr. P. Ghendrih for the fruitful discussions. This work, supported by the European Communities under the contract of Association between EURATOM and CEA, was carried out within the framework of the European Fusion Development Agreement. The views and opinions expressed herein do not necessarily reflect those of the European Commission.

References

[1] Gribov Y *Control System Design and Assessment (CSD), Appendix B: Magnetic configuration and poloidal field scenarios, ITER document N 19 RI 14 R0.1*, August 2004.

[2] Kobayashi M *et al* 2007 *Nucl. Fusion* **47** 61

[3] Federici G *et al* 2007 *J. Nucl. Mater.* **363-365** 346

[4] Cardella A, Skladnov K, Ioki K, Pacher H, Strebkov Y and Daenner W 2002 *Fus. Eng. Des.* **61-62** 111

[5] Jacquinot J and Hoang G T 2004 *Plasma Sci. Technol.* **6** 2101

[6] Kočan M, Gunn J P, Komm M, Pascal J-Y, Gauthier E and Bonhomme G 2008 *Rev. Sci. Instrum.* **79** 073502

[7] McCracken G M *et al* 1987 *J. Nucl. Mater.* **145-147** 181

[8] Matthews G F, Pitts R A, McCracken G M, Stangeby P C 1991 *Nucl. Fusion* **31** 1495

[9] Pitts R A 1991 *PhD Thesis* University of London

[10] Kočan M, Pánek R, Stöckel J, Hron M, Gunn J P and Dejarnac R 2007 *J. Nucl. Mater.* **363-365** 1436

[11] Kočan M, Gunn J P, Pascal J-Y, Bonhomme G, Fenzi C, Gauthier E and Segui J-L 2008 *Plasma Phys. Control. Fusion* **50** 125009

[12] Gunn J P *et al* 2007 *J. Nucl. Mater.* **363-365** 484

[13] Matthews G F 1995 *J. Nucl. Mater.* **220-222** 104

[14] Allen J *et al* 1986 *Plasma Phys. Control. Fusion* **28** 101

[15] Strachan J D *et al* 1985 *12th Eur. Conf. on Controlled Fusion and Plasma Physics* (Budapest, Hungary) part 1, p. 263

[16] Kimura H *et al* 1987 *Nucl. Fusion* **18** 1195

[17] Kimura H, Odajima K, Sugie T, Maeda H 1979 *Japan. J. Appl. Phys.* **18** 2275

[18] Molvik A W 1981 *Rev. Sci. Instrum.* **52** 704

[19] Matthews G F 1984 *J. Phys. D: Appl. Phys.* **17** 2243

[20] Wan A S, Yang T F, Lipschultz B and LaBombard B 1986 *Rev. Sci. Instrum.* **57** 1542

[21] Guo H Y, Matthews G F, Davies S J, Erents S K, Horton L D, Mond R D, Stangeby P C 1996 *Contrib. Plasma Phys.* **36** 81

[22] Shats M G, Rudakov D L, Boswell R W and Borg G G 1997 *Phys. Plasmas* **4** 3629

[23] Raychaudhuri S 1999 *Contrib. Plasma Phys.* **39** 4, 359

[24] Pitts R A, Chavan R, Davies S J, Erents S K, Kaveney G, Matthews G F, Neill G, Vince J E and Ďuran I 2003 *Rev. Sci. Instrum.* **74** 4644

[25] Nedzelskiy I S, Silva C, Figueiredo H, Fernandes H and Varandes C A F 2006 *Rev. Sci. Instrum.* **77** 10E729

[26] Pitts R A, Fundamenski W, Erents S K, Andrew Y, Loarte A, Silva C and JET-EFDA contributors 2006 *Nucl. Fusion* **46** 82

[27] Kočan M and Gunn J P, "First evidence for poloidal asymmetries of radial ion energy transport by ion temperature measurements in the scrape-off layer of Tore Supra" abstract submitted to *36th EPS Conference on Contr. Fusion and Plasma Physics (Sofia, June 29 – July 3)*

[28] Valsaque F, Manfredi G, Gunn J P and Gauthier E 2002 *Phys. Plasmas* **9** 1806

[29] Dejarnac R, Gunn J P, Stöckel J, Adámek J, Brotánková J and Ionita C 2007 *Plasma Phys. Control. Fusion* **49** 1791

[30] Hutchinson I H 1987 *Phys. Fluids* **30** 3777

[31] Chung K S and Hutchinson I H 1988 *Phys. Rev. A* **38** 4721

[32] LaBombard B *et al* 2004 *Nucl. Fusion* **44** 1047

[33] Gunn J P *et al* 2009 "Measurements of lower hybrid hot spots using a retarding field analyzer in Tore Supra" *J. Nucl. Mater.* (in press), doi:10.1016/j.jnucmat.2009.01.232

[34] Böhm C and Perrin J 1993 *Rev. Sci. Instrum.* **64** 31

[35] Gunn J P *et al* 2002 *Czech. J. Phys.* **52** 1107

[36] Silva C, Gonçalves B, Hidalgo C, Pedrosa M A, Erents S K, Matthews G F and Pitts R A 2004 *Rev. Sci. Instrum.* **75** 4314

[37] Pánek R, Pitts R A, Gunn J P and Erents S K 2004 *Czech. J. Phys.* **54** 150

[38] Chodura R 1982 *Phys. Fluids* **25** 1628

[39] Gunn J P 1997 *Phys. Plasmas* **4** 4435

[40] Stangeby P C *The Plasma Boundary of Magnetic Fusion Devices* 2000 (Bristol: Institute of Physics Publishing) p 649

[41] Asakura N 2007 *J. Nucl. Mater.* **363-365** 41

[42] Jones E M 1997 Atomic Collision Processes in Plasma Experiments: Analytic Expressions for Selected Cross-Sections and Maxwellian Coefficients II, Rep. CLM-R 175, Culham Laboratory, Abingdon, Oxfordshire

[43] Pigarov A Y *et al* 2003 *J. Nucl. Mater.* **313-316** 1076

First evidence for poloidal asymmetries of radial ion energy transport by ion temperature measurements in the scrape-off layer of Tore Supra

M. Kočan and J. P. Gunn
CEA, IRFM, F-13108 Saint-Paul-lez-Durance, France

1. Introduction

The intermittent expulsion of plasma filaments, or "blobs", from the last closed flux surface (LCFS) is believed to be responsible for a large fraction of the radial particle transport in the scrape-off layer (SOL) [1]. Blobs appear to be initiated by a ballooning-type instability in the unfavourable curvature region on the low field side (LFS). As they propagate outward, they also expand along the magnetic field lines, driving parallel flows [2]. When the plasma contact point is on the inboard limiters, the blobs propagate freely out to the wall leading to a broad SOL with nearly flat density profiles. On the other hand, it was demonstrated that outboard limiters suppress the radial transport, leading to a very thin SOL [3].

The first evidence for poloidal asymmetry of the radial ion and electron energy transport in the SOL, similar to that of the particle transport [3], is reported. Implications for ITER start-up phase are discussed. Correlation of the asymmetries of SOL ion (T_i) and electron (T_e) temperatures on each side of the probe with changes of the parallel Mach number $M_{//}$, important for the Mach probe theory, is addressed.

2. Experimental results

Tore Supra ohmic discharges with the plasma contact point either on the inboard bumper limiters (referred to as "inboard discharges") or on the outboard antenna protection limiters ("outboard discharges") are studied. The database comprises 22 inboard (including 4 detached) and 4 outboard measurements (including 1 detached), Fig. 1 and Tab. 1. The working gas is deuterium. Both I_p and B_t are oriented clockwise looking from the top of the torus. SOL T_i, T_e and the parallel ion saturation current density j_{sat} have been measured simultaneously from both directions along the magnetic field lines by a bidirectional retarding field analyzer (RFA) [4]. The RFA is located at $R = 2.53\,\mathrm{m}$ and moves vertically, Fig. 1. Electron density and the heat flux density are calculated as $n_e = j_{sat}/[0.35e^{1.5}\sqrt{(T_i+T_e)/m_i}]$ [5] (with $j_{sat} = \sqrt{j_{sat}^{HFS} \cdot j_{sat}^{LFS}}$, HFS/LFS indicating respectively the analyzer facing the high field side and the low field side, Fig. 6) and $q_{//} = \gamma T_e j_{sat}$, respectively. The total heat transmission coefficient γ is calculated from Eq.(25.46) in [6]. T_i is calculated as $(T_i^{HFS} + T_i^{LFS})/2$ [7]. A model for the HFS/LFS asymmetry of T_e is not yet available and T_e is also calculated as $(T_e^{HFS} + T_e^{LFS})/2$.

parameter	inboard	outboard
a [m]	0.60 – 0.68	0.47 – 0.65
R [m]	2.18 – 2.26	2.39 – 2.52
$\langle n_e \rangle$ [10^{19} m^{-3}]	0.9 – 4.7	1.4 – 5
I_p [MA]	0.4 – 1.2	0.3 – 0.7
q_a	3.4 – 9.2	3.5 – 8.5
B_t [T]	3.2 – 4.1	3.5 – 3.7
f_{rad}	0.3 – ~1	0.4 – 0.8
P_{in} [MW]	0.3 – 1.2	0.3 – 0.7

Tab. 1. Macroscopic parameters of the database discharges. From top to bottom: minor radius, major radius, volume averaged density, plasma current, safety factor at a, toroidal magnetic field, radiated power fraction and ohmic input power.

Fig. 2 shows the radial profiles measured in selected inboard and outboard discharges. The former is characterized by a factor of 4 longer e-folding lengths compared to latter. $T_i > T_e$ is consistent with the observations reported from other tokamaks (Fig. 7 in [8]).

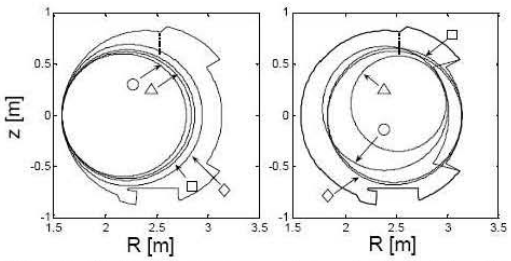

Fig. 1. Poloidal cross sections included in the database. Left: inboard contact point. Right: outboard contact point. Vertical dotted line indicates the RFA location.

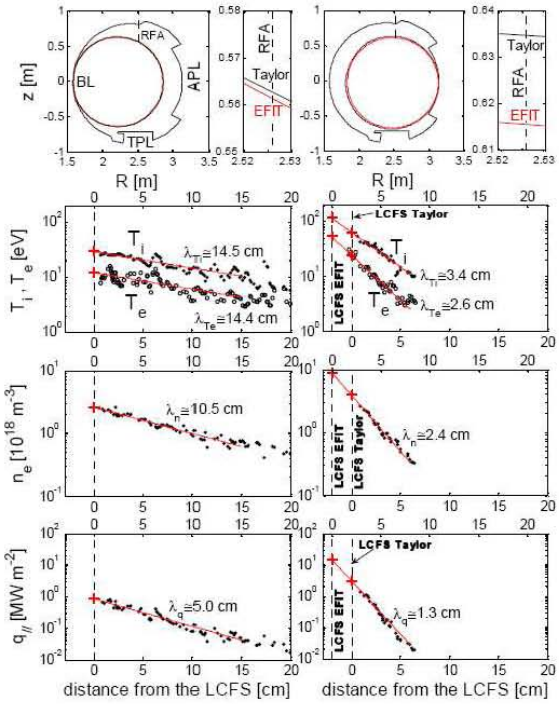

Fig. 2. SOL profiles measured by RFA. Left: inboard discharge. Right: outboard discharge. From top to bottom: LCFS with the magnified region of the RFA location (BL: bumper limiter, APL: antenna protection limiter, TPL: toroidal pump limiter), ion and electron temperatures, electron density, parallel heat flux density with e-folding lengths. Two LCFS reconstructions (Taylor, EFIT) are shown.

Note that for the outboard discharges the LCFS at the RFA location calculated by the EFIT poloidal field reconstruction (referred to as "EFIT LCFS") was found to be shifted inward by up to ~2 cm compared to the LCFS given by the Taylor extrapolation of the magnetic flux measurements (referred to as a "Taylor LCFS"). This leads to a large uncertainty in the LCFS values, Fig. 2. It is not yet clear which magnetic reconstruction is more reliable. However, for deep reciprocations performed by other Langmuir probes in the outboard discharges a sharp increase of T_e and j_{sat} (possibly related to the transition between the SOL and the confined region) coincides with the Taylor LCFS. Therefore, in what follows Taylor LCFS is considered. For the inboard discharges EFIT and Taylor LCFS overlap within a few millimeters.

Fig. 3 shows the e-folding lengths of T_i, T_e, n_e and $q_{//}$ for all database discharges, plotted against the volume averaged density. The e-folding lengths are calculated from the data measured between the LCFS and the next most inner limiter. For a given configuration several macroscopic parameters are varied and their influence on the e-folding lengths thus cannot be decoupled. In general, however, the outboard discharges have substantially shorter e-folding lengths compared to the inboard discharges. For the database discharges $T_i = 5-65$ eV, $T_e = 5-30$ eV and $T_i/T_e = 1-5$ at the LCFS. The lowest T_i, T_e and T_i/T_e is measured in detached plasmas.

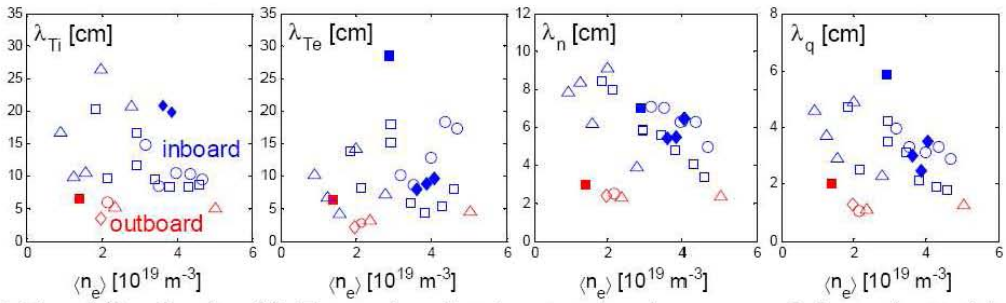

Fig. 3. The e-folding lengths of T_i, T_e, n_e and $q_{//}$ plotted against the volume-averaged plasma density. Inboard / outboard indicate the contact point. Symbols correspond to poloidal cross sections from Fig. 1. Full symbols: detached discharges. λ_{Ti} for two detached discharges is almost infinite and does not appear on graph.

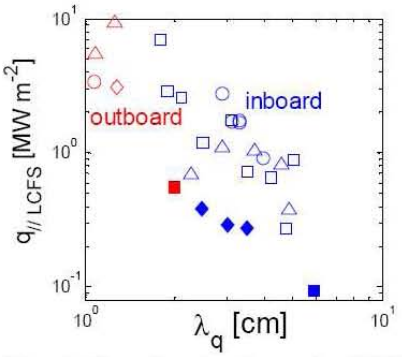

Fig. 4. Heat flux density at the LCFS plotted against the SOL heat flux density e-folding length. Full symbols: detached discharges.

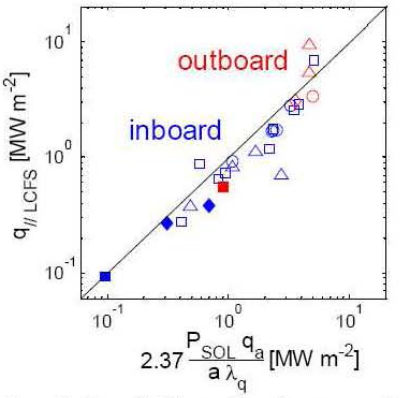

Fig. 5. Parallel heat flux density at the LCFS plotted against the physics-based scaling.

As shown in Figs. 2-4, the poloidal asymmetry in the particle and energy transport makes the e-folding length of $q_{//}$, λ_q, strongly dependent on the plasma contact point. In addition, as seen from Fig. 4 $q_{//}$ at the LCFS $q_{// LCFS} \propto \lambda_q^{-1}$ and is thus highest in the outboard discharges. This has an important consequence e.g. for the ITER start-up phase for which two outboard modular limiters are currently envisaged [9]. $q_{// LCFS} \propto \lambda_q^{-1}$ has a physical background in the conservation of the power in the SOL $P_{SOL} \approx 2\pi R \int q_\theta \, dr \approx 2\pi R q_{\theta LCFS} \lambda_q \approx R q_{// LCFS} \lambda_q (B_\theta / B_{tot}) \approx q_{// LCFS} \lambda_q a / q_a$ (where q_a is the safety factor at the minor radius a), so that $q_{// LCFS} \approx P_{SOL} q_a / (a \lambda_q)$. Fig. 5 shows that such physics-based scaling reproduces well $q_{// LCFS}$ for both contact points and over a large range of parameters. $P_{SOL} q_a / (a \lambda_q)$ in Fig. 5 is multiplied by a constant $C = 2.37$ (for $P_{SOL} = P_{in}(1 - f_{rad})$ in MW, a in meters and λ_q in centimeters) obtained from the linear least-square fit. The predictive capability of the scaling of $q_{// LCFS}$ to ITER plasma is obviously very limited as the database (of the outboard discharges in particular) is statistically insignificant. In addition, for the outboard discharges a large error on $q_{// LCFS}$ should be anticipated because of the uncertainty of the LCFS position (a factor of 3 – 4 higher $q_{// LCFS}$ is obtained for the EFIT LCFS) as well as the extrapolation of the measured $q_{//}$ towards the LCFS over the distance comparable to λ_q. Another important point to consider is that our measurements were performed in circular plasmas so that the scaling might not be valid for the elongated ITER start-up plasma. It is important to note that if T_i were not measured, the usual assumption of $T_i = T_e$ would underestimate $q_{// LCFS}$ up to a factor of ~2.3 for the discharges studied here.

The asymmetries of ion and electron temperatures measured by each side of the RFA were studied in a discharge #42403 during which the plasma contact point was steadily displaced upward along the outboard limiter, Fig. 6. Such displacement is known to be associated with the reversal of the parallel plasma flow [3]. According to kinetic calculations from [7], the flow reversal should be associated with similar changes of the effective T_i measured by each side of the RFA. Fig. 6 shows the radial profiles of T_i, T_e and j_{sat} measured by each side of the RFA. Also shown is the parallel Mach number calculated as $M_{//} \cong 0.4 \ln(j_{sat}^{LFS} / j_{sat}^{HFS})$ [6]. T_i^{LFS} / T_i^{HFS} clearly changes with the change of $M_{//}$ but, in contrary to the theory [7], it does not reverse completely like j_{sat}. This suggests that some of the assumptions in the kinetic modeling of the behavior of the pre-sheath surrounding the RFA [7] might not be valid. Interestingly, a similar asymmetry is also measured for T_e. A model for the asymmetry of T_e is not yet available. In should be noted that one of the assumptions of the fluid Mach probe

theory [5,10] is that the parallel electron velocity distribution is Maxwellian, in which case the same T_e would be measured by each side of the RFA.

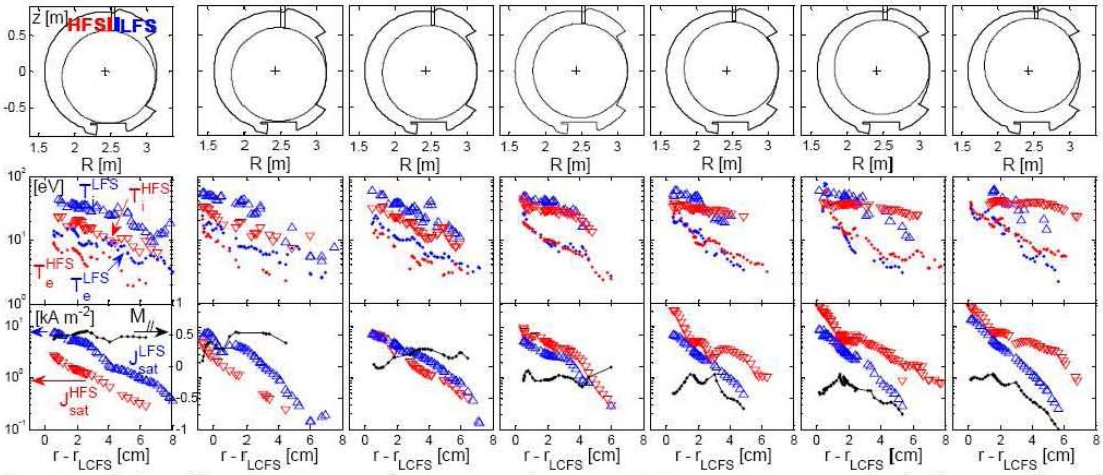

Fig. 6. Radial profiles of T_i, T_e, j_{sat} and $M_{//}$ measured in seven RFA reciprocations in the discharge with steadily displaced outboard contact point. HFS / LFS indicate the side of the RFA. For $M_{//} > 0$ the flow is directed towards the LFS analyzer.

3. Conclusions

New measurements carried out with the RFA in Tore Supra have demonstrated, although on a very limited database, that the poloidal asymmetry of the radial ion and electron energy transport in the SOL is similar to that of the particle transport [3]. These results are particularly important for the ITER start-up phase which is currently envisaged on the outboard modular limiters and for which the modelled peak heat loads on the limiters were found to be considerably close to the engineering limit [9]. The physics-based scaling for the parallel heat flux density at the LCFS $q_{// LCFS} \propto P_{SOL}\lambda_q^{-1}$ was found to agree with measurements. It implies that the outboard start-up is least advantageous with regards to power handling as it may be characterized by large, localized heat loads. We do not attempt to scale the heat flux densities found in Tore Supra to ITER. We suggest that alternative start-up scenarios (e.g. the start-up on the inboard side, eventually in a detached regime) should be evaluated. Systematic measurements of the type presented here, as well as in elongated plasmas, are necessary to enhance the predictive capability of the scaling to ITER.

Acknowledgement

This work, supported by the European Communities under the contract of Association between EURATOM and CEA, was carried out within the framework of the European Fusion Development Agreement. The views and opinions expressed herein do not necessarily reflect those of the European Commission. The authors acknowledge helpful discussions with Dr. François Saint-Laurent about the magnetic surface reconstruction methods and excellent technical assistance of Jean-Yves Pascal.

References

[1] V. Naulin, J. Nucl. Mater. **363-365** (2007) 24, [2] N. Asakura, J. Nucl. Mater. **363-365** (2007) 41, [3] J. P. Gunn *et al.*, J. Nucl. Mater. **363-365** (2007) 484, [4] M. Kočan *et al.*, Rev. Sci. Instrum. **79** (2008) 073502, [5] I. H. Hutchinson, Phys. Fluids **30** (1987) 3777, [6] P. C. Stangeby, *The Plasma Boundary in Magnetic Fusion Devices* (Bristol: Institute of Physics Publishing, 2000) [7] F. Valsaque *et al.*, Phys. Plasmas **9** (2002) 1806, [8] M. Kočan *et al.*, Plasma Phys. Control. Fusion **50** (2008) 125009, [9] M. Kobayashi *et al.*, Nucl. Fusion **47** (2007) 61, [10] J. P. Gunn and V. Fuchs, Phys. Plasmas **14** (2007) 032501.

Chapter 4

Three projects to validate T_i measurements in Tore Supra

As mentioned in section 1.4.1, the ion temperature measured in the SOL of limiter as well as divertor tokamaks was found to higher than electron temperature (see references [Kočan 2008]). The ion-to-electron temperature ratio $\tau > 1$ in the SOL is believed to be due to the cooling effect of the Debye sheath on electrons [Stangeby 2000e].

Recent measurements in Tore Supra using a RFA demonstrated that $\tau > 1$ not just in the SOL but also at the LCFS. Since the temperatures are not measured in the edge of the confined plasma (referred here simply to as "edge") in Tore Supra, it was not possible to identify the radial extension of the region in the edge plasma where $\tau > 1$. The results from Tore Supra are consistent with edge temperature measurements in L-mode and ohmic plasmas in ASDEX Upgrade [Reich 2004, Reich 2004b] and TEXTOR [Huber 2000, Kreter 2001]. These measurements have demonstrated, although on a very limited dataset, that $\tau > 1$ already at $\rho \approx 0.9$ (with $\rho = r/a$) and increases towards the LCFS.

The reason why T_i becomes higher than T_e in the edge is not understood. This could be e.g. because of the propagation of cold electrons from the SOL to the edge which cools the edge electron population or due to the difference in the properties of the ion and electron radial energy transport (i.e. different heat diffusivities and/or the power loss terms) in the edge. Systematic τ measurements in the edge plasma may be particularly important for the core transport codes, which often use $T_i = T_e$ at the LCFS to define the outer boundary conditions (e.g. [Federici 2007]), for the validation of probe measurements but also for the understanding of the energy transport in the edge plasma in general.

As summarized in chapter 2, considerable effort was made to validate SOL T_i measurements by the RFA. Most of the published experimental data (chapter 3) make good sense. The decrease of the ion-to-electron temperature ratio to unity at high core densities is an outstanding example. Nonetheless, doubt can be cast on any unique

diagnostic method as long as simultaneous and independent measurements by another diagnostic are unavailable. In this chapter, three well advanced, ongoing projects to obtain independent validation of the RFA results from Tore Supra are described.

Firstly, it was decided that it would be useful to visit the JET tokamak to make a systematic study of ion-to-electron temperature ratio in the edge region using multiple diagnostics. The results indicate that, in agreement with the multi-machine database (Fig. 7 in [Kočan 2008]), that the ratio is greater than unity over a significant radial distance in the JET edge plasma. These results provoked a strong reaction amongst our JET colleagues, and they have undertaken a study to see if this result could be due to a shift in the electron temperature profile caused by uncertainties of the magnetic reconstruction. The completed analysis and present status of this project are presented in section 4.1.

In Tore Supra CXRS provides measurements of T_i in the core plasma, but in the standard magnetic configuration, the outermost chord is too far from the LCFS to be compared with RFA measurements in the SOL. A dedicated experiment was proposed and executed in order to overlay the two measurements. This was done by making a small plasma leaning on the high field side bumper limiter, whose minor radius was chosen such some the outermost CXRS measurements lay in the SOL. Strong disagreement was found between the two methods. The preliminary analysis can be found in section 4.2.

Finally, in section 4.3, a project to develop a new, independent probe method to measure ion temperature is described. The probe is known as the "segmented tunnel probe", and was developed in collaboration between the CEA and IPP-Prague. The author of this thesis took charge of the design of the probe, had it built by IPP-Prague in a collaborative effort, and installed it on Tore Supra in 2008. The probe worked perfectly from a technical point of view. Kinetic simulations of the probe were performed in order to calibrate it. Initial comparison with the measurements is presented here.

4.1. Edge ion-to-electron temperature ratio in the L-mode plasma in JET

4.1.1. Introduction

In this section, selected results and preliminary status of the analysis of the edge ion-to-electron temperature ratio measurements in L-mode plasmas in the JET tokamak are presented. Edge T_i and T_e are measured by CXRS and ECE diagnostics, respectively. Improving upon similar measurements in TEXTOR and ASDEX Upgrade, τ is studied for a much larger data set and for a wide range of the macroscopic plasma parameters. Values of τ up to 5 just inside the outboard midplane separatrix are measured in JET. Equipartition is restored at $\rho \approx 0.8$ (where ρ is the distance from the plasma centre at the outboard midplane normalized to minor radius a).

It is particularly important to note that in JET the edge T_e measured by the ECE is often found to be lower than T_e measured by the Thomson scattering system LIDAR [Luna 2004]. At the time of writing of this thesis the discrepancy between ECE and LIDAR is still under investigation (deficiencies in the flux surface mapping from the EFIT equilibrium code, which influences the position of the ECE temperature profiles, might be sufficient to explain the discrepancy [Luna 2004]). Therefore, although the ECE measurements analyzed here are taken from the official JET database of validated measurements, the results should be considered as preliminary.

The macroscopic parameters of the database discharges are defined in section 4.1.2. The results are presented in section 4.1.3.

4.1.2. JET L-mode database of edge T_i and T_e

Edge ion and electron temperatures measured during the L-mode phase of the discharge are studied in the region of $0.8 < \rho < 0.95$. The discharges included in the database are characterized by minor radius $a \cong 1\,\mathrm{m}$ so that ρ and r are almost identical.

Edge T_i is measured by the edge CXRS system [Andrew 2006]. The system consists of two periscopes with 16 lines of sight aligned with the neutral injectors. Edge CXRS has a time resolution of 50 ms. T_i is obtained from the Doppler broadening of C^{6+} spectral lines assuming that C^{6+} ions are in thermal equilibrium with fuel ions. T_i measured by edge CXRS has been compared with T_i measured simultaneously at similar radii by the core CXRS diagnostic system [Negus 2006]. As shown in figure 4.1, both CXRS diagnostics provide similar values of ion temperature $r - r_{sep} = -0.05\,\mathrm{m}$ (with r_{sep} being the outer midplane separatrix radius). T_i from the core CXRS appears to be systematically lower by about 80 eV compared to edge CXRS. This is due to the fact that for most of the data points plotted in figure 4.1 the line of sight of the core CXRS is localized by about 1 cm outward from $r - r_{sep} = -0.05\,\mathrm{m}$ and thus measures somewhat lower T_i.

Edge T_e is measured by a multi-channel electron cyclotron emission (ECE) heterodyne radiometer [Luna 2004] with a time resolution of 1 ms (meaning that the measurements of T_i and T_e are separated by less than 1 ms). Like T_i, T_e is also measured at the outer midplane. For the L-mode phase of the discharges included in this study the measurements of T_e by LIDAR Thomson scattering [Gowers 1995] are not available.

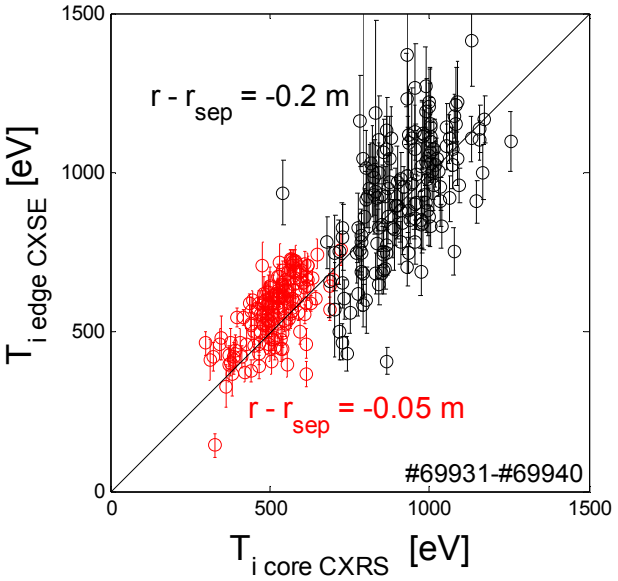

Figure 4.1. T_i measured by the edge and the core CXRS diagnostic systems at two different radial positions. T_i is taken from the lines of sight which are closest to $r - r_{sep} = -0.05$ m and $r - r_{sep} = -0.2$ m, respectively. The measurements by the core and the edge CXRS are separated by less than 10 ms.

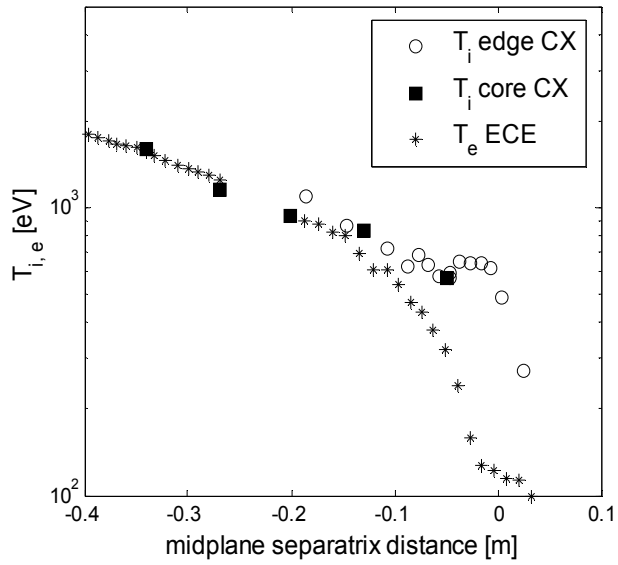

Figure 4.2. Radial profile of the edge ion and electron temperatures measured in the L-mode phase of the JET discharge #69939 at t~54.4 s. Macroscopic parameters are shown in figure 4.3.

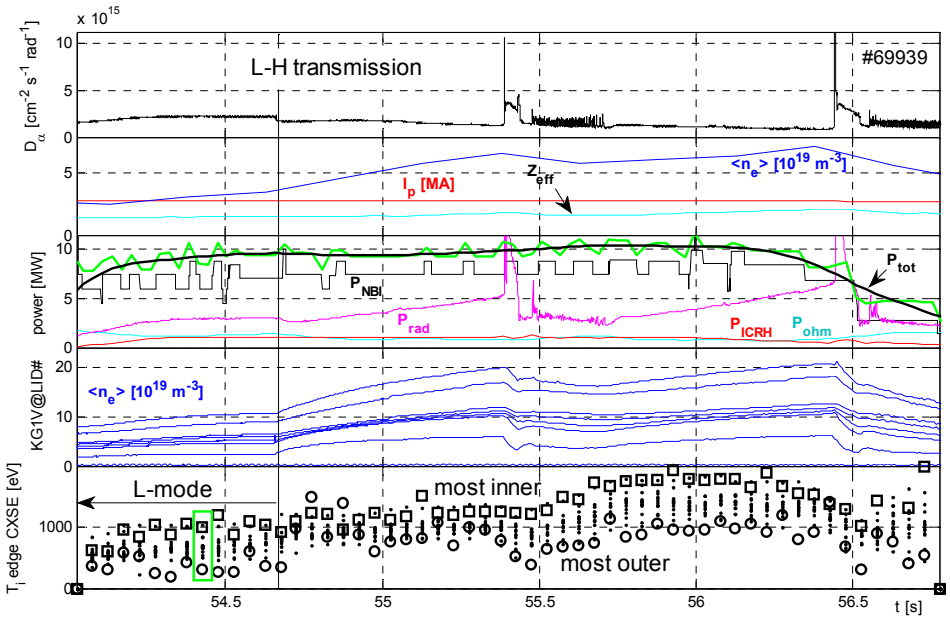

Figure 4.3. Selected macroscopic plasma parameters of the JET discharge #69939. Vertical full line at t=54.7 s indicates the L-H transition which is identified from the drop of D_α (top panel) as well as from the increase of the plasma density (fourth panel from top). T_i from the edge CXRS is plotted in the bottom panel. T_i measured by the most inner (outer) line of sight is indicated by square (circle). The radial profile measured at t~54.4 (indicated by the green square in the bottom panel) is plotted in figure 4.2.

Typical profiles of edge T_i and T_e are shown in figure 4.2 (JET discharge #69939). Ion temperatures measured by the edge and core CXRS are very similar. At $r - r_{sep} \cong -0.2$ m (corresponding to $\rho \cong 0.79$) $T_i = T_e$. For $r - r_{sep} > -0.02$ m T_e decreases faster with radius than T_i. Near the separatrix $T_i / T_e = 2 - 4$.

The edge temperatures are studied for the discharges series #68213-#68224, #68291-#68302 and #69927-#69940 for which the validated L-mode profiles of edge T_i are available. Only the measurements in the L-mode phase of the discharge are included The L-H (H-L) transition was identified from the drop (increase) of the D_α radiation and the increase (drop) of the plasma density. The database contains about 1200 temperature profiles similar to that plotted in figure 4.2, hand-checked for outliers. The range of the macroscopic plasma parameters included in the database is plotted in figure 4.4. All discharges are characterized by a standard JET toroidal field ripple amplitude $\delta = 0.08\,\%$ and by zero lower hybrid current drive power. The database covers a broad range of $\langle n_e \rangle$, Z_{eff}, P_{rad}, P_{ohm}, P_{ICRH}, P_{NBI}, *and* P_{tot}. On the other hand, about 92% of the data were measured at $B_t = 2.8\,T$ and $I_p = 2.5$ MA, which are the standard values for most JET discharges. In addition, contrary to the scan of a single parameter keeping all other parameters constant, the entire parameter set is usually varied from one discharge to

another, which introduces cross-correlation between individual parameters. Some parameters like e.g. P_{rad} and $\langle n_e \rangle$ are naturally coupled (figure 4.5).

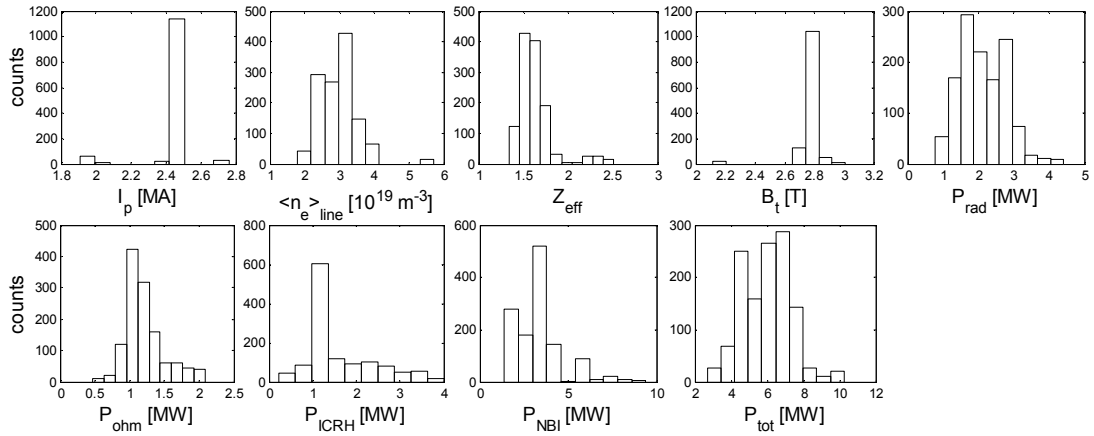

Figure 4.4. The range of the macroscopic plasma parameters covered by the database of the L-mode measurements of T_i and T_e (#68213-#68224, #68291-#68302, #69927-#69940). I_p, $\langle n_e \rangle$, Z_{eff}, B_t, P_{rad}, P_{ohm}, P_{ICRH}, P_{NBI}, and P_{tot} are respectively the plasma current, the central-line averaged density, the effective ion charge, the intensity of the toroidal magnetic field, the total radiated power, the ohmic power, the ion-cyclotron-resonance-heating power, the neutral-beam-injection power and the total heating power.

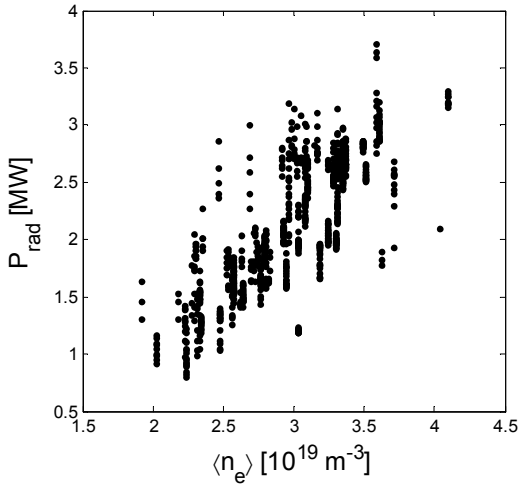

Figure 4.5. Scatter plot of the radiated power versus the central-line-averaged density for the database discharges.

4.1.3. Preliminary results

Figure 4.6 shows T_i, T_e and τ at three different radii in the edge plasma, plotted as a function of $\langle n_e \rangle$. At $\rho = 0.95$, $\tau = 1.5 - 4.5$. Equipartition is restored just at $\rho \approx 0.8$.

At $\rho = 0.8$ and $\rho = 0.9$, τ seems to increase slightly with $\langle n_e \rangle$. However, the coherent variation of $\langle n_e \rangle$ with the heating power does not allow to decouple the scaling of τ with the plasma density and the heating power. T_i and T_e are plotted against P_{ICRH} and P_{NBI} in figure 4.7.

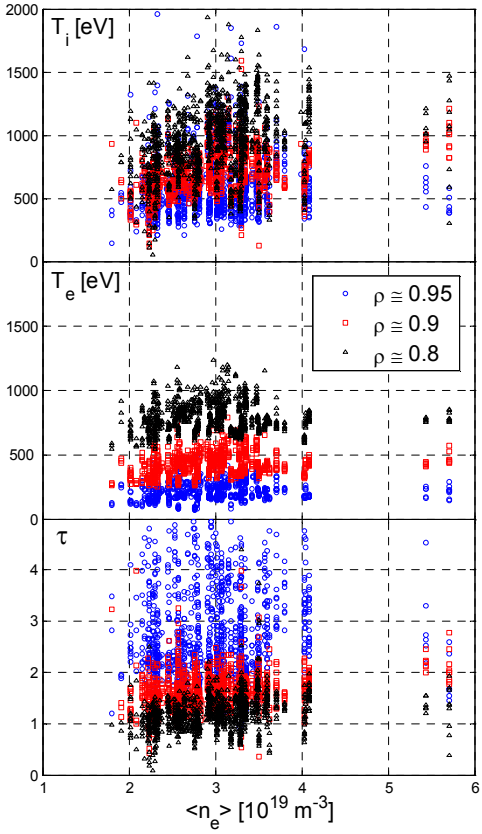

Figure 4.6. From top to bottom: T_i, T_e and $\tau = T_i / T_e$ at three different radii in the edge of the JET L-mode plasma. Data are plotted against the central-line-averaged density.

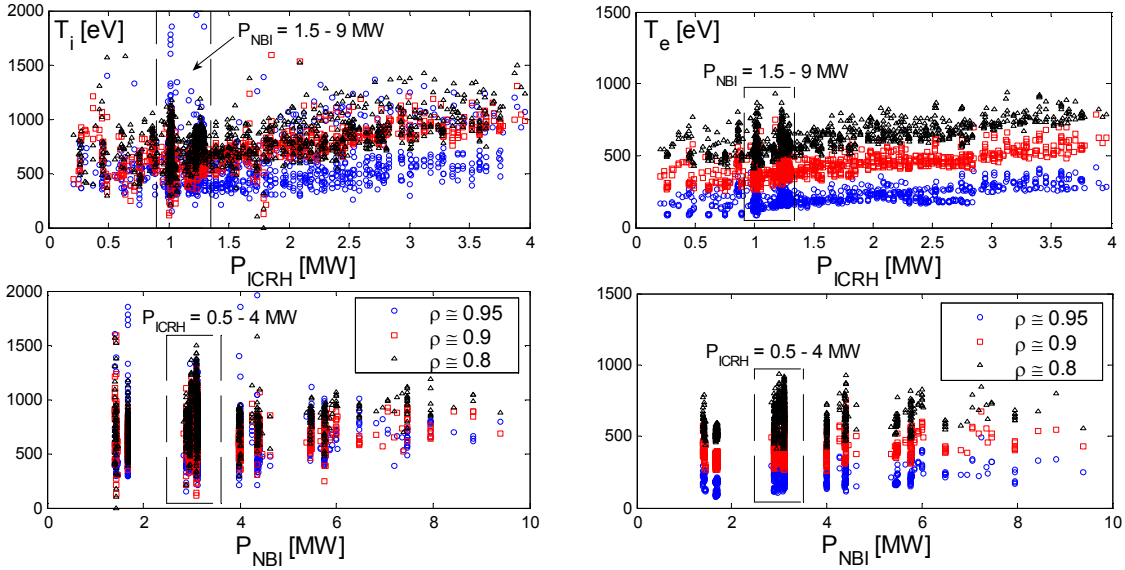

Figure 4.7. T_i (left) and T_e (right) at three different radii in the edge plasma, plotted against P_{ICRH} and P_{NBI}.

In figure 4.8, typical range of τ in the JET L-mode plasma is compared with the multi-machine database of τ measurements [Kočan 2008]. The upper (lower) limit of the range of τ measured in JET is calculated as a mean value from all data points measured at a given radius (figure 4.6) increased (reduced) by the standard deviation. τ in JET appears to be a factor of 2 higher compared to the values measured in ASDEX Upgrade and TEXTOR. However, the measurements reported from ASDEX Upgrade and TEXTOR were performed at relatively low injected power ($P_{NBI} = 1\,\mathrm{MW}$ in [Huber 2000]) dominated by an electron cyclotron resonant heating (ECRH) ($P_{ECRH} = 1.1\,\mathrm{MW}$ in [Reich 2004] and $P_{ECRH} = 0.7\,\mathrm{MW}$ in [Reich 2004b]) and comprises only a few data points. In addition, the database from ASDEX Upgrade and TEXTOR is statistically insignificant. The discrepancy could be also explained by the error in the flux mapping in the edge which, as mentioned in the introduction, could lead to the systematic inward shift of the ECE measurements. As mentioned above, the measurements of T_e by the LIDAR Thomson scattering system (which does not depend on EFIT reconstruction) are not available for the L-mode phase of the database discharges studied here. Assuming, hypothetically, that τ in ASDEX Upgrade, TEXTOR and JET are similar and that T_e from the ECE is underestimated because of a systematic radial shift of the profiles, an outward shift of the ECE measurements by 5 cm would be needed to match JET τ with those reported from ASDEX Upgrade and TEXTOR. In [Saarelma 2005], a similar shift (3.5 – 5.5 cm) was needed to match the electron temperature measured by the ECE and the Thomson scattering. On the other hand, such a radial shift would lead to $T_e = 200 - 300\,\mathrm{eV}$ at the separatrix $T_e(a)$. This is substantially higher compared to $T_e(a)$ measured in the NBI-heated L-mode plasmas in JET ($T_e(a) \cong 60\,\mathrm{eV}$, measured by a Langmuir probe, 3.3 MW of NBI) [Guo 1996], ASDEX Upgrade ($T_e(a) \cong 50\,\mathrm{eV}$, ECE, 1.3 MW of NBI) [Reich 2004], TEXTOR ($T_e(a) \cong 30 - 60\,\mathrm{eV}$, He-beam diagnostic, 1.0 MW of NBI) [Huber 2000] and JT-60U ($T_e(a) \cong 50 - 80\,\mathrm{eV}$, Langmuir probe and Thomson scattering system, 4.0 MW of NBI) [Asakura 1997].

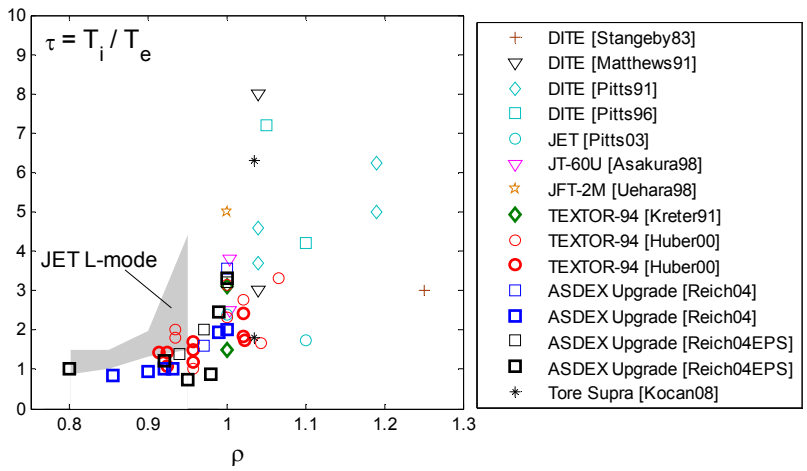

Figure 4.8. Typical range of edge T_i / T_e in the L-mode plasma in JET, juxtaposed to a multi-machine database of T_i / T_e measurements.

4.2. Comparison of the SOL T_i measured by the RFA and CXRS in Tore Supra

A large number of diagnostics for SOL T_i measurements were listed in section 1.4.2. However, the comparison of T_i measured by different diagnostics in similar plasmas are rare [Matthews 1991, Adamek 2008, Kimura1979, El Shaer 1981].

In this section, a dedicated experiment in which SOL T_i was measured for the first time in Tore Supra using the CXRS is described. The ion temperature obtained from the CXRS is compared with the RFA measurements.

The Tore Supra CXRS system is designed to measure the ion temperature in the confined plasma. The outermost line of sight is located at major radius R_{CXRS} = 2.99 m. Therefore, in the standard plasma configuration in Tore Supra ($R = 2.39$ m and $a = 0.72$ m) the outermost measurements are just 12 cm inside the LCFS.

The CXRS measurements described here were performed in a specially arranged plasma configuration with the plasma contact point on the HFS bumper limiter. During the discharge, the plasma volume was increased so that the major radius of the outboard midplane LCFS $R_{mid\,out}$ varied from 2.87 m to 2.93 m and the minor radius varied from 0.64 – 0.68 m, figure 4.9 (right). In such configuration the most outer CXRS viewing lines intersect the SOL. Originally, simultaneous measurements with CXRS and the RFA were planned. However, because of the problems with the neutral beam injector (which is required for the CXRS diagnostic system) and the subsequent replacement of the RFA by another probe, the measurements were performed in separate discharges. The macroscopic plasma parameters of the discharges are stated in table 4.1. Except the total heating power and the intensity toroidal magnetic field, the discharge parameters are very similar.

	CXRS	RFA
shot number	43533	42390
P_{ohm} [MW]	0.6	0.5
P_{NBI} [MW]	0.4	0
I_p [MA]	0.8	0.65
$\langle n_e \rangle$ [10^{19} m^{-3}]	2.2 – 2.4	2.1
B_t [T]	4.0 – 4.1	3.2
q_a	5.6 – 6	5.4

Table 4.1. Macroscopic parameters of the discharges.

SOL T_i was measured by CXRS in discharge #43533. During the discharge, four neutral beam pulses, each with the power of 0.4 MW and with the pulse length of 0.5 s, separated by 0.5 s, were injected into the plasma. Radial profiles of CXRS T_i, averaged over each pulse length, are plotted in figure 4.9 (left). As the plasma expands, the LCFS position at the outboard midplane moves outward. However, as seen from figure 4.9, all

four T_i profiles are very similar within the error bars, independently of the location of the viewing lines with respect to the LCFS. This may be surprising since the viewing lines move inside the LCFS and are therefore expected to measure increasing T_i during the discharge. A possible explanation could be that as the lines of sight moves inward, the plasma volume expands. Since that the heating power and density are almost constant over the discharge, the increase of the plasma volume could lead to a decrease of T_i in the confined plasma and in the SOL. As a consequence the individual lines of sight measure roughly constant ion temperature over the discharge. It must be also taken into account that the radial shift of the lines of sight with respect to the LCFS during the discharges is comparable with the spatial resolution of the CXRS. At the LCFS the ion temperature is about 200 – 300 eV and the T_i profiles flatten.

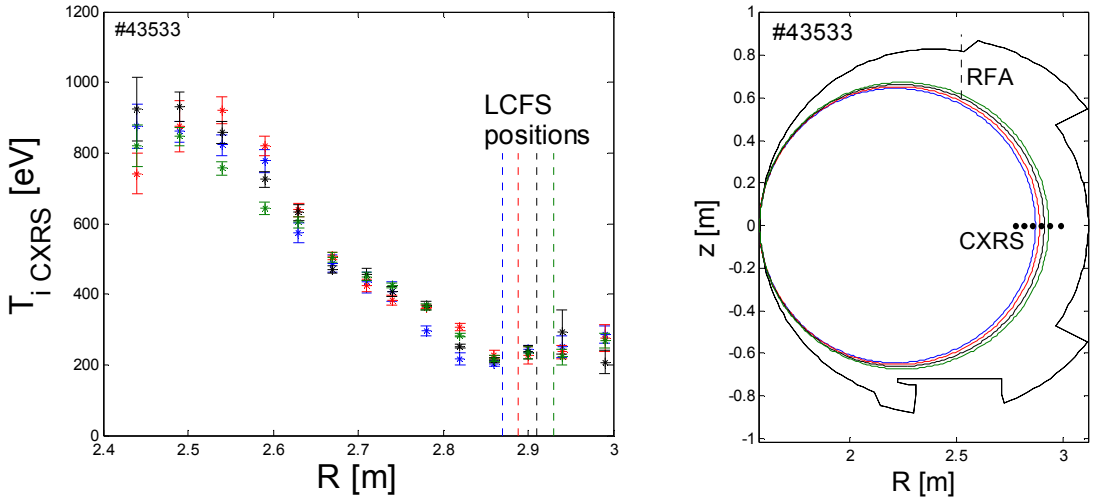

Figure 4.9. Left: radial profiles of the ion temperature measured by CXRS, plotted against the plasma major radius. The major radius of the outer midplane separatrix was shifted steadily from $R_{mid\,out} = 2.87 \rightarrow 2.93\,m$ during the discharge. Right: poloidal cross sections of the plasma during the discharge at the time of the CXRS measurements. Different colours correspond to the T_i profiles shown on the left. The positions of the most outer CXRS viewing lines are indicated by black dots. Although the RFA was not in the plasma during this discharge, its normal poloidal location is indicated by a vertical dotted line.

In figure 4.10, T_i profile measured by the CXRS is compared with T_i obtained from the RFA in the TS discharge #42390. From the database of the RFA T_i measurements this discharge is characterized by the macroscopic parameters that are most similar to that of the discharge #43533 in which the CXRS were performed. The poloidal cross section of the plasma during the RFA reciprocation is identical to that plotted in figure 4.9 (right) in blue. At the LCFS, T_i measured by the RFA is about 50-60 eV which is a factor of ~4 lower than T_i inferred from the CXRS. At the same time, T_i

the profile measure by the RFA decreases with the increase of radius, while the ion temperature measured by the CXRS increases towards the wall in the SOL. The discrepancy could be caused by several possible effects.

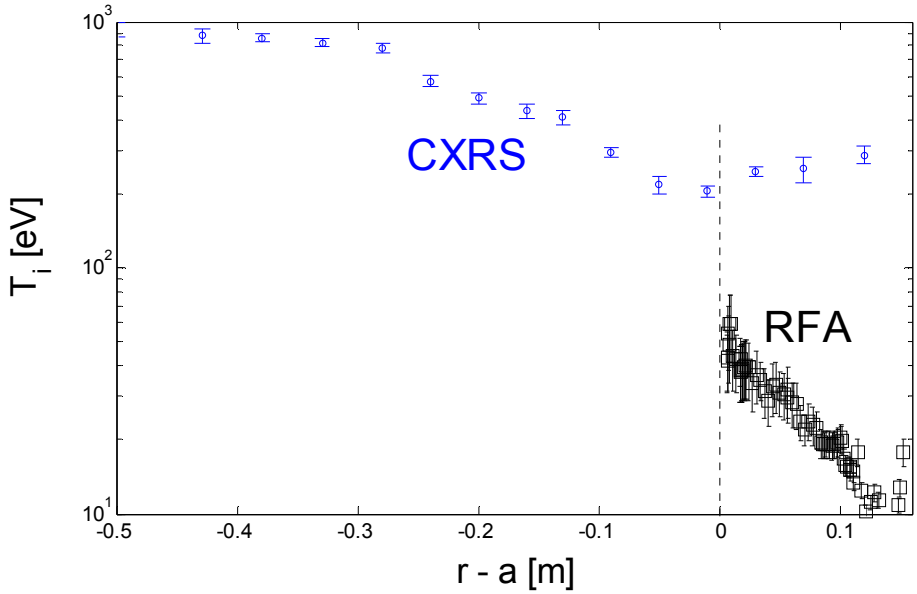

Figure 4.10. Radial profiles of T_i measured by the CXRS (TS discharge #43533) and RFA (TS discharge #42390). Macroscopic parameters of the discharges are stated in table 4.1. Dotted line indicates the position of the LCFS.

First, although the plasma configurations are very similar for both discharges, there is a substantial difference in some macroscopic parameters such as the total heating power and B_t. While the RFA measurements were performed in a pure ohmic plasma with $P_{ohm} \cong 0.5$ MW, the CXRS measurements were performed in the discharge with $P_{ohm} \cong 0.6$ and $P_{NBI} = 0.4$ MW. Although the neutral beam injection system in Tore Supra serves only for the diagnostic purpose and not for the plasma heating, in this particular discharge P_{ohm} is comparable to P_{NBI}. The total heating power during the CXRS measurements is, therefore, almost twice as high as during the RFA reciprocation. On the other hand, the RFA measurements in the plasmas with lower hybrid heating (LHH) and/or ion cyclotron resonance heating (ICRH) powers of several MW revealed T_i of at most 100 eV near the LCFS. It is therefore reasonable to expect that T_i measured by the RFA in the neutral-beam-heated plasma with $P_{NBI} = 0.4$ MW will be substantially lower than this value (assuming, of course, that the effect of P_{NBI}, P_{ICRH} and P_{LHH} on SOL T_i are similar). B_t is also by about 25% lower during the RFA measurements compared to the CXRS measurements. It was demonstrated recently that SOL T_i scales relatively strongly with B_t [Kocan 2009b]. However, according to the scaling reported in [Kocan 2009b] an increase of B_t by 25% would lead to an increase of T_i by up to a factor of ~2.

Therefore, the difference in the heating power or in B_t cannot fully explain the difference in the CXRS and the RFA T_i.

Another source of the discrepancy might be due to the influence of impurities on the RFA measurements. Since the analysis of the RFA *I-V* characteristics assumes Maxwellian singly charged ions SOL, T_i inferred from the RFA measurements may be influenced by impurities [Pitts 1991]. As mentioned in section 2.3, separation of the components of the analyzed ion flux by charge state and temperature has been proposed in [Pitts 1991]. However, the model needs to specify the fractions of the total flux carried by ions with a given charge state as well as their temperatures. Such quantities are not available. In general, in a plasma with singly charged fuel ions the impurities lead to an underestimation of the measured ion temperature. However, if the impurity fluxes were important, the decaying part of the RFA *I-V* characteristic plotted on a semi-logarithmic scale would be characterized by a curvature instead of a linear decay (see e.g. figure 7.1.4 in [Pitts 1991]). Although these effects may be partially masked by the experimental noise, such curvature is not seen on the *I-V* characteristics, indicating perhaps that the effect of impurities on RFA T_i measurements is insignificant.

Several questions concerning the CXRS measurements in the edge plasma and in the SOL, already mentioned in section 1.4.2.10 and discussed in more detail in [Bogen 1995]), need to be addressed. Are the impurity ions in thermal equilibrium with fuel ions at the SOL densities and electron temperatures $n_e < 2.5 \cdot 10^{18}$ m^{-3} and $T_e < 20$ eV, respectively? How does the overlapping of the Doppler-broadened C VI lines by other hydrogen-like lines (or other effects like e.g. atomic fine structure or Zeeman effect) in the SOL influence the spectral analysis? If not in the SOL, at what radial position in the edge plasma can we already believe the CXRS measurements?

A large number of uncertainties mentioned above make a direct comparison of SOL T_i measured by the RFA and the CXRS difficult. It is possible that the discrepancy could be fully explained by combining the individual uncertainties. It is also important to mention that T_i measured by RFA is close to that measured in the similar plasmas in other tokamaks using different probe diagnostics (see references in section 1.4.1). In addition, the flattening or even small increase of SOL T_i measured by the CXRS is also inconsistent with experimental observations reported elsewhere. Moreover, if the CXRS measurements were correct and SOL T_i was 4 times higher compared to what is typically measured by the RFA, then T_i / T_i in the SOL would also be four times higher. This would imply $T_i / T_i = 4$ in detached plasmas and T_i / T_i up to 30 in heated plasmas. Such high values of the ion-to-electron temperature ratio would be inconsistent with the degree of the ion-electron collisisonality in the SOL (see chapter 3).

4.3. The segmented tunnel probe for Tore Supra plasma boundary

As a part of this thesis, a segmented tunnel probe (STP) for fast measurements of temperature and density measurements in the SOL of Tore Supra was designed, built, calibrated by particle simulations, and used for the first time in a large tokamak. This work is summarized in the following sections.

4.3.1. Introduction

It is generally accepted that anomalous transport – one of the key issues in the magnetic fusion research – is due to plasma turbulence (e.g. [Callen 1990, Connor 1993, Hidalgo 1995, Conway 2008]). A better understanding of turbulence in the plasma boundary region requires measurements of the fluctuation-induced conducted ($\left\langle \tilde{T}\,\tilde{E} \right\rangle$) and convected fluxes ($\left\langle \tilde{n}\,\tilde{T} \right\rangle$) [Wootton 1990]. This requires new experimental techniques for the simultaneous measurements of the fluctuations of the ion and electron temperatures, the electron density and the electric field. While the fluctuations of the electron temperature $\tilde{T}_e$ can be measured using Langmuir probes (e.g. [Rudakov 2002]), the measurements of the fluctuations of the ion temperature $\tilde{T}_i$ are extremely rare [Kočan 2006, Stöckel 2006]. In recent simulations of the MAST L-mode plasma using the 3D turbulence code BOUT, the amplitude of the fluctuations of the ion temperature was found to be approximately twice that of the electron temperature, both inside and outside the LCFS [Dudson 2008]. Simultaneous measurements of $\tilde{T}_i$ and $\tilde{T}_e$ on turbulence time-scales (~μs) would thus be very useful for the validation of the codes.

From the experimental techniques described in section 1.4.2, only the E×B analyzer (section 1.4.2.4 and [Staib 1980, Staib 1982, Matthews 1984]) can be used for the fast T_i measurements. However, because of the limited number of collectors, the ion velocity distribution is not measured directly. Instead, the ion currents received by the probe collectors are fit to the distributions obtained from a set of particle simulations. The reliability of the measurements thus depends on how realistic are the simulations (i.e. the velocity distribution of the injected ions, modelled geometry, secondary electron emission from the collectors, etc.). In addition, an E×B probe cannot measure $\tilde{T}_i$, $\tilde{T}_e$ and $\tilde{n}_e$ simultaneously.

A new probe, the STP, for fast measurements of $\tilde{T}_i$, $\tilde{T}_e$, $\tilde{n}_e$ and $\tilde{V}_f$ (with $\tilde{V}_f$ being the fluctuations of the floating potential) has been recently tested in the CASTOR tokamak [Stöckel 2006, Kočan 2007, Adamek 2008]. During the evaluation of the thesis, a new segmented tunnel probe was designed, calibrated, and used in the Tore Supra SOL. Two STPs are placed back to back in a Mach probe arrangement to provide measurements of the parallel flow velocity. All quantities can be measured simultaneously, which, together with some other important advantages (such as the

immunity to sheath expansion effects [Dejarnac 2007], smaller perturbation by fast electrons [Van Rompuy 2007], etc.), makes an impression that a STP could become a "holy grail" of the tokamak probes. Unfortunately, as shown in the following sections, the interpretation of the STP measurements is a subject of difficulties.

In section 4.3.2 the principle of the STP is described. The most important results measured by the prototype STP in CASTOR are summarized in section 4.3.3. The design and the calibration of a new STP for Tore Supra plasma boundary as well as the preliminary results from the measurements in Tore Supra are addressed in section 4.3.4.

4.3.2. STP principle

A STP consists of a hollow conducting tunnel, a few millimeters in diameter and typically a few millimeters deep, closed at one end by an electrically isolated conducting back-plate (figure 4.11). The tunnel axis is aligned with the magnetic field. To repel electrons from the incident plasma flux, constant negative bias is applied to the electrodes. The ions flowing into the tunnel get demagnetized by the electric field gradient in the magnetic pre-sheath (MPS), and redistributed between the tunnel and the back plate.

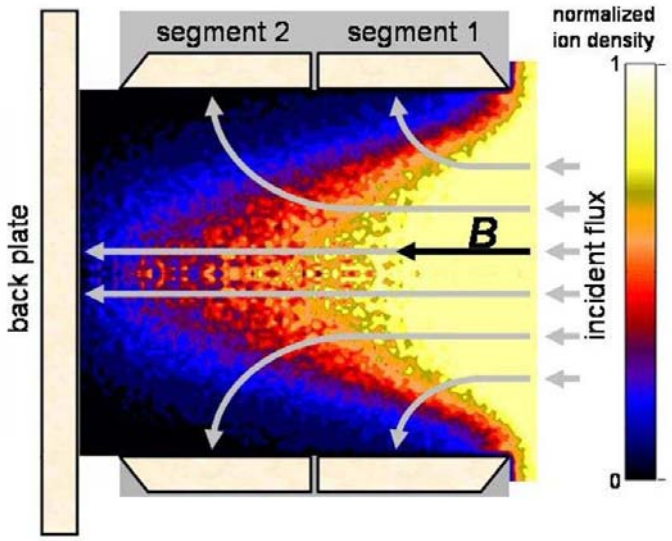

Figure 4.11. Schematic of the segmented tunnel probe. The ion guiding-centre trajectories are indicated by arrows.

Since the MPS thickness L_{MPS} varies with T_e [Chodura 1982, Kim 1995, Gunn 1997], the tunnel-to-back-plate ion current ratio r_{tb} is a function of the electron temperature. Assuming that all ions in the MPS above the tunnel are collected by the tunnel, $r_{tb} \approx r_t^2/(r_t - L_{MPS})^2 - 1$ (where r_t is the tunnel radius).

The sum of the tunnel and the back plate currents divided by the cross-section of the tunnel orifice gives the parallel ion saturation current density j_{sat}. Since the probe is concave, only the ions entering the tunnel orifice can be collected by the STP electrodes. Therefore, the collecting area of the STP is clearly defined by the tunnel orifice and the

measurements of j_{sat} are immune to the sheath expansion [Dejarnac 2007] (this is in contrast to a convex Langmuir probes which, due to the deflection of ions in the MPS, collect the ion fluxes that are larger than that the flux of the ion guiding centres on the geometrical projection of the probe electrode along **B**). In addition, the measurements of j_{sat} are only weakly influenced by secondary electron emission due to ion impact as a large fraction of the incident ion current is collected by the tunnel (The current to the tunnel is not affected by the secondary electron emission. This is because the tunnel surface is aligned with B and any secondary electrons emitted from the tunnel surface return back within less than one electron Larmor period so that the net secondary electron current from the tunnel surface is zero).

The axial distribution of ion flux along the tunnel is determined by the relative strength of the radial acceleration of ions with respect to their incident parallel velocity. Therefore, if the tunnel is divided into two segments the ion temperature T_i could be obtained from the ratio of the ion currents to the tunnel segments r_{seg}.

The spatial resolution of the STP is defined by the tunnel diameter. To resolve the turbulent structures in the SOL, the tunnel diameter must be smaller than the typical radial size of the intermittent plasma filaments, or "blobs", (~1 cm). On the other hand, in order to measure comparable tunnel and back plate currents, the tunnel diameter should be about $4\,L_{MPS}$. L_{MPS} is typically 0.2 – 1 mm in Tore Supra. This implies a tunnel diameter of a few millimeters.

A STP has several advantages compared to simple Langmuir probes. In addition to the simultaneous measurements of j_{sat}, T_e and T_i, its most important advantage is its temporal resolution. Since the measurements are performed at constant negative bias (dc mode), the temporal resolution a STP is limited only by the sampling frequency of the probe electronics. Moreover, as shown in [Gunn 2002b] the tunnel-to-back-plate ion current ratio r_{tb} is relatively insensitive to the angular misalignment between the tunnel axis and B as long as the misalignment is less than 5°. Such tolerances can be easily achieved in experiment, leaving for wide margin of the variation of the edge safety factor. In addition, a recent theoretical study [Van Rompuy 2007] shows that in many conditions a STP may be less affected by hot electrons than a simple Langmuir probe.

On the other hand, the main handicap of the STP is in the difficulty of the interpretation of the temperature measurements. Since the electrostatic potential inside the tunnel is influenced by the local temperatures and densities, the measurements can only be interpreted by calibrating the probe using particle simulations. Typically, a set of PIC simulations (section 4.3.4.2) for given probe dimensions and the various combinations of T_i, T_e, j_{sat} and V_{diff} (with V_{diff} being the potential difference between the unperturbed plasma and the probe electrodes) is performed to produce the calibration curves, i.e. the scaling between the measured r_{tb} and r_{seg} and unknown T_e and T_i, respectively [Kočan 2007]. $V_{diff} = V_{bias} + V_{sf} + V_f$ where V_{bias} is the external bias voltage applied to the electrode, V_{sf} is the floating sheath potential (Eq.(1.9)) and V_f is the floating potential). Since V_f varies in time and space and in some cases it becomes

comparable to or larger than V_{sf} and V_{bias}, an additional electrically floating electrode located near the tunnel entrance is needed to measure V_f simultaneously with r_{tb} and r_{seg}.

4.1.3. A Prototype STP tested in the tokamak CASTOR

A prototype STP was build by the Institute of Plasma Physics (IPP) in Prague, Czech Republic, and tested in the CASTOR tokamak [Stöckel 1999]. The length and the diameter of the tunnel were 5 mm. The tunnel was divided into two segments of equal length, figure 4.12. The STP was calibrated using the two dimensional particle-in-cell (PIC) code XOOPIC [Verboncoeur 1995]. The probe consisted of two identical tunnels mounted back-to-back providing, in addition to T_i, T_e and j_{sat}, measurements of the parallel Mach number $M_{//}$. Four electrically floating pins were installed near the tunnel entrance to measure V_f as well as the radial and poloidal propagation of intermittent structures.

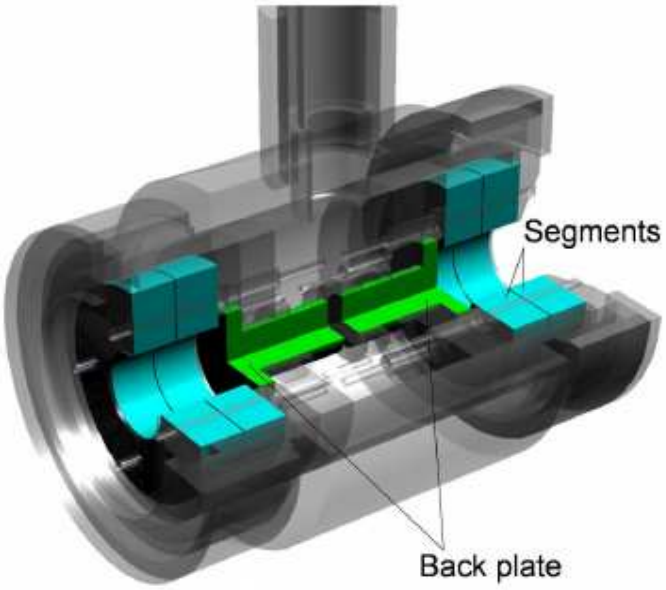

Figure 4.12. Schematic drawing of the STP prototype tested in CASTOR tokamak. Two identical tunnels are mounted back-to-back (taken from [Kočan 2007].

Radial profiles of SOL T_i, T_e and j_{sat}, measured on shot-to-shot basis in reproducible ohmic discharges, were compared with T_e and j_{sat} measured by a radial array of the Langmuir probes [Kočan 2007] (figure 4.13) as well as with T_i measured by the Katsumata probe [Adamek 2008]. T_e and T_i measured by the STP and by the Langmuir and the Katsumata probes, respectively, were found to be similar. A factor of ~1.5 higher j_{sat} measured by the Langmuir probes was attributed to sheath expansion effects on the Langmuir probe. SOL T_i/T_e measured by the STP was found to be

inversely proportional to the central-line-averaged density $\overline{n}_e$ ($T_i/T_e = 2.8 \rightarrow 1$ for $\overline{n}_e \cong 0.2 \rightarrow 0.8 \cdot 10^{18}\ \mathrm{m}^{-3}$), confirming similar results reported e.g. from [Matthews 1991]. The asymmetry in T_i measured by each side of the STP was found to be qualitatively consistent with the kinetic model of Valsaque *et al*. [Valsaque 2000]. First simultaneous measurements of the fast periodic fluctuations of T_i, T_e, j_{sat} and V_f, induced by an insertion of the externally biased electrode, were obtained by the STP (figure 4.14 and [Stöckel 2006, Kočan 2006].

After the promising measurements with the prototype STP in CASTOR it was decided to build a similar probe for the Tore Supra plasma boundary.

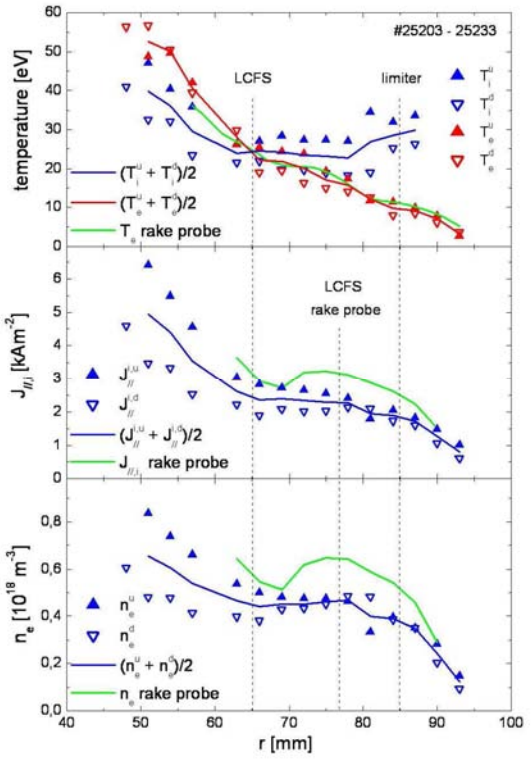

Figure 4.13. Radial profiles of ion and electron temperatures, ion saturation current density and the electron density (from top to bottom) measured by the CASTOR STP. The parameters measured by the upstream ("u") and the downstream ("d") side of the probe are plotted separately. Radial profiles measured by the radial array of Langmuir probes ("rake probe") are plotted for comparison (taken from [Kočan 2007]).

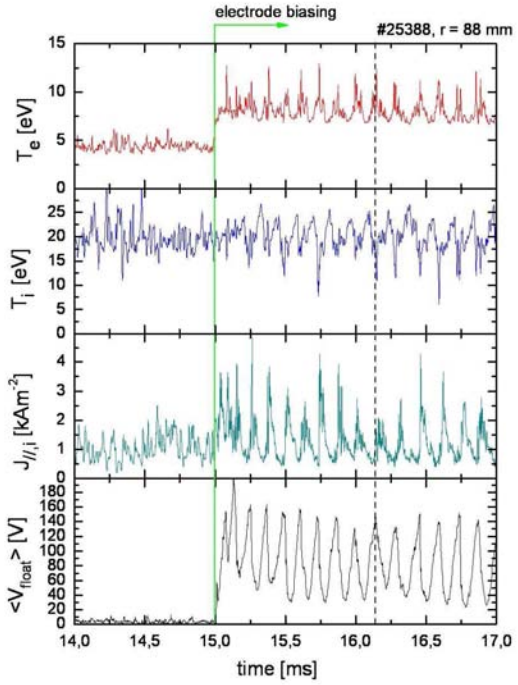

Figure 4.14. Temporal evolution of the electron and ion temperatures, ion saturation current density and floating potential measured by the STP during an experiment with a biased electrode inserted into the plasma. For $t > 15$ ms an external bias of +250 V with respect to vessel ground was applied to the electrode (reproduced from [Stöckel 2006]).

4.3.4. Tore Supra STP

4.3.4.1. Probe design

The STP was designed and fabricated in collaboration between CEA Cadarache and IPP-Prague.

Individual components of the probe head are shown in figure 4.15. The probe consists of two identical STPs mounted back-to-back in a Mach probe arrangement. Each STP consists of a compact electrode stacking arrangement inserted into a boron-nitride (BN) cup (1). BN was chosen for its good electrical insulation properties, low coefficient of thermal expansion, and good machining properties. The cup is designed to accommodate the tunnel components as well as the electrodes for the measurement of the floating potential (referred to as "ring"). A circular aperture with a diameter of 5 mm, which coincides with the tunnel diameter, is drilled into the cup. The aperture steadily expands on the plasma side with an angle of 53° with respect to the tunnel axis. Such a chamfered opening is used in order to reduce the attenuation of the incident ion flux on the BN cup that could make the effective collection area of the STP smaller and lead to an underestimation of j_{sat}. However, the mechanical properties of a relatively fragile material such as the BN do not allow reaching an ideal knife-edge opening of the tunnel aperture. The tunnel electrodes are thus preceded by a BN tunnel of length 0.5 mm. A BN tunnel was included in the PIC simulations described in section 4.3.4.2 (figure 4.19).

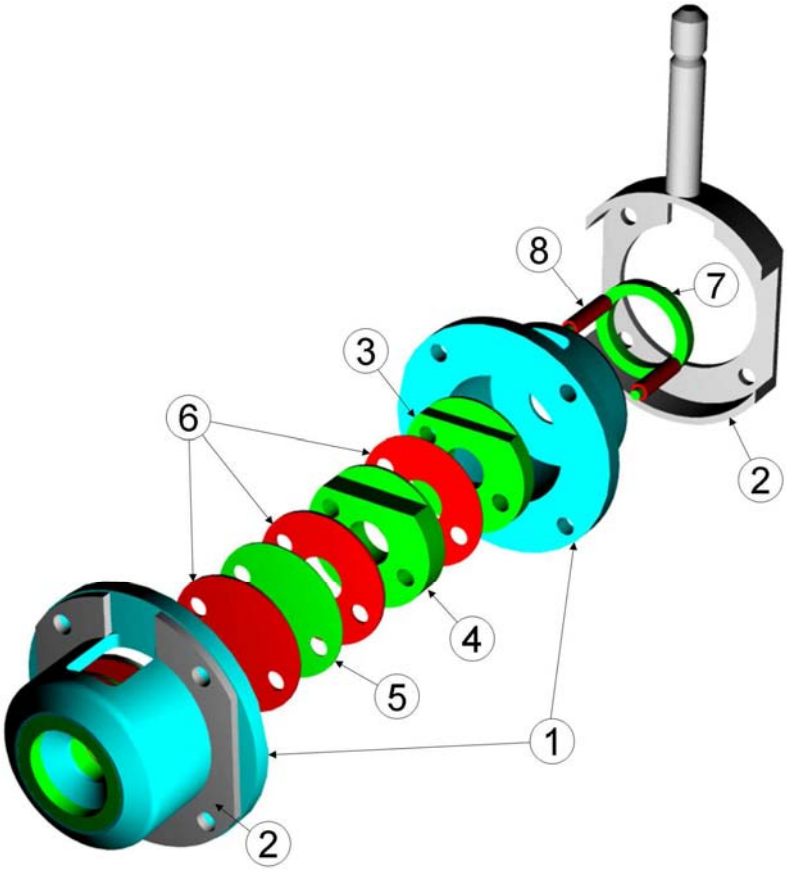

Figure 4.15. Schematic of the Tore Supra segmented tunnel probe.

The STP tunnel consists of two segments (3, 4) and the back plate (5), isolated electrically from each other by mica spacers (6). The segment near the tunnel orifice is referred to as "segment 1". The segment near the back plate is referred to as "segment 2". The tunnel segments and the back plate are made of a low-cobalt unmagnetized stainless steel (Inox 316L). This material is used for all other stainless- steel components of the STP as well. The thicknesses of segment 1 and segment 2 are 2 and 3 mm, respectively. The thickness of the back plate is 0.2 mm. The thickness of the mica sheet between the segments is 0.1 mm, which is negligible compared to the total length of the tunnel. The thickness of the mica sheet between segment 2 and the back plate is 0.4 mm. The natural form of mica was chosen for its low outgassing rates, good electrical isolation properties and easy machining. The same material was successfully used in the omegatron plasma ion mass spectrometer [Nachtrieb 2000b].

The ring (7) is made of stainless steel and has an outer diameter of 12 mm, an inner diameter of 9 mm and thickness of 1.5 mm. A more refined approach would be to use several pins (like in case of the CASTOR STP) instead of a single electrode in order to resolve spatially the intermittent structures in the SOL. However, since the reciprocating probes in Tore Supra have only up to nine cables (which, in addition to a ninth earthing cable from the cable screens, are already fully employed by four segments, two back plates and two rings), V_f can only be measured by a single electrode. Two support rods with the diameter of 1.2 mm, terminated by a thread, are brazed to the ring. The rods, isolated electrically by alumina tubes (8) with the outer diameter of 2 mm, are guided through the holes drilled into the BN cup and into the tunnel components and are secured by the locknuts behind another mica sheet which is attached to the rear of the back plate. The rods also compress all tunnel components and fix them to the BN cup.

Both STPs are pressed back-to-back by a stainless-steel support. A cylindrical holder (diameter of 4 mm) is brazed to the support. The holder is inserted into the central tube of the probe arm and secured by two locknuts. The holder can be rotated which allows aligning the probe head with the magnetic field.

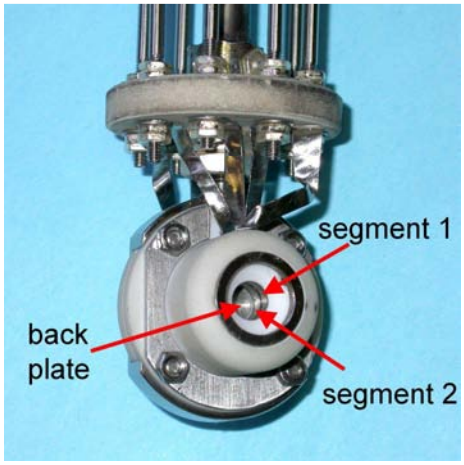

Figure 4.16. Photograph of the Tore Supra STP. Two segmented tunnels are mounted back-to-back.

Figure 4.17. Photograph of the entire probe head before insertion into the CFC housing. The length of the probe from the centre of the tunnel to the end of the pins is 263 mm.

The signals from the probe electrodes are guided via eight molybdenum strips (figure 4.16). The strips are brazed to the STP electrodes, guided through the specially arranged opening in the BN cup and are fixed by the locknuts to the stainless steel rods. The rods (diameter of 2 mm) are guided along the probe arm through two disks and are terminated by silver-coated stainless steel pins (figure 4.17). The lower disk (diameter of 30.9 mm) is pressed against the expanded section of the central tube and secured by a locknut. The upper disk (diameter of 34.8 mm) is pressed against the stainless steel supporting structure located at the end of the central tube. Both disks were originally made of BN. However, the original upper disk was broken during the manipulation with the probe and was replaced by a new desk made of alumina. The length of the probe from the centre of the tunnel to the top of the pins is 263 mm.

The STP is inserted into the protective housing made of carbon fiber composite (CFC). The outer and the inner diameters of the CFC housing are 40 and 31 mm, respectively. Plasma flows towards the tunnel through the orifice drilled into the housing. Ideally, the diameter of the orifice should be larger than the ring diameter (i.e. larger than 12 mm) so that the whole ring will be exposed to the plasma and the measurements of V_f would be averaged over the total circumference of the ring. However, since the probe head is in mechanical contact with the probe arm only through the holder and the molybdenum strips which are relatively thin, it is cooled almost exclusively by radiation (thermal calculations for the STP were not performed because of the complicated shape as well as the material composition of the STP head). In order to prevent damage of the probe head by large heat fluxes (heat flux densities higher than 10 MW m^{-2} are measured in the Tore Supra SOL), a specially arranged orifice (figure 4.18) was drilled into the CFC. If the tunnel and the orifice are both perfectly aligned with B, the edge of the tunnel is 1.5 mm far from the CFC orifice. This is larger than the maximum value of the L_{MPS} in the Tore Supra SOL. It seems, therefore, reasonable to neglect the attenuation of the ion current flowing towards the tunnel by the CFC walls.

Figure 4.18. Photograph of the STP inserted into a CFC protective housing before the installation in Tore Supra. Also indicated are the dimensions of the orifice drilled into the orifice (in millimeters).

4.3.4.2. Probe calibration

The complexity of the tunnel geometry and the dependence of the potential inside the tunnel on the local parameters, such as the temperatures and the densities, makes the analytical derivation of the scaling of T_i (T_e) with the ion current ratios r_{seg} (r_{tb}) impossible. Therefore, in order to interpret the measurements, the STP requires to be calibrated by kinetic simulations. The Tore Supra STP was calibrated using the particle-in-cell code XOOPIC ([Verboncoeur 1995] and section 2.3.1.3). XOOPIC allows for simulations in cylindrical coordinates. Due to the axial symmetry of the probe (and assuming that plasma outside the tunnel is homogeneous along the tunnel diameter), the whole tunnel can be thus modeled by XOOPIC.

The main goal of the XOOPIC calibration is to quantify the proportionality between the temperatures that are unknown in experiment and r_{tb} and r_{seg} that are measured directly. Generally, this requires running a large number of simulations for different combinations of the input parameters (such as T_i, T_e, ion and electron current densities, etc.) within the range that is typically measured in the Tore Supra SOL.

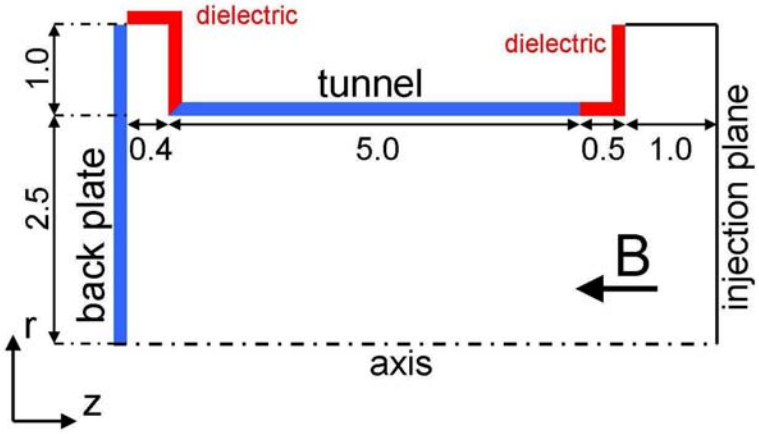

Figure 4.19. Schematic of the simulations domain used for the calibration of the STP by the particle-in-cell code XOOPIC.

The simulations of the STP by XOOPIC are very similar to those described in section 2.3.1.3. The schematic of the simulation domain is illustrated in figure 4.19. Maxwellian ions ($T_i, j_i \equiv j_{sat}, m_i = m_D$) and electrons ($T_e, j_e = j_i\sqrt{m_i / m_e}$) are injected from the RHS boundary (referred to as "injection plane") towards the tunnel. Here *T* and *j* refers to the temperatures and the current densities at injection, respectively. The injection plane is 1 mm from of the tunnel orifice. The total radius of the system is chosen to be 1 mm (i.e. a few Larmor radii) larger than the tunnel diameter in order to eliminate selective ion losses in the perpendicular direction due to ions escaping the system before arriving at the tunnel entrance. The surface near the tunnel entrance facing the injection plane is modelled as a dielectric perpendicular to the tunnel axis. In reality, this surface is at 53° with respect to the tunnel axis (see component 1 in figure 4.15). However, test

simulations revealed that the chamfering does not influence the ion current ratios r_{tb} and r_{seg}. While the chamfered edges near the tunnel orifice are neglected in the simulations, a 0.5 mm long dielectric tunnel attached to segment 1 is taken into account. This is because the dielectric tunnel collects all ions with the Larmor radius larger than their distance from the tunnel surface if the ion parallel transit time along the dielectric tunnel is longer than the Larmor period. For $B = 3.5$ T, $m_i = m_D$, and $T_i = 20$ eV, the Larmor period $T_L = 2\pi m_i/(qB) \cong 3.7 \cdot 10^{-8}$ s, which is only by a factor of ~3 longer than the parallel transit time $t_{//} = L/v_{//}$ (with L being the length of the dielectric tunnel and $v_{//}$ - defined here as $\sqrt{2}v_T$ - the parallel ion velocity). In the test simulations without the dielectric the ion current to segment 1 was by about 25% higher compared to the simulations with the dielectric tunnel, indicating that a non-negligible fraction of ions in the MPS above the tunnel surface can be collected by the dielectric tunnel. The dielectric which separates the tunnel segment (i.e. a mica plate with the thickness of 0.1 mm) is neglected in the simulations. The ion currents to segment 1 and segment 2, $i_{seg\,1}$ and $i_{seg\,2}$, are calculated by integrating the ion current distribution along the tunnel collected in the steady state over the distance corresponding to the length of a given segment.

The injection plane and the boundary attached to it are held at 0 V. The tunnel and the back plate are at $V_{bias} + \phi_{ph}$ (with ϕ_{ph} defined by Eq.(2.5)) with respect to the injection plane. Most of the simulations were performed for $V_{bias} = -100$ V. However, the simulations for different values of V_{bias} are also discussed below (figure 4.21).

The magnetic field $B = 3.5$ T (which is the value of the toroidal magnetic field at the magnetic axis used in most Tore Supra discharges) is aligned with the tunnel axis. PIC simulations for $B = 2.5$ T were also performed for comparison (see figure 4.22).

The calibration was performed for the following range of ion and electron temperatures and ion current densities: $T_i = 5 - 160$ eV, $T_e = 5 - 80$ eV and $j_{sat} = 1 - 8$ kA m^{-2}. While the range if T_i and T_e, typically measured in the Tore Supra SOL, is well covered by the simulations, the ion current densities in the Tore Supra SOL can reach up to 100 kA m^{-2}. The reason why we did not perform the simulations for higher values of j_{sat} is because of the long time needed for single XOOPIC run. The simulation for $j_{sat} = 8$ kA m^{-2} and $T_e = 10$ eV already takes several days to run on a Pentium 4 CPU 3GHz PC, meaning that the simulation for higher j_{sat} would require up to several weeks.

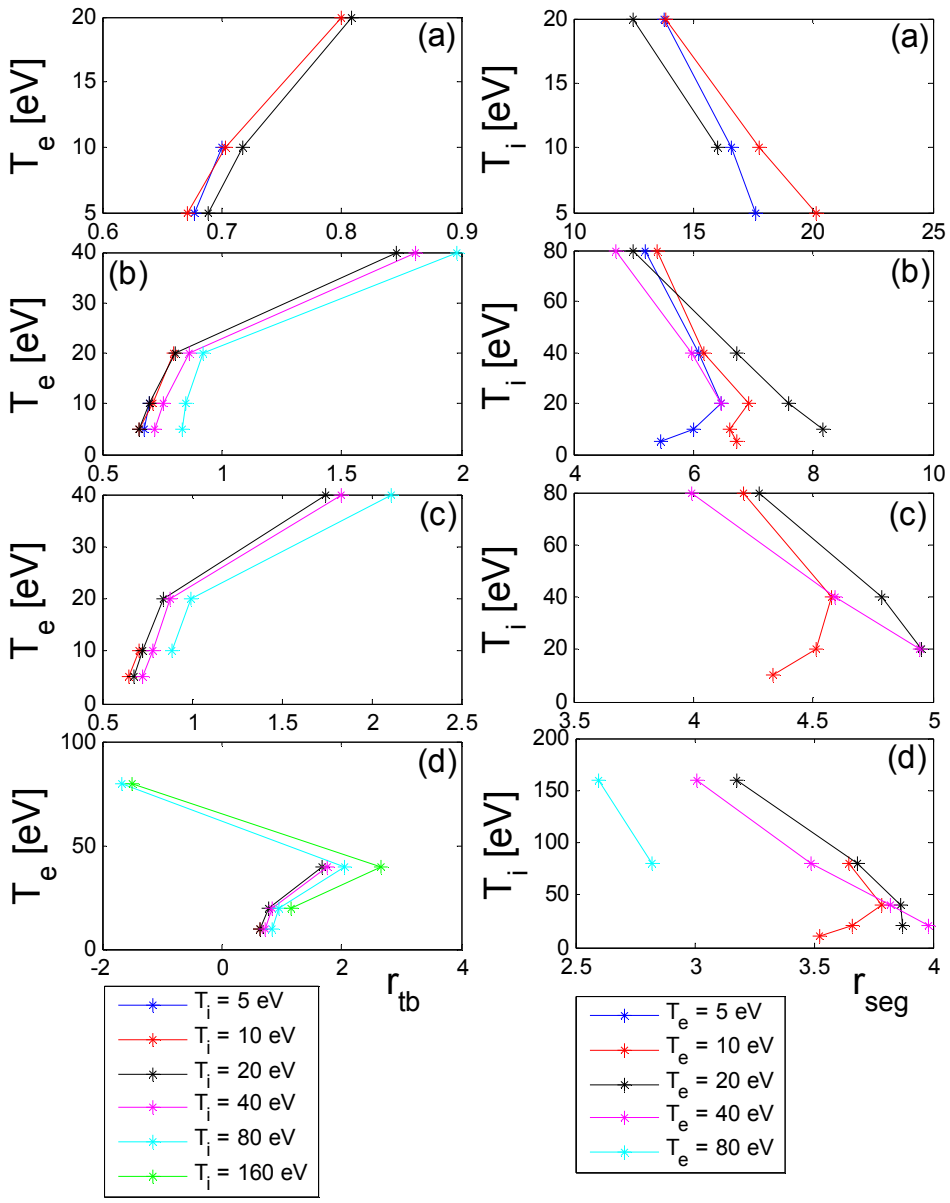

Figure 4.20. Calibration curves obtained from the XOOPIC simulations for j_{sat} of (a) 1, (b) 2, (c) 4, and (d) 8 kA m^{-2}. Left: electron temperature plotted against the tunnel-to-back-plate ion current ratio. Right: ion temperature plotted against the ion current ratio to tunnel segments.

The calibration curves obtained from the simulations for $B = 3.5\,\mathrm{T}$, $V_{bias} = -100\,\mathrm{V}$ and different T_i, T_e and j_{sat} are plotted in figure 4.20. Except for $T_e = 80\,\mathrm{eV}$, r_{tb} increases with T_e. This agrees qualitatively with the theory which predicts the increase of the MPS thickness above the tunnel with T_e [Chodura 1980, Kim 1995, Gunn 1997], so that more ions are deflected towards the tunnel segments at higher electron temperatures. r_{tb} from the simulations seems to be almost independent of j_{sat}. One would expect the decrease of

r_{tb} with the increase of j_{sat} as the tunnel would be better shielded from the unperturbed plasma column along which the ions flow towards the back plate. For $T_e = 80\,\text{eV}$, r_{tb} is negative as the bias voltage applied to probe electrodes is not sufficient to repel all thermal electrons and the current to the back plate becomes dominated by the electrons. Some electrons are collected by the back plate already at $T_e = 40\,\text{eV}$ so that the increase of r_{tb} with T_e is not purely due to the MPS expansion. For most simulations the ratio of ion currents to tunnel segments r_{seg} decreases with the increase of T_i. This is intuitive as the probability that the ion will reach segment 2 before being deflected towards the tunnel surface is expected to increase with the parallel ion energy. However, r_{seg} seems to be a relatively weak function of T_i. The factor of 4 variation of T_i leads to r_{seg} varying by only about 25 %. If the experimentally measured r_{seg} were characterized by such low sensitivity to T_i, it would be practically impossible the measure any variation of T_i just because of the noise on the measured signals. A relatively weak variation of r_{seg} with the variation of T_i was observed earlier. In XOOPIC simulations of the CASTOR STP r_{seg} was almost constant for $j_{sat} > 3.5$ kA m^{-2} and $T_i > 20\,\text{eV}$ (see figure 3 in [Kočan 2005]), meaning that the variation of T_i for ion temperatures above 20 eV is undistinguishable in experiment. Although the ion current densities in the CASTOR SOL are typically lower than 3.5 kA m^{-2}, this might be the reason why the prototype STP measured almost constant T_i profile in the SOL of CASTOR (figure 4.13 and figure 4 in [Kočan 2005]). In the Tore Supra SOL, j_{sat} and T_i is typically much higher compared to CASTOR so that, according to the XOOPIC simulations, the sensitivity of the probe to the variation of T_i might be even lower. By analyzing the results from the XOOPIC simulations for the Tore Supra STP it was also found that the modification of the length of the tunnel segments does not improve significantly the sensitivity of r_{seg} to T_i. Note also that some calibration curves plotted in figure 4.20 predict two distinct values of T_i for a single value of r_{seg}, making the interpretation of the measured r_{seg} impossible. On the other hand, as a constructive criticism to the XOOPIC code, it should be mentioned that the (Maxwellian) parallel velocity distribution of injected ions in XOOPIC does not account for pre-sheath effects and does not satisfy Bohm criterion [Allen 1976]. This leads to the formation of the artificial sheath just in front of the injection plane observed in the simulations and could affect the results obtained from XOOPIC.

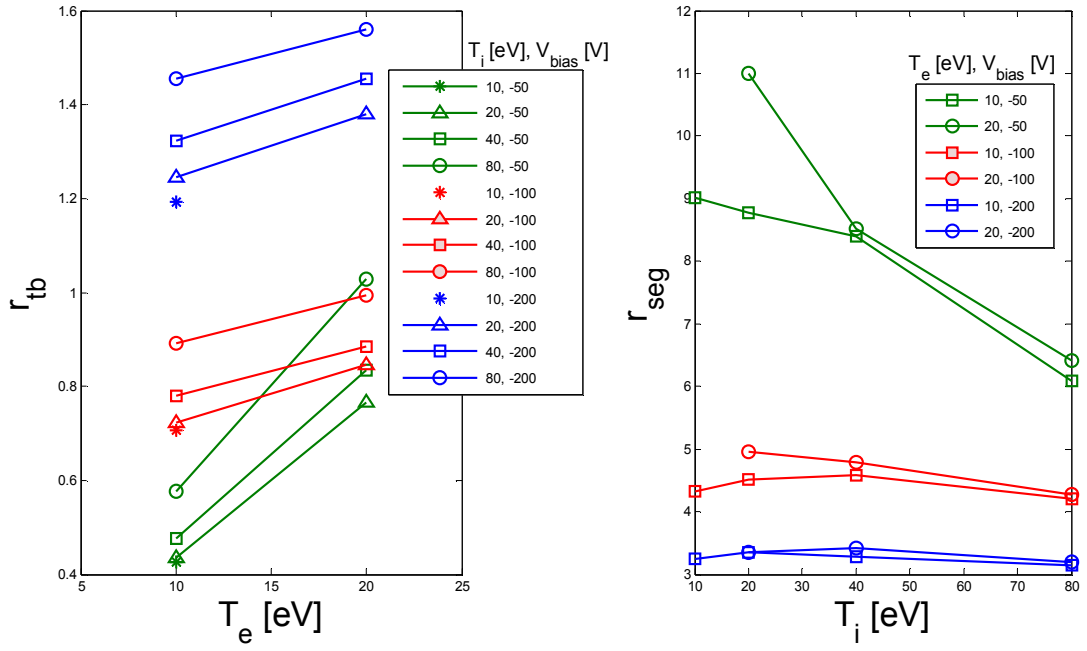

Figure 4.21. Study of the effect of the bias voltage on the sensitivity of the ion current ratios to the variation of T_i and T_e. Left: the tunnel-to-back-plate current ratio plotted against the electron temperature. Right: the ratio of current to tunnel segments plotted against the ion temperature. All simulations are performed for $j_{sat} = 4$ kA m^{-2} and $B = 3.5$ T.

In addition to the simulations for $V_{bias} = -100$ V, a set of simulations for $V_{bias} = -50$ and –200 V and constant $j_{sat} = 4$ kA m^{-2} was performed in order check if the sensitivity of r_{seg} on T_i (and eventually of r_{tb} on T_e) could not be increased by applying a different bias voltage to the electrodes, figure 4.21. For $V_{bias} = -100$ and –200 V the relative variation of r_{tb} with T_e is very similar. For $V_{bias} = -50$ V, r_{tb} seems to be more sensitive to T_e compared to $V_{bias} = -100$ and –200 V. This is, however, mainly due to the fact that $V_{bias} = -50$ V is not sufficient to repel all thermal electrons from the back plate so that the net current to the back plate becomes lower. At $V_{bias} = -200$ V r_{seg} is practically independent of T_i. At $V_{bias} = -50$ V, the relative sensitivity of r_{seg} to T_i is only slightly higher compared to $V_{bias} = -100$ V. These results suggest that the sensitivity of the STP to the variation of both T_i and T_e cannot be improved by applying a different bias voltage to the electrodes.

According to MPS theory, the degree of ion deflection towards the tunnel segments should scale inversely with the intensity of the magnetic field (see section 2.3.1.1). Two simulations for different values of the magnetic field ($B = 2.5$ and 3.5 T) and with all other parameters being fixed ($T_i = 40$ eV, $T_e = 20$ eV, $j_{sat} = 2$ kA m^{-2}, and

$V_{bias} = -100$ V) are compared in figure 4.22. The dependence of r_{seg} and r_{tb} on B agrees qualitative agreement with the theory. The ion current to both tunnel segments decreases with the increase of B whereas the back plate current increases with B. This is because the number of ions that are torn from the magnetic field lines and deflected towards the tunnel segments is lower at higher B. As a consequence, r_{tb} decreases with the increase of B. Since the ion currents to segment 1 and 2 decrease by the same amount with the increase of B but the current to segment 2 is lower in the absolute value compared to the current to segment 1, r_{seg} increases with B.

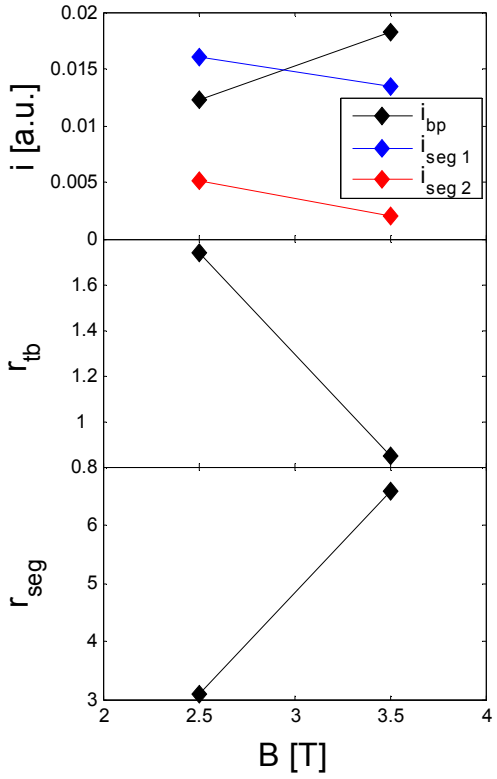

Figure 4.22. Top: ion currents to the tunnel segments (i_{seg1}, i_{seg2}) and to the back plate (i_{bp}). Middle: tunnel-to-back-plate ion current ratio. Bottom: ratio of ion currents to tunnel segments. Results from the XOOPIC simulations for $T_i = 40$ eV, $T_e = 20$ eV, $j_{sat} = 2$ kA m^{-2}, $V_{bias} = -100$ V and for two values of the magnetic field $B = 2.5$ and 3.5 T.

4.3.4.3. Experimental data

The STP was installed in Tore Supra in September 2008. In the period between 16th September and 2nd October, 177 reciprocations were performed with the STP. The probe target position was steadily shifted towards the LCFS in consecutive discharges (figure 4.23, right). For most of the reciprocations the measurements were acquired up to 5 mm outside the LCFS. All STP signals kept their normal behavior even at the maximum target position 4 cm inside the LCFS in an ohmic discharge as well as 2.5 cm outside the LCFS in a plasma heated to 8 MW (figure 4.23, left). The range of the macroscopic plasma parameters covered by the STP is plotted in figure 4.24. Most measurements were performed at the value of B_t close to that used in the PIC simulations (3.5 T).

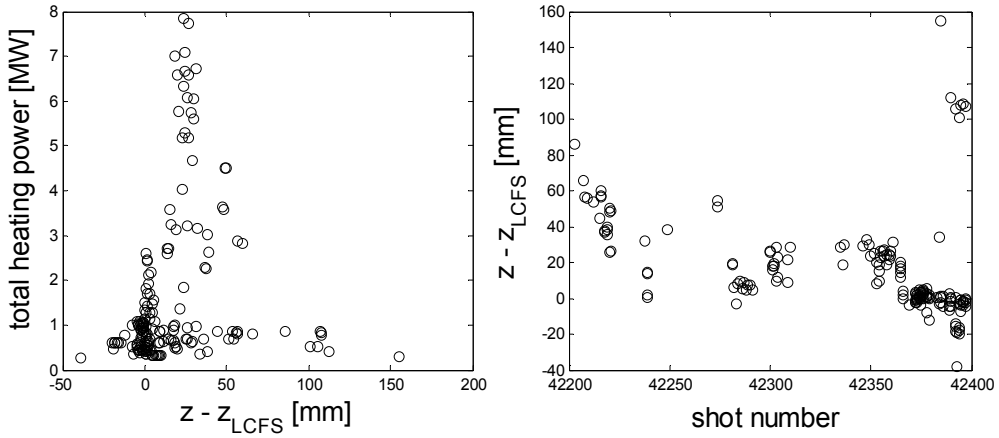

Figure 4.23. Overview of the STP measurements in the Tore Supra plasma boundary (#42203-#42397). Left: total heating power at the time of the STP reciprocation plotted against the vertical distance of the deepest point of measurement from the LCFS. Right: Deepest point of measurement for each reciprocation plotted against the discharge number (data for $z - z_{LCFS} > 100$ mm correspond to a maximum possible probe insertion in small plasmas with the contact point on the inboard bumper limiters).

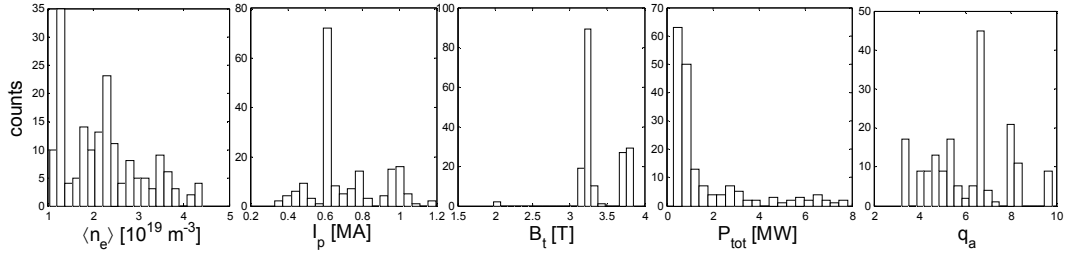

Figure 4.24. The range of the selected macroscopic plasma parameters covered by 177 STP reciprocations in TS discharges #42203-42397.

Originally, it was planned to measure with the STP in a fast mode, i.e. with a 1 MHz sampling frequency. However, since the electronics for the fast measurements was not available at the time of this experiment, the signals were finally measured with a sampling period of 16 μs. A swept voltage was applied to the tunnel segments and back plate, providing measurements of T_e, j_{sat} and V_f using the STP as a simple Langmuir probe. The ring was electrically floating providing additional measurements of V_f. The ion current ratios r_{tb} and r_{seg} measured at $V_{bias} - V_f \cong -100$ V were selected for comparison with PIC simulations (assuming that the sheath potential V_s equals to $0.5T_e \ln[(2\pi m_e / m_i)(1 + T_i / T_e)]$).

Typical raw signals measured by each side of the STP are plotted in figure 4.25. The first row from the top shows the individual currents measured by the tunnel segments (i_{seg1} and i_{seg2}) and the back plate (i_{bp}). Also plotted is the sum of the currents

$i_{tot} = i_{seg1} + i_{seg2} + i_{bp}$. While i_{tot} clearly saturates at high V_{bias} (which is a good sign indicating that all thermal electrons are repelled from the tunnel), i_{bp} and i_{seg1} do not.

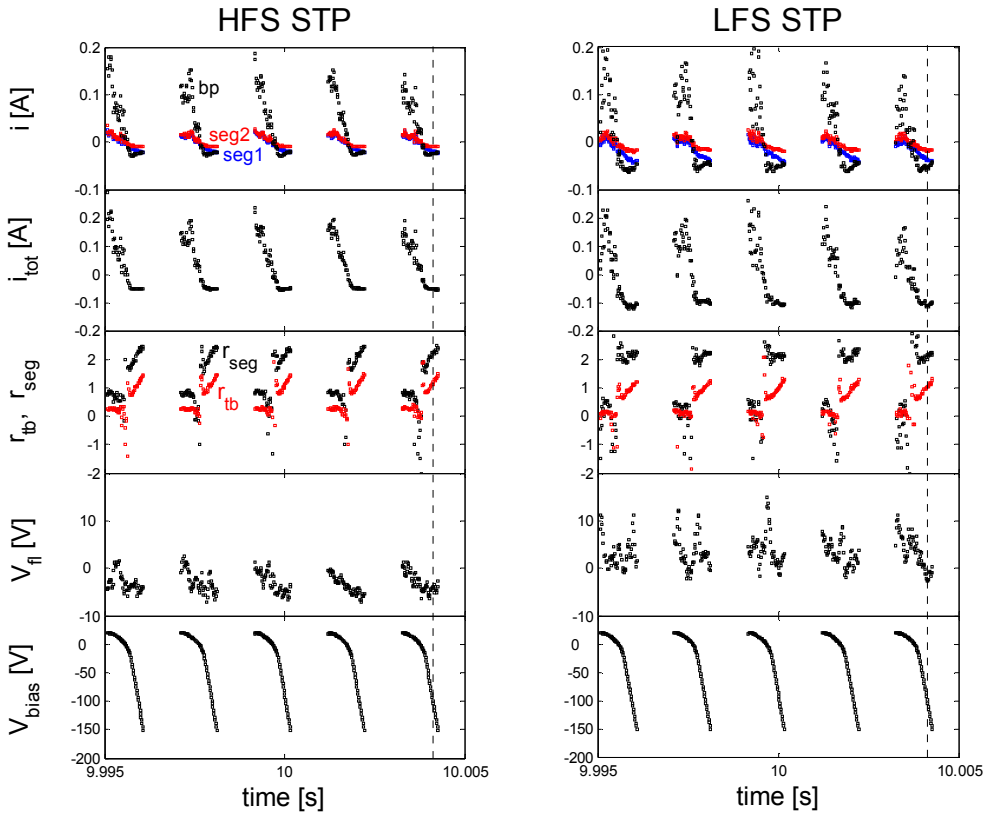

Figure 4.25. Typical raw signals from the STP electrodes measured ~1 cm outside the LCFS in TS discharge #42284. Left: STP facing the HFS. Right: STP facing the LFS. From top to bottom: currents measured by the tunnel segments and the back plate, sum of the tunnel and the back plate currents, ratio of ion currents to tunnel segments and the tunnel-to-back-plate ion current ratio, floating potential measured by the ring, bias voltage applied to the tunnel segments and the back plate. Vertical dashed lines intersect $V_{bias} = -100$ *V.*

At high V_{bias} , the magnitude of i_{bp} decreases whereas that of i_{seg1} increases. At higher V_{bias} the radial electric field E_r above the tunnel surface may become stronger and penetrate deeper towards the tunnel axis so that more ions are deflected towards the first segment rather than flowing to the back plate. Such variation of E_r with V_{bias} is observed in the simulations (figure 4.26).

The measured ion current ratios $r_{tb} = (i_{seg1} + i_{seg2}) / i_{bp}$ and $r_{seg} = i_{seg1} / i_{seg2}$ are plotted in the third row. Both r_{tb} and r_{seg} have singularities at V_f when the net current to the electrodes is zero. The remaining two panels show the time trace of V_f measured by the electrically floating ring and V_{bias} , respectively. V_f and V_{bias} seem to vary coherently. From the analysis of the V_f signal measured far from the plasma, this effect seems to be

caused by the perturbation of the non-ambipolarity near the tunnel entrance by the biasing of the tunnel electrodes into the regime of net electron collection, rather than by cable capacitance. The vertical dashed line intersects $V_{bias} = -100$ V at which $V_f << |V_{bias}|$ so that the corresponding values of r_{tb} and r_{seg} are expected to be close to those obtained from the PIC simulations.

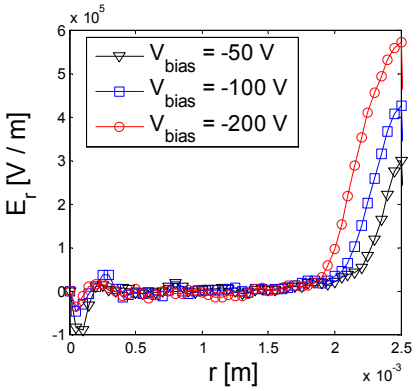

Figure 4.26. Radial electric field along the tunnel radius obtained from the PIC simulations for T_i = 20 eV, T_e = 10 eV, j_{sat} = 4 kA m^{-2}, B_t = 3.5 T and for three different values of the external bias voltage. E_r was measured 1 mm from the leading edge of segment 1.

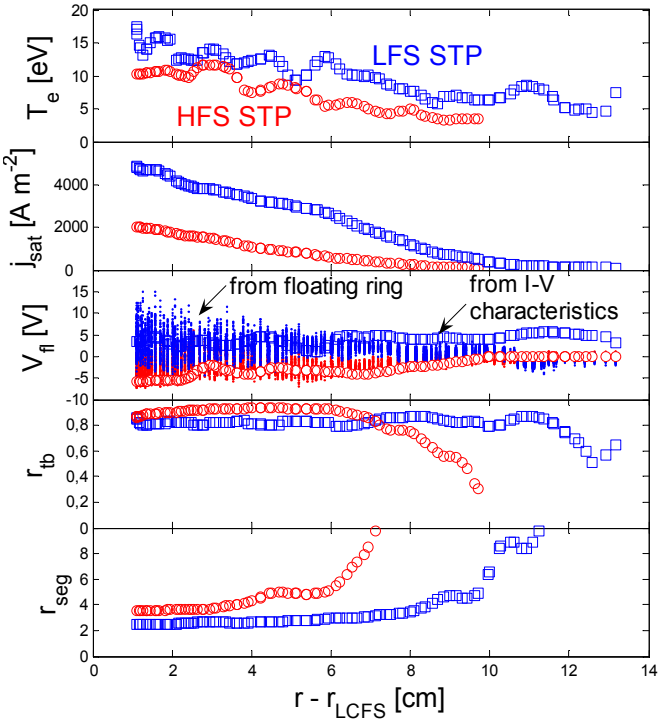

Figure 4.27. Radial profiles of electron temperature, ion saturation current density, floating potential, tunnel-to-back-plate ion current ratio and the ratio of ion current to tunnel segments (from top to bottom). HFS/LFS indicate the STPs facing the high-field side and the low-field side, respectively. T_e, j_{sat} and V_f were measured using the STP as a simple Langmuir probe. V_f is compared with the measurements from the electrically floating ring. TS discharge #42284 ($\langle n_e \rangle = 10^{19}$ m^{-3}, $B_t = 3.8$ T, $I_p = 0.5$ MA, $P_{tot} = 0.33$ MW).

The analysis of the rough data yields the radial profiles plotted in figure 4.27. As mentioned above, T_e, j_{sat} *and* V_f are obtained from standard Langmuir-probe analysis of i_{tot} versus V_{bias} (Eq. 1.15). The radial profiles of T_e and j_{sat} measured by each side of the STP are clearly asymmetric. Similar asymmetries are measured by other reciprocating probes in Tore Sure (see section 2.3.1.3 and [Gunn 2007, Kočan 2009]).

The floating potential obtained from Langmuir-probe analysis of the *I-V* characteristics is juxtaposed to V_f measured by the electrically floating ring located near the tunnel entrance. Both values of V_f are very similar.

Also plotted in figure 4.27 are the radial profiles of r_{tb} and r_{seg} measured at $V_{bias} - V_f \cong -100$ V. For a certain range of $r - r_{LCFS}$ (< 11 cm for the LFS STP and < 6 cm for the HFS STP) r_{tb} is almost independent of radius and decreases with radius for larger radii. This could be explained by two competing effects. While the MPS thickness above the tunnel scales with T_e (so that r_{tb} is expected to increase with T_e), at higher j_{sat}, r_{tb} tends to decrease because of stronger Debye shielding. Since both T_e and j_{sat} increases towards the LCFS, the actual radial dependence of r_{tb} could depend on which parameter, T_e or j_{sat}, has a dominant influence at given radii. This could also explain the variation of the HFS/LFS asymmetry of r_{tb} with radius (if r_{tb} was controlled by T_e only, one would expect to measure higher r_{tb} by the LFS STP for all radii). For $T_e \cong 5-15$ eV and $j_{sat} \cong 1-4$ k Am^{-2}, r_{tb} varies between 0.8 and 1. The experimental r_{tb} is close to that predicted by simulations (more systematic comparison is made below). It should be mentioned that the current measured by the back plate can be influenced by secondary electron emission due to ion impact as each secondary electron counts as a collected ion. In order to account for the secondary electron emission from the back plate, r_{tb} from the PIC simulations (in which the secondary electron emission is neglected) should divided by a factor $1+\delta$. Here δ is the secondary electron emission coefficient due to ion impact, averaged over the incident ion energies and impact angles. For stainless steel and for relevant ion impact energies, δ measured by Thomas [Thomas 1991] varies from 0.4 to 1.

The bottom row in figure 4.27 shows the radial profile of r_{seg} measured for $V_{bias} - V_f \cong -100$ V. r_{seg} decreases with radius up to 3 cm outside the LCFS for the HFS STP and up to 6 cm outside the LCFS for the LFS STP. For smaller radii r_{seg} is almost independent of radius. The decrease of r_{seg} towards the LCFS is intuitive. The probability that the ion will reach a distant part of the tunnel (i.e. segment 2) increases with the parallel ion velocity. The increase of T_i towards the LCFS (which is measured by RFA) should be, therefore, associated with a decrease of r_{seg}. In addition, the HFS STP measures higher r_{seg} than the LFS STP, indicating that the effective ion temperature on that side of the probe could be lower than on the LFS STP. Since the parallel flow is directed towards the LFS STP, such asymmetry in T_i is consistent with the kinetic model of Valsaque *et al.* [Valsaque 2000] as well as with the RFA measurements (section

2.3.1.3 and [Pitts 2003b, Kočan 2009]). In addition, PIC simulations also predict a decrease of r_{seg} with the increase of j_{sat}. In figure 4.27, j_{sat} increases monotonically towards the LCFS but, as mentioned above, r_{seg} saturates at certain radii. T_i is not measured for this discharges but it is typically well correlated with j_{sat} (i.e. both parameters increases towards the LCFS). Therefore, the saturation of r_{seg} could perhaps indicate that at high densities and temperatures the sensitivity of the STP to the variation of T_i becomes very weak. For $T_e \cong 5-15$ eV and $j_{sat} \cong 1-4$ kA m^{-2}, the experimental values of r_{seg} vary between 2 and 6. Except for $j_{sat} \cong 1$ kA m^{-2}, a similar range of r_{seg} is predicted by the PIC simulations.

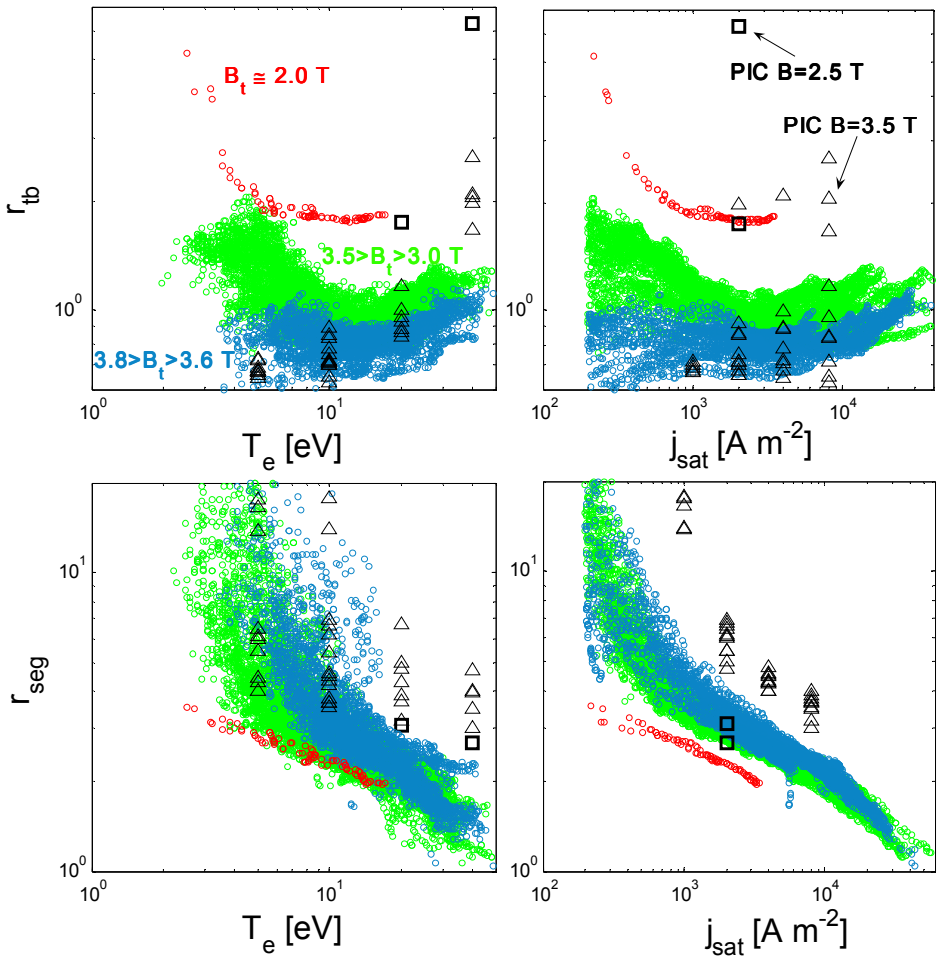

Figure 4.28. Tunnel-to-back plate ion current ratio (top row) and the ratio of ion currents to tunnel segments (bottom row) plotted against the electron temperature (left) and ion saturation current density (right). r_{tb} and r_{seg} are plotted for three different values of the toroidal magnetic field B_t. Data were measured by the LFS STP.
Also plotted are the current ratios obtained from the PIC simulations for two different values of B.

The experimental values of r_{tb} and r_{seg} were found to be close to that predicted by PIC simulations, at least for the discharge discussed above. In addition, the radial variation as well as the asymmetry of r_{tb} and r_{seg} measured by each side of the STP agrees roughly with theory. Therefore, the natural step to follow is to estimate T_i and T_e from r_{tb} and r_{seg}, using the calibration curves produced by PIC simulations. This is where the problems begin.

In figure 4.28, the ion current ratios measured by the LFS STP are compared with those obtained from the PIC simulations. Measurements from 136 reciprocations (comprising more than 13000 data points) are plotted in figure 4.28. The range of B_t is separated into three intervals, each plotted in different color. r_{tb} and r_{seg} are plotted against T_e and j_{sat} obtained from Langmuir probe analysis. Only the data measured for $T_e > 2\,\mathrm{eV}$ and $j_{sat} > 0.2\,\mathrm{A\ m^{-2}}$, characterized by a significant signal-to-noise ratio, are shown in figure 4.28.

For $T_e < 15\,\mathrm{eV}$ and $j_{sat} < 3\,\mathrm{kA\ m^{-2}}$, r_{tb} decreases with the increase of both T_e and j_{sat} (except at highest B_t for which the scatter of the data points is too large to identify any trends. For higher T_e and j_{sat} the trend is opposite. We shall note that the cross-correlation between T_e and j_{sat} is relatively strong (cross-correlation coefficient of 0.82), figure 4.29, and the individual effects of these parameters on r_{tb} thus cannot be decoupled. These observations suggest that for low-to-moderate T_e and j_{sat}, r_{tb} is affected mainly by the degree of the shielding of the probe tunnel from the unperturbed central column (so that r_{tb} tends to decrease with increasing j_{sat}) and becomes dominated by the MPS expansion (so that r_{tb} tends to increase with T_e) at moderate-to-high temperatures and densities. It must be also taken into account that for $T_e < 15\,\mathrm{eV}$ and $j_{sat} < 3\,\mathrm{kA\ m^{-2}}$ the shielding of the tunnel from the unperturbed central column might be so poor that the potential in the tunnel is nearly the same as the vacuum potential, and the current ratios are governed mainly by ballistic orbits, i. e. T_i has a strong effect.

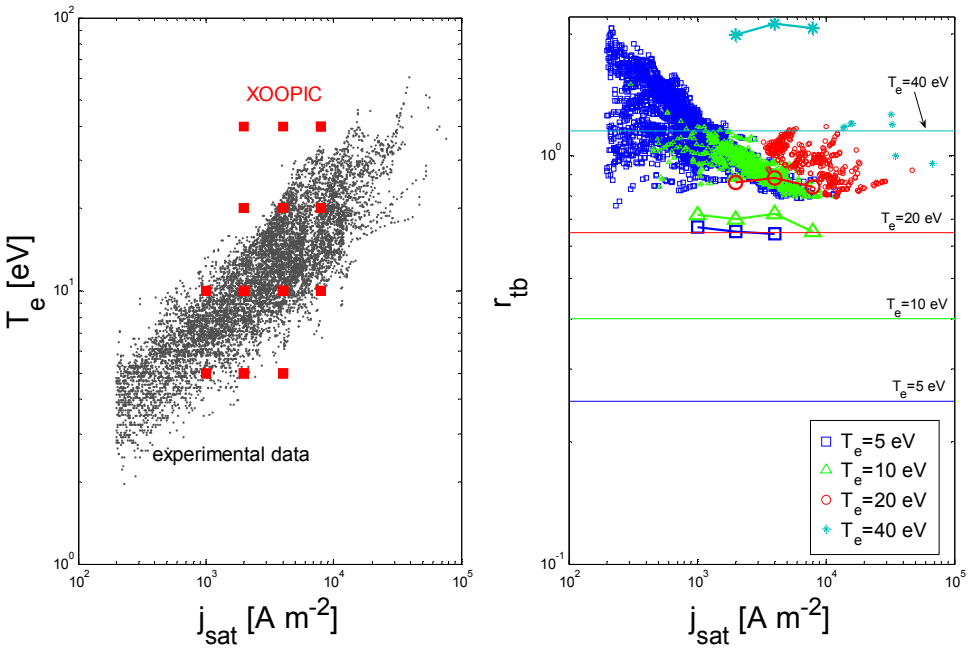

Figure 4.29. Left: Experimental data measured for B_t = 3 – 3.5 T (dots) compared with the database of all XOOPIC simulations for V_{bias} = -100 V (squares). Right: Tunnel-to-back-plate ion current ratio plotted against j_{sat}. The experimental data measured for B_t = 3 – 3.5 T and four discrete values of T_e (small symbols) are compared with PIC simulations for T_i = 2 T_e (large symbols) and with the results from a simple model (horizontal lines).

r_{tb} scales inversely with B which is consistent with theory; for low B the ions are less magnetized and are more easily deflected towards the tunnel wall. PIC simulations predict a similar dependence of r_{tb} on B. On the other hand, the measured dependences of r_{tb} on T_e and j_{sat} are not reproduced by PIC simulations. While the absolute values of r_{tb} measured at moderate T_e are similar for both simulations and experiment, r_{tb} from the PIC simulations increases monotonically with T_e and is practically independent of j_{sat}.

Figure 4.29 (left) shows all experimental data measured for $B_t = 3-3.5$ T as well as the PIC simulations performed for different combinations of T_e and j_{sat} and for $V_{bias} = -100$ V. The experimental range of T_e and j_{sat} is well covered by the PIC simulations except at highest as well as lowest values of T_e and j_{sat}. In the PIC simulations for $T_e = 40$ eV, the values of j_{sat} are lower than those measured experimentally at similar electron temperatures (as mentioned in section 4.1.4.2 the simulations for $j_{sat} > 8$ kA m^{-2} were not performed because of a unrealistically long time required for a single run). On the other hand, the simulations for $T_e = 5$ eV were performed for the values of j_{sat} that are up to a factor of 2 higher compared to those measured by the STP. Since the combination of high T_e and low j_{sat} (and vice versa) is

practically never measured in experiment, one can anticipate that the corresponding current ratios obtained from the PIC simulations will be outside the range of the experimental values. Such mismatch in r_{tb} between the PIC simulations and the experimental data for $T_e = 5$ eV and 40 eV is seen in figure 4.28.

More details about the dependence of r_{tb} on T_e are given in figure 4.29 (right). r_{tb} is plotted against j_{sat}. Only the experimental values measured at $B_t = 3 - 3.5$ T and for four discrete values of $T_e = 5$, 10, 20 and 40 eV (within ±1 eV) are shown. Also plotted are the values of r_{tb} obtained from the PIC simulations for the same set of T_e values (with $T_i = 2T_e$). Horizontal lines are the values of r_{tb} calculated from a simple geometrical assumptions addressed in section 4.1.2 (with the scaling of the L_{MPS} taken from [Gunn 1997], section 2.3.1.1). For both the PIC simulations and the experimental data, r_{tb} is almost independent of T_e for $T_e = 5 - 10$ eV and increases strongly with T_e for higher electron temperatures. This is in contrast to the model which predicts roughly linear increase of r_{tb} with T_e. In addition, except at highest T_e, r_{tb} given by the model is generally lower compared to the PIC simulations and the experimental data. This could be explained by the fact that in the cylindrical geometry L_{MPS} could be larger than that given by the slab geometry model [Gunn 1997], leading to higher values of r_{tb}.

r_{seg} measured experimentally (figure 4.28) decreases with both T_e and j_{sat} (however, we recall the strong correlation between these two parameters). The coherent variation of r_{seg} with B is, again, qualitatively consistent with the PIC simulations (see figure 4.22). However, as for the r_{tb}, the simulations and the experimental data are not matched. For example, for r_{seg} plotted against j_{sat} both the measurements and the simulations produce similar trends, but the PIC simulations predict r_{seg} which is a factor of 2-3 higher compared to the experimental values.

To summarize, the results discussed so far, the ion current ratios measured by the STP and obtained from the PIC simulations are characterized by some similar trends which agree qualitatively with theory. The disagreement between the simulations and the measurements as well as some ambiguous trends on the simulated r_{seg} does not allow interpreting the STP measurements for both T_i and T_e. The discrepancy between the simulations and the measurements could be e.g. due to the difference in the real dimensions of the STP electrodes and the idealized system assumed in the simulations. Since the ion current distribution along the tunnel decreases strongly with the distance from the tunnel entrance, r_{seg} is sensitive to the precise length of segment 1. If segment 1 was shorter compared to what is assumed in the PIC simulations (or the real attenuation of the incident ion flux by the dielectric at the tunnel orifice was stronger than that predicted by the PIC simulations), r_{seg} obtained from the PIC simulations would be overestimated. Such effects could partially explain the discrepancy seen in figure 4.28. Dissembling of the STP would be required in order to measure the precise length of the segments. Secondary electron emission from the back plate could explain the disagreement between the PIC simulations and the experimental data for r_{tb} at high T_e (at

high T_e the ion impact energies on the back plate might be also higher, producing higher secondary electron flux from the back plate that could underestimate of the measured values of r_{tb}). Also important for the validation of the XOOPIC results would be the benchmarking with another PIC code. Alternative solution is to abandon PIC simulations and to calibrate the probe for T_i and T_e measurements by comparing r_{tb} with T_e obtained from the Langmuir probe analysis of the STP *I-V* characteristics and r_{seg} with T_i measured by the RFA in similar plasmas, respectively.

4.3.4.4. Measurements of the large floating potentials in the ICRH power scan

Interesting results were obtained from the electrically floating ring in the ICRH power scan in which the LFS STP was magnetically connected with the ICRH antenna, figure 4.30. The LFS STP measured large V_f in the layer $z - z_{LCFS} = 6 - 10$ cm. Similar results were measured earlier by the Mach probes in Tore Supra [Colas 2007, Gunn 2008]. The amplitude of the V_f of the data plotted in figure 4.30 seems to increase with P_{ICRH} and saturates at high P_{ICRH}. However, in other discharges with $P_{ICRH} \cong 3.8\,\mathrm{MW}$, V_f did not exceed 70 V (#42359-#42361), indicating that P_{ICRH} might not be the only parameter which controls the magnitude of V_f (for these shots the plasma density and the edge safety factor varies by less than 10% and the plasma shape does not change between discharges). The HFS STP that was connected to the HFS limiter target measured $|V_f| < 15\,\mathrm{V}$ along the whole profile, meaning that the flux tube on the opposite side of the probe is not perturbed by the antenna. Large floating potentials are also obtained from the analysis of the *I-V* characteristics (figure 4.31) measured by the LFS STP. However, V_{bias} is not adapted to measure V_f higher than a few tens of volts. Therefore, no data are available in the radii where V_f is highest.

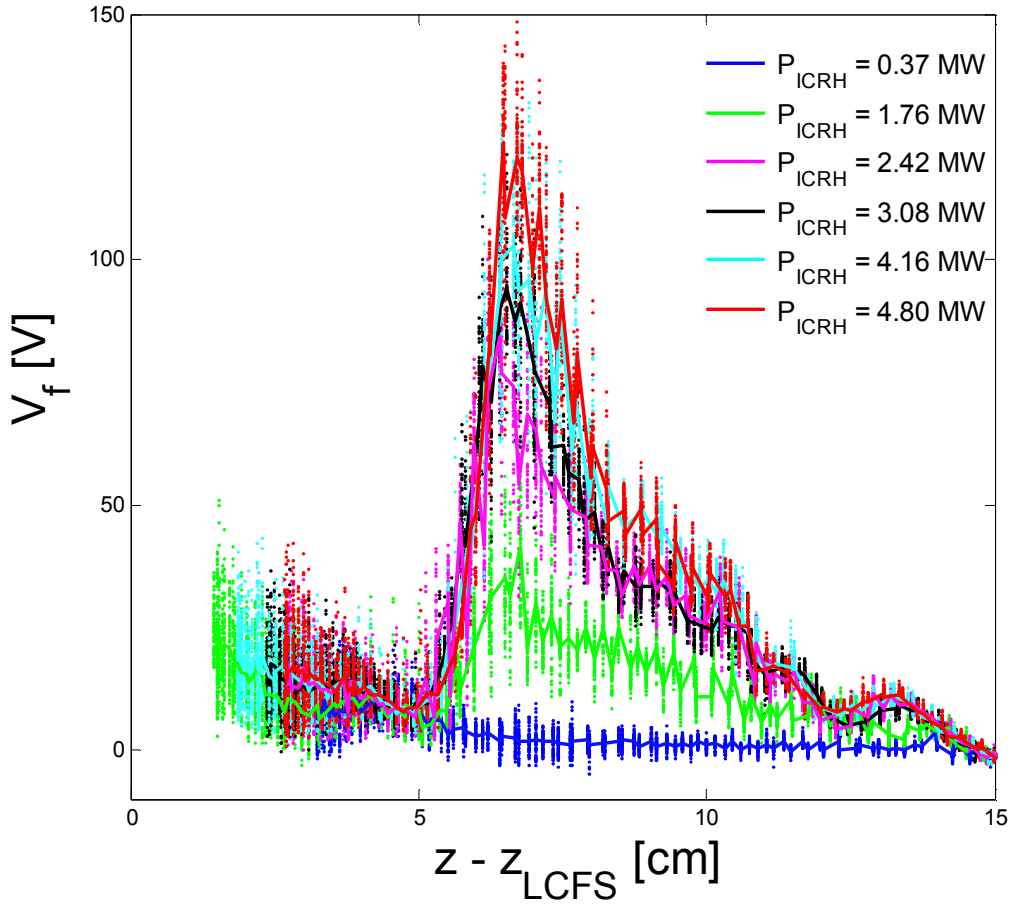

Figure 4.30. The floating potential V_f measured by the electrically floating ring on the LFS STP (connected magnetically to the ICRH antenna) in the ICRH power scan. V_f is plotted against the vertical distance from the LCFS. The data were measured in the TS discharges #42348, #42350, #42354, #42355 and #42357. The discharges were characterized by lower hybrid heating power $P_{LH} = 2.5 - 3\,MW$, volume averaged density $\langle n_e \rangle = 3.7 - 4.3 \cdot 10^{19}\,m^{-3}$, plasma current $I_p = 0.6\,MA$, toroidal magnetic field $B_t = 3.7\,T$, and safety factor at the LCFS $q_a \cong 8$. $|V_f| < 15\,V$ was measured by the HFS STP, connected magnetically to the HFS toroidal pump limiter.

The mechanism which causes the floating potentials on the flux tube connected to the ICRH antenna to increase by an order of magnitude above the electron temperature is not fully understood. The increase is believed to be generated by the strong electric field in front of the antenna [Gunn 2008]. The side of the probe that is not connected to the antenna but to the HFS of the toroidal pump limiter does usually not register large V_f, as it is the case of the measurements shown in figure 4.30. However, when the probe intersects the flux tube passing in front of the lower edge of the antenna box, large floating potentials are, surprisingly, registered also by the side of the probe that is not

connected to the antenna but to the HFS of the toroidal pump limiter (figure 5 in [Gunn 2008]).

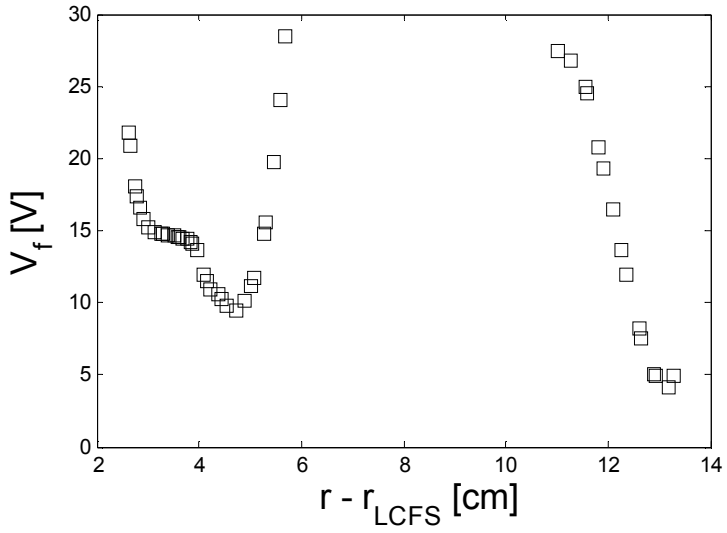

Figure 4.31. Radial profile of the floating potential obtained from the analysis of the I-V characteristics measured by the LFS STP connected to the ICRH antenna (TS discharge #42355, $P_{ICRH} = 4.8\,MW$, see captions to figure 4.30 for other macroscopic plasma parameters). Because of inappropriate bias voltages, no measurements of V_f are available for $r - r_{LCFS} = 6 - 11\,cm$.

Conclusions

The tokamak plasma boundary plays a critical role in controlling the confined region. An important step towards improving our understanding of the plasma surface interaction in tokamaks is the experimental study of the scrape-off layer plasma. This thesis addressed the measurement of ion temperature – an important but yet rarely measured quantity – in the SOL of the Tore Supra tokamak using a retarding field analyzer.

An independent validation of the RFA T_i measurements is not yet available due to a lack of simultaneous measurements with other relevant diagnostics. Therefore, a large part of the thesis focused on a study of the instrumental effects of RFAs and their influence on T_i measurements.

The attenuation of the ion current on the protective plate of the RFA was studied by means of self-consistent particle simulations. While the effect of the attenuation on T_i measurements was found to be negligible for the range of the plasma parameters and the bias voltages typically applied to the RFA slit plate, the attenuation of the incident ion current was found to be significant (factor of 1.7 – 3) and could lead to an underestimation of the collector current and the slit transmission factor. A less perturbing knife-edge geometry was proposed for the RFA protective plate.

Selective ion transmission through the RFA slit plate was analyzed by an analytical model and by self-consistent particle simulations. Even for relatively thick slit plates selective ion transmission accounts for an overestimation of T_i by less than 14% percent. Thick slit plates can be therefore used to advantage since they reduce the risk of melting during off-normal events, the neutral pressure inside the RFA cavity that can lead to electrical breakdown, and the positive space charge. The influence of slit plate misalignment with respect to the magnetic field as well as the influence of the electron repelling grid was proved to be negligible. Since the ion current transmission is almost independent of the misalignment angle, a tilted slit plate could be used as an effective method for preventing electrons from the plasma from entering the analyzer, independently of their kinetic energy. This could be of a large assistance e.g. in the experiments aimed at measurements of the energies of fast ions generated by the RF antennas.

The effect of positive space charge inside the RFA cavity and its influence on T_i measurements was studied. It was demonstrated that even for relatively strong ion currents, the potential inside the RFA cavity is dominated by the vacuum potential and the effect of space charge on T_i measurements can be neglected. In addition, the defocusing of the ion beam because of the positive space charge as well as large ion Larmor radii compared to the slit width (both neglected in the model) reduces further the influence of the positive space charge.

It is often observed experimentally that the upper region of the decaying part of the RFA *I-V* characteristics is rounded instead of being exponential. This is attributed to the non-Maxwellian (pre-sheath) part of the parallel ion velocity distribution. By analyzing the artificial *I-V* characteristics constructed from the ion velocity distribution at the sheath edge obtained from the kinetic Mach probe model [Chung 1988], it was

demonstrated that T_i calculated from the standard fit to the *I-V* characteristics can be overestimated by up to 12% if the non-exponential part of the characteristic is included in the fit. This error can be partially reduced by decreasing the upper limit of the collector current included in the fit.

In general, the influence of instrumental effects of RFAs addressed in this thesis was found to relatively low, increasing confidence in T_i measured by the RFA. On the other hand, perhaps one of the most important factors – the effect of impurities on T_i measurements – has not been addressed here. The model [Pitts 1991] that includes the effect of impurities needs to specify the fractions of the total flux carried by ions with a given charge state as well as their temperatures. Such measurements are not available in Tore Supra. Simultaneous measurements by a RFA and a plasma ion mass spectrometer (which measures the fluxes carried by different impurity ions) would be of large assistance in characterizing the effect of impurities.

The measurements of T_i (as well as other parameters like e.g. the electron temperature and density, the ion saturation current density, the heat flux density and the SOL e-folding lengths) in the Tore Supra SOL were compiled in Chapter 3.

In general, SOL T_i was systematically found to be higher that T_e by up to a factor of 7 which is consistent with earlier similar measurements reported from other tokamaks. Equal temperatures were measured only in detached plasma or at the highest plasma densities. The first continuous T_i / T_e profile from the edge of the confined region into the SOL was constructed using data from several tokamaks. It was demonstrated that T_i / T_e increases with radius and $T_i / T_e > 1$ already in the edge of the confined plasma. Relatively high ion-to-electron temperature ratios measured in the SOL of Tore Supra are, therefore, inconsistent with the assumption of the thermal equipartition, usually applied in the models.

T_i, T_e and T_i / T_e were found to be inversely proportional to the plasma density. The decrease of T_i and T_e with the plasma density could be explained by the conservation of the pressure in the SOL. The decrease of T_i / T_e with plasma density was found to be consistent with the increase of SOL ion-electron collisionality.

In helium plasma T_i was found to be higher by a factor of ~2 compared to T_i measured in deuterium plasma at similar plasma densities. This could be due to lower charge-exchange losses of ions in helium compared to deuterium as well as the presence of singly-charged helium ions in the helium discharges that could lead to an overestimation of T_i by up to a factor of 2 at highest plasma densities.

An increase of the radiated power fraction by about 30% (with all other parameters being fixed) was found to be associated with a decrease of SOL T_i by a factor of 2 but T_e was almost unaffected. The drop of T_i is also associated with the decrease of the power in the SOL by a similar factor, indicating that the power lost due to radiation comes mainly from the ion channel. A simple power balance model for the temperatures in the edge of the confined plasma, with radiation and equipartition being the only volumetric loss terms included, was employed. The model reproduces well a strong decrease of T_i with the increase of the radiated power and shows that the power loss on

electrons in the edge of the confined region can be, through ion-electron collisional coupling, compensated from the ion channel. Almost constant T_e independently of the radiated power is not reproduced by the model; the ratio T_i/T_e in the model remains roughly constant. A two dimensional model which comprises both the edge of the confined plasma as well as SOL needs to be employed to study further the edge temperatures.

A previously unobserved strong dependence of SOL T_i on the intensity of the toroidal magnetic field B_t was reported. While SOL T_i increases with B_t, SOL T_e was found to be almost independent of B_t. The only other parameter found thus far that strongly correlates with B_t is the core electron temperature. Measurements of the core ion temperature were not available. We speculate that, due to collisional coupling, core T_i increases with B_t similarly to core T_e and that SOL T_i is simply related to core T_i through radial transport. A mechanism that would decouple the SOL electrons from the core plasma needs to be identified. At the same time, data from the recent CXRS measurements in a magnetic field scan need to be analyzed in order to verify if T_i in the core and in the SOL changes in a similar way with B_t.

Dedicated experiments with the plasma contact point either on the inboard bumper limiters or on the outboard modular limiters have demonstrated that the poloidal asymmetry of the radial ion and electron energy transport in the SOL is similar to that of the particle transport. When the plasma contact point is on the inboard side, the temperature and density e-folding lengths are up to a factor of 5 longer compared to the outboard side plasma. These results are particularly important for the ITER start-up phase which is currently envisaged on the outboard modular limiters and for which the modelled peak heat loads on the limiters were found to be considerably close to the engineering limit. The parallel heat flux density at the LCFS was found to be proportional to the power in the SOL and inversely proportional to the parallel heat flux density e-folding length. These results imply that the outboard start-up is least advantageous with regards to power handling as it may be characterized by large, localized heat loads. Alternative start-up scenarios like, for example, the start-up on the inboard side, eventually in a detached regime should be evaluated.

The asymmetries of ion and electron temperatures measured by each side of the RFA were studied in a discharge during which the plasma contact point was steadily displaced upward along the outboard limiter, leading to the reversal of the parallel plasma flow. The asymmetry of T_i was found to be correlated with a change of the parallel Mach number $M_{//}$ but, in contrary to the theory [Valsaque 2002], T_i it does not reverse completely like $M_{//}$. This suggests that some of the assumptions in the kinetic modeling of the behavior of the pre-sheath surrounding the RFA [Valsaque 2002] might not be valid or the poloidal temperature gradient may play a role. Interestingly, a similar asymmetry is also measured for T_e. A model for the asymmetry of T_e is not yet available. In should be noted that one of the assumptions of the fluid Mach probe theory

[Hutchinson 1987, Gunn 2007b] is that the parallel electron velocity distribution is Maxwellian, in which case the same T_e would be measured by each side of the RFA.

Three ongoing projects aimed at the validation of RFA T_i measurements in Tore Supra were summarized in Chapter 4.

The selected results and the preliminary status of the analysis of the edge ion-to-electron temperature ratio measurements in the JET L-mode plasma were presented. Values of T_i / T_e up to 5 just inside the outboard midplane separatrix were obtained. Equal temperatures were measured just at $\rho \approx 0.8$. However, it is important to note that because of the uncertainly in the radial position of the T_e measurements by ECE due to the flux surface mapping (which was not resolved at the time of writing) these results are only preliminary.

SOL T_i was measured for a first in Tore Supra by charge exchange recombination spectroscopy. SOL T_i measured by the CXRS was found to be a factor of 4 higher compared to T_i measured by the RFA in a similar discharge. Further study is needed to track down the causes of this discrepancy. Some possible candidates (like e.g. the difference in the main plasma parameters during the CXRS and the RFA measurements, the effect of impurities on Ti measured by the RFA, etc.) were outlined.

A segmented tunnel probe for fast SOL T_i measurements has been designed, built, calibrated by particle simulations, and used for the first time in a large tokamak, Tore Supra. In some aspects the results obtained from the PIC simulations and in experiment are similar and consistent with simple theoretical assumptions. However, a significant quantitative disagreement was found between the PIC simulations and the experimental data, making the calculation of the SOL temperatures from the experimental data impossible. Further analysis of the geometrical effects as well as the benchmarking with other PIC codes is needed. Large positive floating potentials (V_f up to 150 V), possibly generated by a strong electric field in front of the ICRH antenna, were measured in the ICRH power scan by the side of the segmented tunnel probe that was magnetically connected with the ICRH antenna.

From the experimental data presented in this thesis as well as reported from other tokamaks there is a clear evidence that in most plasmas $T_\mathrm{i} > T_\mathrm{e}$ in the SOL, at the LCFS, and in the edge of the confined plasma. While the tendency for $T_\mathrm{i} > T_\mathrm{e}$ in the SOL can be explained by the cooling of the electrons in the Debye sheath (alternative explanation could be the heating of ions in the SOL due to strong turbulent fluctuations of plasma potential [Bellan 1993]), $T_\mathrm{i} > T_\mathrm{e}$ in the edge of the confined plasma is not understood. It is not yet clear whether the faster drop of T_e just inside the LCFS is due to the cooling of the edge electrons by the propagation of the cold electrons from the SOL into the edge or by the difference in the ion and electron energy transport in the edge plasma. A two-dimensional model which comprises both the edge plasma as well as the SOL needs to be employed to study further the edge temperatures. At the same time, an effort should be

devoted to the experimental study of ion temperature for different plasma geometry (circular and X-point plasma) or at different poloidal locations. Overlapping probe/CXRS T_i profiles and the comparison of T_i measured by different probes are important for the validation of T_i measurements.

The optimization of the ITER start-up phase and the design the ITER first wall requires understanding the correlation between the plasma contact point and the SOL e-folding lengths. Now that it appears we are reaching this point, it is necessary to study systematically the SOL parameters in the discharges with the HFS and LFS contact in order to increase the confidence of the recent results demonstrated on a limited dataset [Kočan 2009]. Detached HFS/LFS start-up, the scaling of the e-folding lengths with the main plasma parameters, measurements in elongated plasmas are certainly worthy of further investigation.

The ELM ion energies in the SOL have been measured only recently using a RFA [Pitts 2006]. These results, although obtained for a single set of the discharge parameters and a single value of the bias voltage, combined with the transient model for the propagation of an ELM filament in the SOL, demonstrated that in ITER the ELM ions can arrive at the non-divertor components with the energies above the sputtering threshold for all candidate materials for the ITER first wall. A more systematic investigation of the ELM ion energies in the SOL is clearly called for. We can study several important questions: What is the ELM ion energy as a function of the distance from the separatrix, SOL density, SOL/pedestal temperatures, ELM type, etc.?

During the thesis a collaborative project with the UKAEA (U.K.) aimed at the measurements of the far SOL ELM ion energies in the MAST tokamak using the Tore Supra RFA was established. The experiments in MAST were performed shortly before the submission of the thesis. Strong peaks of RFA collector current correlated with the peaks on D_α signal were measured during type I and type III ELMs up to 20 cm outside the separatrix. These results are being analyzed and are not included in this thesis. However, they suggest that ELMs can transport radially over a large distance a significant fraction of their pedestal energies, confirming the results from JET. At the same time, during the evaluation of this thesis a new RFA was designed for the ASDEX Upgrade tokamak within the framework of the collaboration between the CEA and the Max Planck Institut für Plasmaphysik in Garching, Germany. The probe is now under construction and is planned to be used to for studying the ELM ion energies as well as ion temperature in the ASDEX Upgrade plasma boundary.

References

[Adamek 2008] Adamek J, Kočan M, Panek R, Gunn J P, Martines E, Stöckel J, Ionita C, Popa G, Costin C, Brotankova J, Schrittwieser R and Van Oost G 2008 *Contrib. Plasma Phys.* **48** 1

[Allen 1976] Allen J E 1976 *J. Phys D: Appl. Phys.* **9** 2331

[Allen 1986] Allen J *et al* 1986 *Plasma Phys. Control. Fusion* **28** 101

[Amemiya 1989] Amemiya H 1989 *Jpn. J. Appl. Phys.* **28** 1109

[Amemiya 1994] Amemiya H and Uehara K 1994 *Rev. Sci. Instrum.* **65** 2607

[Andrew 2006] Andrew Y *et al* 2006 *Rev. Sci. Instrum.* **77** 10E913-1

[Asakura 1997] Asakura N, Koide Y, Itami K, Shimizu K, Tsuji-Iio S, Sakurai S and Sakasai A 1997 *J. Nucl. Mater.* **241-243** 559

[Asakura 2000] Asakura N, Sakurai S, Shimada M, Koide Y, Hosogane N, Itami K 2000 *Phys. Rev. Lett.* **84** 3093

[Asakura 2007] Asakura N 2007 *J. Nucl. Mater.* **363-365** 41

[ASDEX Team] ASDEX Team 1989 *Nucl. Fusion* **29** 1959

[Basiuk 2001] Basiuk V *et al* 2001 *Nucl. Fusion* **41** 477

[Behringer 1986] Behringer K *et al* 1986 *Proc 11th Int. Conf. on Plasma Phys. and Controlled Nuclear Fusion Research (Kyoto 1986)* IAEA-CN-47/A-IV-1

[Bellan 1993] Bellan P M 1993 *Plasma Phys. Control. Fusion* **35** 169

[Bethe 1979] Bethe H A 1979 *Physics Today* (May 1979)

[Bogen 1995] Bogen P, Hey J D, Hintz E, Lie Y T, Rusbüldt D and Samm U 1995 *J. Nucl. Mater.* **220-222** 472

[Bohm 1993] Bohm C and Perrin J 1993 *Rev. Sci. Instrum.* **64** 31

[Bush 1990] Bush C E *et al* 1990 *J. Nucl. Mater.* **176-177** 786

[Callen 1990] Callen J D 1990 *Phys Fluids B* **2** 2869

[Carpentier 2009] Carpentier S *et al* 2009 *J. Nucl. Mater.* **390-391** 955

[Cebulla 1998] Cebulla R *et al* 1998 *J. Appl. Phys.* **83** 1087

[Charles 2000] Charles C *et al* 2000 *Phys. Plasma* **7** 5232

[Chodura 1982] Chodura R 1982 *Phys. Fluids* **25** 1628

[Chung 1988] Chung K S and Hutchinson I H 1988 *Phys. Rev. A* **38** 4721

[Cohen 1979] Cohen S A and McCracken G M 1979 *J. Nucl. Mater.* **84** 157

[Colas 2007] Colas L *et al* 2007 *J. Nucl. Mater.* **363-365** 555

[Connor 1993] Connor J W 1993 *Plasma Phys. Control. Fusion* **35** B293

[Conway 2008] Conway G B 2008 *Plasma Phys. Control. Fusion* **50** 124026

[Dejarnac 2007] Dejarnac R, Gunn J P, Stöckel J, Adámek J, Brotánková J and Ionita C 2007 *Plasma Phys. Control. Fusion* **49** 1791

[Demidov 1999] Demidov V I, Ratynskaia S V and Rypdal K 1999 *Rev. Sci. Instrum.* **70** 4266

[Demidov 1999b] Demidov V I, Ratynskaia S V, Armstrong R J and Rypdal K 1999 *Phys. Plasmas* **6** 35

[Dionne 2005] Dionne M 2005 *Master Thesis, Université du Québec, INRS Energie, Matériaux, et Télécommunications*

[Doyle 2007] Doyle E J *et al* 2007 *Nucl. Fusion* **47** S18

[Druyvesteyn 1930] Druyvesteyn M J 1930 *J. Phys.* **64** 781
[Dudson 2008] Dudson B D *et al* 2008 *Plasma Phys. Control. Fusion* **50** 124012
[El Shaer 1981] El Shaer M 1981 *PhD thesis* Scientific and Medical University of Grenoble
[Enloe 1992] Enloe C L and Shell J R 1992 *Rev. Sci. Instrum.* **63** 1788
[Erents 1982] Erents S K and Stangeby P C 1982 *J. Nucl. Mater.* **111-112** 165
[Erents 2004] Erents S K, Pitts R A, Fundamenski W, Gunn J P and Matthews G F 2004 *Plasma Phys. Control. Fusion* **46** 1757
[Federici 2007] Federici G *et al* 2007 J. Nucl. Mater. **363-365** 346
[Fedorczak 2009] Fedorczak N, Gunn J P, Ghendrih Ph, Monier-Garbet P and Pocheau A 2009 *J. Nucl. Mater.* **390-391** 368
[Fundamenski 2006] Fundamenski W, Pitts R A and JET EFDA contributors 2006 *Plasma Phys. Control. Fusion* **48** 109
[Fundamenski 2007] Fundamenski W, Pitts R A and JET EFDA contributors 2007 *J. Nucl. Mater.* **363-365** 319
[Garcia-Cortes 2000] Garcia-Cortes I *et al* 2000 *Plasma Phys. Control. Fusion* **42** 389
[Giruzzi 2009] Giruzzi G on behalf of the Tore Supra team 2009 *Tore Supra special issue, Fus. Sci. Tech. (to be published)*
[Gohar 2001] Gohar Y 2001 *Fusion Engineering and Design* **58-59** 1097
[Goto 1972] Goto K and Ishikawa K 1972 *Rev. Sci. Instrum.* **43** 427
[Gowers 1995] Gowers C *et al* 1995 *Rev. Sci. Instrum.* **66** 471
[Gribov 2004] Gribov Y *Control System Design and Assessment (CSD), Appendix B: Magnetic configuration and poloidal field scenarios, ITER document N 19 RI 14 R0.1* (August 2004)
[Gunn 1997] Gunn J P 1997 *Phys. Plasmas* **4** 4435
[Gunn 2001] Gunn J P 2001 Phys Plasmas **8** 1040
[Gunn 2002] Gunn J P *et al* 2002 *Czech J. Phys.* **52** 1107
[Gunn 2002b] Gunn J P *et al* 2002 *Proc. 29th EPS Conference on Plasma Physics and Contr. Fusion Montreux, 17-21 June 2002 ECA Vol.* ***26 B****, P-5.093*
[Gunn 2007] Gunn J P *et al* 2007 *J. Nucl. Mater.* **363-365** 484
[Gunn 2007b] Gunn J P and Fuchs V 2007 *Phys. Plasmas* **14** 032501
[Gunn 2008] Gunn J P *et al* 2008 *Proc. 22nd IAEA Int. Conference on Fusion Energy (Geneva 2008)*
[Gunn 2009] Gunn J P, Petrzilka V, Ekedahl A, Fuchs V, Gauthier E, Goniche M, Kočan M and Saint-Laurent F 2009 *J. Nucl. Mater.* **390-391** 90
[Gunther 1990] Gunther K, Herrmann A, Laux M, Pech P and Reiner H-D 1990 *J. Nucl. Mater.* **176-177** 236
[Guo 1996] Guo H Y, Matthews G F, Davies S J, Erents S K, Horton L D, Mond R D and Stangeby P C 1996 *Contrib. Plasma Phys.* **36** 81
[Heifetz 1982] Heifetz D *et al* 1982 *J. Comput. Phys.* **46** 309
[Hey 1994] Hey J D, Lie Y T, Rusbüldt D and Hintz E 1994 *Contrib. Plasma Phys.* **34** 725
[Hoffman 2002] Hoffman E A and Stacey W M 2002 *Fusion Engineering and Design* **63-64** 87

[Höthker 1990] Höthker K, Belitz H-J, Bieger W and Amemiya H 1990 *Rev. Sci. Instrum.* **61** 114
[Huber 2000] Huber A, Pospieszczyk A, Unterberg B, Brix M, Mertens Ph, Philipps V and Schweer B 2000 *Plasma Phys Control. Fusion* **42** 569
[Hutchinson 1987] Hutchinson I H 1987 *Phys. Fluids* **30** 3777
[Hutchinson 1991] Hutchinson I 1991 *Phys. Fluids B* **3** 847
[Jaquinot 1999] Jaquinot J and the JET Team 1999 *Plasma. Phys. Control. Fusion* **41** A13
[Jacquinot 2004] Jacquinot J and Hoang G T 2004 *Plasma Sci. and Technol.* **6** 2101
[Jiang 2005] Jiang N *et al* 2005 *Nucl. Instr. and Meth. In Phys. Res. B* **229** 508
[Johnson 2003] Johnson S D, El-Gomati M M and Enloe L 2003 *J. Vac. Sci. Technol. B* **21** 350
[Katsumata 1967] Katsumata I and Okazaki M 1967 *Jpn. J. Appl. Phys.* **6** 123
[Kim 1995] Kim G-H, Hershkowitz N, Diebold N A and Cho M-H 1995 *Phys. Plasmas* **2** 3222
[Kimura 1978] Kimura H *et al* 1987 *Nucl. Fusion* **18** 1195
[Kimura 1979] Kimura H, Odajima K, Sugie T and Maeda H 1979 *Jpn. J. Appl. Phys.* **18** 2275
[Kirnev 2004] Kirnev G S *et al* 2004 *Plasma Phys. Control. Fusion* **46** 621
[Kočan 2005] Kočan M, Pánek R, Gunn J P, Stöckel J and Skalný J D 2009 *Proc. 32nd EPS Conference on Contr. Fusion and Plasma Physics (Tarragona, June 27 – July 1) ECA Vol. **29C**, P-2.082*
[Kočan 2006] Kočan M 2006 *Master thesis, Comenius University*
[Kočan 2007] Kočan M, Pánek R, Stöckel J, Hron M, Gunn J P and Dejarnac R 2007 *J. Nucl. Mater.* **363-365** 1436
[Kočan 2008] Kočan M, Gunn J P, Pascal J-Y, Bonhomme G, Fenzi C, Gauthier E and Segui J-L 2008 *Plasma Phys. Control. Fusion* **50** 125009
[Kočan 2008b] Kočan M *et al* 2008 *Proc. 35th EPS Conference on Plasma Physics (Hersonissos, June 9 – 13) ECA Vol. **32D**, P-1.006*
[Kočan 2008c] Kočan M, Gunn J P, Komm M, Pascal J-Y, Gauthier E and Bonhomme G 2008 *Rev. Sci Instrum.* **79** 073502
[Kočan 2009] Kočan M and Gunn J P 2009 *"First evidence for poloidal asymmetries of radial ion energy transport by ion temperature measurements in the scrape-off layer of Tore Supra" submitted to 36th EPS Conference on Plasma Physics (Sofia, June 29 – July 3)*
[Kočan 2009b] Kočan M *et al* 2009 *J. Nucl. Mater.* **390-391** 1074
[Kočan 2009c] Kočan M *et al* 2009 *"Influence of the plasma density and the radiated power fraction on the Tore Supra scrape-off layer", submitted to Plasma Phys. Control. Fusion (2009)*
[Kojima 1984] Kojima H, Sugari H, Mori T, Toyada H and Okuda T 1984 *J. Nucl. Mater.* **128-129** 965
[Kreter 2001] Kreter A 2001 *PhD thesis, Düsseldorf University*
[LaBombard 2004] LaBombard B *et al* 2004 *Nucl. Fusion* **44** 1047
[Laframbois 1990] Laframbois G J and Rubinstein J 1990 *Phys. Fluids* **19** 1976
[Lawson 1957] Lawson J D 1957 *Proc. Phys. Soc. B* **70** 6

[Lefaucheux 2006] Lefaucheux P 2006 *Proc. Atelier analyse de plasmas par sondes électrostatiques 8/17*, 14 – 16 June, Saracenas, France
[Lloyd 2007] Lloyd *et al* 2007 *Nucl. Fusion* **47** S658-S667
[Loarte 2007] Loarte A *et al* 2007 *Nucl. Fusion* **47** S203
[Luna 2004] Luna E de la *et al* 2004 *Rev. Sci. Instrum.* **75** 3831
[Manos 1982] Manos D M, Budny R, Satake T and Cohen S A 1982 *J. Nucl. Mater.* **111-112** 81
[Maeda 1997] Maeda M, Uehara K and Amemiya H 1997 *Jpn. J. Appl. Phys.* **36** 6992
[Matthews 1984] Matthews G F 1984 *J. Phys. D: Appl. Phys.* **17** 2243
[Matthews 1985] Matthews G F 1985 *PhD thesis* University of Oxford
[Matthews 1989] Matthews G F 1989 *Plasma Phys. Control. Fusion* **31** 841
[Matthews 1990] Matthews G F, Pedgely J M, Pitts R A and Stangeby P C 1990 *J. Nucl. Mater.* **176-177** 1032
[Matthews 1991] Matthews G F, Pitts R A, McCracken G M and Stangeby P C 1991 *Nucl. Fusion* **31** 1495
[Matthews 1994] Matthews G F 1994 *Plasma. Phys. Control. Fusion* **36** 1595
[Matthews 1997] Matthews G F 1997 *J. Nucl. Mater.* **241-243** 450
[McCracken 1987] McCracken G M *et al* 1987 *J. Nucl. Mater.* **145-147** 181
[Mizuuchi 2005] Mizuuchi T *et al* 2005 *J. Nucl. Mater.* **337–339** 332
[Molvik 1981] Molvik A W 1981 *Rev. Sci. Instrum.* **52** 704
[Mott-Smith 1926] Mott-Smith H M and Langmuir I 1926 *Phys. Review* **28** 727
[Nachtrieb 2000] Nachtrieb R 2000 *PhD thesis, Massachusetts Institute of Technology*
[Nachtrieb 2000b] Nachtrieb R, LaBombard B and Thomas E 2000 *Rev Sci. Instrum.* **71** 4107
[Naulin 2007] Naulin V 2007 *J. Nucl. Mater.* **363-365** 24
[Nedzelskiy 2006] Nedzelskiy I S, Silva C, Figueiredo H, Fernandes H and Varandas C A F 2006 *Rev. Sci. Instrum.* **77** 10E729-1
[Negus 2006] Negus C R *et al* 2006 *Rev. Sci. Instrum.* **77** 10F102-1
[Nifnecker 1999] Nifenecker H, David S, Loiseaux J M and Giorni A 1999 *Progress in Particle and Nuclear Physics* **43** 683-827
[Olthoff 1994] Olthoff J K *et al* 1994 *J. Appl. Phys.* **75** 116
[O'Rourke 1985] O'Rourke J *et al* 1985 *Proc. 12th EPS Conf. (Budapest 1985 vol 1 155)*
[Pánek 2004] Pánek R, Pitts R A, Gunn J P and Erents S K 2004 *Czech J. Phys.* **54** 150
[Pégourié 2009] Pégourié B *et al* 2009 *J. Nucl. Mater.* **390-391** 550
[Pitts 1989] Pitts R A, McCracken G M and Matthews G F 1989 *J. Nucl. Mater.* **162-164** 568
[Pitts 1991] Pitts R A 1991 *PhD thesis, University of London*
[Pitts 1991b] Pitts R A 1991 *Phys. Fluids* B **3** 2871
[Pitts 1996] Pitts R A 1996 *Contrib. Plasma Phys.* **36** 87
[Pitts 2003] Pitts R A, Chavan R, Davies S J, Erents S K, Kaveney G, Matthews G F, Neill G, Vince J E and Ďuran I 2003 *Rev. Sci. Instrum.* **74** 4644

[Pitts 2003b] Pitts R A *et al* 2003 *30th EPS Conference on Contr. Fusion and Plasma Phys. St. Petersburg, 7-11 July 2003 ECA Vol.* ***27A****, P-2.84*

[Pitts 2006] Pitts R A, Fundamenski W, Erents S K, Andrew Y, Loarte A, Silva C and JET-EFDA contributors 2006 *Nucl. Fusion* **46** 82

[Pitts 2007] Pitts R A *et al* 2007 *J. Nucl. Mater.* **363-365** 505

[Press 1992] Press W H, Teukolsky S A, Vetterling W T and Flannery B P 1992 *Numerical Recipes in Fortran 77*, Cambridge University Press, Cambridge, Chap. 16

[Radford 1996] Radford G, Chankin A, Corrigan G, Simonini R and Spence J *et al* 1996 *Contrib. Plasma Phys.* **26** 187

[Ratynskaia 2002] Ratynskaia S V, Demidov V I and Rypdal K 2002 *Rev. Sci. Instrum* **73** 4232

[Raychaudhuri 1999] Raychaudhuri S 1999 *Contrib. Plasma Phys.* **39** 359

[Reich 2004] Reich M, Wolfrum E, Schweinzer J, Ehmler H, Horton L D, Neuhauser J and ASDEX Upgrade Team 2004 *Plasma Phys. Control. Fusion* **46** 797

[Reich 2004b] Reich M, Wolfrum E, Horton L D, Schweinzer J, Neuhauser J and ASDEX Upgrade Team 2004 *31st EPS Conf. on Plasma Physics (London, 28 June – 2 July 2004)*

[Reiter 1991] Reiter D, Börner P, Küppers B, Baelmans M, and Maddison G 1991 *Final report on KFA-NET contract 428/90-8/FU-D*

[Reiter 1991b] Reiter D *et al* 1991 *Plasma Phys. Control. Fusion* **33** 1579

[Riyopoulos 1996a] Riyopoulos S 1996 *Phys. Plasmas* **3** 2511

[Riyopoulos 1996b] Riyopoulos S 1996 *Phys. Plasmas* **3** 4355

[Rudakov 2002] Rudakov D L *et al* 2002 *Plasma Phys. Control. Fusion* **44** 717

[Saarelma 2005] Saarelma S *et al* 2005 *Plasma Phys. Control. Fusion* **47** 713

[Samm 1993] Samm U *et al* 1993 *Plasma Phys. Control. Fusion* **35** 167

[Shats 1997] Shats M G, Rudakov D L, Boswell R W and Borg G G 1997 *Phys. Plasmas* **4** 3629

[Shimada 2007] Shimada M *et al* 2007 *Nucl. Fusion* **47** S1

[Simpson 1961] Simpson J A 1961 *Rev. Sci. Instrum.* **32** 1283

[Spitzer 1962] Spitzer L1962 *Physics of Fully Ionized Gases, 2nd ed. (Interscience, New York, 1962)*

[Stacey 2002] Stacey W M *et al* 2002 *Fusion Engineering and Design* **63-64** 81

[Staib 1972] Staib P 1972 *Vacuum* **22** 481

[Staib 1977] Staib P and Dinklage U 1977 *J. Phys. E: Sci. Instrum.* **10** 914

[Staib 1980] Staib P 1980 *J. Nucl. Mater.* **93-94** 351

[Staib 1982] Staib P 1982 *J. Nucl. Mater.* **111-112** 109

[Stangeby 1982] Stangeby P C 1982 *J. Phys. D: Appl. Phys.* **15** 1007

[Stangeby 1983] Stangeby P C, McCracken G M, Erents S K, Vince J E and Wilden R 1983 *J. Vac. Sci. Technol. A* **1** 1302

[Stangeby 1984] Stangeby P C 1984 *Phys. Fluids* **27** 2699

[Stangeby 2000] Stangeby P C 2000 *The Plasma Boundary of Magnetic Fusion Devices (Institute of Physics Publishing 2000)* p 73

[Stangeby 2000b] Stangeby P C 2000 *The Plasma Boundary of Magnetic Fusion Devices (Institute of Physics Publishing 2000)* p 649
[Stangeby 2000c] Stangeby P C 2000 *The Plasma Boundary of Magnetic Fusion Devices (Institute of Physics Publishing 2000)* p 81-82
[Stangeby 2000d] Stangeby P C 2000 *The Plasma Boundary of Magnetic Fusion Devices (Institute of Physics Publishing 2000)* p 160
[Stangeby 2000e] Stangeby P C 2000 *The Plasma Boundary of Magnetic Fusion Devices (Institute of Physics Publishing 2000)* p 95
[Staudenmaier 1980] Staudenmaier G, Staib P, Poschenrieder W 1980 *J. Nucl. Mater.* **121-126** 121
[Stenzel 1982] Stenzel R L *et al* 1982 *Rev. Sci. Instrum.* **57** 1027
[Stöckel 1999] Stöckel J *et al* 1999 *Plasma Phys. Control. Fusion* **41** A577
[Stöckel 2006] Stöckel J *et al* 2006 *Problems of Atomic Science and Technology No.6 Series: Plasma Physics (12) 19-23*
[Strachan 1985] Strachan J D *et al* 1985 *12th Eur. Conf. on Controlled Fusion and Plasma Physics* (Budapest, Hungary) part 1, p. 263
[Tagle 1987] Tagle J A, Stangeby P C and Erents S K 1987 *Plasma Phys. Control. Fusion* **29** 297
[Thomas 1991] Thomas E W 1991 *Suppl. Nucl. Fusion* **1** 79
[Uehara 1998] Uehara K, Tawakami T, Amemiya H, Höthker K, Cosler A and Bieger W 1998 *Nucl. Fusion* **38** 1665
[Valsaque 2002] Valsaque F, Manfredi G, Gunn J P and Gauthier E 2002 *Phys. Plasmas* **9** 1806
[Van Rompuy 2007] Van Rompuy T, Gunn J P, Dejarnac R, Stöckel J and Van Oost G 2007 *Plasma Phys. Control. Fusion* **49** 619
[Verboncoeur 1995] Verboncoeur J P, Langdon A B and Gladd N T 1995 *Comp. Phys. Comm.* **87** 199-211
[Wagner 1982] Wagner F *et al* 1982 *Phys. Rev. Lett.* **49** 1408
[Wampler 1981] Wampler W R *et al* 1981 *J. Nucl. Mater.* **102** 304
[Wampler 1982] Wampler W R 1982 *Appl. Phys. Lett.* **41** 335
[Wampler 1983] Wampler W R and Manos D M 1982 *J. Vac. Sci. Technol. A* **1** (2) 827
[Wan 1986] Wan A S, Yang T F, Lipschultz B and LaBombard B 1986 *Rev. Sci. Instrum.* **57** 1542
[Winter 1990] Winter J 1990 *J. Nucl. Mater.* **176-177** 14
[Wootton 1990] Wootton A J *et al* 1990 *Phys Fluids B* **12** 2879
[Zou 2000] Zou Y 2000 *PhD Thesis, University of Maryland*
[Zou 2002] Zou Y *et al* 2002 *Phys. Rev. Spec. Topics - Accelerators and beams* **5** 072801